Thermomechanical modelling and simulation of laser powder bed fusion processes

von der Fakultät Maschinenbau
der Technischen Universität Dortmund
zur Erlangung des akademischen Grades

Doktor-Ingenieur (Dr.-Ing.)

genehmigte Dissertation

von

M.Sc. Isabelle Viktoria Noll

aus Lünen

Vorsitz:	Prof. Dr.-Ing. habil. F. Walther
Hauptreferent:	Prof. Dr.-Ing. habil. A. Menzel
Korreferenten:	Prof. Dr.-Ing. J. Mergheim
	JProf. Dr.-Ing. P. Woizeschke
Tag der Einreichung:	22.10.2023
Tag der mündlichen Prüfung:	26.02.2024

"Let us choose for ourselves our path in life, and let us try to strew that path with flowers."

Émilie du Châtelet (1706 − 1749)

Acknowledgements

Zusammenfassung

Die vorliegende Arbeit behandelt einen neuartigen mikromechanisch motivierten Rahmen zur Modellierung und Simulation von Laser-Pulver-Bett-Fusion (LPBF) Prozessen. LPBF Verfahren gehören zur additiven Fertigung, welche die schichtweise Herstellung von Bauteilen ermöglicht. (Metallische) Partikel einer Pulverschicht werden durch einen Laserstrahl selektiv geschmolzen, um ein Bauteil zu fertigen. Dadurch ergeben sich innovative Möglichkeiten hinsichtlich Design, Struktur, Materialkombinationen und maßgeschneiderten Teilen. Aufgrund des hohen Temperatureintrags treten komplexe thermische, mechanische und metallurgische Phänomene auf, darunter auch Phasenumwandlungen von Pulver über geschmolzenes zu wieder erstarrtem Material. Diese Hochtemperaturzyklen mit schnellem Aufheizen und Abkühlen verursachen verschiedene Defekte, wie zum Beispiel Hohlräume, Verzug und Eigenspannungen. Um die verschiedenen Fehler eines mit LPBF hergestellten Werkstücks besser vorhersagen zu können, sind neue Ansätze erforderlich. Der erste Schwerpunkt dieser Arbeit liegt auf der Entwicklung eines physikalisch motivierten Materialmodells, das thermodynamisch konsistent ist und auf der Minimierung der freien Energiedichte basiert. Dieses Modell wird im kleinen Maßstab einer einzelnen Schmelzspur angewendet. Im zweiten Teil der Arbeit wird ein Multiskalen-Ansatz entwickelt, der das Phasentransformationsmodell mit der Methode der inhärenten Dehnung kombiniert, um ein vollständiges Teil simulieren zu können. Dieses stellt im Hinblick auf physikalische Genauigkeit und Rechenzeit einen vernünftigen Kompromiss dar. Hierfür wird ein vollständig thermomechanisch gekoppelter Framework verwendet, welcher mithilfe des kommerziellen Finite Elemente Programms Abaqus gelöst wird. Die Simulationen werden auf die α-β-Titanaluminiumlegierung Ti_6Al_4V angewendet, die je nach Abkühlgeschwindigkeit eine unterschiedliche Zusammensetzung der Mikrostruktur entwickelt. Daher wird im letzten Teil der Arbeit ein Festkörper-Phasentransformationsansatz mit einer neuartigen Dissipationsfunktion vorgestellt, um das entsprechende kontinuierliche Zeit-Temperatur-Umwandlungsschaubild modellieren zu können. Das thermodynamisch und physikalisch fundierte Modell wird anschließend auf LPBF-Temperaturprofile auf lokaler Ebene angewendet.

Abstract

The present work deals with a novel micromechanically motivated framework for the modelling and simulation of laser powder bed fusion (LPBF) processes. LPBF processes belong to additive manufacturing (AM) which allows the layer-wise manufacturing of components. (Metallic) particles of a powder layer are selectively molten by a laser beam to construct a part. This opens up innovative possibilities in terms of design, structure, material combinations and custom-made parts. Due to the high temperature input, complex thermal, mechanical and metallurgical phenomena occur, including phase changes from powder to molten to re-solidified material. These high temperature cycles of rapid heating and cooling cause diverse defects such as voids, warpage and residual stresses. New approaches are necessary in order to better predict the various defects of a workpiece manufactured with LPBF. The first focus of this work is set on developing a physically well-motivated material model that is thermodynamically consistent based on the minimisation of the free energy density. This model is then applied to the small scale of a single melt track. Secondly, a multiscale approach is developed combining the phase transformation model with the inherent strain (IS) method to simulate a complete part. This represents a reasonable compromise in view of physical accuracy and computational time. For this purpose, a fully thermomechanically coupled framework is employed using the commercial finite element programme Abaqus. The material used for the simulations is the α-β titan aluminium alloy Ti_6Al_4V, which developes a different microstructure composition based on the cooling rate. Therefore, in the last part of the work, a solid-state phase transformation approach with a novel dissipation function is presented in order to be able to model the respective continuous cooling transformation diagram. The thermodynamically and physically sound model is then applied to LPBF temperature profiles at the local scale.

Publications

This thesis is based on the following peer-reviewed journal articles, which were either published or submitted during the progress of this thesis. Alterations of the original articles were made whenever considered relevant to, e.g. prevent repetitions, strengthen the understanding and improve the reading flow of this work.

1. T. Bartel, I. Guschke, A. Menzel, Towards the simulation of Selective Laser Melting processes via phase transformation models, *Journal of Computers & Mathematics with Application*, 78(7):2267–2281, 2019 [14].

2. I. Noll, T. Bartel, A. Menzel: A computational phase transformation model for Selective Laser Melting processes, *Computational Mechanics*, 66:1321–1342, 2020 [131].

3. H. Dehghani, I. Noll, R. Penta, A. Menzel, J. Merodio: The role of microscale solid matrix compressibility on the mechanical behaviour of poroelastic materials, *European Journal of Mechanics - A / Solids*, 83:103996, 2020 [41].

4. I. Noll, T. Bartel, A. Menzel: On the incorporation of a micromechanical material model into the inherent strain method - application to the modelling of selective laser melting, *GAMM-Mitteilungen, Surveys for Applied Mathematics and Mechanics*, 44(3):202100015, 2021 [132].

5. I. Noll, L. Koppka, T. Bartel, A. Menzel: A micromechanically motivated multiscale approach for laser powder bed fusion processes, *Additive Manufacturing*, 60:103277, 2022, [129].

6. I. Noll, T. Bartel, A. Menzel: A thermodynamically consistent phase transformation model for multiphase alloys – application to Ti_6Al_4V in LPBF processes, *Computational Mechanics*, available online, 2024, [130].

For journal articles 2 and 4-6, the author of this thesis contributed essential aspects with regard to the outline of the theory, carried out all of the numerical implementations and simulations, and prepared the articles. Moreover, for the results based on the theory presented in article 1, the author of this thesis carried out all of the numerical implementations and simulations and prepared parts of the article. For article 3, the writing, theory and implementation with respect to Abaqus stems from the author of this thesis.

In addition, the following contributions were published during and alongside the preparation of this thesis.

1. I. Guschke, T. Bartel, A. Menzel: A thermomechanical modelling framework for selective laser melting based on phase transitions, *Proceedings in Applied Mathematics and Mechanics*, 78(7):2267–2281, 2019 [66].

2. I. Guschke, T. Bartel, A. Menzel: A thermomechanical finite element based framework for phase transitions in laser based additive manufacturing processes, *Proceedings of the 8th GACM colloquium on Computational Mechanics*, 327–330, 2019 [65].

The content of these proceedings, which are related to conference participations of the author of this thesis, is included in the peer reviewed articles [14, 131]. Overall, the present work directly followed the authors's bachelor and master thesis, where the first investigations for additive manufacturing processes in Abaqus were made.

Contents

1 Introduction

This thesis develops a thermodynamically consistent and thermomechanically coupled phase transformation model for laser powder bed fusion processes applied to small scales in Chapters 3 and 4. Moreover, an extension to determine the distortion and residual stress of complete parts based on a multiscale framework by using inherent strains is established in Chapter 5. Finally, a phase transformation model to incorporate different solid phases for the titan aluminium alloy Ti_6Al_4V is developed in Chapter 6. As basis for all chapters, both thermomechanical setting and implementation into the commercial finite element software Abaqus are introduced in Chapter 2. The main features regarding the laser powder bed fusion process and the current state of the art are presented in Section 1.1, and the outline and aim of the thesis at hand is given in Section 1.2. Chapter 7 closes this thesis with a summary of the main results and gives a brief outlook on future research options.

1.1 Motivation and state of the art

Additive manufacturing of metallic parts – such as the laser powder bed fusion process – has gained high interest in the industry, as it allows the manufacturing of components layer by layer which offers a new design freedom and a production of custom-made assemblies. However, especially high temperature gradients caused by the laser beam heat input and phase changes influence the characteristics of the part, i.e. the mechanical eigenstresses and plastic deformations of the component. In particular, coupled thermal, mechanical and metallurgical processes arise during the production. Furthermore, the component's quality is highly influenced by the numerous present process parameters. Additive manufacturing and especially the laser powder bed fusion process itself are briefly described in Section 1.1.1. Furthermore, the origins of different material defects are discussed to explain the necessity of micromechanically motivated models for finite element simulations. Moreover, Section 1.1.2 gives an overview of present modelling approaches for laser powder bed fusion processes for small scales and regarding complete parts, as well as phase transformations models in the context of additive manufacturing to consequently discuss open issues in the literature. Novel modelling approaches are necessary to predict and minimise the diverse defects and residual stresses of a part made by laser powder bed fusion.

1.1.1 Additive manufacturing processes and material defects

Additive manufacturing (hereinafter referred to as AM) technologies – starting with stereolithography in 1986 – have developed into one of the most promising methods for the manufacturing of almost arbitrarily shaped and thus complex workpieces and structures. In contrast to subtractive or formative manufacturing technologies, e.g. milling or moulding, additive techniques are characterised by the fact that the part is fabricated by sequentially adding material to create the workpiece layer by layer. Thus, the final part has little geometrical and material restrictions. Customised parts can be manufactured at relatively low cost and in a comparatively short amount of time. Due to the advantages of this rather new technology, it offers a considerable potential for possible and promising applications in areas such as aerospace, automotive, rapid tooling, and biomedical technology. AM can in particular demonstrate its benefits in the context of custom-made designs and lightweight constructions. Significant and general advantages are exemplified by the fact that AM does not require any tools during the essential process (except for post-process surface treatments for instance), that manufacturing processes can be quickly initiated, and that changes to such processes can be easily implemented. Overall, a reduction of process steps and less process planning is required compared to conventional technologies. Furthermore, it saves time and expense and helps to conserve resources because less waste occurs. However, there are some disadvantages such as slow building rates and limited part sizes, which hinder implementation into regular assembly lines. Above all, it is difficult to select and predict the correct process parameters that ensure a part with high accuracy and quality. These issues are discussed later on in this section.

Nowadays, there are various technologies that differ e.g. in the material used (mostly powder or wire), in the heat source and in the general principle. An overview of (single-step) AM processes for metallic materials is given in Figure 1.1. Single-step AM processes refer to such processes during which the geometry of the part is created simultaneously in one operation. Similar materials, e.g. powder, are usually fused during the process. There are different (single-step) process principles for ceramic and polymer materials, which are not within the scope of this thesis. In this work, the focus is set on the laser powder bed fusion (LPBF) process, also referred to as selective laser melting (SLM), in which a work piece is manufactured in a – in this case – metal powder bed. The process can be classified as shown in Figure 1.1.

Looking at the process chain, the part is directly built based on a three-dimensional computer aided design (CAD) model, leading to AM being often referred to as near-net shaping technique. The CAD model is then converted into a standard triangulation language (STL) format that is widely used for all AM machines. It represents the geometry of the CAD model as a simple mesh. This file is digitally sliced into thin cross-sectional layers and can then be constructed by the chosen AM process and scan pattern. The production is carried out by depositing and bonding of these layers. Thus, no additional tools are required to initiate the AM process (except for any necessary

post-processing).
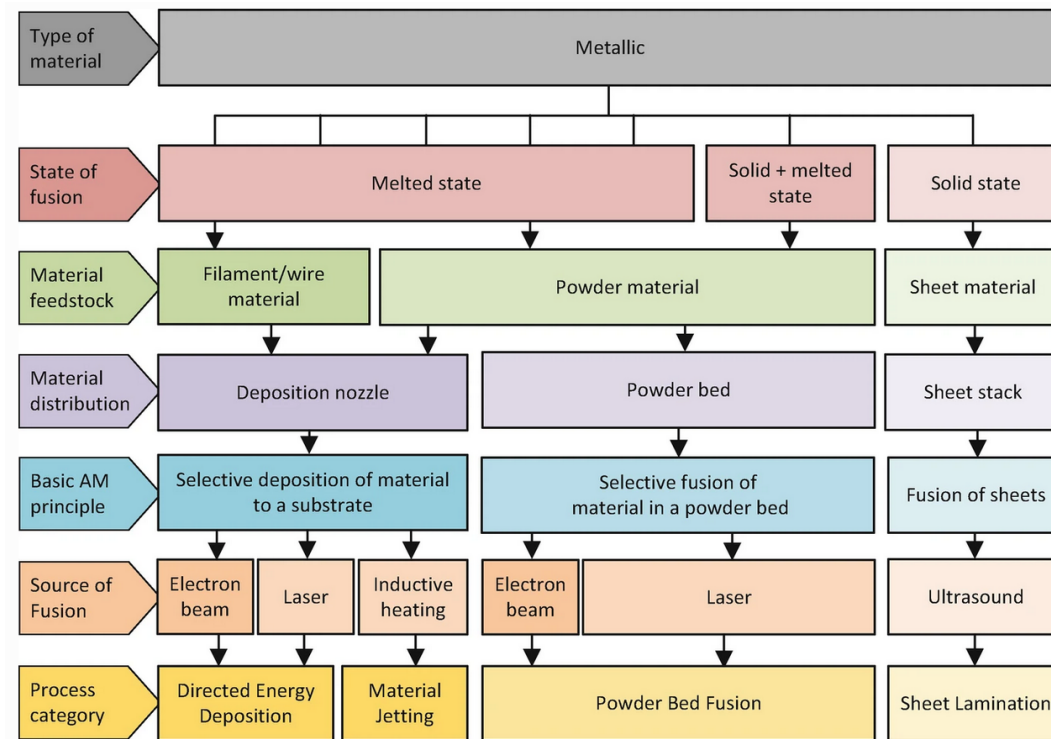
Figure 1.1: Overview of single-step AM processing principles for metallic materials, [7]. From Additive Manufacturing Technologies, Springer Cham, Gibson, I., Rosen, D., Stucker, B., Khorasani, M., Copyright (2021), [59]. Reproduced with permission from Springer Nature.

A brief overview of this specific AM technique – namely LPBF – is to be given, since the understanding of a build cycle is mandatory for the modelling in the subsequent chapters. The LPBF process can be subdivided into several essential steps: Starting from the input data, e.g. a STL file as previously described, a layer of powder is applied to a build platform. A moving laser beam heat source then selectively melts the powder particles of the corresponding layer according to the defined model resulting in rapid heating of the material. The layer height and the hatching distance has to be selected according to the size of the melt pool in such a way that a complete fusion of neighbouring layers and melt tracks is guaranteed. After a cooling period the material re-solidifies again. The build platform is then lowered and a new layer of powder is applied. This combination of material deposition, selective melting the powder material, and lowering of the platform is repeated until final geometry of the part is achieved. Finally, the remaining unmelted powder is removed and can be reused for new LPBF processes. A detailed representation of the LPBF process with its most important properties is illustrated in Figure 1.2. Thereby, almost arbitrary scan patterns are possible, which can be constant for the complete part, i.e. line scanning, or based on smaller regions,

referred to as scan islands. Between the layers the pattern may be constant or may rotate. An overview of different scan patterns is given in, e.g., [5, 33, 93, 162]. In a post-processing step, the support structure can be removed and residual stresses can be relaxed by heat treatment. Overall, it is possible to manufacture parts by melting metal powder in a layer-upon-layer technique.

In general, particle dynamics, thermal fluid dynamics, solid-state transformation and solid mechanics are present during an LPBF process, compare Figure 1.3 for an overview of the physical phenomena that occur in the melt pool. Particle dynamics is not a subject of this work and therefore not further described. With regard to thermal fluid dynamics, some fundamentals are important for the modelling of the molten phase. The melt pool behaves like a fluid, whereby the melt pool shape is influenced by surface tension and capillary forces, as well as by the wetting behaviour. Heat transfer within the melt flow is governed by Marangoni convection rather than by heat conduction, compare [117]. The focus is set on solid mechanics and on the different state transformations due to the heat input of the laser beam. As a consequence of the high temperature impact, the powder particles first melt and then solidify after a cooling period, resulting in a dense part. Depending on the heat impact, there is not only the phase transformation between solid and liquid, but to some extent also vapour when the evaporation temperature is exceeded. A detailed view of the three specific material states – powder, melt pool, and re-solidified material– is pictured in Figure 1.2 for the LPBF process. During the cooling process, solidification begins, which affects the material properties of the final part. Depending on the exact position of the laser beam and the section of material examined, the cooling rates, respectively the temperature gradients, of the material significantly differ: Material that is directly in the focus of the laser beam exhibits significantly higher cooling rates than material outside of the laser impact zone. The area in which the material is not melted but is exposed to high temperatures and thereby has changing material properties is referred to as heat affected zone (HAZ). As a consequence, the associated thermal eigenstrains are heterogeneously distributed, leading to bending due to the temperature gradient mechanism (TGM) as described in [29, 93, 183]. This process not only causes distortion, but also potential failure of the part due to delamination or cracking. In addition, the three different states of the material exhibit different material properties as well as significantly changing mass densities, so that the phase changes evoke relevant process-induced eigenstrains. Moreover, depending on the material, non-negligible solid-state phase transformation can occur. This results in high residual stresses within the part that can have a major impact on the mechanical properties of the final product, in particular with respect to the long-term behaviour and its lifetime. Besides large-scale material defect such as cracks, delamination and undesired deformation, various types of small-scale defects are also present, e.g. voids due to lack of fusion, unwanted grain structure, surface deformation and keyhole porosity, see [18].

The aerospace, automotive and biomedical sectors in particular promote the LPBF process, where parts with long durability, high load capacity and geometrical accuracy

laser beam

feedstock, e.g. powder

detail

roller

part

feed region

build chamber

build platform

detail - front view

scanning direction

melting pool

laser beam

re-solidified
material

powder

layer height

layers

detail - top view

hatching distance
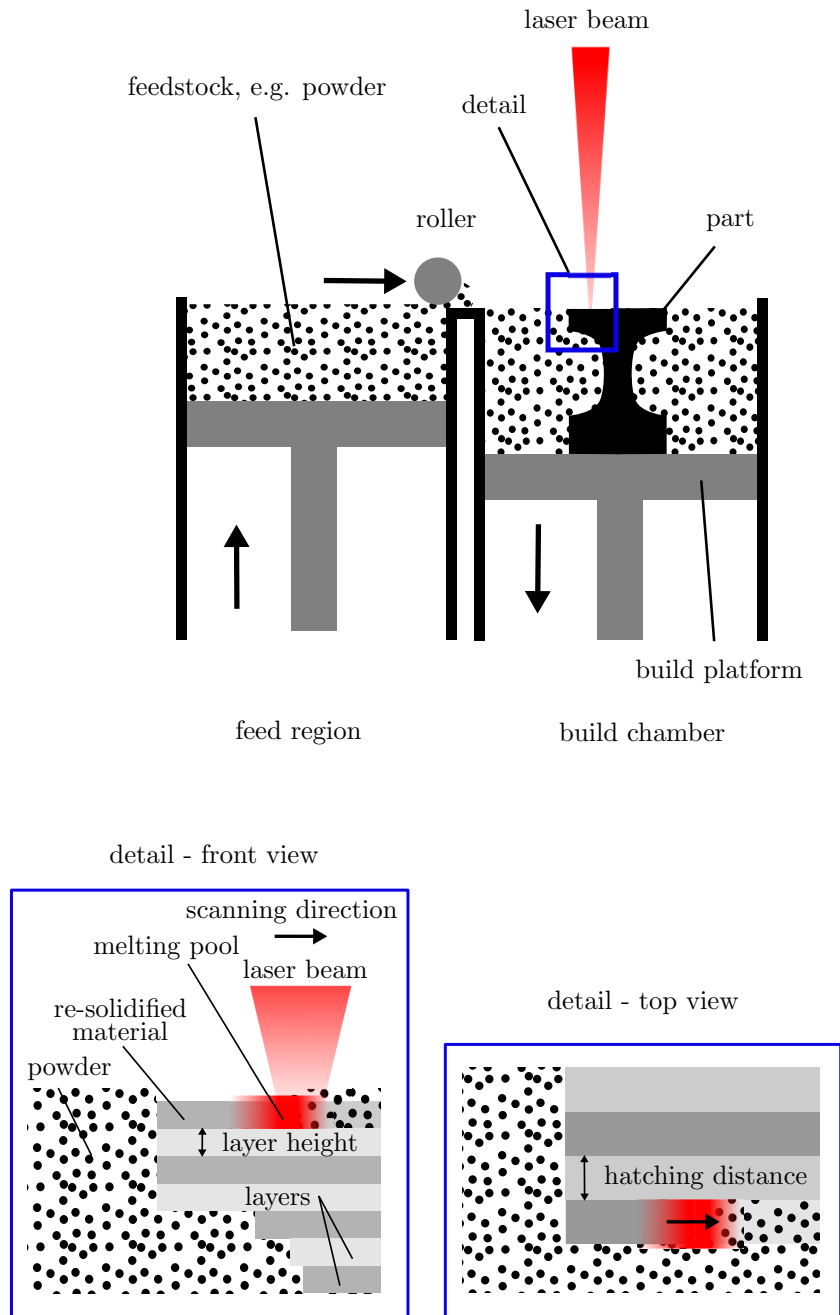
Figure 1.2: Schematic view of the complete LPBF process. Adapted from [132] under the terms of the Creative Commons Attribution License (CC BY).
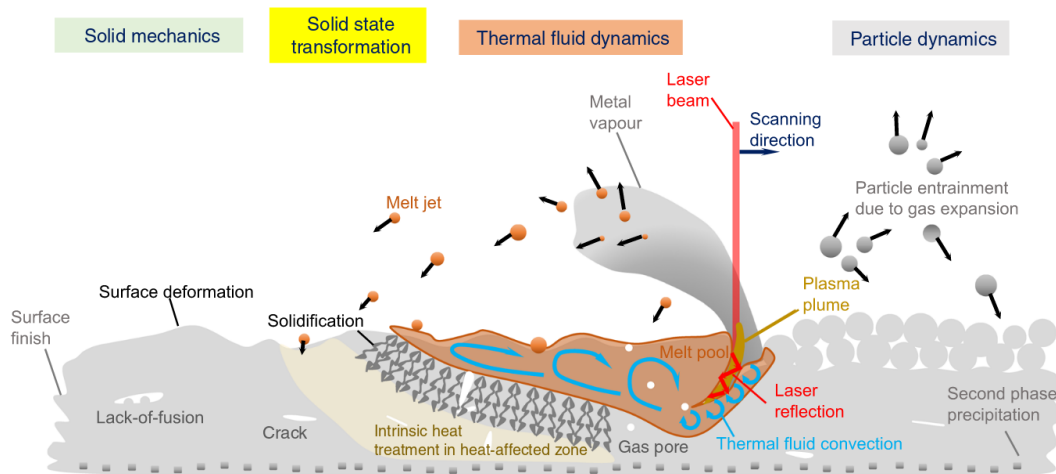
Figure 1.3: Schematic illustration of the different phenomena during the LPBF process based on coupled thermal, mechanical and metallurgical processes which also include different scales. Reprinted from [139] under the terms of the Creative Commons Attribution License (CC BY).

are especially important. Predicting the influence of the AM process parameters on the workpiece's properties is still challenging, as these effects have not yet been comprehensively studied. This necessitates the modelling and simulation of the LPBF process or, more generally speaking, AM processes, with an overview of the current state of research being given in the subsequent Section 1.1.2.

1.1.2 Modelling and simulation of laser powder bed fusion processes

So far, experiments have mostly been made in order to identify the optimal parameter configuration on a purely empirical level. However, simple experiments alone are not sufficient to investigate and determine the origin of defects, as it is difficult to cover, respectively characterise, all physical effects in experiments. Especially since the LPBF process involves multiple phenomena and scales. In addition, experiments are costly and time consuming. Therefore, simulations with physically well-motivated models are necessary to gain a deeper understanding of the relation between e.g. process parameters and the eigenstresses of the LPBF manufactured part. As a consequence, numerical schemes such as the finite element (FE) method are useful to acquire further insight into the mechanical, thermal and metallurgical phenomena visualised in Figure 1.3 and into the underlying physics, so that manufactured parts are correctly predicted. This thesis covers and connects several areas of modelling and simulation approaches based on continuum mechanics. Therefore, the state of the art is divided into three parts, namely welding models, LPBF models and phase transformation models in the context of AM.

Welding models

LPBF has similar process characteristics to welding when considering the complex coupled process interactions during manufacturing, in particular the thermal and metallurgical properties. However, modelling and simulating these LPBF processes comes along with additional challenges compared to welding including but not restricted to the addition of material, plenty of laser passes and finer bead width, cf. [42] and the references cited therein. Nevertheless, the established modelling methods regarding, e.g., heat source models and multiscale frameworks are adapted or extended for the LPBF process. Using a volumetric heat source with Gaussian distribution for the laser beam stems from the modelling of welding processes and is also referred to as Goldak heat source based on [60]. In addition, the inherent strain (IS) method has been introduced in [169] for welding simulations. Various thermal expansions and contractions occur within the weld seam leading to residual strains and plastic deformations of the original part. It is concluded that the residual or so-called inherent strains $\varepsilon^{\mathrm{inh}}$ are the reason for the high eigenstresses within the final part. With this method, accurate predictions for welding simulations have been performed. These inherent strains are extracted from a thermo-mechanical analysis for one joint and can then be applied to the modelling of the total welding distortion by using a purely mechanical analysis, where the total strains are governed by an elastic and an inherent contribution, i.e. $\varepsilon = \varepsilon^{\mathrm{el}} + \varepsilon^{\mathrm{inh}}$. This approach has been further developed and applied for welding processes in, e.g., [67, 123, 182]. In the latter, the inherent strains are additively decomposed into $\varepsilon^{\mathrm{inh}} = \varepsilon^{\mathrm{pl}} + \varepsilon^{\mathrm{th}} + \varepsilon^{\mathrm{cr}} + \varepsilon^{\mathrm{trans}}$, each representing a plastic, thermal, creep and transformation contribution, respectively.

LPBF models

In the following, a literature overview of LPBF models based on the different scales (small-scale and part-scale) and modelling methods (finite element and others) is given. Here, the small-scale models mostly refer to frameworks, where a single-line melt track is simulated.

Finite Element models on small-scale

Starting with [164] in 1991, pioneering works with respect to LPBF process simulations are based on the finite element method for small scales, i.e. considering only single-line melt tracks. The finite element-based solution of the purely thermal problem and the related determination of the process-induced temperature distribution is shown for example in [37, 54, 71, 89, 100, 101, 150, 159, 165]. More sophisticated thermomechanical small strain models are available in literature, e.g., [36, 55, 68, 72, 148, 149, 181, 190], where the calculations with respect to the temperature field are enhanced by the prediction and analysis of the residual stresses and by the alteration of the geometry. The advantage of a thermomechanical model and the difference in the temperature evolution is also presented in [55]. Most of these frameworks have in common that the material

is considered at the local scale as a homogeneous medium with temperature-dependent properties such as density, heat capacity or elastic stiffness. The different states of the material – powder, molten, and re-solidified – are rather implicitly captured by one-to-one correlations between the local temperature and the present state of the material. Furthermore, the powder is considered as an already homogenised continuum in these simulations.

Alternative models on small-scale

In [84], the arbitrary Lagrangian Eulerian (ALE) method is used for the coupling of thermal diffusion and hydrodynamics. The particles are randomly distributed and also exhibit temperature-dependent material properties. Alternatively, as shown in [96], a two-dimensional lattice Boltzmann model can be used to model and simulate the material deposition and the melting process. This approach allows for the consideration of capillary effects within the powder as well as of the surface topology of previously applied layers. In such models, the stochastic character of the powder material is particularly taken into account which, at the same time, increases the time required for the associated calculations. Therefore, compromises between physical plausibility and computational effort have been proposed, as for example shown in [56]. This model is based on a coupling between the discrete element method for the powder material – the constituents of which are modelled as thermally and mechanically interacting spheres – and on finite differences with respect to the substrate. Thermal fluid dynamics are necessary when considering all interactions within the melt pool such as convective flow, wettability, capillary effects and recoil pressure. However, only small scales regarding time and domain can be simulated. In [118], a smoothed particle hydrodynamics formulation is used to model the capillary phase change with the complete set of thermal and mechanical interface fluxes. Here, the focus is set on the melt pool dynamics as visualised in Figure 1.3 rather than on the complete process. These alternative frameworks are based on the modelling of the powder material as conglomerate of discrete particles. A comprehensive overview of different models for the distinct length scales, i.e. the resolution of the part, the powder particles or the metallurgical microstructure, can be found in [117]. One of the few thermomechanical finite deformation frameworks is developed in [174, 175] to predict the melting and solidification process on the powder scale by using the optimal transportation mesh-free algorithm.

Finite element models on part-scale

Accurate thermomechanical models that resolve all individual laser scans and layers require a high element density and a fine time discretisation to properly capture the great temperature gradients of the heat impact, see for example the studies in [184]. Even with increasing computational capabilities, the size of a physically accurate model is limited to a few laser passes or layers, as the AM process involves various physical processes and multiple scales. For industrial use, the influence of process parameters, product quality and the prediction of deformation and residual stresses still remains challenging for a

physically real component. So far, especially the high computational cost of part-scale simulations and the difficult quantification of the parameter sensitivity have made further studies in the direction of optimisation difficult. With the appropriate simulation tools it is then possible to determine the pre-deformed shape and optimal initial build orientation of the part to overcome problems due to warpage and high residual stresses. Therefore, researchers are currently focusing on advanced models for the numerical investigation of larger parts contrary to single-line melt tracks. Based on the goal of modelling complete parts in industrial applications, two different methods are available in the literature. On the one hand, the computational effort is reduced. In consequence, high performing finite element algorithms are developed to speed up computation time, for example in [58, 88, 124, 125, 136]. On the other hand, various other simplifications with regard to the physics, i.e. the heat source model, the scan pattern and the layer thickness are possible for which a comprehensive overview is given in [62, 92]. The different (indirect) approaches existing in the literature can be divided into four groups: flash heating, process agglomeration, inherent strain method and multiscaling laws.

Flash heating refers to a layer-wise heating of the part as applied in, e.g., [91, 126, 140, 157, 183, 187]. In particular, the simulation of each layer at the same time is used to speed up the process. There are models in the literature in which, for example, 20 layers in [183], or only three layers in [140] are combined. The drawbacks in view of accuracy are partly improved by the sequential flash heating as introduced in [18]. The scan pattern cannot be examined in flash heating simulations, although it is known and shown to have a high impact on the final deformation and stress state, cf. [5, 33, 94, 104].

Process agglomeration or lumping is used for example in [57, 69, 162], where an enlarged layer and beam size is used with an elaborated material model for the solid phase. In this case, the scanning strategy of the laser beam can still be evaluated to some extent, since the complete layer is not heated up at once. Overall, sufficiently accurate simulation results can be achieved with process agglomeration. However, the influence of the scan pattern cannot be examined in detail. The difference of the strain values for the simulation of the continuous and island scan pattern is rather small in comparison to the experiments, see [57]. Moreover, the computational time is still quite large. Adding sophisticated adaptive mesh refinement routines to this approach further reduces the computation time, cf. [58]. Nevertheless, the developing and application of such routines is quite advanced.

Multiscaling laws, also referred to as multiscale models, employ distinct scales to achieve an efficient prediction of part distortion and residual stresses. In [99], a thermomechanical multiscale model for the heat source approach is developed. Three distinct scales, i.e. the microscale, the mesoscale and the macroscale, are present in e.g. [81, 82, 99, 157]. The multiscale approach of the latter contribution is more advantageous to those methods, in which the calculation time is reduced by exposing whole layers at once and by directly combining multiple layers, where the scanning strategy can no longer be taken into account. Another method to model large parts is developed in [156]

by using a sequentially coupled three-dimensional thermal model and a two-dimensional mechanical plane stress model.

The **Inherent strain method** stems from welding and has meanwhile established itself as a standard method for the modelling of LPBF processes, for instance in [82, 102, 153, 158]. The application of the inherent strain (IS) method for LPBF is justified by the similar temperature history of each micro-weld seam, i.e. single-line melt track. This results in a stationary problem, where the size of the problem can be reduced to a small hatching region. However, the size of each hatch, also called scan island, influences the overall mechanical properties of the manufactured part, see e.g. [112]. Overall, the challenge in using this method lies in the correct determination of the IS tensor $\varepsilon^{\mathrm{inh}}$.

The IS, also referred to as eigenstrain, has to be properly defined either by simulations using a detailed thermomechanical model or by experimental data for an inverse analysis. The latter approach is used in [158, 160], where the IS is determined by measuring test samples. These strains are then applied in mechanical simulations to model the distortion of arbitrary parts. A similar approach is also used in commercial AM software such as AdditiveLab. However, with this method it is still necessary to construct test samples and measure the deformation of the built specimens for all possible combinations of process parameters. In the multiscale approach developed in [81, 82], an IS is extracted from a detailed thermomechanical simulation of a small-scale model, which is then applied to a real-sized part in a linear elastic mechanical analysis. Here, the IS tensor is not experimentally measured, but determined by using the finite element method. A similar approach is used in [26], where a mesoscale submodel is used to determine the eigenstrains for the macroscale part model.

In [102], a modified inherent strain method usable for direct energy deposition has been developed, which has also been employed in [29, 46, 103] for other AM processes such as LPBF. The modified inherent strain method refers to two different time states t_1 (intermediate state) and t_2 (steady state), whereas the standard IS approach only considers the steady state. It is defined by $\varepsilon^{\mathrm{inh}} = \varepsilon^{\mathrm{el}}_{t_1} - \varepsilon^{\mathrm{el}}_{t_2} + \varepsilon^{\mathrm{pl}}_{t_1}$, where the difference $\varepsilon^{\mathrm{el}}_{t_1} - \varepsilon^{\mathrm{el}}_{t_2}$ between the elastic intermediate and elastic steady state contribution shall capture the influence of the thermal shrinkage and where $\varepsilon^{\mathrm{pl}}_{t_1}$ denotes the plastic strain of the intermediate state. Consequently, multiple layers (at least two) are modelled. With this, the build cycle of the building process shall be better captured.

Altogether, different magnitudes of IS can be found throughout the literature. In particular, there is a large discrepancy between the values obtained by the modified method, cf. [30, 103], and the standard or experimental approach, e.g. [158, 160]. On the one hand, these two approaches are essentially different regarding the determination of the IS. On the other hand, the respectively used material models with the chosen material parameters as well as the modelling approaches for the laser beam differ significantly. In addition, there is a variance regarding the tensor components incorporated. Overall, simulations using the IS method are rather fast and the scan pattern can be examined in a straightforward manner. This enables optimisations of the scan pattern in terms of minimal bending, which is part of [30], by using the modified IS method. In addition,

the IS framework can also be used either to determine the necessary pre-deformation of the manufactured part according to the calculated deformation of the original design, cf. [82] or to optimise the support structure of a part, for instance in [188]. The primary drawback of the IS procedure is based on the purely mechanical simulation approach on the part scale, so that no temperature history of the part is included. This results in different problems, e.g. for the correct deformation of larger parts or different geometries, as described in [26, 143]. Because computational time is quite small, the increased usability for large models nevertheless leads to the incorporation of the IS method in different kinds of commercial software, e.g. MSC Simufact, Amphyon Works, GE GenonX as stated in [26, 29]. The commercial software Abaqus recently also added a feature to easily incorporate IS simulations (since 2019) by using the `AM-Modeler`, [1]. However, with all these commercial software-based approaches, the IS tensor itself, which can then be applied in a simulation to model complete parts, has to be already known.

Phase transformation models

When considering phase transformation models, a distinction has to be made between two model types: those that explicitly take into account the different aggregate states, namely liquid, i.e. melt pool, and solid, i.e. powder and re-solidified material, and sometimes even gas, i.e. vapour, and those that incorporate solid-state phase transformations within the re-solidified material. Regarding the aggregate states, various modelling approaches exist. In, e.g., [68], the standard thermomechanical finite element approach is enhanced by explicitly taking into account the phase change in terms of using Stefan-Neumann equations. The level set method is used in [31] to model the interface between solid and gas. A different approach is employed in [89], where a mathematical phase change function is calibrated by experiments. In [151], a purely thermal model is developed which explicitly incorporates two state variables for both the phase and the porosity. This enables the capturing of the consolidation of the material. All these works conclude that incorporating the phase transformation improves the simulation results compared to experiments. However, most researchers use the melting point temperature to indicate the phase changes, so that these are purely temperature-driven with temperature-dependent material properties.

Different modelling approaches can be found in the literature for solid-state phase transformations, most of them relying on algebraic equations for isothermal conditions based on the Johnson-Mehl-Avrami(-Kolmogorov) (JMA(K)) theory, compare [8, 76, 90] and the concept of additivity as introduced in, e.g., [115]. In addition, the Koistinen-Marbuerger (KM) model, see [87], is frequently used for martensitic transformations. In [185], not only the physical state changes, i.e. melting and solidification, but also the metallurgical solid-state phase transformations are incorporated. Here, the physical state changes are based on the solidus and liquidus temperatures (rather temperature-driven), whereas a phenomenological approach is used for the solid-state phase transformation. To be more specific, the time temperature transformation (TTT) diagram, an extended

JMA model for diffusional transformations and the KM model are combined. Five different phases of Ti_6Al_4V are considered in the generic parent-child framework, where the critical cooling rates are taken from [4]. For a homogeneous stress state, two different heating-cooling cycles are prescribed and the resulting microstructure is discussed. However, no predictions are made regarding the stress-strain behaviour. Other recent publications in the field of AM that are based on the JMA and KM models are, e.g., [10, 19, 40, 50, 180]. The model in [180] not only predicts the distribution of the different solid-state phases during the process and after heat treatment, but also proposes a Rosenthal-based solidification process map for LPBF. In [50], a visualisation of the difference and improvement in residual stress prediction incorporating martensitic phase transformations for tool steel is shown. A part-scale model coupled with the JMA equation is used in [40, 170]. In [109], the authors present an integrated simulation framework distinguishing between a thermal process model, a predictive solidification model for the molten pool and a solid-state phase transformation model for $\beta \rightarrow \alpha/\alpha'$. One of the few thermally coupled models is [19], where a process-based finite element model simulating a thin walled structure is presented. An Abaqus model is presented in [10], where not only the JMA and KM equation are incorporated, but also a purely temperature driven melting and solidification. However, the above described models are purely empirical. It appears that micromechanically motivated and thermodynamically consistent material models appropriately predicting stress and strain states are missing.

As an alternative, a phase field approach for the solid-state phase transformation is suggested in [2] for welds, which could also be applied to AM processes. In [106], a framework based on crystal plasticity is presented for H13 tool steel. An extended two-dimensional finite element model is developed in [155], where a phase transformation contribution is calculated and added to better predict the behaviour of partially austenitic and martensitic steels with evolving phase fractions. In [17], a different approach is chosen where temperature-dependent functions are fitted to account for the different material properties of the α'- and β-phases. Therefore, the respective function of the solid phase is used based on the current temperature θ and the β-tansus temperature $\theta_{\beta,\text{trans}}$. However, no rate dependency is incorporated. In [127], a stochastic approach is used to model the microstructure evolution during solidification. Based on the work of [4], the authors of [128] developed a phenomenological material model which captures the phase transformations during LPBF processes. In this contribution, the β, α, α'-phases are considered, the evolution of which are either diffusion-based or non-diffusion based. The model parameters are determined by an inverse identification process based on TTT diagram data. With this framework at hand, continuous cooling transformation (CCT) diagram data can be predicted with sufficient accuracy. The authors in [166] propose a new concept denoted time-phase transformation-block to simultaneously take into account the different phase transformation mechanisms. Applications of this concept in the context of direct energy deposition are shown. The results obtained with this approach may help to adapt and improve the present JMA and KM models in the future. However, the aforementioned time-phase transformation-block

model is rather complicated as it includes quite many parameters and, in addition, it does not provide a relation between stresses and strains. More simple models are presented in [28, 34], where a phenomenological and explicit relation between the phase fractions and the present temperature as well as the cooling rate is used.

1.2 Objective of this work

Overall, the different approaches in the literature overlap and, so far, there is not one model that can take into account all physical processes during LPBF in an adequate simulation time. In addition, there is still a lack of comprehensive understanding of the phase transformation processes, especially for the rapid temperature cycles present in LPBF, which is essential to ensure adequate mechanical properties. The most challenging reasons are stated in [88] as: highly localised and moving temperature gradients, nonlinearities due to phase changes of the material, growing and large computational domains compared to melt pool size, large range of spatial and temporal scales and coupled multi-physics. Altogether, different formulations are available for the simulation of the distinct scales with help of the finite element method. However, from the author's point of view, no frameworks exist which take into account the mechanical material model and phase change in a physically well-motivated approach. The temperature profiles associated with these processes, which are highly heterogeneous in space and time, further increase the complexity regarding the finite element model and appropriate computing time and have to be considered when developing novel frameworks.

The key aspect of **Chapter 3** is the treatment of the different (aggregate) states of the material – powder, molten, and (re-)solidified – as different phases of the material, compare Figure 1.2. During the transformation process, the material first melts and then solidifies. Thus, the transitions between these states are treated as phase transformations. Adapted from frameworks for solid-solid phase transformations provided in, e.g, [12, 13, 78] in the context of shape memory alloys, the constitutive behaviour of each phase is modelled via phase energy densities with reference values for the underlying material constants. The constitutive model for the case of coexisting phases is obtained via a mixture rule and specific homogenisation assumptions which yield the averaged energy density, where particularly the volume fractions of each phase are taken into account. These are determined via energy minimisation depending on the current state of local strains and temperature. This approach is specifically designed for the consideration of more than just one solid phase which forms during the cooling period which is discussed in Chapter 6. The formulation of the material model as well as the finite element model consider full thermomechanical coupling. Due to the computing time, however, only a single melt track can be efficiently considered.

Chapter 4 focuses on the advancement of the model presented in the previous chapter. As the density of the different material states varies considerably, this effect shall be incorporated in the phase transformation framework motivated by existing literature. The effect of volume shrinkage of the powder bed due to porosity has been investigated in [37] by using a purely thermal model. In [55, 149] a thermomechanical model is used where a pseudo-thermal expansion is implemented to take into account not only the thermal expansion of the material, but also the shrinkage of the powder bed. In [31], the apparent volume shrinkage is incorporated for ceramics by a compressible Newtonian law. In particular, the present modelling framework explicitly takes into account the mass fractions of the different phases, their mass densities, and specific inelastic strain contributions. Thus, a formulation based on mass fractions is developed. The internal state variables including the mass fractions of the different phases are calculated by using thermodynamically consistent evolution equations solved at the material point level. The transformation strains are introduced as material constants to capture the significant change of the mass densities during the phase changes. The present investigations aim at the accurate prediction of essential process-induced quantities such as eigenstresses. Furthermore, the present modelling framework can be used to calculate effective inelastic strains for a multiscale framework, which is introduced in the subsequent chapter.

Within **Chapter 5**, a part-scale simulation shall be developed, which uses a reasonable compromise in view of considered phenomena according to Figure 1.3 and computation time. This results in simpler yet faster process simulations to simulate residual stresses and deformation of complete parts. So far, it is still challenging to predict the characteristics of real-sized manufactured workpieces, e.g. the residual stresses and the final deformation, which reduces the ability to use additively manufactured parts in industrial applications. This shows the necessity of simulation tools and appropriate material models, not only for the single melt track, but also on the part scale, to gain a deeper understanding of the relation between optimal process parameters and the final part so that time and cost consuming practical trials can be avoided. However, finding appropriate simulation models regarding accuracy and efficiency is a rather challenging task. If deformations and eigenstresses are to be predicted, a thermomechanical analysis will be necessary. Therefore, a multiscale approach is elaborated which is physically sound and micromechanically motivated. This method allows the consideration of different simplifying assumptions regarding the complexity of material models and heat source models, in order to significantly reduce the required computation time for part-scale simulations. In particular, a combination of a multiscale relation is used to determine the inherent strain (IS) and the application of the established IS method based on [81]. By coupling a complex and appropriate model at the small scale – the laser scan model for the single melt track – and with simplifications regarding the layer hatch model, which is used to model a scan island, it is possible to extract an IS for the mechanical finite element simulation of complete parts in an appropriate time span. Nevertheless, this method and the models used incorporate physically well-motivated assumptions of the

different material models. With this enhanced approach, it is possible to establish an efficient simulation framework to predict residual stresses and the final geometry for larger process simulations. More complex geometries and laser beam paths can be modelled without the need for extremely time consuming simulations. Altogether, it is possible to demonstrate the influence of process parameters and scan patterns for a twin cantilever beam. The presented model can predict the eigenstress evolution during manufacturing and after the partition from the build platform.

Chapter 6 sets the focus on the incorporation of modelling solid-state phase transformations for multiphase alloys, such as Ti_6Al_4V, an enhancement the phase transformation modelling framework of the previous chapters is specifically designed for. This extension is considered highly important for two reasons: the cooling rate during the manufacturing process of the part as well as possible subsequent reheating or heat treatments alter the microstructure evolution and residual stress state of the manufactured part. Thus, the consideration of the transitions between the related β- and α-phases is of considerable importance for the modelling and simulation of additive manufacturing processes such as, e.g., LPBF processes, as the crystal structure and material properties of the phases differ. This is supported by in-situ experimental validation of the microstructure during LPBF such as, e.g., [83, 172]. Therefore, especially for heat treatable alloys like Ti_6Al_4V, the incorporation and monitoring of solid-state phase transformation cannot be neglected, as the strongly cooling rate dependent phase composition needs to be additionally considered. In this context, the aim of the present chapter is to develop a material model, which is capable of simulating phase transformations between (two) different solid phases as well as their effect on deformation and – if incorporated into a finite element approach in future – on residual stresses based on a linear elasticity analysis. The focus is set on the prediction of phase fractions during temperature-induced transformations for different temperature rates on a local scale. The fact that the model is based on the principles of thermodynamics and appropriate homogenisation assumptions (in contrast to, e.g. [10, 19, 28, 34]) should, in principle, lead to more accurate predictions of effective quantities. In order to adapt the modelling framework to the complex behaviour of Ti_6Al_4V, a new approach with respect to the dissipation function is developed. The material parameters incorporated in the material model and, in particular, in the new dissipation function are identified using continuous cooling temperature (CCT) curves available from the literature. With this framework, the formation of different solid phases as well as evolving strain and stress states can be adequately predicted for distinct cooling rates.

2 Thermomechanical framework

First of all, the notation which is used in this thesis is briefly presented in Section 2.1. Here, an overview of the symbolic and index notation of tensors as well as its products is given. The aim of this chapter is to introduce the foundations of continuum mechanics in terms of kinematics in Section 2.2, as well as the kinetics for the thermomechanical setting. This incorporates the used strain measure as well as the underlying thermomechanically fully coupled balance equations in their strong and weak forms. In the following chapters of this thesis, the mechanical or thermomechanically fully coupled framework is used for different boundary value problems in the context of finite element simulations in the commercial software Abaqus. Thus, the basic balance equations, the constitutive relations and the finite element (FE) framework is summarised in the following Sections 2.3, 2.4 and 2.5, respectively, where the content is adapted from standard literature. In addition, a first insight into using Abaqus for thermomechanical simulations and the used user subroutines is given in Section 2.6.

2.1 Notation

For the reader's convenience, the essential relations of tensor calculus used in this thesis are collected and provided in the following. For a more complete overview of tensor calculus, the interested reader is referred to the textbook of, e.g., [73]. For the sake of simplicity, this thesis is based in the three-dimensional Euclidean space $\mathbb{E}^3$, where the Cartesian basis vectors $\boldsymbol{e}_p, p = 1,\, 2,\, 3$ are used to span the tensors

$$\alpha \,, \qquad\qquad \text{(zero-order tensor, i.e. scalar)} \qquad (2.1)$$

$$\boldsymbol{a} = a_i\, \boldsymbol{e}_i \,, \qquad\qquad \text{(first-order tensor, i.e. vector)} \qquad (2.2)$$

$$\boldsymbol{A} = A_{ij}\, \boldsymbol{e}_i \otimes \boldsymbol{e}_j \,, \qquad\qquad \text{(second-order tensor)} \qquad (2.3)$$

$$\mathsf{A} = \mathsf{A}_{ijkl}\, \boldsymbol{e}_i \otimes \boldsymbol{e}_j \otimes \boldsymbol{e}_k \otimes \boldsymbol{e}_l \,, \qquad \text{(fourth-order tensor)} \qquad (2.4)$$

using Einstein's summation convention. With this, the corresponding second order-identity tensor can be defined as

$$\boldsymbol{I} = \delta_{ij}\, \boldsymbol{e}_i \otimes \boldsymbol{e}_j \,, \qquad\qquad\qquad\qquad\qquad (2.5)$$

with the Kronecker delta symbol

$$\delta_{ij} = \boldsymbol{e}_i \cdot \boldsymbol{e}_j = \begin{cases} 1 & \text{if} \quad i = j \\ 0 & \text{else} \end{cases} \quad . \tag{2.6}$$

In addition, it is possible to define inner tensor products, where the number of dots refer to the number of contractions, resulting in

$$\boldsymbol{a} \cdot \boldsymbol{b} = a_i\, b_i \ , \tag{2.7}$$
$$\boldsymbol{A} \cdot \boldsymbol{b} = A_{ij}\, b_j\, \boldsymbol{e}_i \ , \tag{2.8}$$
$$\boldsymbol{A} \cdot \boldsymbol{B} = A_{ij}\, B_{jk}\, \boldsymbol{e}_i \otimes \boldsymbol{e}_k \ , \tag{2.9}$$
$$\boldsymbol{A} : \boldsymbol{B} = A_{ij}\, B_{ij} \ , \tag{2.10}$$
$$\mathsf{A} : \boldsymbol{B} = \mathsf{A}_{ijkl}\, B_{kl}\, \boldsymbol{e}_i \otimes \boldsymbol{e}_j \ , \tag{2.11}$$
$$\mathsf{A} : \mathsf{B} = \mathsf{A}_{ijkl}\, \mathsf{B}_{klmn}\, \boldsymbol{e}_i \otimes \boldsymbol{e}_j \otimes \boldsymbol{e}_m \otimes \boldsymbol{e}_n \ . \tag{2.12}$$

In the following, the inverse $\boldsymbol{A}^{-1}$ and the transpose $\boldsymbol{A}^{\mathrm{t}}$ of a tensor are often used and are defined as

$$\boldsymbol{A} \cdot \boldsymbol{A}^{-1} = \boldsymbol{I} \ , \tag{2.13}$$
$$\boldsymbol{A}^{\mathrm{t}} \cdot \boldsymbol{b} = \boldsymbol{b} \cdot \boldsymbol{A} \ . \tag{2.14}$$

With help of Voigt and Kelvin notation, tensor-valued quantities can be described as vectors and matrices. For Voigt notation, this generally results in

$$[\boldsymbol{A}]^{\mathrm{voi}} = [A_{11},\, A_{22},\, A_{33},\, A_{12},\, A_{13},\, A_{23}]^{\mathrm{t}} \ , \tag{2.15}$$
$$[\mathsf{A}]^{\mathrm{voi}}_{3\times3\times3\times3} = [\mathsf{A}_{ij}]_{6\times6} \ . \tag{2.16}$$

If $\boldsymbol{A}$ equals the strain tensor $\boldsymbol{\varepsilon}$, the following relation

$$[\boldsymbol{\varepsilon}]^{\mathrm{voi}} = [\varepsilon_{11},\, \varepsilon_{22},\, \varepsilon_{33}, 2\,\varepsilon_{12},\, 2\,\varepsilon_{13},\, 2\,\varepsilon_{23}]^{\mathrm{t}} \tag{2.17}$$

is valid. Thereby, the order is based on the (non-standard) Abaqus convention. For Kelvin notation, a slightly different relation is applied, precisely

$$[\boldsymbol{S}]^{\mathrm{kel}} = [S_{11},\, S_{22},\, S_{33},\, \sqrt{2}\,S_{12},\, \sqrt{2}\,S_{13},\, \sqrt{2}\,S_{23}]^{\mathrm{t}} \ , \tag{2.18}$$

where the elements are weighted so that the norm of the tensor is preserved.

Finally, the gradient of quantity ($\bullet$) with respect to the reference configuration is defined as

$$\nabla_{\boldsymbol{X}}\bullet = \mathrm{GRAD}(\bullet) = \partial(\bullet)/\partial\boldsymbol{X} \ . \tag{2.19}$$

The material time derivative of a quantity ($\bullet$) with respect to the reference configuration is introduced as

$$\dot{\bullet} = \left.\frac{\mathrm{d}\bullet}{\mathrm{d}t}\right|_{\boldsymbol{X}} \; . \tag{2.20}$$

2.2 Kinematics

In this section, the deformation and motion of a body shall be briefly described. With this at hand, it is possible to derive the respective strain measure, which is needed for the definition of the balance equations in Section 2.3. For a more complete overview of different strain measures and continuum mechanics in general, the interested reader is referred to the textbooks by e.g. [24, 70, 107, 141, 168, 176]. The following derivations are based on an orthogonal Cartesian basis for simplicity.

The notation used in this thesis follows standard conventions: Let $\boldsymbol{X} \in \mathcal{B}_0$ be the spatial coordinates of material points or, in other words, particles defined for the reference configuration $\mathcal{B}_0$ of the body under consideration. The motion under loading of material points $\boldsymbol{x}$ of a deformed body with configuration $\mathcal{B}_t$ is described by a nonlinear mapping

$$\boldsymbol{x} = \boldsymbol{\varphi}(\boldsymbol{X}, t) \in \mathcal{B}_t \tag{2.21}$$

as a function of the particles in the reference configuration $\boldsymbol{X}$ and time t. The mapping is visualised in Figure 2.1, where $\boldsymbol{X}$ and $\boldsymbol{x}$ denote the location of particles in the reference configuration $\mathcal{B}_0$ and current configuration $\mathcal{B}_t$. Visually speaking, in the Lagrangian description (reference configuration) the movement of particle $\boldsymbol{X} \in \mathcal{B}_0$ is followed in time, whereas the change of motion with time t is captured by the Eulerian description (current configuration) for a fixed point in space $\boldsymbol{x} \in \mathcal{B}_t$. The displacement vector is introduced as

$$\boldsymbol{u}(\boldsymbol{X}, t) = \boldsymbol{\varphi}(\boldsymbol{X}, t) - \boldsymbol{X} = \boldsymbol{x} - \boldsymbol{X} \; . \tag{2.22}$$

The deformation gradient can then be defined as

$$\boldsymbol{F} = \nabla_{\boldsymbol{X}}\, \boldsymbol{\varphi}(\boldsymbol{X}, t) = \partial \boldsymbol{x} / \partial \boldsymbol{X} = \nabla_{\boldsymbol{X}}\left[\boldsymbol{X} + \boldsymbol{u}(\boldsymbol{X}, t)\right] = \boldsymbol{I} + \boldsymbol{H} \; , \tag{2.23}$$

where the tensor $\boldsymbol{H} = \nabla_{\boldsymbol{X}}\boldsymbol{u}$ denotes the referential displacement gradient. These measures can then be used to derive further deformation and strain tensors, see for example [141, 176]. A multiplicative split of the deformation gradient

$$\boldsymbol{F} = \boldsymbol{F}^{\mathrm{rev}} \cdot \boldsymbol{F}^{\mathrm{irr}} \tag{2.24}$$

into a reversible part $\boldsymbol{F}^{\mathrm{rev}}$ and irreversible part $\boldsymbol{F}^{\mathrm{irr}}$ can be introduced. The reversible part may be an elastic and thermal contribution, whereas the irreversible part may include a viscous, plastic and transformation contribution.
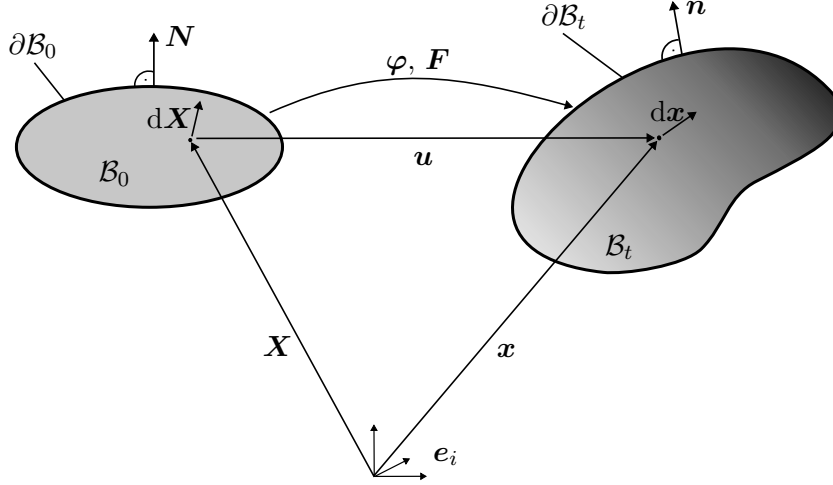
Figure 2.1: Reference (initial, material) configuration $\mathcal{B}_0$ and current (deformed, spatial) configuration $\mathcal{B}_t$ of a deformable body.

The transformation of differential elements, i.e. volume, area and line, can be summarised as

$$\mathrm{d}v = \det(\boldsymbol{F})\,\mathrm{d}V = J\,\mathrm{d}V \tag{2.25}$$

$$\mathrm{d}\boldsymbol{a} = \boldsymbol{n}\,\mathrm{d}a = J\,\boldsymbol{F}^{-\mathrm{t}}\cdot\boldsymbol{N}\,\mathrm{d}A = J\,\boldsymbol{F}^{-\mathrm{t}}\cdot\mathrm{d}\boldsymbol{A} = \mathrm{cof}(\boldsymbol{F})\cdot\mathrm{d}\boldsymbol{A} \tag{2.26}$$

$$\mathrm{d}\boldsymbol{x} = \boldsymbol{F}\cdot\mathrm{d}\boldsymbol{X} \tag{2.27}$$

with the determinant $J = \det(\boldsymbol{F}) > 0$ and the cofactor $\mathrm{cof}(\boldsymbol{F}) = \partial J/\partial\boldsymbol{F} = J\,\boldsymbol{F}^{-\mathrm{t}}$. In addition, $\boldsymbol{N}$ and $\boldsymbol{n}$ define the outward unit normal vectors in the respective configurations on the boundaries $\partial\mathcal{B}_0$ and $\partial\mathcal{B}_t$, respectively.

In the further course of this thesis, the small strain theory is considered to be appropriate, as the elastic and inelastic strains occurring during the manufacturing process are considered small. In other words, the finite strain theory, where one distinguishes between the initial and deformed configuration, is no longer required and the configuration shall be denoted as $\mathcal{B}$. Therefore, an infinitesimal strain theory is established based on the linearised strain measure $\boldsymbol{\varepsilon}$. The linearised strain measure follows from the Green-Lagrange strain tensor

$$\boldsymbol{E} := \frac{1}{2}\left[\boldsymbol{F}^{\mathrm{t}}\cdot\boldsymbol{F} - \boldsymbol{I}\right] \overset{(2.23)}{=} \frac{1}{2}\left[\boldsymbol{H} + \boldsymbol{H}^{\mathrm{t}} + \boldsymbol{H}^{\mathrm{t}}\cdot\boldsymbol{H}\right]\,. \tag{2.28}$$

For the small strain theory, which assumes geometric linearity, the assumption $\|\boldsymbol{H}\| = \|\nabla_{\boldsymbol{X}}\boldsymbol{u}\| \ll 1$ is valid such that the higher order term can be neglected. This results in the infinitesimal or linear strain measure

$$\boldsymbol{\varepsilon} = \frac{1}{2}\left[\boldsymbol{H} + \boldsymbol{H}^{\mathrm{t}}\right] = \frac{1}{2}\left[\nabla_{\boldsymbol{X}}\boldsymbol{u} + [\nabla_{\boldsymbol{X}}\boldsymbol{u}]^{\mathrm{t}}\right] = \nabla_{\boldsymbol{X}}^{\mathrm{sym}}\boldsymbol{u}\;, \tag{2.29}$$

which corresponds to the symmetric part of the displacement gradient, whereas $\boldsymbol{u}$ denotes the displacement field. In this setting, the total strains can be additively decomposed as follows

$$\boldsymbol{\varepsilon} = \boldsymbol{\varepsilon}^{\mathrm{el}} + \boldsymbol{\varepsilon}^{\mathrm{inel}} \tag{2.30}$$

into an elastic part $\boldsymbol{\varepsilon}^{\mathrm{el}}$ and an inelastic part $\boldsymbol{\varepsilon}^{\mathrm{inel}}$. This is in contrast to the multiplicative split for large strains, compare eq. (2.24). The inelastic strains reflect the combination of various effects e.g. viscous, thermal or plastic strains and the combination thereof, and transformation strains, i.e. eigenstrains, capturing the phase transformation of the material, as discussed in subsequent chapters.

2.3 Balance equations

This section briefly introduces the balance equations for the infinitesimal strain theory, which are used within this thesis. This considerably simplifies the balance equations compared with the large strain theory, see also Remark 1. To simulate the underlying LPBF process, a thermodynamically fully coupled model is proposed. Thus, the problem at hand is based on the balance of linear momentum and on the energy equation which follows from the first law of thermodynamics. The thermomechanical forces are introduced for a finite body, compare Figure 2.1, where $\boldsymbol{t}$ refers to the surface traction vector, $\boldsymbol{b}$ defines the body forces, e.g. gravity, q_n represents heat supply through the body's surface and r^{ext} introduces external volume heat supply (per unit volume), e.g. chemical reaction or latent heat during solid-solid phase transformations. Such a coupled problem requires suitable boundary conditions on $\partial\mathcal{B}$ and initial conditions as well. Dirichlet boundary conditions refer to prescribed fields, such as temperature $\theta = \overline{\theta}$ and displacement $\boldsymbol{u} = \overline{\boldsymbol{u}}$. Surface quantities are prescribed for Neumann boundary conditions, i.e. surface tractions $\boldsymbol{t} = \overline{\boldsymbol{t}}$ and heat supply though the body surface $q_n = \overline{q}_n$.

Remark 1. *For a large strain formulation, it is possible to derive the balance equations with respect to both, the referential and spatial, configurations of a body. In addition, different stress and strain measures can be used. These basics are not discussed in this thesis, but can be found in e.g. [70, 107, 176].*
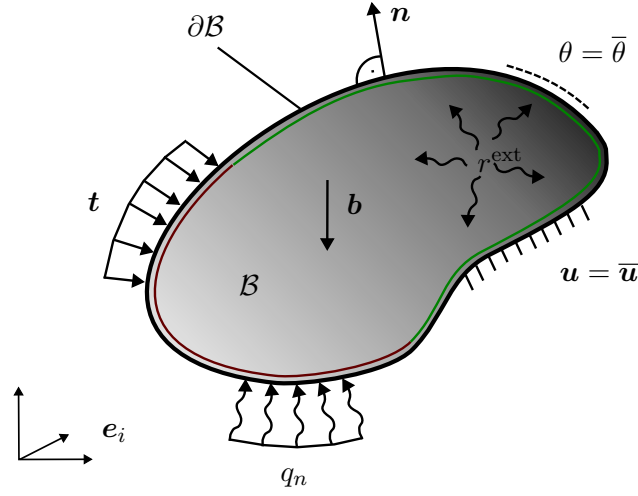
Figure 2.2: Thermomechanical setting for a finite body $\mathcal{B}$.

Conservation of mass: For so-called closed systems, mass is a conserved quantity, so that $\dot{m} = 0$, where no material is exchanged over its boundaries or produced within the body over time. This results in the integral form

$$\frac{\mathrm{d}m}{\mathrm{d}t} = \frac{\mathrm{d}}{\mathrm{d}t} \int_{\mathcal{B}} \rho \, \mathrm{d}V = 0 \,, \tag{2.31}$$

where ρ denotes the mass density of the body $\mathcal{B}$.

Balance of linear and angular momentum: The change in linear momentum, also called the material time derivative during deformation, equals the sum of all external forces acting on the body $\mathcal{B}$. These are the body force $\boldsymbol{b}$ (per unit volume) and the stress vector $\boldsymbol{t}$. The balance of linear momentum in integral form thus reads

$$\frac{\mathrm{d}}{\mathrm{d}t} \int_{\mathcal{B}} \rho \, \dot{\boldsymbol{u}} \, \mathrm{d}V = \int_{\mathcal{B}} \boldsymbol{b} \, \mathrm{d}V + \int_{\partial\mathcal{B}} \boldsymbol{t} \, \mathrm{d}A \,. \tag{2.32}$$

Notation $\dot{\bullet}$ denotes the time derivative of the respective quantity $\bullet$. Cauchy's theorem $\boldsymbol{t} = \boldsymbol{\sigma} \cdot \boldsymbol{n}$ and Gauß's divergence theorem $\int_{\partial\mathcal{B}} \boldsymbol{\sigma} \cdot \boldsymbol{n} \, \mathrm{d}A = \int_{\mathcal{B}} \nabla \cdot \boldsymbol{\sigma} \, \mathrm{d}V$ is applied for the last term in eq. (2.32). Here, $\boldsymbol{n}$ describes the outward normal unit vector and $\boldsymbol{\sigma}$ refers to the (Cauchy) stress tensor. With this, the local spatial form is derived as

$$\rho \, \ddot{\boldsymbol{u}} = \boldsymbol{b} + \nabla \cdot \boldsymbol{\sigma} \,. \tag{2.33}$$

The material time derivative of angular momentum with respect to a given point in a body changes according to the sum of all external moments with respect to the same

given point. From the balance of angular momentum it directly follows that only symmetric (Cauchy) stress tensors are allowed, i.e.

$$\boldsymbol{\sigma} = \boldsymbol{\sigma}^{\mathrm{t}} \ . \tag{2.34}$$

Using a constitutive law which enforces symmetry of the (Cauchy) stress fulfils the angular momentum a priori, cf. [107]. This is the case for the model at hand, as a standard mechanical continuum is regarded where body couples are neglected.

First law of thermodynamics (Balance of energy):
The first law of thermodynamics defines the interconversion of energy, which states that the rate of change of the total energy of a body equals the sum of external powers acting on the body. The total energy can be decomposed into kinetic energy

$$\mathcal{K} = \frac{1}{2} \int_{\mathcal{B}} \rho \, \|\dot{\boldsymbol{u}}\|^2 \, \mathrm{d}V \tag{2.35}$$

and internal energy

$$\mathcal{E} = \int_{\mathcal{B}} \rho \, e \, \mathrm{d}V \ , \tag{2.36}$$

where e symbolises the specific internal energy, also referred to as energy density. One can distinguish between the external mechanical input $\mathcal{P}^{\mathrm{ext}}$ from the mechanical loads $\boldsymbol{b}$ and $\boldsymbol{t}$ and the thermal power supply $\mathcal{Q}^{\mathrm{ext}}$ from q_n and r^{ext}, such that

$$\mathcal{P}^{\mathrm{ext}} = \int_{\mathcal{B}} \boldsymbol{b} \cdot \dot{\boldsymbol{u}} \, \mathrm{d}V + \int_{\partial\mathcal{B}} \boldsymbol{t} \cdot \dot{\boldsymbol{u}} \, \mathrm{d}A \ , \tag{2.37}$$

$$\mathcal{Q}^{\mathrm{ext}} = \int_{\mathcal{B}} r^{\mathrm{ext}} \, \mathrm{d}V + \int_{\partial\mathcal{B}} q_n \, \mathrm{d}A \ . \tag{2.38}$$

The global form of the balance of energy thus reads $\dot{\mathcal{E}} + \dot{\mathcal{K}} = \mathcal{P}^{\mathrm{ext}} + \mathcal{Q}^{\mathrm{ext}}$. Applying Cauchy's theorem and Gauß's divergence theorem together with both the balance of linear momentum eq. (2.33) and angluar momentum eq. (2.34), one can reformulate eq. (2.37) to

$$\mathcal{P}^{\mathrm{ext}} = \int_{\mathcal{B}} \rho \, \ddot{\boldsymbol{u}} \cdot \dot{\boldsymbol{u}} \, \mathrm{d}V + \int_{\mathcal{B}} \boldsymbol{\sigma} : \dot{\boldsymbol{\varepsilon}} \, \mathrm{d}V \ . \tag{2.39}$$

In addition, the heat flux vector $q_n = -\boldsymbol{q} \cdot \boldsymbol{n}$ holds, where $\boldsymbol{q}$ refers to the heat flux. Eq. (2.38) is simplified by using Gauß's divergence theorem to

$$\mathcal{Q}^{\mathrm{ext}} = \int_{\mathcal{B}} r^{\mathrm{ext}} \, \mathrm{d}V - \int_{\mathcal{B}} \nabla \cdot \boldsymbol{q} \, \mathrm{d}V \ . \tag{2.40}$$

As conservation of mass, eq. (2.31), is assumed, the expression $\dot{\rho} = 0$ is valid. This results in the local form of the energy equation

$$\rho \dot{e} = \boldsymbol{\sigma} : \dot{\boldsymbol{\varepsilon}} + r^{\text{ext}} - \nabla \cdot \boldsymbol{q} \, , \tag{2.41}$$

where $\boldsymbol{\sigma} : \dot{\boldsymbol{\varepsilon}}$ refers to the rate of mechanical work.

Second law of thermodynamics (Balance of entropy): The second law of thermodynamics defines the direction of energy conversion. It states that the entropy production $\dot{\mathcal{S}}$ is always larger than or equal to the rate of entropy input $\mathcal{R}^{\text{ext}}$, thus

$$\dot{\mathcal{S}} - \mathcal{R}^{\text{ext}} \geq 0 \, . \tag{2.42}$$

Entropy is defined as

$$\mathcal{S} = \int_{\mathcal{B}} \rho \, s \, \mathrm{d}V \, , \tag{2.43}$$

where s refers to the specific entropy. It is assumed that the input of entropy is proportional to the thermal power supply $\mathcal{Q}^{\text{ext}}$ so that

$$\mathcal{R}^{\text{ext}} = \int_{\mathcal{B}} \frac{r^{\text{ext}}}{\theta} \, \mathrm{d}V + \int_{\partial\mathcal{B}} \frac{q_n}{\theta} \, \mathrm{d}A \tag{2.44}$$

with the absolute temperature $\theta > 0$. With this, the entropy inequality in global form, also referred to as Clausius-Duhem inequality, follows as

$$\int_{\mathcal{B}} \rho \, \dot{s} \, \mathrm{d}V \geq \int_{\mathcal{B}} \frac{r^{\text{ext}}}{\theta} \, \mathrm{d}V - \int_{\partial\mathcal{B}} \frac{q_n}{\theta} \, \mathrm{d}A \, . \tag{2.45}$$

Using some mathematical conversions to reformulate the surface integral into a volume integral, the second law of thermodynamics in local form reads

$$\rho \, \theta \dot{s} \geq r^{\text{ext}} - \nabla \cdot \boldsymbol{q} + \frac{1}{\theta} \boldsymbol{q} \cdot \nabla\theta \, . \tag{2.46}$$

The second law of thermodynamics, i.e. eq. (2.46), can be reformulated in terms of the dissipation symbolised with $\mathcal{D}$ and split into a mechanical and thermal part, i.e.

$$\mathcal{D} = \mathcal{D}_{\text{mech}} + \mathcal{D}_{\text{therm}} \geq 0 \, . \tag{2.47}$$

Moreover, each contribution is assumed to be non-negative. This results in the Fourier inequality for the thermal contribution on the one hand,

$$\mathcal{D}_{\text{therm}} = -\frac{1}{\theta}\, \boldsymbol{q} \cdot \nabla \theta \geq 0 \;, \tag{2.48}$$

and in the Clausius-Planck inequality on the other hand,

$$\mathcal{D}_{\text{mech}} = \theta\,\rho\,\dot{s} - r^{\text{ext}} + \nabla \cdot \boldsymbol{q} \overset{(2.41)}{=} \theta\,\rho\,\dot{s} - \rho\,\dot{e} + \boldsymbol{\sigma}:\dot{\boldsymbol{\varepsilon}} \geq 0 \;. \tag{2.49}$$

A material model can be called thermodyamically consistent, if eqs. (2.48) and (2.49) are fulfilled.

A fully coupled thermomechanical model is necessary for the AM process. For the simulation of the underlying LPBF process, quasi-static conditions are postulated, such that dynamic effects $\ddot{\boldsymbol{u}} \equiv \boldsymbol{0}$ are neglected. In addition, body forces are assumed to be negligible hereafter, such that $\boldsymbol{b} \equiv \boldsymbol{0}$. Thus, the balance of linear momentum in eq. (2.33) simplifies to

$$\boldsymbol{0} = \nabla \cdot \boldsymbol{\sigma} \;. \tag{2.50}$$

The system of equations is completed together with the energy equation, compare eq. (2.41).

2.4 Constitutive relations

In order to define the material response of a body, constitutive relations are necessary. In the following, the second law of thermodynamics is used to determine the internal dissipation and to introduce the constitutive relations. As proposed in [35], the specific Helmholtz free energy density Ψ shall be used for a thermodynamic consistent derivation. In order to reformulate the problem depending on the absolute temperature θ as state variable rather than on the entropy s, the specific Helmholtz free energy Ψ is obtained via the Legendre transformation

$$e = \Psi + s\,\theta \;, \tag{2.51}$$
$$\Rightarrow \dot{e} = \dot{\Psi} + s\,\dot{\theta} + \dot{s}\,\theta \;. \tag{2.52}$$

In general, the Helmholtz free energy $\Psi(\boldsymbol{\varepsilon}, \theta, \mathcal{V})$ depends on the total strains $\boldsymbol{\varepsilon}$, the absolute temperature θ and – at this point not further specified – on internal variables $\mathcal{V}$.

Thus, the set of independent thermodynamic variables is defined. With this at hand, the time derivative of the Helmholtz free energy results in

$$\dot{\Psi} = \frac{\partial \Psi}{\partial \boldsymbol{\varepsilon}} : \dot{\boldsymbol{\varepsilon}} + \frac{\partial \Psi}{\partial \theta} \dot{\theta} + \frac{\partial \Psi}{\partial \mathcal{V}} \bullet \dot{\mathcal{V}} \,, \tag{2.53}$$

where $\bullet$ represents a generalised scalar product. By using eq. (2.52), it is now possible to reformulate eq. (2.49) such that

$$\mathcal{D}_{\mathrm{mech}} = \boldsymbol{\sigma} : \dot{\boldsymbol{\varepsilon}} - \rho \, s \, \dot{\theta} - \rho \, \dot{\Psi} \,. \tag{2.54}$$

Inserting eq. (2.53) into eq. (2.54) and rearranging terms for the purpose of simplification results in

$$\left[\boldsymbol{\sigma} - \rho \frac{\partial \Psi}{\partial \boldsymbol{\varepsilon}} \right] : \dot{\boldsymbol{\varepsilon}} - \rho \left[s + \frac{\partial \Psi}{\partial \theta} \right] \dot{\theta} - \rho \frac{\partial \Psi}{\partial \mathcal{V}} \bullet \dot{\mathcal{V}} \geq 0 \,. \tag{2.55}$$

Following the lines of the Coleman-Noll procedure, cf. [35], the constitutive equations based on the Helmholtz free energy density can be directly extracted, i.e.

$$\boldsymbol{\sigma} = \rho \frac{\partial \Psi}{\partial \boldsymbol{\varepsilon}} \,, \tag{2.56}$$

$$s = -\frac{\partial \Psi}{\partial \theta} \,. \tag{2.57}$$

From this, the definition of the stresses $\boldsymbol{\sigma}$ and the entropy s can be determined in a straightforward manner. As a further abbreviation, the generalised energy-conjugated and thermodynamic consistent driving force

$$\mathcal{F} = -\rho \frac{\partial \Psi}{\partial \mathcal{V}} \tag{2.58}$$

of the respective internal variable $\mathcal{V}$ is introduced. Substituting these results by eq. (2.55) finally leads to the reduced form of the mechanical dissipation as

$$\mathcal{D}_{\mathrm{mech}} = \mathcal{F} \bullet \dot{\mathcal{V}} \geq 0 \,. \tag{2.59}$$

With these derivations at hand, eq. (2.41) can be rewritten in the more convenient form

$$0 = - \nabla \cdot \boldsymbol{q} - \rho \, c \, \dot{\theta} + r^{\mathrm{ext}} + \mathcal{D}_{\mathrm{mech}} + \theta \, \partial_\theta \big[\boldsymbol{\sigma} : \dot{\boldsymbol{\varepsilon}} - \mathcal{D}_{\mathrm{mech}} \big] \,, \tag{2.60}$$

where the specific heat capacity is defined by

$$c = -\theta \frac{\partial^2 \Psi}{\partial \theta \, \partial \theta} \tag{2.61}$$

and where

$$r_{\mathrm{mech}} = \mathcal{D}_{\mathrm{mech}} + \theta\, \partial_\theta [\, \boldsymbol{\sigma} : \dot{\boldsymbol{\varepsilon}} - \mathcal{D}_{\mathrm{mech}} \,] \tag{2.62}$$

determines the volumetric heat generation caused by mechanical working of the material. Here, the term $\partial_\theta [\, \boldsymbol{\sigma} : \dot{\boldsymbol{\varepsilon}}]$ refers to the Gough-Joule effect, whereas the remaining parts are caused by internal variables.

In the following sections, it is assumed that the (unspecific) Helmholtz free energy density is defined as $\psi = \rho\, \Psi$. With this it is possible to rewrite eq. (2.60) as

$$0 = -\nabla \cdot \boldsymbol{q} - \widetilde{c}\dot{\theta} + r^{\mathrm{ext}} + r_{\mathrm{mech}} \,, \tag{2.63}$$

with the volume specific heat capacity

$$\widetilde{c} = -\theta\, \frac{\partial^2 \psi}{\partial\theta\, \partial\theta} \,. \tag{2.64}$$

2.5 Finite element framework

The discretised weak forms shall be derived in detail by considering the contributions from both mechanical equilibrium in the absence of mechanical body forces and heat equation for a thermodynamically fully coupled system as introduced in Section 2.3. Based on this, the model equations are transformed into discrete forms. The FE implementation into the commercial FE programme Abaqus is briefly discussed in Section 2.6. The weak forms are obtained by multiplying eqs. (2.33) and (2.60) by an arbitrary test function for the displacement and temperature field, $\delta\boldsymbol{u}$ and $\delta\theta$, respectively, that is admissible regarding the continuity and the Dirichlet boundary conditions. Subsequently, the resulting equations are integrated with respect to the volume of the underlying body $\mathcal{B}$. Finally, integration by parts and the divergence theorem are applied. This yields

$$\int_{\partial\mathcal{B}} [\boldsymbol{\sigma} \cdot \boldsymbol{n}] \cdot \delta\boldsymbol{u}\, \mathrm{d}A - \int_{\mathcal{B}} \boldsymbol{\sigma} : \nabla\delta\boldsymbol{u}\, \mathrm{d}V = \boldsymbol{0} \,, \tag{2.65}$$

$$-\int_{\partial\mathcal{B}} \boldsymbol{q} \cdot \boldsymbol{n}\, \delta\theta\, \mathrm{d}A + \int_{\mathcal{B}} \boldsymbol{q} \cdot \nabla\delta\theta\, \mathrm{d}V + \int_{\mathcal{B}} \rho\, r^{\mathrm{ext}}\, \delta\theta\, \mathrm{d}V - \int_{\mathcal{B}} \rho\, c\, \dot{\theta}\, \delta\theta\, \mathrm{d}V$$

$$+ \int_{\mathcal{B}} \mathcal{D}_{\mathrm{mech}}\, \delta\theta\, \mathrm{d}V + \int_{\mathcal{B}} \theta\, \partial_\theta [\boldsymbol{\sigma} : \dot{\boldsymbol{\varepsilon}} - \mathcal{D}_{\mathrm{mech}}]\, \delta\theta\, \mathrm{d}V = 0 \,. \tag{2.66}$$

Using Cauchy's theorem, surface tractions per unit area are represented by $\boldsymbol{t} = \boldsymbol{\sigma} \cdot \boldsymbol{n}$. The heat flux $q_n = -\boldsymbol{q} \cdot \boldsymbol{n}$ is analogously defined.

To discretise the problem in space, the body $\mathcal{B}$ under consideration is decomposed into n_{el} non-overlapping finite elements $\mathcal{B}^e$, i.e. $\mathcal{B} \approx \bigcup_{e=1}^{n_{\mathrm{el}}} \mathcal{B}^e$. The spacial discretisation of the weak forms is represented by

$$\sum_{e=1}^{n_{\mathrm{el}}} \left[\int_{\partial \mathcal{B}^e} \boldsymbol{t} \cdot \delta \boldsymbol{u}^e \, \mathrm{d}A - \int_{\mathcal{B}^e} \boldsymbol{\sigma} : \nabla \delta \boldsymbol{u}^e \, \mathrm{d}V \right] = 0 \,, \tag{2.67}$$

$$\sum_{e=1}^{n_{\mathrm{el}}} \left[\int_{\partial \mathcal{B}^e} q_n \, \delta \theta^e \, \mathrm{d}A + \int_{\mathcal{B}^e} \boldsymbol{q} \cdot \nabla \delta \theta^e \, \mathrm{d}V + \int_{\mathcal{B}^e} \rho \, r^{\mathrm{ext}} \, \delta \theta^e \, \mathrm{d}V - \int_{\mathcal{B}^e} \rho \, c \, \dot{\theta} \, \delta \theta^e \, \mathrm{d}V \right.$$
$$\left. + \int_{\mathcal{B}^e} \mathcal{D}_{\mathrm{mech}} \, \delta \theta^e \, \mathrm{d}V + \int_{\mathcal{B}^e} \theta \, \partial_\theta [\boldsymbol{\sigma} : \dot{\boldsymbol{\varepsilon}} - \mathcal{D}_{\mathrm{mech}}] \, \delta \theta^e \, \mathrm{d}V \right] = 0 \,. \tag{2.68}$$

In addition, the test functions are analogously discretised element-wise

$$\delta \boldsymbol{u}^e \approx \sum_{A=1}^{n_{\mathrm{en}}^u} N_A^u \, \delta \boldsymbol{u}^{eA} \,, \qquad \delta \theta^e \approx \sum_{C=1}^{n_{\mathrm{en}}^\theta} N_C^\theta \, \delta \theta^{eC} \,, \tag{2.69}$$

where n_{en}^θ and n_{en}^u refer to the respective number of element nodes. N_A^u and N_C^θ denote the standard Lagrange-type interpolation polynomials or, in other words, the corresponding set of shape functions. The contributions $\delta \boldsymbol{u}^{eA}$ and $\delta \theta^{eC}$ represent the respective values of the test function at the corresponding nodes A or C of element e. With these relations at hand, and by additionally defining the assembly operator $\mathbf{A}$, the discretised weak form finally reads

$$\underset{\substack{A=1 \\ e=1}}{\overset{\substack{n_{\mathrm{el}} \\ n_{\mathrm{en}}^u}}{\mathbf{A}}} \left[\int_{\partial \mathcal{B}^e} \boldsymbol{t} \, N_A^u \, \mathrm{d}A - \int_{\mathcal{B}^e} \boldsymbol{\sigma} \cdot \nabla N_A^u \, \mathrm{d}V \right] = \mathbf{0} \,, \tag{2.70}$$

$$\underset{\substack{C=1 \\ e=1}}{\overset{\substack{n_{\mathrm{el}} \\ n_{\mathrm{en}}^\theta}}{\mathbf{A}}} \left[\int_{\partial \mathcal{B}^e} q_n \, N_C^\theta \, \mathrm{d}A + \int_{\mathcal{B}^e} \boldsymbol{q} \cdot \nabla N_C^\theta \, \mathrm{d}V + \int_{\mathcal{B}^e} \rho \, r^{\mathrm{ext}} \, N_C^\theta \, \mathrm{d}V - \int_{\mathcal{B}^e} \rho \, c \, \dot{\theta} \, N_C^\theta \, \mathrm{d}V \right.$$
$$\left. + \int_{\mathcal{B}^e} \mathcal{D}_{\mathrm{mech}} \, N_C^\theta \, \mathrm{d}V + \theta \int_{\mathcal{B}^e} \partial_\theta [\boldsymbol{\sigma} : \dot{\boldsymbol{\varepsilon}} - \mathcal{D}_{\mathrm{mech}}] \, N_C^\theta \, \mathrm{d}V \right] = \mathbf{0} \,, \tag{2.71}$$

independent of the respective test function values. In analogy to the test functions, the same approximation is applied for the underlying physical fields such that

$$\boldsymbol{u} \approx \boldsymbol{u}^e = \sum_{B=1}^{n_{\mathrm{en}}^u} N_B^u \, \boldsymbol{u}^{eB} \,, \quad \theta \approx \theta^e = \sum_{D=1}^{n_{\mathrm{en}}^\theta} N_D^\theta \, \theta^{eD} \,, \tag{2.72}$$

from which the occurring gradients and rates can be derived as well. With this, the residual form of the equilibrium equations follows as $\mathbf{r}_u$ referring to eq. (2.70) and $\mathbf{r}_\theta$ to eq. (2.71), respectively, such that

$$\begin{bmatrix} \mathbf{r}_u \\ \mathbf{r}_\theta \end{bmatrix} \overset{!}{=} \begin{bmatrix} \mathbf{0} \\ \mathbf{0} \end{bmatrix} \, , \tag{2.73}$$

where $\mathbf{r}_\bullet$ refers to the respective global residual vector. This results in a system of nonlinear equations which have to be solved iteratively with e.g. Newton-Raphson algorithm. In the subsequent Section 2.6, a possible solution scheme is discussed, where the commercial FE programme Abaqus is used.

2.6 Thermomechanical simulations with Abaqus

In this section, we discuss the possibilities of implementing thermomechanical simulations into the commercial FE programme Abaqus. Abaqus provides a built-in feature for thermomechanical simulations, also referred to as fully coupled thermal-stress analysis, cf. [1]. For this case, the update of the residuals introduced in eq. (2.73) reads

$$\mathbf{r}_\bullet^{i+1} = \mathbf{r}_\bullet^i + \Delta \mathbf{r}_\bullet \tag{2.74}$$

with

$$\Delta \mathbf{r}_\bullet = \frac{\mathrm{d}\mathbf{r}_\bullet}{\mathrm{d}\mathbf{u}} \cdot \Delta \mathbf{u} + \frac{\mathrm{d}\mathbf{r}_\bullet}{\mathrm{d}\theta} \Delta\theta \, , \tag{2.75}$$

which is based on a linearisation at iteration step i. Newton's method then solves the nonlinear coupled system for every iteration step i, such that

$$\begin{bmatrix} \mathbf{K}_{uu} & \mathbf{K}_{u\theta} \\ \mathbf{K}_{\theta u} & \mathbf{K}_{\theta\theta} \end{bmatrix} \cdot \begin{bmatrix} \Delta\mathbf{u} \\ \Delta\theta \end{bmatrix} = - \begin{bmatrix} \mathbf{r}_u \\ \mathbf{r}_\theta \end{bmatrix} \tag{2.76}$$

is derived for an exact implementation. Thereby, $\Delta\mathbf{u}$ and $\Delta\theta$ are the corrections to the displacements and temperature, $\mathbf{K}_{\bullet *} = \mathrm{d}\mathbf{r}_\bullet/\mathrm{d}*$ define the submatrices of the fully coupled Jacobian, also referred to as stiffness matrices. In addition, $\mathbf{r}_u$ and $\mathbf{r}_\theta$ are the corresponding mechanical and thermal residual vectors, compare eq. (2.73). The solution vector, that is the displacements and the temperature, is updated after each iteration until the norm of the global residuum is below a predefined tolerance.

In contrast, the submatrices $\mathbf{K}_{u\theta}$ and $\mathbf{K}_{\theta u}$ are set to zero for an approximate implementation, when only a weak coupling between temperature and displacements is present. This does not affect the overall solution in Abaqus, but the convergence rate and solver time, compare [1].

Abaqus integrates the temperature rate in time in eq. (2.71) via a Backward-Euler scheme. In general, all time derivatives $\dot{\bullet}$ are approximated in the following by

$$\dot{\bullet} = \frac{\mathrm{d}(\bullet)}{\mathrm{d}t} \approx \frac{[\bullet_{n+1} - \bullet_n]}{\Delta t} \, , \tag{2.77}$$

wherein $\bullet_n$ refers to the previous and $\bullet_{n+1}$ to the current time step of the quantity $\bullet$. The time increment is defined as $\Delta t = t_{n+1} - t_n$.

Without self-implemented subroutines, the user can only employ standard material models recorded within Abaqus and standard heat transfer without internal heat generation. If more complex material behaviour shall be implemented, this can be conducted by using user subroutines coded in Fortran, cf. [1]. The fully coupled model developed as this thesis proceeds, which is solved in Abaqus, is based on a phase transformation model, as discussed in the following chapters. In addition, mechanical dissipation shall be consistently taken into account, compare eq. (2.62). Therefore, it is necessary to adapt the mechanical and thermal material behaviour by the user with the respective subroutines `UMAT` and `UMATHT`. These subroutines are called at each integration point within the Abaqus solver for eq. (2.76). To gain a better understanding of the implementation into Abaqus, the specific structure and all return values for both subroutines shall be analysed. This will be discussed in detail in the following Sections 2.6.1 and 2.6.2 for small strains. For a large strain formulation, the interested reader is referred to e.g. [134].

Another way of implementing this model is by using the most powerful and complex subroutine `UEL`, where a user-defined element including the stiffness matrix, the state variables and energy related quantities have to be defined, see for example [86]. Contrary to the formulation of a user element in Abaqus via `UEL`, the time for development and for testing the model is less when using a coupled temperature-displacement analysis together with `UMAT` and `UMATHT`. This also enables the usage of all standard features within Abaqus.

2.6.1 UMAT – User subroutine for a mechanical material model

For a mechanical user material, the general return quantities `STRESS`, `STATEV`, `DDSDDE` have to be defined. Within the subroutine, not only the strain tensor $\boldsymbol{\varepsilon}$ is provided as an input variable, but also the temperature θ. This is necessary to implement a thermomechanically coupled user material. For this case, the thermomechanical quantities `RPL`, `DRPLDT`, `DRPLDE` and `DDSDDT` must be evaluated within the `UMAT` user subroutine for the coupled material model. These abbreviations are summarised in Table 2.1.

In detail, the states of the underlying global variables, namely strains $\boldsymbol{\varepsilon}_n$ and temperature θ_n, as well as the values of the respective internal state dependent variables $\mathcal{V}_n$ and the mechanical material parameters are passed to the subroutine. These can be accessed for the calculation of the current values, where a finite time step $\Delta t = t_{n+1} - t_n$

is considered. Thus, the total strain and temperature at the beginning of the time step have to be updated

$$\theta_{n+1} = \theta_n + \Delta\theta \ , \tag{2.78}$$
$$\varepsilon_{n+1} = \varepsilon_n + \Delta\varepsilon \ . \tag{2.79}$$

Attention should be paid to the structure of the total strains, where Abaqus uses engineering components for storage rather than tensor components, meaning $\gamma_{ij} = 2\,\varepsilon_{ij}$. In addition, the strains are passed into the subroutine in Voigt notation, compare eq. (2.17). Using the constitutive relations of the material model, all state variables $\mathcal{V}_{n+1}$ have to be updated for the current time step t_{n+1}. The specific procedure and the definition of the corresponding values will be subject of the following chapters. Depending on the number of scalar valued quantities, which can be saved within `STATEV`, enough storage space has to be allocated by using the keyword *`DEPVAR`. These variables are also referred to as state dependent variables `SDV` in the output format. The total stress $\boldsymbol{\sigma}_{n+1}$ is then calculated as introduced in eq. (2.56). Attention has to be paid especially regarding the storage scheme of Abaqus. All tensor valued quantities have to be transformed to classic Voigt notation as introduced in Section 2.1, and indicated in Table 2.1. Precisely speaking, the stress variable then reads

$$[\boldsymbol{\sigma}]^{\mathrm{voi}} = [\sigma_{11}, \sigma_{22}, \sigma_{33}, \sigma_{12}, \sigma_{13}, \sigma_{23}]^{\mathrm{t}} \ . \tag{2.80}$$

For a thermomechanically coupled model, the volumetric heat generation caused by mechanical working r^{mech} has to be determined as defined in eq. (2.62). Within this quantity, dissipation due to internal variables and the Gough-Joule effect is expected. Finally, the respective derivatives, i.e. the contributions to the Jacobian within the Newton-Raphson-based solution scheme, can be computed, as summarised in Table 2.1. Simplifying the contributions of the Jacobian does not influence the results itself, but only affects the convergence rate of the outer Newton-Raphson scheme as introduced in Section 2.6.

2.6.2 UMATHT – User subroutine for a thermal material model

Abaqus generally provides a standard treatment of the heat transfer problem without the need of further subroutines. However, if thermal quantities depend on internal variables $\mathcal{V}$, the usage of the specific subroutine is necessary. The thermal material model can be defined – and adapted – within the user subroutine `UMATHT`. In addition, the heat equation and with it the subroutine `UMATHT` has been manipulated before, see for example Appendix A.1 for a porous media model based on the continuity equation (temperature $\theta \leftarrow p$ pore pressure) and [134] for a finite deformation gradient-enhanced damage model (temperature field $\theta \leftarrow \phi$ non-local damage field).

Table 2.1: Specification of all Abaqus variables when implementing the user subroutine `UMAT` for a fully coupled thermomechanical model.

`UMAT` variable	thermomechanical model
PROPS	all material parameters
STATEV	$\mathcal{V}$
STRESS	$[\boldsymbol{\sigma}]^{\mathrm{voi}}$
DDSDDE	$\left[\dfrac{\mathrm{d}\boldsymbol{\sigma}}{\mathrm{d}\boldsymbol{\varepsilon}}\right]^{\mathrm{voi}} = \left[\mathbf{E}^{\mathrm{algo}}\right]^{\mathrm{voi}}$
DDSDDT	$\left[\dfrac{\mathrm{d}\boldsymbol{\sigma}}{\mathrm{d}\theta}\right]^{\mathrm{voi}} = \left[\boldsymbol{\beta}_{\mathrm{algo}}\right]^{\mathrm{voi}}$
RPL	r^{mech}
DRPLDE	$\left[\dfrac{\mathrm{d}r^{\mathrm{mech}}}{\mathrm{d}\boldsymbol{\varepsilon}}\right]^{\mathrm{voi}} = \left[\boldsymbol{\gamma}_{\mathrm{algo}}\right]^{\mathrm{voi}}$
DRPLDT	$\dfrac{\mathrm{d}r^{\mathrm{mech}}}{\mathrm{d}\theta} = \delta_{\mathrm{algo}}$

Within this subroutine, the thermal material parameters and the current internal variables $\mathcal{V}$ as determined in the subroutine `UMAT` are accessible. The quantities and respective derivatives `U`, `DUDT`, `DUDG` for the internal energy and `FLUX`, `DFDT`, `DFDG` for the heat flux have to be specified. These variables are presented in Table 2.2. In general, the strong form of the energy balance in Abaqus [1] is defined as

$$\rho\,\dot{e} = -\nabla \cdot \boldsymbol{q} + r^{*}\,, \tag{2.81}$$

where r^{*} summarises all effective heat sources of the model. This format is more convenient for the implementation into commercial FE programmes. Following the derivations in Sections 2.3 and 2.4, some differences are visible, compare also eq. (2.60) with eq. (2.81). Overall, the heat sources in a thermomechanical problem can be additively decomposed into the sum of external heat supply r^{ext} and the volumetric heat generation caused by mechanical working of the material r_{mech} as defined in eq. (2.62). This results in

$$r^{*} = r_{\mathrm{mech}} + r^{\mathrm{ext}}\,. \tag{2.82}$$

All terms contributing to r_{mech} are calculated within the user subroutine `UMAT` as contributions to the variable `RPL` as defined in Section 2.6.1. In a thermomechanical analysis,

this contribution – if specified – is automatically added to the external heat sources. In doing so, it is possible to directly include the influence of mechanical working and dissipation in Abaqus. The update of the internal thermal energy per unit mass e and its derivatives, as well as the heat flux vector $\boldsymbol{q}$ and its derivatives have to be actualised within the subroutine. Following the derivations in Section 2.3, $e = c\,\theta$ is valid for standard heat transfer. For the approach at hand, the update is defined as

$$e_{n+1} = e_n + c\,\Delta\theta \;, \tag{2.83}$$

with the (mass) specific heat capacity c, compare eq. (2.61). In view of the specific heat capacity the following aspect should be noted: The local energy balance in eq. (2.81) already includes a density ρ, which cannot be directly changed within the subroutine itself, but which is defined within Abaqus as an initial material condition of the whole model. Finally, heat conduction is governed by the isotropic Fourier law

$$\boldsymbol{q}_{n+1} = -\widetilde{k}_{\text{eff}}\,\boldsymbol{I}\cdot\nabla\theta \;, \tag{2.84}$$

where $\widetilde{k}_{\text{eff}}$ refers to the averaged thermal conductivity of the mixture and where $\boldsymbol{I}$ denotes the second order identity tensor. The values of the variables c and $\widetilde{k}_{\text{eff}}$ will be discussed in the following chapters. Finally, the respective derivatives have to be defined, see Table 2.2.

Table 2.2: Specification of all Abaqus variables when implementing the user subroutine `UMATHT` for a thermal model.

UMATHT **variable**	**standard heat transfer**
PROPS	all material parameters
STATEV	$\mathcal{V}$
U	e
DUDT	$\dfrac{\mathrm{d}e}{\mathrm{d}\theta}$
DUDG	$\dfrac{\mathrm{d}e}{\mathrm{d}\nabla\theta}$
FLUX	$\boldsymbol{q}$
DFDT	$\dfrac{\mathrm{d}\boldsymbol{q}}{\mathrm{d}\theta}$
DFDG	$\dfrac{\mathrm{d}\boldsymbol{q}}{\mathrm{d}\nabla\theta}$

A Appendix

A.1 Using Abaqus for porous media

The implementation of a porous media problem is usually performed by using a coupled pore fluid diffusion-stress analysis. Abaqus provides a built-in feature for such a problem. However, it is assumed that both solid and fluid phases are intrinsically incompressible, which in turn means that Biot's modulus approaches infinity. Therefore, this assumption is not appropriate for other poroelastic problems. In the following, the respective equations for poroelasticity are introduced and related to the heat equation, before defining its computational treatment. The implementation into Abaqus by using the fully coupled thermal-stress analysis as introduced in Section 2.6 is discussed, where the porous media material model is achieved with help of the subroutines `UMAT` and `UMATHT`. This allows the implementation of the framework at hand without writing a user element subroutine `UEL`.

First, the implementation of the macroscale system of equations into the commercial finite element (FE) programme Abaqus is discussed. The mechanical equilibrium statement for the porous medium, i.e. the simplified balance of linear momentum, compare eq. (2.50), is considered together with the continuity statement, respectively the conservation of mass,

$$\dot{p}^{(0)} = -M \left[\nabla_{\boldsymbol{x}} \cdot \langle \boldsymbol{v} \rangle_{rf} + \tilde{\boldsymbol{\alpha}} : \dot{\boldsymbol{\varepsilon}} \right] \tag{2.85}$$

for its liquid phase, where $p^{(0)}$ describes the present pore pressure, $\langle \boldsymbol{v} \rangle_{rf}$ represents the relative pore fluid velocity, M and $\tilde{\boldsymbol{\alpha}}$ are the Biot modulus and the Biot tensor, respectively. The Biot tensor is defined as $\tilde{\boldsymbol{\alpha}} = \tilde{\alpha} \, \boldsymbol{I}$, where $\tilde{\alpha}$ represents the Biot coefficient and $\boldsymbol{I}$ is the second order identity tensor. In order to close the overall system of equations, the following constitutive relations shall be introduced for the stresses as well as for the relative pore fluid velocity, to be specific

$$\boldsymbol{\sigma} = \tilde{\mathbf{E}} : \boldsymbol{\varepsilon} - p^{(0)} \, \tilde{\boldsymbol{\alpha}} \,, \tag{2.86}$$

$$\langle \boldsymbol{v} \rangle_{rf} = - \langle \boldsymbol{W} \rangle_f \cdot \nabla_{\boldsymbol{x}} p^{(0)} \,, \tag{2.87}$$

where $\tilde{\mathbf{E}}$ denotes the effective elasticity tensor and where $\langle \boldsymbol{W} \rangle_f$ symbolises the hydraulic conductivity. For further explanations, the reader is referred to [41] and the references therein.

Following the FE derivation in Section 2.5, the discretised weak form of eq. (2.85) is derived as

$$
\mathop{\mathbf{A}}_{\substack{C=1 \\ e=1}}^{\substack{n_{\mathrm{el}} \\ n_{\mathrm{en}}^{p}}} \left[\int_{\mathcal{B}^e} \frac{1}{M}\, \dot{p}^{(0)}\, N_C^p \,\mathrm{d}V_0 + \int_{\partial\mathcal{B}^e} \langle \boldsymbol{v}\rangle_{rf} \cdot \boldsymbol{n}\, N_C^p \,\mathrm{d}S_0 \right.
$$

$$
\left. - \int_{\mathcal{B}^e} \langle \boldsymbol{v}\rangle_{rf} \cdot \nabla\, N_C^p \,\mathrm{d}V_0 + \int_{\mathcal{B}^e} \tilde{\boldsymbol{\alpha}} : \dot{\boldsymbol{\varepsilon}}\, N_C^p \,\mathrm{d}V_0 \right] = \mathbf{0}\,, \tag{2.88}
$$

where N_C^p denotes the corresponding set of shape functions for the pore pressure. In general, the assumptions made for the temperature degree of freedom θ are now applied to the pore pressure $p^{(0)}$, compare eqs. (2.69) and (2.72).

Comparing eq. (2.88) with eq. (2.71), it can be summarised that the heat equation as well as the continuity equation are both partial differential equations (PDE) in a similar form. The mechanical and thermal material behaviour with the respective subroutines `UMAT` and `UMATHT` can be adapted by the user, as summarised in Sections 2.6.1 and 2.6.2. By doing so, the heat equation is "manipulated", such that the temperature degree of freedom θ is equal to the pore pressure $p^{(0)}$ and that the heat flux $\boldsymbol{q}$ corresponds to the relative pore fluid velocity $\langle \boldsymbol{v}\rangle_{rf}$. Thus, the heat transfer equation is "abused" to solve the PDE of the pore pressure, so that Abaqus can be used to implement the discretised macroscale system of equations as defined in eqs. (2.70) and (2.88).

Following Sections 2.6.1 and 2.6.2, the implementation into Abaqus is possible in a straightforward manner, if the temperature degree of freedom θ is substituted by the pore pressure $p^{(0)}$. For a thermomechanically coupled user material, the mechanical quantities as well as the coupling terms have to be defined as introduced in Section 2.6.1. The respective quantities for the porous media model are summarised in Table 2.3. The return variable `STRESS` is updated according to the constitutive eq. (2.86). In view of eq. (2.88), the only contribution dependent on the displacement field, namely volumetric heat generation caused by mechanical working

$$
r^{\mathrm{mech}} = -\tilde{\boldsymbol{\alpha}} : \dot{\boldsymbol{\varepsilon}} \approx -\frac{1}{\Delta t}\, \tilde{\boldsymbol{\alpha}} : \left[{}^{n+1}\boldsymbol{\varepsilon} - {}^{n}\boldsymbol{\varepsilon} \right]\,, \tag{2.89}
$$

is incorporated into `RPL`. An implicit Backward Euler integration scheme is adapted for the time discretisation of the strain rate $\dot{\boldsymbol{\varepsilon}}$. The continuity statement eq. (2.88) is incorporated within `UMATHT` following the derivations in Section 2.6.2, where the respective counterparts and derivatives for poroelasticity are specified in Table 2.4. These quantities can be directly defined when comparing eq. (2.88) with eq. (2.71). The constitutive relation (2.87) is used for the return variable `FLUX`.

The results obtained by solving the macroscale system of poroelastic PDEs introduced above can be found in [41]. Here, the authors present the numerical solution of the one-dimensional Terzaghi's problem and of biological tissues, such as brain white and grey matter and cell aggregates.

Table 2.3: Specification of all return values for the porous media model when implementing the user subroutine `UMAT`, where the temperature degree of freedom θ is substituted by the pore pressure $p^{(0)}$, compare Table 2.1.

UMAT variable	porous media model
STATEV	-
STRESS	$\boldsymbol{\sigma} = \tilde{\mathbf{E}} : \boldsymbol{\varepsilon} - p^{(0)} \, \tilde{\boldsymbol{\alpha}}$
DDSDDE	$\dfrac{\mathrm{d}\boldsymbol{\sigma}}{\mathrm{d}\boldsymbol{\varepsilon}} = \tilde{\mathbf{E}}$
DDSDDT	$\dfrac{\mathrm{d}\boldsymbol{\sigma}}{\mathrm{d}p^{(0)}} = -\tilde{\boldsymbol{\alpha}}$
RPL	$r^{\mathrm{mech}} = -\tilde{\boldsymbol{\alpha}} : \dot{\boldsymbol{\varepsilon}} \approx -\dfrac{1}{\Delta t} \, \tilde{\boldsymbol{\alpha}} : \left[\, {}^{n+1}\boldsymbol{\varepsilon} - \, {}^{n}\boldsymbol{\varepsilon} \right]$
DRPLDE	$\dfrac{\mathrm{d}r^{\mathrm{mech}}}{\mathrm{d}\boldsymbol{\varepsilon}} = -\dfrac{\tilde{\boldsymbol{\alpha}}}{\Delta t}$
DRPLDT	$\dfrac{\mathrm{d}r^{\mathrm{mech}}}{\mathrm{d}p^{(0)}} = 0$

Table 2.4: Specification of all return values for the porous media model when implementing the user subroutine `UMATHT`, where the temperature degree of freedom θ is substituted by the pore pressure $p^{(0)}$, compare Table 2.2.

UMATHT variable	porous media model
U	$U = \dfrac{1}{M} \, p^{(0)}$
DUDT	$\dfrac{\mathrm{d}U}{\mathrm{d}p^{(0)}} = \dfrac{1}{M}$
DUDG	$\dfrac{\mathrm{d}U}{\mathrm{d}\nabla p^{(0)}} = \mathbf{0}$
FLUX	$\langle \boldsymbol{v} \rangle_{rf} = - \langle \boldsymbol{W} \rangle_f \cdot \nabla_{\boldsymbol{x}} p^{(0)}$
DFDT	$\dfrac{\mathrm{d}\boldsymbol{q}}{\mathrm{d}p^{(0)}} = \mathbf{0}$
DFDG	$\dfrac{\mathrm{d}\boldsymbol{q}}{\mathrm{d}\nabla p^{(0)}} - \langle \boldsymbol{W} \rangle_f$

3 A phase transformation framework based on volume fractions

The complex multiphysical processes occurring during LPBF necessitates the establishment of appropriate constitutive and process models in order to quantitatively predict the properties of the final workpiece. In particular, the accurate determination of process-induced eigenstresses is a challenging yet important task. The overall material behaviour is determined according to a solid-solid phase transformation model, see, e.g. [11–13, 78, 85]. In this chapter, a constitutive modelling framework stemming from solid-solid phase transformations in shape memory alloys is adapted to the modelling of the changes of state during LPBF processes. This model is based on energy densities and energy minimisation in general, without taking into account the changing mass densities of the material. As a first step, the present overall material model comprises three phases of the material, namely powder, molten, and re-solidified material. It specifically serves as a basis for further enhancements in the following Chapters, such as the consideration of mass densities and mass conservation in Chapter 4 and multiple solid phases in Chapter 6.

This chapter is structured as follows: the phase transformation model is discussed in Section 3.1 in detail. The thermodynamically fully coupled FE-based process model incorporates approaches for, e.g., the laser beam impact zone and the layer construction model, which are explained in Section 3.2. It also comprises the numerical solution strategies, e.g. in terms of the underlying inequality constraints, and the discussion concerning user-defined Abaqus routines. In Section 3.3, numerical results are shown in terms of a purely academic study in order to achieve a general proof of concept and a basic LPBF process simulation.

3.1 Constitutive framework

In this section, the constitutive model shall be discussed in detail. This comprises the specification of the phase transformation model in Section 3.1.1 as well as the approaches adapted for the underlying thermal problem in Section 3.1.2. The models are thermo-mechanically fully coupled with respect to the macro and micro scale. As this work proceeds, the following simplifications shall be applied to eq. (2.63): The mechanical

dissipation $\mathcal{D}_{\mathrm{mech}}$ due to phase transitions described in the following Sections is considered negligible which is identical to setting $\mathcal{F} \equiv 0$ and, as a consequence, also $\partial_\theta \mathcal{F} \equiv 0$. In addition, all dependencies of $\boldsymbol{\sigma}$ with respect to θ shall be neglected, thus $\partial_\theta \boldsymbol{\sigma} \approx \boldsymbol{0}$. It follows that the heat equation simplifies to

$$0 = -\nabla \cdot \boldsymbol{q} - \widetilde{c}\dot{\theta} + r^{\mathrm{ext}} . \tag{3.1}$$

3.1.1 Material model

The material model shall not solely rely on temperature-dependent material parameters, where the phase transition is enforced by the melting temperature, see e.g. [54, 99, 185], but rather on fundamental constitutive relations for each phase of the material. In this context, the term phase is used in a broader sense here: Each state of the material – namely powder, molten, and re-solidified – is considered as a solid-type phase of the material. This can be considered only as an approximation, in particular with respect to the molten phase. However, this assumption may be justified due to the fact that the molten phase is not present for a significant period of time and that the associated fluid structure interaction during this period can thus be considered negligible. Furthermore, both the powder and the molten phase cannot transfer tension forces. Such tension forces, however, do not occur in these phases within the present simulations so that the constitutive framework at this stage does not account for this tension-compression asymmetry.

Phase energies and mixture energy

First, the averaged volume specific energy density $\overline{\psi}(\boldsymbol{X})$ of a material point $\boldsymbol{X}$ on the macro scale is given by

$$\overline{\psi}(\boldsymbol{X}) = \frac{1}{\mathrm{d}V_0} \int_{\mathcal{B}} \psi\left(\boldsymbol{\varepsilon}\left(\boldsymbol{X}\right)\right) \,\mathrm{d}V , \tag{3.2}$$

where $\psi\left(\boldsymbol{\varepsilon}\left(\boldsymbol{X}\right)\right)$ denotes the respective quantity on the micro scale and where $\mathrm{d}V_0$ is the total volume of the considered representative volume element (RVE) at the micro scale, in other words the (infinitesimal) initial volume. The micro scale decomposes into the aforementioned phases which in general occupy regimes $\mathcal{B}_{\mathrm{pow}}$, $\mathcal{B}_{\mathrm{mel}}$, and $\mathcal{B}_{\mathrm{sol}}$ with related volumes $V_{\mathcal{B}_{\mathrm{pow}}}$, $V_{\mathcal{B}_{\mathrm{mel}}}$, and $V_{\mathcal{B}_{\mathrm{sol}}}$. The strain field on the micro scale is now supposed to be piecewise constant, namely

$$\boldsymbol{\varepsilon}\left(\boldsymbol{X}\right) = \begin{cases} \boldsymbol{\varepsilon}_{\mathrm{pow}} & , \quad \text{if } \boldsymbol{X} \in \mathcal{B}_{\mathrm{pow}} \\ \boldsymbol{\varepsilon}_{\mathrm{mel}} & , \quad \text{if } \boldsymbol{X} \in \mathcal{B}_{\mathrm{mel}} \\ \boldsymbol{\varepsilon}_{\mathrm{sol}} & , \quad \text{if } \boldsymbol{X} \in \mathcal{B}_{\mathrm{sol}} \end{cases} . \tag{3.3}$$

Accordingly, the distribution of the energy density is generally given by

$$\psi\left(\boldsymbol{\varepsilon}\left(\boldsymbol{X}\right)\right) = \begin{cases} \psi_{\mathrm{pow}}\left(\boldsymbol{\varepsilon}_{\mathrm{pow}}\right) & , \quad \text{if } \boldsymbol{X} \in \mathcal{B}_{\mathrm{pow}} \\ \psi_{\mathrm{mel}}\left(\boldsymbol{\varepsilon}_{\mathrm{mel}}\right) & , \quad \text{if } \boldsymbol{X} \in \mathcal{B}_{\mathrm{mel}} \\ \psi_{\mathrm{sol}}\left(\boldsymbol{\varepsilon}_{\mathrm{sol}}\right) & , \quad \text{if } \boldsymbol{X} \in \mathcal{B}_{\mathrm{sol}} \end{cases} . \tag{3.4}$$

With this ansatz at hand, one can rewrite the energy density as

$$\overline{\psi}(\boldsymbol{X}) = \frac{1}{\mathrm{d}V_0} \left[\int\limits_{\mathcal{B}_{\mathrm{pow}}} \psi_{\mathrm{pow}} \, \mathrm{d}V + \int\limits_{\mathcal{B}_{\mathrm{mel}}} \psi_{\mathrm{mel}} \, \mathrm{d}V + \int\limits_{\mathcal{B}_{\mathrm{sol}}} \psi_{\mathrm{sol}} \, \mathrm{d}V \right] \tag{3.5}$$

$$= \frac{1}{\mathrm{d}V_0} \left[\int\limits_{\mathcal{B}_{\mathrm{pow}}} \mathrm{d}V \, \psi_{\mathrm{pow}} + \int\limits_{\mathcal{B}_{\mathrm{mel}}} \mathrm{d}V \, \psi_{\mathrm{mel}} + \int\limits_{\mathcal{B}_{\mathrm{sol}}} \mathrm{d}V \, \psi_{\mathrm{sol}} \right] . \tag{3.6}$$

By using the definitions

$$\xi_{\bullet} := \frac{1}{\mathrm{d}V_0} \int\limits_{\mathcal{B}_{\bullet}} \mathrm{d}V = \frac{V_{\mathcal{B}_{\bullet}}}{\mathrm{d}V_0} \tag{3.7}$$

for the respective volume fractions of each phase, one obtains

$$\overline{\psi}(\boldsymbol{X}) = \xi_{\mathrm{pow}} \, \psi_{\mathrm{pow}}\left(\boldsymbol{\varepsilon}_{\mathrm{pow}}\right) + \xi_{\mathrm{mel}} \, \psi_{\mathrm{mel}}\left(\boldsymbol{\varepsilon}_{\mathrm{mel}}\right) + \xi_{\mathrm{sol}} \, \psi_{\mathrm{sol}}\left(\boldsymbol{\varepsilon}_{\mathrm{sol}}\right) = \sum_{i=1}^{n_{\mathrm{ph}}} \xi_i \, \psi_i\left(\boldsymbol{\varepsilon}_i\right) , \tag{3.8}$$

where n_{ph} refers to the number of phases present. The volume fractions thus connect the transformed volume $V_{\mathcal{B}_{\bullet}}$ to the initial volume $\mathrm{d}V_0$.

The respective energy densities, which define the constitutive behaviour of each single phase as linear elastic, are chosen as

$$\psi_{\mathrm{pow}} := \frac{1}{2} \, \boldsymbol{\varepsilon}_{\mathrm{pow}} : \mathbf{E}_{\mathrm{pow}} : \boldsymbol{\varepsilon}_{\mathrm{pow}} - \widetilde{c}_{\mathrm{pow}} \, \theta \, \ln(\theta) , \tag{3.9}$$

$$\psi_{\mathrm{mel}} := \frac{1}{2} \, \boldsymbol{\varepsilon}_{\mathrm{mel}} : \mathbf{E}_{\mathrm{mel}} : \boldsymbol{\varepsilon}_{\mathrm{mel}} - \widetilde{c}_{\mathrm{mel}} \, \theta \, \ln(\theta) - L_{\mathrm{mel}} \, \frac{\theta - \theta_{\mathrm{mel}}^{\mathrm{ref}}}{\theta_{\mathrm{mel}}^{\mathrm{ref}}} , \tag{3.10}$$

$$\psi_{\mathrm{sol}} := \frac{1}{2} \left[\boldsymbol{\varepsilon}_{\mathrm{sol}} - \boldsymbol{\varepsilon}_{\mathrm{sol}}^{\mathrm{th}} \right] : \mathbf{E}_{\mathrm{sol}} : \left[\boldsymbol{\varepsilon}_{\mathrm{sol}} - \boldsymbol{\varepsilon}_{\mathrm{sol}}^{\mathrm{th}} \right] - \widetilde{c}_{\mathrm{sol}} \, \theta \, \ln(\theta) . \tag{3.11}$$

In these definitions, $\mathbf{E}_{\bullet}$ denotes the respective fourth-order elasticity tensor, $\widetilde{c}_{\bullet} = c \, \rho_{\bullet}$ is the weighted specific heat capacity, i.e. volume specific heat capacity, and θ the current temperature. The energy density for the molten pool includes the weighted latent heat $L_{\mathrm{mel}} = L \, \rho_{\mathrm{mel}}$ as well as a constant reference temperature $\theta_{\mathrm{mel}}^{\mathrm{ref}}$. The only inelastic strain contribution considered in the present framework is exemplified by thermal strains

$\varepsilon_{\mathrm{sol}}^{\mathrm{inel}} = \varepsilon_{\mathrm{sol}}^{\mathrm{th}}$ present in the re-solidified phase. The relation between the different occupy regimes and strains are visualised in Figure 3.1. More insight into the structure and interpretation of phase energy densities is given in Section 4.1.1, where also a more complex material model is incorporated.
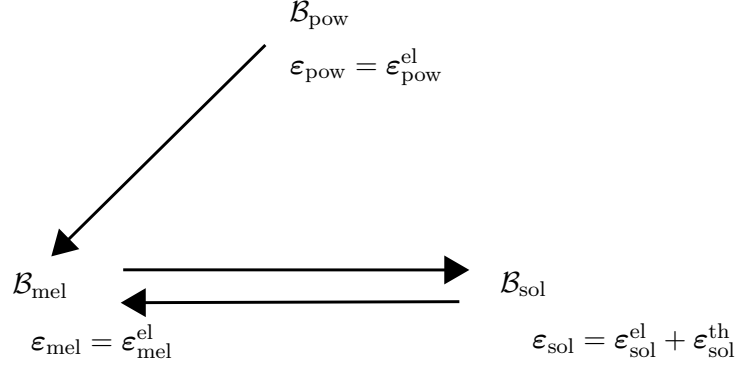

$$\mathcal{B}_{\mathrm{pow}}$$
$$\varepsilon_{\mathrm{pow}} = \varepsilon_{\mathrm{pow}}^{\mathrm{el}}$$

$$\mathcal{B}_{\mathrm{mel}} \qquad\qquad \mathcal{B}_{\mathrm{sol}}$$
$$\varepsilon_{\mathrm{mel}} = \varepsilon_{\mathrm{mel}}^{\mathrm{el}} \qquad\qquad \varepsilon_{\mathrm{sol}} = \varepsilon_{\mathrm{sol}}^{\mathrm{el}} + \varepsilon_{\mathrm{sol}}^{\mathrm{th}}$$

Figure 3.1: Visualisation of small strain kinematics for the modelling approach based on volume fractions.

Homogenisation approach

The relation (3.8) together with eqs. (3.9) to (3.11) defines the constitutive framework except for the determination of different total strains in each phase, namely $\varepsilon_{\mathrm{pow}}$, $\varepsilon_{\mathrm{mel}}$, and $\varepsilon_{\mathrm{sol}}$. To this end, specific homogenisation assumptions have to be made. In the present framework, it is assumed that the strain states of each phase will take on values which minimise the overall energy density at the micro scale subject to the restriction

$$\boldsymbol{r}^{\varepsilon} := \boldsymbol{\varepsilon} - \xi_{\mathrm{pow}}\,\boldsymbol{\varepsilon}_{\mathrm{pow}} - \xi_{\mathrm{mel}}\,\boldsymbol{\varepsilon}_{\mathrm{mel}} - \xi_{\mathrm{sol}}\,\boldsymbol{\varepsilon}_{\mathrm{sol}} = \boldsymbol{0}\ , \tag{3.12}$$

where $\boldsymbol{\varepsilon}$ is the (prescribed) strain state at the macro scale. Therefore, eq. (3.12) is also referred to as compatibility condition. The related minimisation problem

$$\{\boldsymbol{\varepsilon}_{\mathrm{pow}}, \boldsymbol{\varepsilon}_{\mathrm{mel}}, \boldsymbol{\varepsilon}_{\mathrm{sol}}\} = \arg\min\left\{\overline{\psi}\right\} \qquad \text{subject to } \boldsymbol{r}^{\varepsilon} = \boldsymbol{0} \tag{3.13}$$

leads to the calculation of the Reuss-bound, where constant or homogeneous stress states at the micro scale are assumed in each phase. For further insight, Remark 2 gives an overview of different types of homogenisation assumptions. The resulting effective energy obtained by this minimisation also coincides with the convex hull, which is identical to Sachs bound, as illustrated in Figure 3.2. In addition, the phase volume fractions are assumed to minimise the energy density as well which leads to the enhancements

$$\{\xi_{\mathrm{pow}}, \xi_{\mathrm{mel}}, \xi_{\mathrm{sol}}\} = \arg\min\left\{\overline{\psi}\right\} \tag{3.14}$$

subject to

$$\xi_{\text{pow}} + \xi_{\text{mel}} + \xi_{\text{sol}} = 1 \tag{3.15}$$

and

$$0 \leq \xi_{\bullet} \leq 1 \tag{3.16}$$

as constraints for every phase. In contrast to standard solid-solid phase transformation, see e.g. [11, 13, 78], an additional constraint is necessary regarding the evolution of the powder phase. Due to the physical behaviour of powder particles, the melting of powder is not reversible. Thus, the physically motivated restrictions eqs. (3.15) and (3.16) need to be extended by

$$\dot{\xi}_{\text{pow}} \leq 0 \,, \tag{3.17}$$

so that the powder – once molten – cannot re-transform to powder and thus its volume fraction can only decrease or remain constant. This behaviour is also illustrated in Figure 3.1. The equality constraint (3.15) can be incorporated by, e.g., the substitution

$$\xi_{\text{pow}} = 1 - \xi_{\text{mel}} - \xi_{\text{sol}} \,. \tag{3.18}$$

In total, the effective constitutive model is defined by the optimisation problem

$$\{\boldsymbol{\varepsilon}_{\text{pow}}, \boldsymbol{\varepsilon}_{\text{mel}}, \boldsymbol{\varepsilon}_{\text{sol}}, \xi_{\text{mel}}, \xi_{\text{sol}}\} = \arg\min\left\{\overline{\psi}\right\} \tag{3.19}$$

subject to the constraints

$$
\begin{aligned}
\boldsymbol{r}^{\boldsymbol{\varepsilon}} &:= \boldsymbol{\varepsilon} - [1 - \xi_{\text{mel}} - \xi_{\text{sol}}]\,\boldsymbol{\varepsilon}_{\text{pow}} - \xi_{\text{mel}}\,\boldsymbol{\varepsilon}_{\text{mel}} - \xi_{\text{sol}}\,\boldsymbol{\varepsilon}_{\text{sol}} = \boldsymbol{0} \,, & (3.20)\\
r_1 &:= -\xi_{\text{mel}} \leq 0 \,, & (3.21)\\
r_2 &:= -\xi_{\text{sol}} \leq 0 \,, & (3.22)\\
r_3 &:= \xi_{\text{mel}} + \xi_{\text{sol}} - 1 \leq 0 \,, & (3.23)\\
r_4 &:= \dot{\xi}_{\text{pow}} \leq 0 \,. & (3.24)
\end{aligned}
$$

For conceptual simplicity, we define

$$\mathbf{r} := \begin{bmatrix} r_1 & r_2 & r_3 & r_4 \end{bmatrix} \tag{3.25}$$

and the related quantity

$$\boldsymbol{\lambda} := \begin{bmatrix} \lambda_1 & \lambda_2 & \lambda_3 & \lambda_4 \end{bmatrix} \tag{3.26}$$

containing Lagrange multipliers. Together with the equivalent quantity $\boldsymbol{\lambda}^\varepsilon$ related to $\boldsymbol{r}^\varepsilon$ the Lagrangian

$$\mathcal{L} := \overline{\psi} + \boldsymbol{\lambda}^\varepsilon : \boldsymbol{r}^\varepsilon + \boldsymbol{\lambda} \cdot \mathbf{r} \tag{3.27}$$

may be defined. The related necessary conditions for the minimum then read

$$\partial_{\boldsymbol{\varepsilon}_{\text{pow}}}\mathcal{L} = \mathbf{0} \,, \tag{3.28}$$
$$\partial_{\boldsymbol{\varepsilon}_{\text{mel}}}\mathcal{L} = \mathbf{0} \,, \tag{3.29}$$
$$\partial_{\boldsymbol{\varepsilon}_{\text{sol}}}\mathcal{L} = \mathbf{0} \,, \tag{3.30}$$
$$\partial_{\boldsymbol{\lambda}^\varepsilon}\mathcal{L} = \mathbf{0} \,, \tag{3.31}$$
$$\partial_{\xi_{\text{mel}}}\mathcal{L} = 0 \,, \tag{3.32}$$
$$\partial_{\xi_{\text{sol}}}\mathcal{L} = 0 \,, \tag{3.33}$$

which are completed by the complementarity conditions

$$r_i \leq 0 \quad , \quad \lambda_i \geq 0 \quad , \quad r_i\,\lambda_i = 0 \quad , \quad i = 1,...,4 \,, \tag{3.34}$$

also referred to as Karush-Kuhn-Tucker conditions. Conditions (3.28) to (3.31) can be used to derive analytical solutions for optimal strain states in each phase, namely

$$\varepsilon^*_{\text{pow}} = \widetilde{\mathbf{E}}^{-1} : \left[\mathbf{E}_{\text{sol}} : \mathbf{E}_{\text{pow}} : \left[\varepsilon - \xi_{\text{sol}}\,\varepsilon^{\text{th}}_{\text{sol}}\right]\right] \,, \tag{3.35}$$

$$\varepsilon^*_{\text{mel}} = \widetilde{\mathbf{E}}^{-1} : \left[\mathbf{E}_{\text{mel}} : \mathbf{E}_{\text{sol}} : \left[\varepsilon - \xi_{\text{sol}}\,\varepsilon^{\text{th}}_{\text{sol}}\right]\right] \,, \tag{3.36}$$

$$\varepsilon^*_{\text{sol}} = \widetilde{\mathbf{E}}^{-1} : \left[\mathbf{E}_{\text{mel}} : \mathbf{E}_{\text{pow}} : \left[\varepsilon - \xi_{\text{sol}}\,\varepsilon^{\text{th}}_{\text{sol}}\right]\right] + \varepsilon^{\text{th}}_{\text{sol}} \,, \tag{3.37}$$

with

$$\widetilde{\mathbf{E}} := \xi_{\text{mel}}\,\mathbf{E}_{\text{sol}} : \mathbf{E}_{\text{pow}} + \xi_{\text{sol}}\,\mathbf{E}_{\text{pow}} : \mathbf{E}_{\text{mel}} + \left[1 - \xi_{\text{mel}} - \xi_{\text{sol}}\right]\mathbf{E}_{\text{mel}} : \mathbf{E}_{\text{sol}} \,, \tag{3.38}$$

as well as the Lagrange parameter

$$\boldsymbol{\lambda}^\varepsilon \equiv \boldsymbol{\sigma} = \widetilde{\mathbf{E}}^{-1} : \left[\mathbf{E}_{\text{mel}} : \mathbf{E}_{\text{sol}} : \mathbf{E}_{\text{pow}}\right] : \left[\varepsilon - \xi_{\text{sol}}\,\varepsilon^{\text{th}}_{\text{sol}}\right] \,, \tag{3.39}$$

which turns out to be identical to the resulting stresses $\boldsymbol{\sigma}$. As discussed later on, this has an effect on the algorithmic treatment as well. With these solutions at hand, the problem reduces to

$$\{\xi_{\text{mel}}, \xi_{\text{sol}}\} = \arg\min\{\mathcal{L}^* := \psi^* + \boldsymbol{\lambda} \cdot \mathbf{r}\} \,, \tag{3.40}$$

where

$$\psi^* := \overline{\psi}\big|_{\varepsilon_{\text{pow}} \leftarrow \varepsilon^*_{\text{pow}}, \varepsilon_{\text{mel}} \leftarrow \varepsilon^*_{\text{mel}}, \varepsilon_{\text{sol}} \leftarrow \varepsilon^*_{\text{sol}}} \,. \tag{3.41}$$

The remaining necessary conditions for the minimum of $\mathcal{L}^*$ now read

$$\partial_{\xi_{\mathrm{mel}}}\mathcal{L}^* \;=\; 0 \;, \tag{3.42}$$
$$\partial_{\xi_{\mathrm{sol}}}\mathcal{L}^* \;=\; 0 \;, \tag{3.43}$$

together with

$$r_i \leq 0 \quad , \quad \lambda_i \geq 0 \quad , \quad r_i\,\lambda_i = 0 \quad , \quad i = 1,...,4 \;. \tag{3.44}$$

Specifications of the derivatives present in eqs. (3.42) and (3.43) are, of course, possible but will not be explicitly mentioned here due to the fact that the resulting terms are rather lengthy, but are exemplarily determined for the framework of Chapter 4 in Appendix B. The algorithms and numerical methods used to solve this problem are elaborated in Section 3.2.1.

Remark 2. *As summarised in, e.g., [152], different types of homogenisation assumptions can be made. Especially Voigt's assumption, also referred to as Taylor's bound and the Reuss' assumption, also called Sachs bound, are well known. Thereby, Voigt [171] defines the upper bound with a homogeneous strain state and Reuss [147] determines the lower bound of a problem, where a uniform stress field is assumed. These assumptions are illustrated in Figure 3.2 for two arbitrary energy densities. Visually speaking, Voigt-type homogenisation is exemplified by parallel springs, whereas Reuss-type homogenisation is represented by serial springs.*
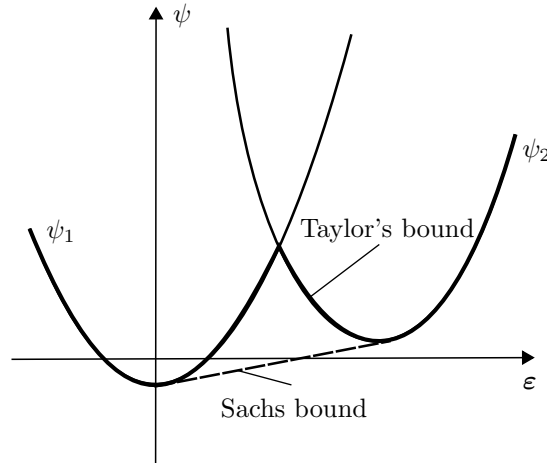

Figure 3.2: Visualisation of homogenisation assumptions based on two arbitrary energy wells.

3.1.2 Heat effects

As heat transfer mechanism, only heat expansion and conduction are considered and shall be briefly discussed in what follows. Radiation and convection are neglected at

this point, but are incorporated in Section 4.1.5, while the minor effect is discussed in Appendix B.3.

With respect to the heat expansion model and related thermal strains $\boldsymbol{\varepsilon}^{\mathrm{th}}_{\mathrm{sol}}$, a standard linear relation of the form

$$\boldsymbol{\varepsilon}^{\mathrm{th}}_{\mathrm{sol}} := \alpha_{\mathrm{sol}} \left[\theta - \theta^{\mathrm{ini}} \right] \boldsymbol{I} \, , \tag{3.45}$$

is used, where α_{sol} represents the (isotropic) heat expansion coefficient of the solid phase and where θ^{ini} denotes the initial or reference temperature at which the material is defined as undeformed in the absence of mechanical loads. The heat expansion of the powder and molten phase is negligible compared to the expansion of the solid phase. As introduced in eqs. (2.63) and (2.64), the balance equations depend on the effective volume specific heat capacity which can be specified for the model at hand by

$$\widetilde{c}_{\mathrm{eff}} := - \, \theta \, \partial^2_{\theta\theta} \overline{\psi} = \left[1 - \xi_{\mathrm{mel}} - \xi_{\mathrm{sol}} \right] \widetilde{c}_{\mathrm{pow}} + \xi_{\mathrm{mel}} \, \widetilde{c}_{\mathrm{mel}} + \xi_{\mathrm{sol}} \, \widetilde{c}_{\mathrm{sol}} \, . \tag{3.46}$$

In addition, a standard isotropic Fourier-type form is used for the heat conduction model, viz. in eq. (2.84) with $\widetilde{k}_{\mathrm{eff}}$ as averaged heat conduction of the phase mixture. This quantity is chosen as

$$\widetilde{k}_{\mathrm{eff}} := \left[1 - \xi_{\mathrm{mel}} - \xi_{\mathrm{sol}} \right] k_{\mathrm{pow}} + \xi_{\mathrm{mel}} \, k_{\mathrm{mel}} + \xi_{\mathrm{sol}} \, k_{\mathrm{sol}} \, , \tag{3.47}$$

where $k_{\bullet}$ represents the respective heat conductivity for each phase. Eq. (3.47) represents a Voigt-type homogenisation assumption, cf. Remark 2, whereby a Reuss-type format – in analogy to the elastic problem – could have been chosen as well, see for example eq. (4.64).

3.2 Implementation and algorithmic treatment

The framework at hand has been realised with help of the commercial FE-based software Abaqus. Thus, the focus in this section will also lie on specific aspects regarding related algorithmic issues. The implementation does not only comprise the incorporation of the local material routine in Section 3.2.1, but also for example the construction of different powder layers in Section 3.2.2 and the modelling of the laser heat source in Section 3.2.3. Finally, the specific implementation of the user-defined routines is summarised in Section 3.2.4.

3.2.1 Numerical solution strategies

The following aspects refer to the local part of the overall model, i.e. the material routine. Prior to the algorithmic formulation, restriction (3.24) needs to be specified in terms of a time discretisation, cf. eq. (2.77). To this end, the rate of ξ_{pow}, i.e.

$$\dot{\xi}_{\mathrm{pow}} = -\dot{\xi}_{\mathrm{mel}} - \dot{\xi}_{\mathrm{sol}} \tag{3.48}$$

is discretised according to

$$\dot{\xi}_{\mathrm{pow}} \approx -\frac{{}^{n+1}\xi_{\mathrm{mel}} - {}^{n}\xi_{\mathrm{mel}}}{\Delta t} - \frac{{}^{n+1}\xi_{\mathrm{sol}} - {}^{n}\xi_{\mathrm{sol}}}{\Delta t} \ . \tag{3.49}$$

This time discretisation also affects the complete set of equations or inequalities (3.42) to (3.44) in the sense that the quantities ξ_{mel} and ξ_{sol} are now substituted by their time-discrete counterparts ${}^{n+1}\xi_{\mathrm{mel}}$ and ${}^{n+1}\xi_{\mathrm{sol}}$.

With these specifications at hand, the problem to be solved reads

$$\left\{ {}^{n+1}\xi_{\mathrm{mel}}, {}^{n+1}\xi_{\mathrm{sol}} \right\} = \arg\min\left\{ \mathcal{L}^* \right\} \tag{3.50}$$

which leads to

$$\partial_{{}^{n+1}\xi_{\mathrm{mel}}}\mathcal{L}^* = \partial_{{}^{n+1}\xi_{\mathrm{mel}}}\psi^* - \lambda_1 + \lambda_3 - \frac{1}{\Delta t}\lambda_4 \ = \ 0 \ , \tag{3.51}$$

$$\partial_{{}^{n+1}\xi_{\mathrm{sol}}}\mathcal{L}^* = \partial_{{}^{n+1}\xi_{\mathrm{sol}}}\psi^* - \lambda_2 + \lambda_3 - \frac{1}{\Delta t}\lambda_4 \ = \ 0 \ , \tag{3.52}$$

subject to eq. (3.44). The latter conditions are implemented into the algorithmic framework via the Fischer-Burmeister nonlinear complementarity problem functions

$$\sqrt{r_i^2 + \lambda_i^2} + r_i - \lambda_i = 0 \quad , \quad i = 1, \ldots, 4 \ . \tag{3.53}$$

This approach was established in [51] and was first applied to problems in continuum mechanics in [154]. These functions have proven to work well in the context of material modelling, for instance for shape memory alloys, cf. [12, 15, 85], and piezoceramics, cf. [48]. With this approach at hand, the residual

$$\mathbf{r} := \begin{bmatrix} \partial_{{}^{n+1}\xi_{\mathrm{mel}}}\mathcal{L}^* \\ \partial_{{}^{n+1}\xi_{\mathrm{sol}}}\mathcal{L}^* \\ \sqrt{r_1^2 + \lambda_1^2} + r_1 - \lambda_1 \\ \vdots \\ \sqrt{r_4^2 + \lambda_4^2} + r_4 - \lambda_4 \end{bmatrix} = \begin{bmatrix} 0 \\ 0 \\ 0 \\ \vdots \\ 0 \end{bmatrix} \tag{3.54}$$

is defined. The vector of unknown variables corresponds to

$$\mathbf{f} := [\xi_{\text{mel}} \quad \xi_{\text{sol}} \quad \lambda_1 \quad \lambda_2 \quad \lambda_3 \quad \lambda_4]^{\text{t}} \ . \tag{3.55}$$

Using the Fischer-Burmeister nonlinear complementarity function has the advantage that a standard solver is applicable even though inequality conditions have to be fulfilled. Without going into further detail, this system of equations can be solved by using standard Newton-type approaches, see Remark 3, where specific smoothing techniques have to be applied with respect to the Fischer-Burmeister functions, see, e.g., [79].

Remark 3. *For the system of equation* (3.54)*, the vector of unknowns* (3.55) *needs to be updated. Therefore, the local Jacobian matrix*

$$\mathbf{J} = \frac{\partial \mathbf{r}}{\partial \mathbf{f}} \tag{3.56}$$

is introduced. The updated value for iteration i is then determined via

$$\mathbf{f}^{i+1} = \mathbf{f}^i - \mathbf{J}^{-1} \cdot \mathbf{r} \ . \tag{3.57}$$

The new residuum is then calculated with the updated variables. This procedure is repeated until the tolerance of the residual vector is sufficiently small, e.g. $\|\mathbf{r}\| < \epsilon = 10^{-8}$.

3.2.2 Layer construction model

The layer construction model is based on the so-called element birth and death strategy for the construction of multiple layers proposed in [110, 150]. This technique has also been employed in, e.g., [36, 53]. Accordingly, the number of applied layers has to be known in advance and all of them are a priori considered within the initial FE mesh. At the beginning of the simulation, all redundant layers are deactivated. This is called the element death. This means for example that they do not contribute to the stiffness (matrix) of the body under consideration. The addition of a new powder layer coincides with the activation of a complete set of elements, referred to as element birth. Hence, these elements also affect the stiffness (matrix). The conceptual steps of the layer construction model are visualised in Figure 3.3.

Within the software Abaqus, this can be accomplished with the help of the command MODEL CHANGE, where sets of elements can be defined which are then removed from or added to the complete FE model, respectively. As suggested in [1], the "newborn" elements are activated as strain-free within an additional short time step. This procedure is used to closely approximate the actual processes of the LPBF. It is noteworthy that the activation of new elements additionally affects the algorithms within the subroutine DFLUX since the reference height for the heat flux distribution changes, see Section 3.2.4.
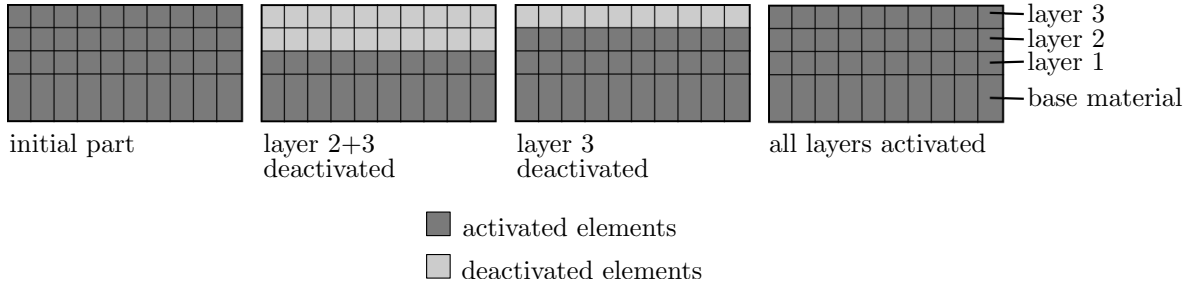
Figure 3.3: Illustration of the layer construction during the simulation based on element 'birth death' technique. Reprinted from [14].

3.2.3 Laser beam model

Various models exist for the application of the heat flux r_ext generated by the laser beam in order to model the impact of the laser beam as accurately as possible. Specific models for the laser beam and its impact zone are provided in [36, 37, 53, 72, 89, 150] in terms of surface heat flux models. Extension in terms of different volume heat flux models are given in [42, 64, 68, 116, 148, 164, 175]. For this model, a moving and non-uniformly distributed volumetric heat source is prescribed, where the laser beam profile is modelled as a Gaussian distribution. As proposed by Goldak in [60] for welding, the Gaussian heat source is adjusted for LPBF and is defined via

$$r_\text{ext}(x_1', x_2', x_3') = \frac{4\sqrt{2}\,P}{r_0^3\,\pi\,\sqrt{\pi}}\,\exp\left(-\frac{2\left[x_1'^{\,2} + x_2'^{\,2} + x_3'^{\,2}\right]}{r_0^2}\right)\,, \tag{3.58}$$

where P defines the laser power and where r_0 is the characteristic (focus) radius of the laser beam. For eq. (3.58), approximately 85 % of the total energy lies within the maximum radius spot, thus the concentration coefficient equals two, see [146]. The heat flux in the x_1-x_2-plane is illustrated in Figure 3.4. The coordinates x_i' introduced in eq. (3.58) are defined with respect to a moving orthonormal frame: In view of the numerical examples, where the laser will move in positive x_1 direction (cf. Figure 3.6), the following relations are applied

$$x_1' = x_1 - [t - t_0]\,\overline{v}^\text{lsr}\,, \quad x_2' = x_2\,, \tag{3.59}$$

with $\overline{v}^\text{lsr}$ as prescribed velocity of the laser. To incorporate such a non-uniform distributed heat flux, the subroutine DFLUX is necessary, see Section 3.2.4 for further details, where the precise relation for x_3' will be discussed and is defined in eq. (3.60).

3.2.4 User-defined routines

In order to define user specified mechanical and thermal material behaviour in Abaqus, the subroutines UMAT and UMATHT are provided. These are used to incorporate the afore-
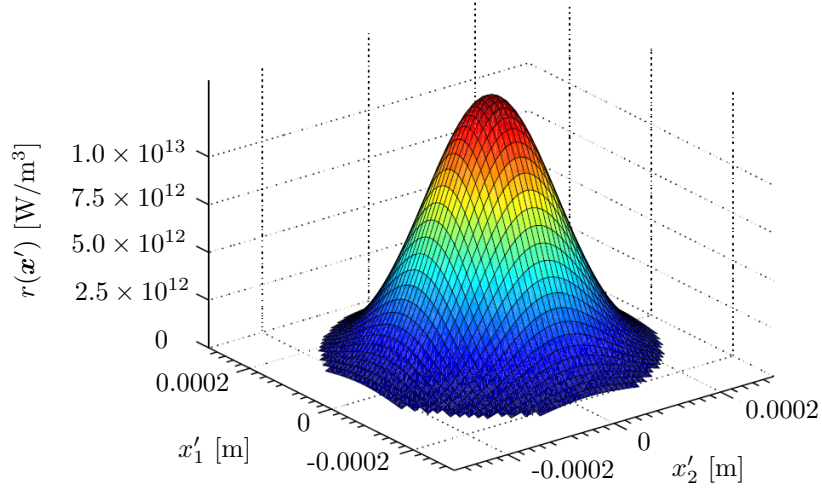
Figure 3.4: Distribution $r_{\text{ext}}(x_1', x_2', x_3')$ of heat flux for Goldak heat source as defined in eq. (3.58) with focus radius $r_0 = 0.0002$ m and laser power $P = 110$ W.

mentioned constitutive model and to adapt the calculation of the heat transfer equations for the thermodynamically fully coupled simulations. In addition, the subroutine `DFLUX` is used to define the non-uniform and moving heat flux of the laser beam model.

DFLUX

The subroutine `DFLUX` is used in order to define the direction, power and the velocity of the non-uniform heat source. This subroutine is called up at the beginning of each iteration. While being activated, it determines the magnitude of the heat flux `FLUX(1)` as defined in the source code. The volumetric heat source is modelled in Abaqus as a body heat flux through all subjacent layers. By doing so, it is guaranteed that the heat flow can spread unhindered through the whole body. The laser parameters and initial positions are defined within the subroutine, whereas the position (x_1, x_2, x_3) by the variable `COORDS` and the current time t, respectively `TIME(1)`, are passed in for usage by Abaqus. Due to the layer activation as defined in Section 3.2.2, the reference height x_3' within the subroutine `DFLUX` changes. Thus, the coding has to adapt the height of the part in accordance to the respective step, as the origin of the volumetric heat flux x_3' depends on the height h_{lyr} of a single layer and on the current number of applied (activated) layers n_{lyr}. To be specific, the relation

$$x_3' = x_3 + n_{\text{lyr}} \, h_{\text{lyr}} \tag{3.60}$$

holds. With this information at hand, it is now possible to determine the current heat flux $r_{\text{ext}}(x_1', x_2', x_3')$ as defined in eqs. (3.58) to (3.60). Different models for the laser beam are able to be incorporated into the algorithm in a straightforward manner.

UMAT

The constitutive model of the phase transformation is implemented into the subroutine `UMAT`. The general properties have been introduced in Section 2.6.1. The states of the underlying global variables, namely strains $\boldsymbol{\varepsilon}$ and temperature θ, as well as the values of the respective internal state dependent variables `SDV` – here, the quantities ξ_{mel} and ξ_{sol} – are passed to the subroutine and can be accessed for the calculation of the current `SDV` via eq. (3.54) and, as a consequence, for the determination of current stresses via eq. (3.39).

In addition to the `SDV` and the stresses themselves, their total derivative with respect to strains – frequently denoted as algorithmic tangent operator $\mathbf{E}^{\mathrm{algo}}$ – has to be provided as output parameter within the `UMAT` subroutine. Here, we use an approximation of this quantity, viz.

$$\mathbf{E}^{\mathrm{algo}} \approx \frac{\partial \boldsymbol{\sigma}}{\partial \boldsymbol{\varepsilon}} = \widetilde{\mathbf{E}}^{-1} : [\mathbf{E}_{\mathrm{mel}} : \mathbf{E}_{\mathrm{sol}} : \mathbf{E}_{\mathrm{pow}}] \ , \tag{3.61}$$

for conceptual simplicity. The simplification does not affect the results themselves, but only the convergence rate of the outer Newton-Raphson scheme (see Abaqus user subroutine reference guide [1]). This is suitable since the time steps of the global calculations need to be rather small in view of the thermomechanical coupling. Therefore, the convergence of the outer Newton-Raphson scheme is sufficiently high during the simulation. Due to the fact that the assumptions $\partial \boldsymbol{\sigma} / \partial \theta \approx \mathbf{0}$ and that the underlying mechanical dissipation $\mathcal{D}_{\mathrm{mech}}$ is set to zero, no further derivatives are required in this case, i.e. the thermomechanical coupling `RPL` equals zero.

UMATHT

Abaqus generally provides a standard treatment of the heat transfer problem, see eq. (2.81), without the need of further subroutines. However, the effective heat conduction $\widetilde{k}_{\mathrm{eff}}$, see eq. (3.47), and the effective heat capacity $\widetilde{c}_{\mathrm{eff}}$, see eq. (3.46), depend on `SDV` ξ_{mel} and ξ_{sol}, necessitating the use of the subroutine `UMATHT`. As the internal variables are available within the subroutine, averaging the thermal quantities is then possible. In the context of the present framework, the density of the whole model ρ is set equal to ρ_{pow}, i.e. the mass density of the powder. In order to account for the different densities of the remaining phases which cannot be changed within the subroutine `UMATHT`, the averaged volume specific heat capacity defined in eq. (3.46) needs to be redefined to a effective specific heat capacity as follows

$$c_{\mathrm{eff}} := [1 - \xi_{\mathrm{mel}} - \xi_{\mathrm{sol}}] \, \frac{\widetilde{c}_{\mathrm{pow}}}{\rho_{\mathrm{pow}}} + \xi_{\mathrm{mel}} \, \frac{\widetilde{c}_{\mathrm{mel}}}{\rho_{\mathrm{pow}}} + \xi_{\mathrm{sol}} \, \frac{\widetilde{c}_{\mathrm{sol}}}{\rho_{\mathrm{pow}}} \ , \tag{3.62}$$

as proposed in, e.g., [189]. Another approach is presented in [75], where the overall density equals one, while the volume specific heat capacity is defined in the subroutine

`UMATHT`. This contribution also discusses the positive influence of using the correct density on the simulation results. Overall, this concept assures a thermal material behaviour corresponding to the previously defined constitutive framework.

3.3 Numerical examples

In this section, representative numerical examples generated with the previously defined material model are discussed. For the numerical examples, the material properties of a Ti-based alloy, namely Ti_6Al_4V, are used. This material is one of the materials frequently used in research for additive manufacturing. The respective thermomechanical material properties are summarised in Table 3.1, see also Remark 4. The material parameters are adapted from [121] and [148], where the reference temperatures 1073.15 K (for the solid and powder phase) and 2273.15 K (for the molten phase) have been used. Furthermore, the required values of the initial and the reference temperature are chosen as $\theta^{\text{ini}} = 273.15\,\text{K}$ and $\theta^{\text{ref}}_{\text{mel}} = 1873.15\,\text{K}$. Material parameters are assumed constant for each phase and that their respective effective counterparts follow from the phase mixture in contrast to material models which directly incorporate temperature-dependent effective material properties.

Table 3.1: Overview of the used material parameters of Ti_6Al_4V adapted from [121] and [148].

Material parameters		Powder	Melt	Solid
Extraction temperature	θ [K]	1073.15	2273.15	1073.15
Mechanical parameters				
Density	ρ [kg/m^3]	4309	3700	4309
Poisson's ration	ν [$-$]	0.33	0.45	0.33
Young's modulus	E [GPa]	7.6	2.9	63.4
Thermal parameters				
Expansion coefficient	α [1/K]	-	-	11e-06
Heat capacity	c [J/(kgK)]	714	831	714
Conductivity	k [W/(mK)]	9.5	33.4	17.8
Latent heat	L [kJ/kg]	-	286	-

Remark 4. *Within Abaqus, no explicit units are prescribed. Thus, consistent SI-units can be freely chosen. However, the present choice affects the convergence rate of the constitutive framework at material point level due to the numerical solution strategies defined in Section 3.2.1. The usage of the Fischer-Burmeister necessitates similar magnitudes for the field variables. Instead of the standard SI-units [m,kg,s,K], the material parameters are incorporated based on [mm,kg,ms,K]. This results in stress having the unit [GPa] and in energy being based on [kN mm].*

3.3.1 Proof of concept

Prior to the implementation into the overall complex FE model, the constitutive framework derived in Section 3.1.1 shall be discussed. Therefore, a single material point is considered and its behaviour due to cyclic thermal loading is investigated. At the beginning, the temperature is linearly increased in a time interval $\Delta t = 1\,\mathrm{ms}$ from $\theta = 873\,\mathrm{K}$ to $\theta = 2873\,\mathrm{K}$, then decreased back to $\theta = 873\,\mathrm{K}$ in the same time span, see Figure 3.5a. Therefore, a homogeneous stress state with zero Neumann boundary conditions is assumed. The strain components are iteratively calculated in such a manner that the related stress components vanish. The material shall initially purely consist of powder, thus $\xi_{\mathrm{pow}} = 1$. The resulting strain components ε_{11}, ε_{22} and ε_{33} evolve homogeneously, as shown in Figure 3.5b, and the occurring phase volume fractions are shown in Figure 3.5c. The volume fractions of the respective phases change when reaching the melting point of $\theta^{\mathrm{melt}} = 1873.15$ K as defined in the material model. Due to the fact that the solid phase is the only one exhibiting inelastic/thermal strains, the evolution of the solid phase induces residual strains.
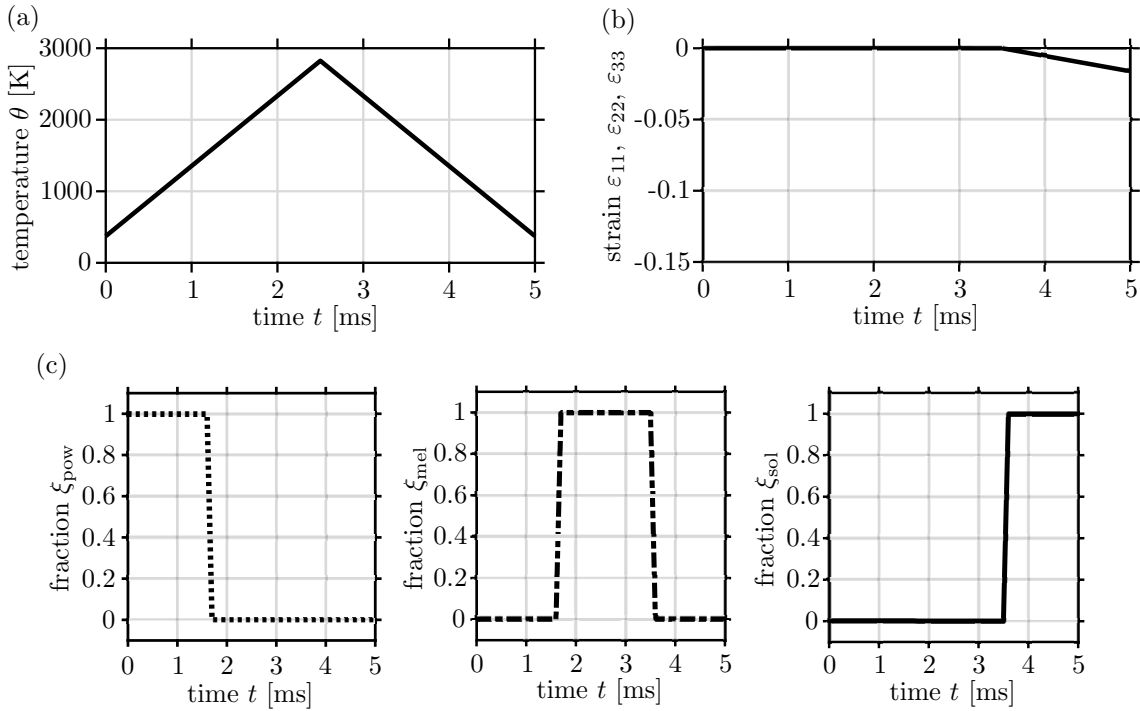

Figure 3.5: Simulation results of the temperature-driven calculations (3.5a) in terms of the strain evolution (3.5b) and the evolution of volume fractions $\xi_{\bullet}$ (3.5c) for homogeneous stress state with zero Neumann boundary conditions.

3.3.2 Simulation of a basic process

This section deals with the modelling and simulation of a basic LPBF process. The main geometrical model for the build chamber is illustrated in Figure 3.6a, where the final configuration is conceptually shown. The height of a single layer is given by $h_{\mathrm{lyr}} = 50\ \mu$m. The height of the base material has to be chosen in such a way that it will not melt completely, in particular during the application of the first layer. Therefore, its height is set to 200 μm. For symmetry reasons, only one half of the chamber is considered so that the centre of the moving laser beam will be applied exactly along one edge of the modelled part, i.e. at positions with $x_2 = 0$, see Figure 3.6b.
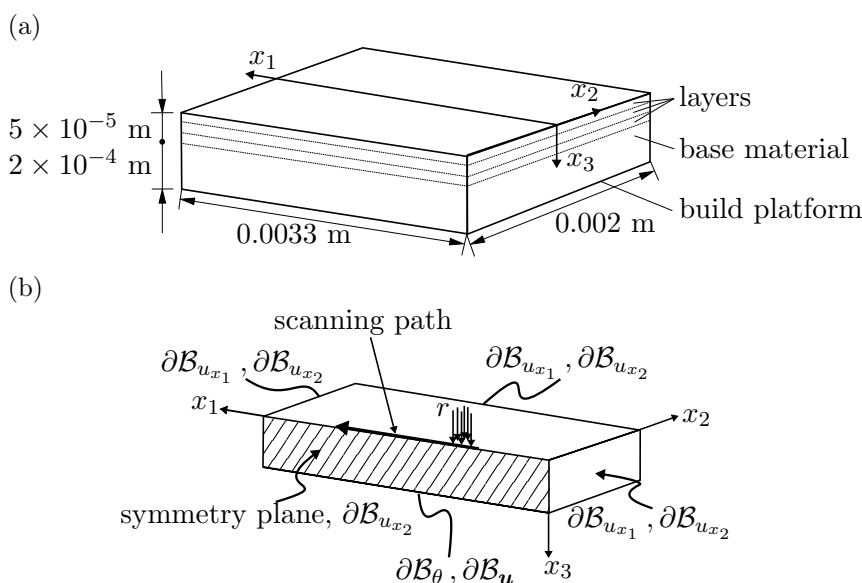

Figure 3.6: Geometry (3.6a) and boundary conditions (3.6b) of the used LPBF example to demonstrate a basic process simulation. (3.6b) reprinted from [14].

The applied boundary conditions are indicated in Figure 3.6b: At the bottom face of the part, homogeneous Dirichlet conditions are applied with respect to displacements, and the temperature is prescribed to 373.15 K throughout the calculations. The displacement boundary conditions on the side edges of the part only allow displacements in x_3-direction where the upper edge is subjected to homogeneous Neumann boundary conditions with respect to the displacement field. Except for the bottom face, only homogeneous Neumann boundary conditions are applied with respect to the temperature field.

The laser beam power is set to $P = 100$ W with $r_0 = 100\ \mu$m, and the velocity of the laser beam is $\overline{v}^{\mathrm{lsr}} = 1$ m/s, cf. eq. (3.59). The time step used by Abaqus was constantly set to $\Delta t = 2 \times 10^{-5}$ s, which means – in view of the prescribed scanning velocity of the laser beam –, that 50 time steps will be used for the scanning period of 10^{-3} s for each layer. The spatial discretisation in terms of finite elements is carried out via element

type `C3D8T` which exhibit 8 displacement nodes in addition to a temperature degree. Due to high temperature gradients and laser velocity, a dense mesh is used close to the laser beam path. Within this region, a characteristic element length of $l_{\mathrm{char}} \approx 15\,\mu\mathrm{m}$ is applied, compare also Figure 4.9.

At first, the part – which initially only consists of the powder material and where the first layer of material is already activated – is homogeneously pre-heated via the prescribed temperature boundary conditions at the bottom face. After the necessary period of time for the pre-heating, the laser beam is applied along the scanning path in the aforementioned way. Before activating the second layer of new powder, a cooling period of 0.01 s is applied. Then, after the activation of the new layer, the laser beam is applied once more. This procedure is repeated one more time so that three layers of powder have been added in total.

The calculation results of the above process shall be discussed in what follows: Figure 3.7 shows the temperature evolution as the laser beam moves along the scanning path (Figures 3.7a to 3.7d) and during the subsequent cooling period (Figures 3.7e and 3.7f) prior to the application of the new powder layer. The "tail" occurring behind the laser beam position is due to the fact that the conductivity of the forming re-solidified material (cf. Figure 3.8) is significantly higher than that of the surrounding powder. The legend of Figure 3.7 is not linear in the sense that all temperature values above 1923 K are displayed in the same red colour. The maximum temperatures reach values of approximately 3400 K.

Figure 3.8 shows the spatial distribution of the powder phase, the molten pool, and the re-solidified material at different time steps. It can be observed how the distribution of the molten pool and the re-solidified material follows the path of the applied laser beam. Due to the fact that, according to the chosen material parameters, the phase transformations are mainly temperature-driven, the evolution of the solid phase is very similar to the temperature distribution displayed in Figure 3.7. The dimensions of the molten pool during the laser impact can be estimated to be 375 μm in length ($\approx$ 25 elements), 120 μm in width ($\approx$ 2 times 4 elements), and 60 μm in depth ($\approx$ 4 elements). In the same way, the final dimension of the solid material can be estimated to be 1005 μm in length and – still – 120 μm in width as well as 60 μm in depth. The apparent intermediate values of the phase fractions (green colour) mainly stem from the internal interpolations used within Abaqus for illustration purposes.

The dimensions of the final manufactured part are illustrated in Figure 3.9a, where the phase fractions of the solidified material are shown after the consecutive application of three powder layers and a subsequent cooling period. It becomes obvious that the final part is not of regular shape as presumably desired. This is a direct consequence of the model for the heat source supplied by the laser beam and, in addition, of the underlying process parameters. This result shows that the presented framework is capable of providing a deeper understanding and insight into the interaction between system parameters and the quality/properties of the final product.
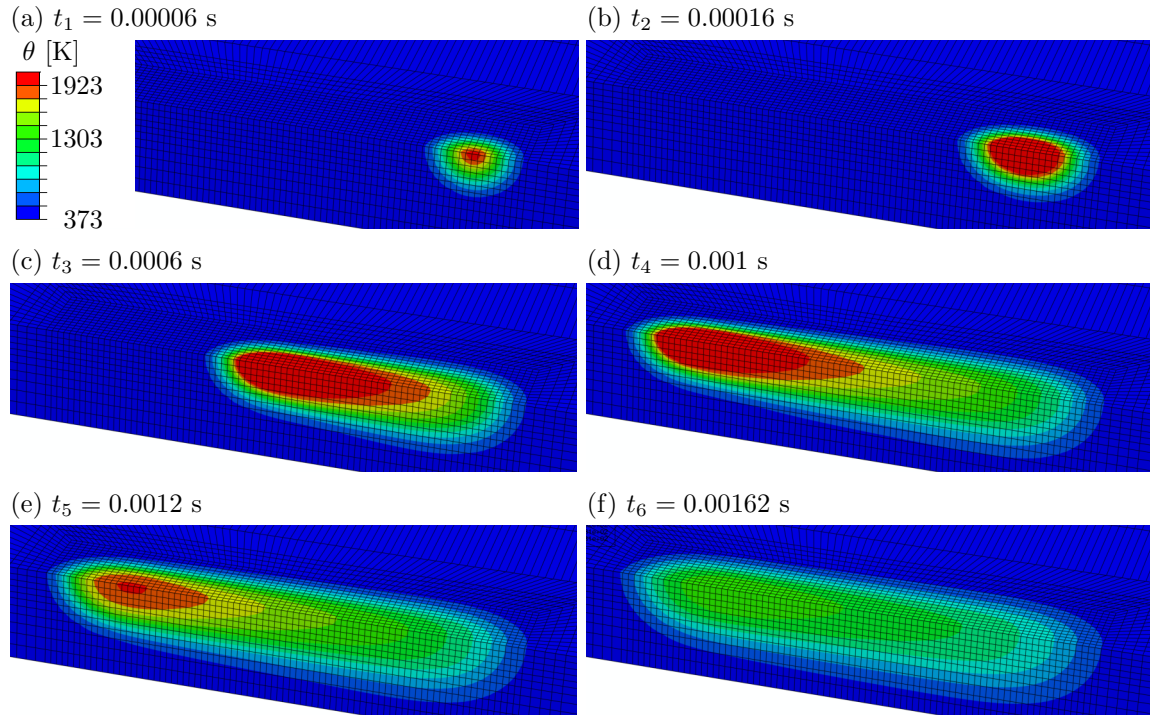
(a) $t_1 = 0.00006$ s

θ [K]

1923

1303

373

(b) $t_2 = 0.00016$ s

(c) $t_3 = 0.0006$ s

(d) $t_4 = 0.001$ s

(e) $t_5 = 0.0012$ s

(f) $t_6 = 0.00162$ s

Figure 3.7: Temperature evolution $\theta(\boldsymbol{x})$ during the impact of the moving laser beam (3.7a - 3.7d) and during the subsequent cooling period (3.7e - 3.7f). Temperatures above 1923 K are displayed in the same red colour, where the maximum values are approximately 3400 K. Reprinted from [14].

Finally, Figure 3.10 depicts the distribution of stresses after finishing the manufacturing process, here in terms of the normal stresses in each direction, i.e. $\sigma_{11}, \sigma_{22}, \sigma_{33}$, and of the von Mises equivalent stresses σ_{vM}. It becomes evident that the manufacturing process induces high eigenstresses which then may have significant effects on the component's quality and usability. For instance, possible fatigue, damage, and related delamination processes may be affected by these eigenstresses. In this context, high eigenstresses occur at the interface between the different material layers applied which are chosen three elements thick in the calculations. According to the simulation results, these interfaces are subject to high tensile stress states in x_1-direction and high compression states in x_2-direction as well as to moderate compressive normal stresses in x_3-direction. This could hint at the fact that the final workpiece may be prone to Mode II-type failure (shearing) and Mode III-type failure (tearing) and, conversely, exhibits improved resistance with respect to Mode I-type failure (opening) referring to potential cracks aligned with the x_1-direction.
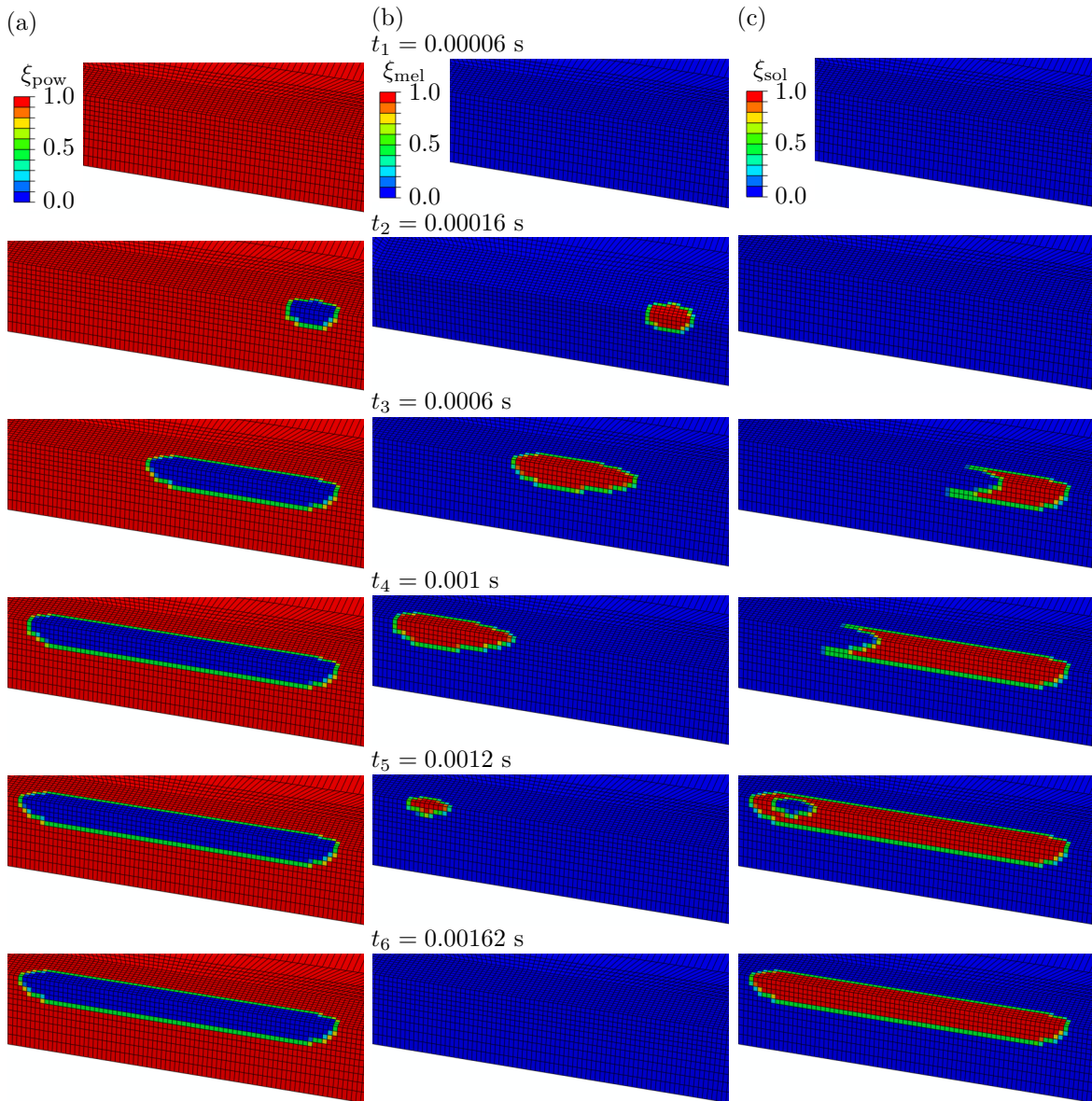
Figure 3.8: Evolution of the volume fractions of the powder (3.8a), the molten pool (3.8b) and the re-solidified material (3.8c) at different time steps. The laser impact is active up to $t_4 = 0.001$ s so that the distributions shown for t_5 and t_6 reflect the evolution of the underlying phases during the cooling sequence. Reprinted from [14].
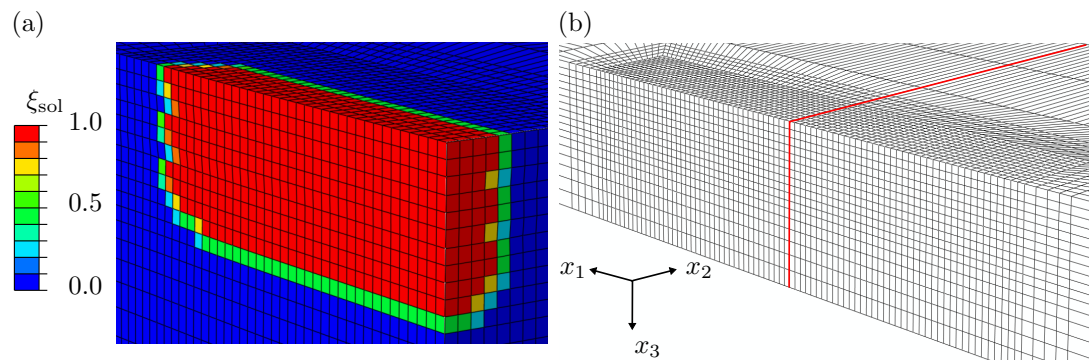
Figure 3.9: Distribution of the volume fraction of the re-solidified material after the application of three consecutive layers (3.9a), the cross-section normal to x_1 is obtained by a virtual cut indicated by red lines in (3.9b). Reprinted from [14].
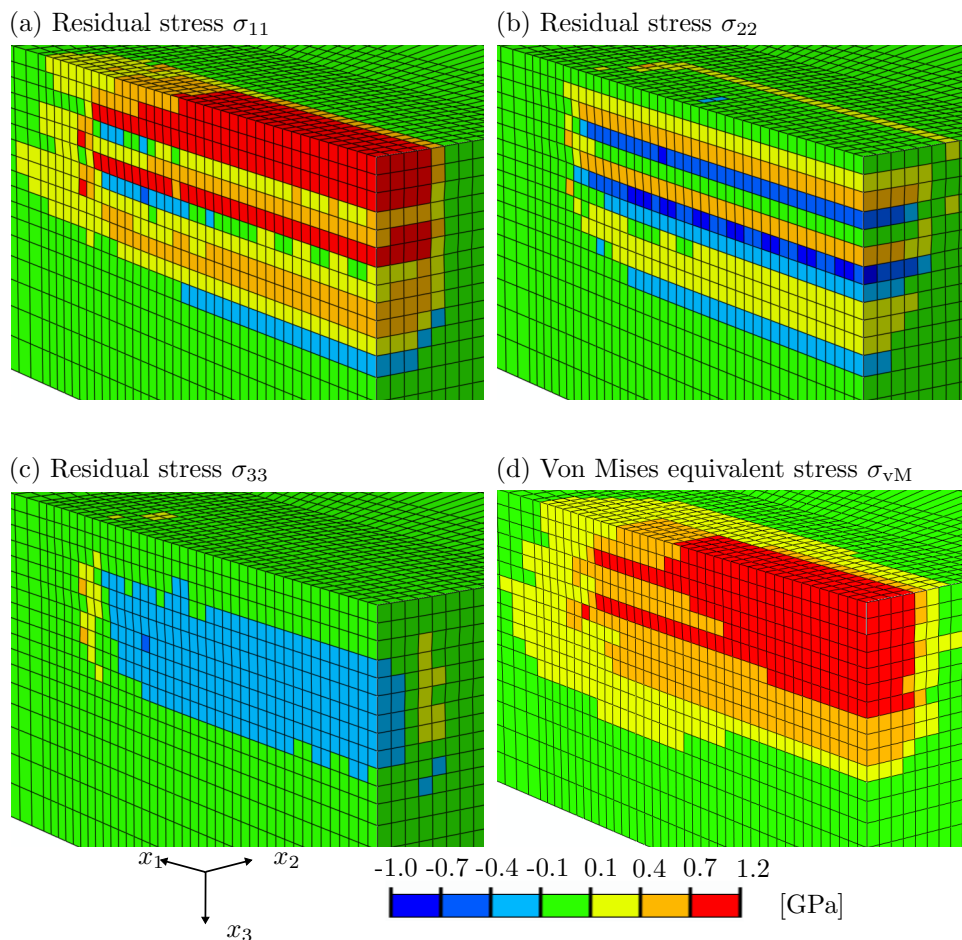

Figure 3.10: Distribution of different residual stresses after cooling the final workpiece to the initial temperature along the cross-section as defined in Figure (3.9b). Reprinted from [14].

4 A phase transformation framework based on mass fractions

The reproduction of the constitutive and structural response of LPBF processes is challenging due to the complex material behaviour and its interactions. This motivates the aims of this chapter: To establish a more sophisticated material model that accounts for the behaviour of the different phases occurring during LPBF but that still allows the use of (basic) process simulations, where the focus lies on the advancements of the model presented in the previous Chapter 3. First of all, a thermodynamically fully coupled framework is incorporated without any simplifications. In addition, an advanced material model is used for the molten and re-solidified phase, where several inelastic strain contributions are taken into account. More precisely speaking, viscous strains and transformation strains are considered in the molten phase as well as thermal strains, plastic strains, and transformation strains in the solid phase. The transformation strains are introduced as material constants and capture the significant change of the mass densities during the phase changes. The thermodynamically fully coupled framework is then implemented into the software Abaqus. The numerical examples emphasise the capabilities of the framework to predict, e.g., essential process-induced quantities such as eigenstresses, also referred to as residual stresses, occurring in the final part. Furthermore, a post-processing of averaged inelastic strains is presented yielding a micromechanics-based motivation for inherent strains, which will be employed for the multiscale simulations in subsequent Chapter 5.

This chapter is set up as follows: In Section 4.1, the phase energy densities and the inelastic strains are specified to introduce the constitutive material model which is based on mass fractions. The formulation of the material model as well as the FE model consider full thermomechanical coupling. A deeper insight is given into the local algorithm and Abaqus implementation of the framework at hand in Section 4.2. Calculations at the material point level designed to yield a proof of concept as well as representative three-dimensional boundary value problems are studied in Section 4.3.

4.1 Constitutive framework

The thermomechanical material model based on phase energy densities is introduced in this section. The overall material behaviour is determined according to a phase transformation model. Furthermore, the specifications of the thermal problem are introduced. Altogether, both models are thermodynamically fully coupled.

4.1.1 Phase energy densities

As already indicated in Section 3.1.1, each state of the material is represented by an energy density. Altogether, the material response of the complete model is determined with the help of a homogenisation approach. The material model is based on the averaged Helmholtz free energy density $\overline{\psi}$, where additively decomposed energy densities

$$\psi_i := \psi_i^{\mathrm{mech}} + \psi_i^{\mathrm{pl}} + \psi_i^{\mathrm{cal}} \tag{4.1}$$

are chosen for each possible phase denoted by the index i. The first part describes the mechanical energy density ψ_i^{mech}, ψ_i^{pl} denotes a possible plastic contribution of the energy density, while the last part ψ_i^{cal} is a purely caloric contribution due to the temperature dependence of the material model. The mechanical part of the energy density is defined as

$$\psi_i^{\mathrm{mech}} := \frac{1}{2} \left[\boldsymbol{\varepsilon}_i - \boldsymbol{\varepsilon}_i^{\mathrm{inel}} \right] : \mathbf{E}_i : \left[\boldsymbol{\varepsilon}_i - \boldsymbol{\varepsilon}_i^{\mathrm{inel}} \right] \ , \tag{4.2}$$

whereas the caloric part is a function of temperature and specific material parameters, i.e. heat capacity and latent heat, and which is to be defined later. The ansatz for the caloric heat contribution is adapted from [52]. Here, the latent heat refers to the remaining temperature change after an adiabatic transformation cycle and is not directly related to the change of entropy. Furthermore, $\boldsymbol{\varepsilon}_i$ denote the total strains of each phase, $\boldsymbol{\varepsilon}_i^{\mathrm{inel}}$ describe the inelastic strains and $\mathbf{E}_i$ represents a fourth-order elasticity tensor of the respective phase. Each energy density represents a potential well which is shifted due to ψ_i^{cal} and $\boldsymbol{\varepsilon}_i^{\mathrm{inel}}$. The influence of the caloric part and the inelastic strains on the potential well is visualised in Figure 4.1.

At this point, three distinct phases representing the different states of the material, namely powder, molten, and re-solidified, are explicitly taken into account. All of these phases are modelled as a solid continuum, which may be arguable in particular for the molten phase with respect to the (viscous) solid approach and for the powder phase regarding the continuum ansatz. Motivations for these simplifications are, however, provided in the subsequent paragraphs.
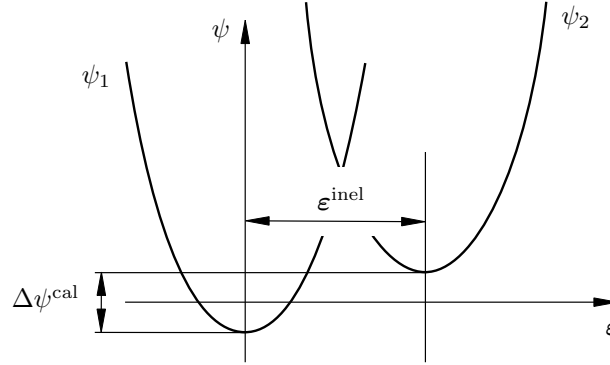
Figure 4.1: Influence of the different contributions on the phase energy densities. Reprinted from [131] under the terms of the Creative Commons Attribution License (CC BY).

Powder phase

Powder particles are assumed to move freely due to their high degree of porosity between the powder grains. Therefore, the material behaves solely elastic. It has to be kept in mind that only compression strains are admissible within the powder particles. In the framework at hand, the powder is modelled as a continuum with a significantly higher compliance than the solid material. Overall, the powder shall not undergo states of high stress or strain levels. In the initial state, only the powder phase is present. In addition, due to the high porosity of the powder phase, any existing thermal strains are neglected for this state of the material. Thus, the powder is considered as the parent phase so that no inelastic strains are incorporated for this phase, i.e. $\varepsilon_{\text{pow}}^{\text{inel}} = \mathbf{0}$. The energy density of the powder is approximated by

$$\psi_{\text{pow}} := \frac{1}{2}\,\varepsilon_{\text{pow}} : \mathbf{E}_{\text{pow}} : \varepsilon_{\text{pow}} - \widetilde{c}_{\text{pow}}\,\theta\ln(\theta) + L_{\text{pow}}\,\frac{\theta - \theta_{\text{pow}}^{\text{ref}}}{\theta_{\text{pow}}^{\text{ref}}}\;, \tag{4.3}$$

where $\widetilde{c}_{\text{pow}} = \rho_{\text{pow}}\,c$ is the weighted heat capacity of the powder, and where $L_{\text{pow}} = \rho_{\text{pow}}\,L$ describes the weighted latent heat of the powder at a constant reference temperature $\theta_{\text{pow}}^{\text{ref}}$. The weighted volumetric values are calculated by the mass density of the powder ρ_{pow} and the specific value of the heat capacity c and latent heat L, respectively.

Molten phase

The molten phase shall also be approximated as a solid-type phase. This behaviour is assumed to be appropriate, as the molten pool is only present for a brief time span. Fluid effects such as the Marangoni flow are therefore neglected. However, to include a fluid-like behaviour of the molten pool in the material model, a visco-elastic strain contribution $\varepsilon_{\text{mel}}^{\text{ve}}$ is included, which shall be used to enable full stress relaxation within the molten phase. Furthermore, the mass density of the three phases varies considerably. A transformation strain $\varepsilon_{\text{mel}}^{\text{trans}}$ is incorporated to take into account the volume change,

respectively shrinkage, of the material due to the different mass densities of the powder and the molten phases. Both inelastic strains will be further defined in what follows. Overall, an additive split of the inelastic strains is used for the molten phase, i.e.

$$\boldsymbol{\varepsilon}_{\mathrm{mel}}^{\mathrm{inel}} = \boldsymbol{\varepsilon}_{\mathrm{mel}}^{\mathrm{trans}} + \boldsymbol{\varepsilon}_{\mathrm{mel}}^{\mathrm{ve}} \ . \tag{4.4}$$

As the molten phase is the high temperature phase, the influence of the latent heat is only integrated into the powder and re-solidified phases. With this information at hand, the specific energy density of the molten phase is defined as

$$\psi_{\mathrm{mel}} := \frac{1}{2} \left[\boldsymbol{\varepsilon}_{\mathrm{mel}} - \boldsymbol{\varepsilon}_{\mathrm{mel}}^{\mathrm{inel}} \right] : \mathbf{E}_{\mathrm{mel}} : \left[\boldsymbol{\varepsilon}_{\mathrm{mel}} - \boldsymbol{\varepsilon}_{\mathrm{mel}}^{\mathrm{inel}} \right] - \widetilde{c}_{\mathrm{mel}} \, \theta \ln(\theta) \ , \tag{4.5}$$

with the heat capacity defined as $\widetilde{c}_{\mathrm{mel}} = \rho_{\mathrm{mel}} \, c$ and the mass density of the molten phase denoted as ρ_{mel}.

Re-solidified phase

An additive decomposition of the inelastic strains into three parts is chosen according to

$$\boldsymbol{\varepsilon}_{\mathrm{sol}}^{\mathrm{inel}} = \boldsymbol{\varepsilon}_{\mathrm{sol}}^{\mathrm{th}} + \boldsymbol{\varepsilon}_{\mathrm{sol}}^{\mathrm{pl}} + \boldsymbol{\varepsilon}_{\mathrm{sol}}^{\mathrm{trans}} \tag{4.6}$$

for the re-solidified phase. The transformation strains $\boldsymbol{\varepsilon}_{\mathrm{sol}}^{\mathrm{trans}}$ take into account the volume changes of the material during the phase transition from the molten phase to the re-solidified phase due to the changing mass densities. In contrast to the previously introduced phases, two further inelastic strain contributions are considered. Plastic deformation can arise due to high eigenstrains after the phase transformation and due to high temperature gradients present. A plastic strain tensor $\boldsymbol{\varepsilon}_{\mathrm{sol}}^{\mathrm{pl}}$ is used to capture this behaviour whose evolution will be further defined in Section 4.1.4. Furthermore, thermal strains $\boldsymbol{\varepsilon}_{\mathrm{sol}}^{\mathrm{th}}$ are considered in the re-solidified phase to take into account inelastic strains stemming from the high temperature changes during the process. These strains are already defined in Section 3.1.2. Special attention has to be paid to the used reference temperature, as only the cooling (and thus shrinkage) of the material is taken into account for the laser scan model and as no previous heating (and thus expansion) is considered. This also motivates the inclusion of heat expansion within the inelastic strains in eq. (5.1). Finally, the energy density of the re-solidified phase is defined by analogy with the previously introduced energies as

$$\begin{aligned} \psi_{\mathrm{sol}} := &\frac{1}{2} \left[\boldsymbol{\varepsilon}_{\mathrm{sol}} - \boldsymbol{\varepsilon}_{\mathrm{sol}}^{\mathrm{inel}} \right] : \mathbf{E}_{\mathrm{sol}} : \left[\boldsymbol{\varepsilon}_{\mathrm{sol}} - \boldsymbol{\varepsilon}_{\mathrm{sol}}^{\mathrm{inel}} \right] + \frac{H_{\mathrm{sol}}}{2} \, [k_{\mathrm{sol}}^{\mathrm{hard}}]^2 \\ &- \widetilde{c}_{\mathrm{sol}} \, \theta \ln(\theta) + L_{\mathrm{sol}} \, \frac{\theta - \theta_{\mathrm{sol}}^{\mathrm{ref}}}{\theta_{\mathrm{sol}}^{\mathrm{ref}}} \ . \end{aligned} \tag{4.7}$$

The heat capacity and the latent heat are defined in an analogous manner as $\widetilde{c}_{\text{sol}} = \rho_{\text{sol}}\, c$ and $L_{\text{sol}} = \rho_{\text{sol}}\, L$. The mass density of the solid phase is denoted by ρ_{sol}. In addition, H_{sol} defines the hardening modulus of the solid phase, whereas $k_{\text{sol}}^{\text{hard}}$ indicates the accumulated equivalent plastic strain related to isotropic hardening. This is assumed to be appropriate as non-cyclic mechanical loading is present. In the energy density, no further direct thermomechanical coupling, except the thermal strains, is included in eq. (4.7).

Altogether, an overview of all inelastic strain contributions, which contribute to the total strains, are given in Figure 4.2. In comparison to Chapter 3, where the material model is visualised in Figure 3.1, the previous approach is considerably simpler.
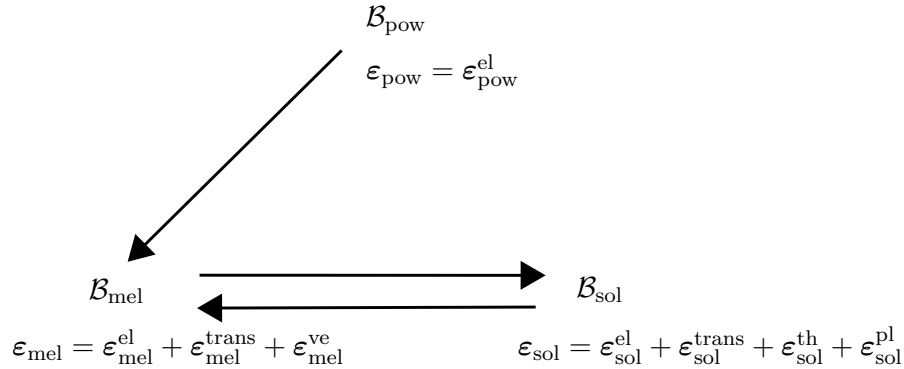
$$\mathcal{B}_{\text{pow}}$$
$$\varepsilon_{\text{pow}} = \varepsilon_{\text{pow}}^{\text{el}}$$

$$\mathcal{B}_{\text{mel}}$$
$$\varepsilon_{\text{mel}} = \varepsilon_{\text{mel}}^{\text{el}} + \varepsilon_{\text{mel}}^{\text{trans}} + \varepsilon_{\text{mel}}^{\text{ve}}$$

$$\mathcal{B}_{\text{sol}}$$
$$\varepsilon_{\text{sol}} = \varepsilon_{\text{sol}}^{\text{el}} + \varepsilon_{\text{sol}}^{\text{trans}} + \varepsilon_{\text{sol}}^{\text{th}} + \varepsilon_{\text{sol}}^{\text{pl}}$$

Figure 4.2: Visualisation of small strain kinematics for the modelling approach based on mass fractions.

4.1.2 Specification of transformation strains

The transformation strains $\varepsilon_i^{\text{trans}}$ of the molten and re-solidified phases shall be introduced next, as they are solely dependent on the transformation process and on material parameters previously introduced. These strains shall capture the volume changes of the material during phase transitions due to the different mass densities, as illustrated in Figure 4.3. A transformation strain can straightforwardly be calculated. In fact, the validity of the small strain theory needs to be carefully scrutinised in view of physically plausible transformation strains. The incorporation of volume shrinkage has been introduced and discussed in, e.g., [37].

Initially, the material solely consists of the mass density ρ_0 and mass contribution $\mathrm{d}m_0$, thus it is possible to derive the transformed volume as

$$\mathrm{d}V_0 = \frac{\mathrm{d}m_0}{\rho_0} \ . \tag{4.8}$$

Changes in volume are included by phase transitions due to different mass densities $\rho_\bullet$. Hypothetically assuming that this infinitesimal volume element of the parent phase,

i.e. powder, fully transforms into one of the other phases, i.e. molten and re-solidified material, the volume of the new phase is given by

$$\mathrm{d}V_\bullet = \frac{\mathrm{d}m_0}{\rho_\bullet} = [1 + \mathrm{tr}(\boldsymbol{\varepsilon}_\bullet^{\mathrm{trans}})]\,\mathrm{d}V_0 \;. \tag{4.9}$$

Conservation of mass shall be fulfilled in every material point. In consequence, the mass of an infinitesimal material volume remains constant, i.e. $\mathrm{d}m_0 = \mathrm{const}$, (compare *conservation of mass* in Section 2.3). Using eqs. (4.8) and (4.9) together with the physically sound assumption of $\boldsymbol{\varepsilon}_\bullet^{\mathrm{trans}}$ being purely volumetric, these transformation strains are specifically given by

$$\boldsymbol{\varepsilon}_\bullet^{\mathrm{trans}} = \frac{1}{3}\left[\frac{\rho_0}{\rho_\bullet} - 1\right]\boldsymbol{I} \;, \tag{4.10}$$

where $\boldsymbol{I}$ corresponds to the second order identity tensor. For this case, the initial mass density corresponds to the density of the powder phase, i.e. $\rho_0 = \rho_{\mathrm{pow}}$. This results in the transformation strains

$$\boldsymbol{\varepsilon}_{\mathrm{mel}}^{\mathrm{trans}} = \frac{1}{3}\left[\frac{\rho_{\mathrm{pow}}}{\rho_{\mathrm{mel}}} - 1\right]\boldsymbol{I} \tag{4.11}$$

for the molten phase and

$$\boldsymbol{\varepsilon}_{\mathrm{sol}}^{\mathrm{trans}} = \frac{1}{3}\left[\frac{\rho_{\mathrm{pow}}}{\rho_{\mathrm{sol}}} - 1\right]\boldsymbol{I} \tag{4.12}$$
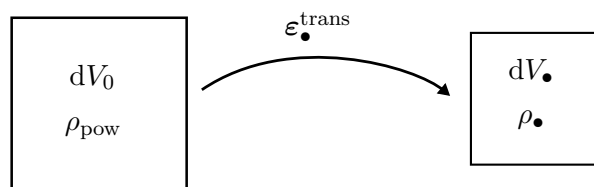
for the re-solidified phase.

Figure 4.3: Visualisation of transformation strains.

4.1.3 Homogenisation via convexification

In Chapter 3, a material model for solid-solid phase transformations has been introduced as a first approach for LPBF processes. It uses volume fractions as state variable, cf. eq. (3.7), and as conserved quantity, compare eq. (3.15). This is motivated for shape memory alloys by the fact that the mass densities of, e.g., austenite and martensite can be considered identical. However, in the context of AM, the mass densities of the

powder, molten phase and re-solidified material differ significantly. Thus, conservation of mass does not coincide with conservation of volume. The volume consequently cannot be used as a conserved quantity, and the homogenisation algorithm needs to be reformulated accordingly by using mass specific quantities. This makes it possible to consistently take into account the different mass densities of the powder, molten and re-solidified phase.

For the application at hand, the algorithm introduced in Section 3.1.1 needs to be enhanced and re-formulated with respect to the mass fractions

$$\zeta_i = \frac{\mathrm{d}m_i}{\mathrm{d}m_0} \, , \tag{4.13}$$

which correlate the current mass $\mathrm{d}m_i$ of the respective phase to the initial mass $\mathrm{d}m_0$ of an infinitesimal volume element $\mathrm{d}V_0$. These mass fractions can be related to the volume fractions introduced in eq. (3.7) via

$$\zeta_i = \frac{\rho_i \, \mathrm{d}V_i}{\mathrm{d}m_0} = \frac{\rho_i \, \xi_i \, \mathrm{d}V_0}{\mathrm{d}m_0} \quad \Leftrightarrow \quad \xi_i = \frac{\zeta_i \, \mathrm{d}m_0}{\rho_i \, \mathrm{d}V_0} \, , \tag{4.14}$$

where $\mathrm{d}V_i$ denotes the corresponding volume of the respective phase (instead of $V_{\mathcal{B}_i}$). For the sake of consistency, the algorithm shall now be developed based on mass fractions and on the averaged mass specific energy $\overline{\Psi}$. While working with mass fractions ζ_i, some adaptions to the aforementioned approach have to be made.

The averaged mass specific energy density $\overline{\Psi}$ is, analogously to eq. (3.2), calculated via a linear mixture rule of the mass specific phases Ψ_i, thus

$$\overline{\Psi} = \frac{1}{\mathrm{d}m_0} \int_{\mathcal{B}} \Psi \, \mathrm{d}m = \frac{1}{\mathrm{d}m_0} \int_{\mathcal{B}_i} \sum_{i=1}^{n_{\mathrm{ph}}} \Psi_i \, \mathrm{d}m_i = \sum_{i=1}^{n_{\mathrm{ph}}} \zeta_i \, \Psi_i = \frac{\mathrm{d}V_0}{\mathrm{d}m_0} \sum_{i=1}^{n_{\mathrm{ph}}} \xi_i \, \psi_i \, , \tag{4.15}$$

where the relation between the volume and mass specific energy density $\psi_i = \rho_i \Psi_i$ still holds and where eq. (4.14) is already employed. The use of mass fractions in particular affects the compatibility condition

$$\boldsymbol{r}^{\boldsymbol{\varepsilon}} = \boldsymbol{\varepsilon} - \sum_{i=1}^{n_{\mathrm{ph}}} \zeta_i \, \boldsymbol{\varepsilon}_i = \mathbf{0} \, , \tag{4.16}$$

which defines the admissible strain state $\boldsymbol{\varepsilon}_i$, as well as

$$0 \leq \zeta_i \leq 1 \quad \text{and} \quad \sum_{i=1}^{n_{\mathrm{ph}}} \zeta_i = 1 \tag{4.17}$$

as constraints for the admissible region of the mass fractions. By doing so, the mass is the conserved quantity. One can see the similarities between eqs. (4.15) and (3.8). This is advantageous for the implementation, as will be explained in Section 4.2.1.

For the LPBF process, three phases – representing the powder, molten pool and re-solidified material – are used within the framework such that $n_{\mathrm{ph}} = 3$. Each of these different material states are represented by an energy density $\psi_\bullet$, as introduced in Section 4.1.1, where $\bullet = \{\mathrm{pow}, \mathrm{mel}, \mathrm{sol}\}$, corresponding to the powder, molten and re-solidified material, respectively. Therefore, the explicit averaged energy density or, in other words, the effective energy density employed for the modelling framework at hand is given by

$$\overline{\Psi} = \frac{\mathrm{d}V_0}{\mathrm{d}m_0} \left[\xi_{\mathrm{pow}} \, \psi_{\mathrm{pow}} \left(\boldsymbol{\varepsilon}_{\mathrm{pow}}, \theta, \mathcal{V} \right) + \xi_{\mathrm{mel}} \, \psi_{\mathrm{mel}} \left(\boldsymbol{\varepsilon}_{\mathrm{mel}}, \theta, \mathcal{V} \right) + \xi_{\mathrm{sol}} \, \psi_{\mathrm{sol}} \left(\boldsymbol{\varepsilon}_{\mathrm{sol}}, \theta, \mathcal{V} \right) \right] \,, \tag{4.18}$$

where the aforementioned state variable $\mathcal{V}$ includes the mass fractions but is not restricted to these, so that $\mathcal{V} = \{\zeta_{\mathrm{pow}}, \zeta_{\mathrm{mel}}, \zeta_{\mathrm{pow}}, \mathcal{I}\}$. The newly introduced quantity $\mathcal{I}$ symbolises further, at this point still unspecified, internal variables. This averaged energy density has to be minimised subject to the constraints regarding the domain of feasible mass fractions $\zeta_\bullet \in \mathcal{A}$ with

$$\mathcal{A} = \{0 \le \zeta_\bullet \le 1 \,, \quad \zeta_{\mathrm{pow}} + \zeta_{\mathrm{mel}} + \zeta_{\mathrm{sol}} = 1\} \tag{4.19}$$

and the domain of the admissible strain distributions $\boldsymbol{\varepsilon}_\bullet \in \mathcal{E}$ with

$$\mathcal{E} = \{\zeta_{\mathrm{pow}} \, \boldsymbol{\varepsilon}_{\mathrm{pow}} + \zeta_{\mathrm{mel}} \, \boldsymbol{\varepsilon}_{\mathrm{mel}} + \zeta_{\mathrm{sol}} \, \boldsymbol{\varepsilon}_{\mathrm{sol}} = \boldsymbol{\varepsilon}\} \,. \tag{4.20}$$

Eq. (4.20) states that the differently weighted strain contributions always equal the total strain. This constrained minimisation problem results in the so-called convexification of $\overline{\Psi}$, i.e.

$$\mathrm{C}\overline{\Psi} = \inf_{\zeta_\bullet \in \mathcal{A}} \inf_{\boldsymbol{\varepsilon}_\bullet \in \mathcal{E}} \overline{\Psi} \,, \tag{4.21}$$

where $\mathrm{C}\overline{\Psi}$ is also known as the convex hull of the energy densities $\Psi_\bullet$, which is identical to the Reuss bound. This is qualitatively visualised in Figure 4.4. In addition, the evolution of the powder phase as introduced in eq. (3.17) is reformulated to

$$\dot{\zeta}_{\mathrm{pow}} \le 0 \,, \tag{4.22}$$

which has to be fulfilled in addition to the constraints in eq. (4.19), as the melting of powder is non-reversible.

At this point, only the determination of the optimal strains shall be discussed. The evolution equations of the mass fractions will be considered in detail in Section 4.1.4.
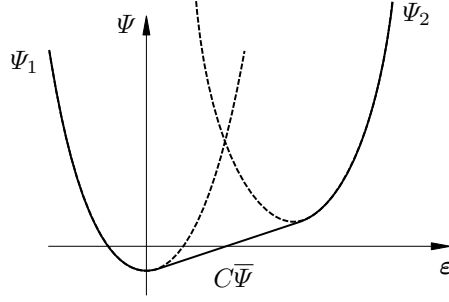
Figure 4.4: Qualitative illustration of the convex hull $C\overline{\Psi}$ of two energy potential wells Ψ_1 and Ψ_2. Adapted from [131] under the terms of the Creative Commons Attribution License (CC BY).

The strain states in each phase shall minimise the averaged specific energy density while considering eq. (4.20). The aforementioned minimisation problem subject to the respective equality constraint can be solved with help of a Lagrangian

$$\mathcal{L} = \overline{\Psi} + \boldsymbol{\lambda}^{\varepsilon} \colon \boldsymbol{r}^{\varepsilon} \ , \tag{4.23}$$

where $\boldsymbol{\lambda}^{\varepsilon}$ contains the Lagrange multipliers, see also Remark 5. It is assumed that the different strain states $\boldsymbol{\varepsilon}_i$ minimise eq. (4.23). Consequently, the necessary conditions for the present minimisation are specified as

$$\partial_{\boldsymbol{\varepsilon}_{\text{pow}}}\mathcal{L} = \mathbf{0} \ , \quad \partial_{\boldsymbol{\varepsilon}_{\text{mel}}}\mathcal{L} = \mathbf{0} \ , \quad \partial_{\boldsymbol{\varepsilon}_{\text{sol}}}\mathcal{L} = \mathbf{0} \ , \quad \partial_{\boldsymbol{\lambda}^{\varepsilon}}\mathcal{L} = \mathbf{0} \ . \tag{4.24}$$

With this information at hand, it is possible to derive an analytical expression for the Lagrange multipliers and the optimal strain distributions of each phase. By using eq. (4.24) and by solving these equations with respect to the Lagrange multipliers one gains

$$\boldsymbol{\lambda}^{\varepsilon} = \frac{1}{\rho_{\bullet}} \frac{\partial \psi_{\bullet}}{\partial \boldsymbol{\varepsilon}_{\bullet}} \ . \tag{4.25}$$

After taking into account eqs. (4.20) and (4.25), the following analytical results are obtained for the respective optimal strains of each phase

$$\boldsymbol{\varepsilon}_{\text{pow}}^{\star} = \widetilde{\mathbf{E}}^{-1} \colon \left[\rho_{\text{pow}} \, \mathbf{E}_{\text{sol}} \colon \mathbf{E}_{\text{mel}} \colon \boldsymbol{\varepsilon}^{\text{el}}\right] \ , \tag{4.26}$$

$$\boldsymbol{\varepsilon}_{\text{mel}}^{\star} = \widetilde{\mathbf{E}}^{-1} \colon \left[\rho_{\text{mel}} \, \mathbf{E}_{\text{sol}} \colon \mathbf{E}_{\text{pow}} \colon \boldsymbol{\varepsilon}^{\text{el}}\right] + \boldsymbol{\varepsilon}_{\text{mel}}^{\text{inel}} \ , \tag{4.27}$$

$$\boldsymbol{\varepsilon}_{\text{sol}}^{\star} = \widetilde{\mathbf{E}}^{-1} \colon \left[\rho_{\text{sol}} \, \mathbf{E}_{\text{mel}} \colon \mathbf{E}_{\text{pow}} \colon \boldsymbol{\varepsilon}^{\text{el}}\right] + \boldsymbol{\varepsilon}_{\text{sol}}^{\text{inel}} \ , \tag{4.28}$$

with the abbreviation

$$\widetilde{\mathbf{E}} = \zeta_{\text{pow}} \, \rho_{\text{pow}} \, \mathbf{E}_{\text{sol}} \colon \mathbf{E}_{\text{mel}} + \zeta_{\text{mel}} \, \rho_{\text{mel}} \, \mathbf{E}_{\text{sol}} \colon \mathbf{E}_{\text{pow}} + \zeta_{\text{sol}} \, \rho_{\text{sol}} \, \mathbf{E}_{\text{pow}} \colon \mathbf{E}_{\text{mel}} \ , \tag{4.29}$$

$$\boldsymbol{\varepsilon}^{\text{el}} = \boldsymbol{\varepsilon} - \zeta_{\text{mel}} \, \boldsymbol{\varepsilon}_{\text{mel}}^{\text{inel}} - \zeta_{\text{sol}} \, \boldsymbol{\varepsilon}_{\text{sol}}^{\text{inel}} \ . \tag{4.30}$$

In line with the hyperelastic format, the overall stress can then be calculated corresponding to eq. (2.56) via

$$\boldsymbol{\sigma} = \frac{\partial \overline{\psi}}{\partial \boldsymbol{\varepsilon}} = \sum_{i=1}^{n_{\mathrm{ph}}} \xi_i \frac{\partial \psi_i}{\partial \boldsymbol{\varepsilon}} = \frac{\mathrm{d}m_0}{\mathrm{d}V_0} \widetilde{\mathbf{E}}^{-1} : [\mathbf{E}_{\mathrm{pow}} : \mathbf{E}_{\mathrm{mel}} : \mathbf{E}_{\mathrm{sol}}] : \boldsymbol{\varepsilon}^{\mathrm{el}} \tag{4.31}$$

in a compact form. For the specific case at hand, no assumptions regarding the mechanical dissipation $\mathcal{D}_{\mathrm{mech}}$ are initially made. Thus, this quantity is included within the mechanical working r_{mech}, as defined in eq. (2.62), in the present model to ensure a fully coupled thermomechanically framework. The specific contributions of the dissipation based on eq. (2.59) are determined in Appendix B.1.

In summary, the homogenisation approach for mass fractions is similar to the one introduced for volume fractions in Section 3.1.1. However, the consolidated notation for eqs. (4.26) to (4.28) and (4.31) can only be derived in case $\mathbf{E}_\bullet$ is an isotropic tensor, as the Lagrange multiplier in eq. (4.25) differs for all phases. This assumption seems to be appropriate for the material at hand, as defined in Section 4.3. With this, the structure of the overall stress in eq. (4.31) and the optimal strains of each phase in eqs. (4.26) to (4.28) are comparable to eqs. (3.39) and (3.35) to (3.37), respectively.

Remark 5. *As already described in Section 3.1.1, compare eq. (3.27) and following, the inequality constraints regarding the feasible domain $\mathcal{A}$ can also be realised by using the Lagrangian. Furthermore, it is also possible to incorporate a dissipation function $\mathcal{C}$, which is introduced in Section 4.1.4, within a Lagrangian, such that*

$$\mathcal{L} = \overline{\Psi} + \boldsymbol{\lambda}^{\varepsilon} : \boldsymbol{r}^{\varepsilon} + \boldsymbol{\lambda} \cdot \mathbf{r} + \int_t \mathcal{C} \, \mathrm{d}t \,, \tag{4.32}$$

where $\mathbf{r}$ denotes the constraints regarding $\mathcal{A}$ and where $\boldsymbol{\lambda}$ contains the respective Lagrange multiplier.

4.1.4 Evolution equations

In line with, e.g., [22], it is possible to derive evolution equations for state variables $\mathcal{V}$ from a dissipation function $\mathcal{C}$, i.e.

$$\partial_{\mathcal{V}} \, \overline{\psi} + \partial_{\dot{\mathcal{V}}} \mathcal{C} = -\Gamma \, \partial_{\mathcal{V}} r \,, \tag{4.33}$$

with the consistency parameter Γ and the generalised inequality constraint $r \leq 0$. For each inequality constraint r, a respective consistency parameter Γ has to be introduced. For specific cases, it may be more convenient to use the dual dissipation function $\mathcal{C}^\star$ instead. This quantity depends on the driving force

$$\mathcal{F} = -\frac{\partial \overline{\psi}}{\partial \mathcal{V}} \tag{4.34}$$

and can be computed by applying the Legendre-Fenchel transformation

$$\mathcal{C}^{\star} = \max_{\dot{\mathcal{V}}} \left\{ \mathcal{F}\dot{\mathcal{V}} - \mathcal{C} \right\} . \tag{4.35}$$

As an alternative to (4.33), the evolution equation is then given by

$$\dot{\mathcal{V}} - \partial_{\mathcal{F}}\,\mathcal{C}^{\star} = -\Gamma\,\partial_{\mathcal{V}}\,r . \tag{4.36}$$

This concept is now applied in order to derive the evolution equations for the model-specific independent internal state variables

$$\mathcal{V} = \left\{ \xi_{\mathrm{mel}}, \boldsymbol{\varepsilon}_{\mathrm{mel}}^{\mathrm{ve}}, \xi_{\mathrm{sol}}, \boldsymbol{\varepsilon}_{\mathrm{sol}}^{\mathrm{pl}}, k_{\mathrm{sol}}^{\mathrm{hard}} \right\} . \tag{4.37}$$

The mass fraction of the powder is substituted by

$$\zeta_{\mathrm{pow}} = 1 - \zeta_{\mathrm{mel}} - \zeta_{\mathrm{sol}} \tag{4.38}$$

according to conservation of mass. As the volume and mass fractions can be converted into one another, compare eq. (4.14), the following framework is derived based on volume fractions $\xi_{\bullet}$ rather than on mass fractions $\zeta_{\bullet}$, see also Remark 6. This enables the enforcement of the minimisation based on the Helmholtz free energy $\overline{\psi}$ without weighting the equation itself with the respective mass density $\rho_{\bullet}$. The stresses can then be calculated in a straightforward manner via eq. (4.31).

Remark 6. *From a computational viewpoint, it is beneficial to use volume fractions as the degree of freedom, despite the fact that the constraint minimisation problem in eq. (4.21) is based on mass fractions. Volume fractions enable the use of the averaged specific volume energy density $\overline{\psi}$, which is also taken into account for the calculation of the overall stress and for the evolution equations of the viscous strains. With this reformulation at hand, the mass density $\rho_{\bullet}$ of the different phases is no longer explicitly included, so that the homogenisation approach reaches physically feasible results. However, the inequality conditions $r_{\bullet}$ still consider the physically sound region of the mass fractions $\zeta_{\bullet}$ as introduced in eq. (4.19).*

Volume fractions

It is sufficient to define two evolution equations, e.g. for ξ_{mel} and ξ_{sol}, as the third quantity can be computed with the help of the equality relation $\sum_{i}^{n_{\mathrm{ph}}} \zeta_i = 1$. In view of establishing evolution equations for the volume fractions ξ_{mel} and ξ_{sol}, a dissipation

function $\mathcal{C}^\xi$ referred to the volume fractions $\xi_\bullet$ is introduced together with the inequality constraints

$$r_{\text{mel}} = -\zeta_{\text{mel}} \leq 0 \ , \tag{4.39}$$

$$r_{\text{sol}} = -\zeta_{\text{sol}} \leq 0 \ , \tag{4.40}$$

$$r_{\text{pow}} = -1 + \zeta_{\text{mel}} + \zeta_{\text{sol}} \leq 0 \ , \tag{4.41}$$

$$r_\Delta = \dot{\zeta}_{\text{pow}} \leq 0 \ , \tag{4.42}$$

derived from eq. (4.19). The phase transformation shall develop over a finite temperature range instead of jumping from zero to one, respectively from one to zero. A dissipative quantity η^ξ can influence the temperature range in which the phase transformation occurs. To ensure a smooth transition, a time dependent dissipation function is defined, i.e.

$$\mathcal{C}^\xi = \frac{\eta^\xi}{2} \left[\dot{\xi}_{\text{pow}}^2 + \dot{\xi}_{\text{mel}}^2 + \dot{\xi}_{\text{sol}}^2 \right] \ . \tag{4.43}$$

This results in a viscous approach, which additionally stabilises the computational framework.

Altogether, two Biot-equations

$$-\mathcal{F}'_{\xi_{\text{mel}}} + \partial_{\dot{\xi}_{\text{mel}}} \mathcal{C}^\xi = -\Gamma_{\text{mel}} \, \partial_{\xi_{\text{mel}}} \, r_{\text{mel}} - \Gamma_{\text{pow}} \, \partial_{\xi_{\text{mel}}} \, r_{\text{pow}} - \Gamma_\Delta \, \partial_{\xi_{\text{mel}}} \, r_\Delta \ , \tag{4.44}$$

$$-\mathcal{F}'_{\xi_{\text{sol}}} + \partial_{\dot{\xi}_{\text{sol}}} \mathcal{C}^\xi = -\Gamma_{\text{sol}} \, \partial_{\xi_{\text{sol}}} \, r_{\text{sol}} - \Gamma_{\text{pow}} \, \partial_{\xi_{\text{sol}}} \, r_{\text{pow}} - \Gamma_\Delta \, \partial_{\xi_{\text{sol}}} \, r_\Delta \ , \tag{4.45}$$

are carried out which govern the evolution of the independent volume fractions. Using the averaged energy density together with the constitutive model, the current phase (mixture) can be determined. In this case,

$$\mathcal{F}'_\bullet = -\frac{\partial \overline{\Psi}}{\partial \mathcal{V}_\bullet} \tag{4.46}$$

refers to the driving force based on the free energy density $\overline{\Psi}$, such that eqs. (4.44) and (4.45) are specified as

$$\frac{\mathrm{d}V_0}{\mathrm{d}m_0} \frac{\partial \overline{\psi}}{\partial \xi_{\text{mel}}} + \eta^\xi \, \dot{\xi}_{\text{mel}} + \frac{\rho_{\text{mel}}}{\rho_{\text{pow}}} \eta^\xi \, \dot{\xi}_{\text{pow}} = -\Gamma_{\text{mel}} \, \partial_{\xi_{\text{mel}}} \, r_{\text{mel}} - \Gamma_{\text{pow}} \, \partial_{\xi_{\text{mel}}} \, r_{\text{pow}}$$
$$- \Gamma_\Delta \, \partial_{\xi_{\text{mel}}} \, r_\Delta \ , \tag{4.47}$$

$$\frac{\mathrm{d}V_0}{\mathrm{d}m_0} \frac{\partial \overline{\psi}}{\partial \xi_{\text{sol}}} + \eta^\xi \, \dot{\xi}_{\text{sol}} + \frac{\rho_{\text{sol}}}{\rho_{\text{pow}}} \eta^\xi \, \dot{\xi}_{\text{pow}} = -\Gamma_{\text{sol}} \, \partial_{\xi_{\text{sol}}} \, r_{\text{sol}} - \Gamma_{\text{pow}} \, \partial_{\xi_{\text{sol}}} \, r_{\text{pow}}$$
$$- \Gamma_\Delta \, \partial_{\xi_{\text{sol}}} \, r_\Delta \ . \tag{4.48}$$

Viscous strains

The evolution of viscous strains $\boldsymbol{\varepsilon}_{\mathrm{mel}}^{\mathrm{ve}}$ within the molten pool is determined via a visco-elastic and thus rate-dependent primal dissipation function

$$\mathcal{C}^{\mathrm{ve}} = \frac{\eta_{\mathrm{mel}}^{\mathrm{ve}}}{2} \, \|\dot{\boldsymbol{\varepsilon}}_{\mathrm{mel}}^{\mathrm{ve}}\|^2 \; . \tag{4.49}$$

Therein, $\eta_{\mathrm{mel}}^{\mathrm{ve}}$ denotes a viscosity related material constant. For this evolution equation no inequality constraints have to be taken into account, therefore the right hand side in eq. (4.33) equals zero when applied to the evolution of viscous strain contributions. In general, the driving force is calculated via eq. (4.34), such that the standard driving force for the viscous strains is defined as

$$\mathcal{F}^{\mathrm{ve}} := -\frac{\partial \overline{\psi}}{\partial \boldsymbol{\varepsilon}_{\mathrm{mel}}^{\mathrm{ve}}} = \zeta_{\mathrm{mel}} \, \boldsymbol{\sigma} \; . \tag{4.50}$$

Here, the driving force $\mathcal{F}^{\mathrm{ve}}$ equals the stress tensor weighted with ζ_{mel}. However, this driving force is a quantity averaged over a domain due to the homogenisation framework applied, whereas the domain can contain multiple phases and changing mass fractions, as visualised in Figure 4.5. This domain corresponds to an infinitesimal surrounding of a material point. As a consequence, a local driving force

$$\mathcal{F}_{\mathrm{loc}}^{\mathrm{ve}} := -\frac{1}{\zeta_{\mathrm{mel}}} \frac{\partial \overline{\psi}}{\partial \boldsymbol{\varepsilon}_{\mathrm{mel}}^{\mathrm{ve}}} = \boldsymbol{\sigma} \tag{4.51}$$

has to be defined that affects only the molten phase within the domain considered, see Figure 4.5 and also Remark 7. This driving force is incorporated into the evolution
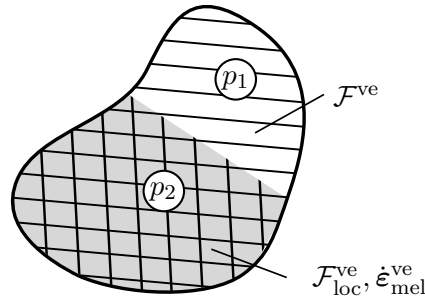

Figure 4.5: Explanation of the standard driving force $\mathcal{F}^{\mathrm{ve}}$ taking into account the whole domain, in contrast to the local driving force $\mathcal{F}_{\mathrm{loc}}^{\mathrm{ve}}$ being effective in the molten phase p_2 (grey), whereas p_1 (white) corresponds to all other possible phases present, also including p_2. Reprinted from [131] under the terms of the Creative Commons Attribution License (CC BY).

equation, such that

$$\dot{\boldsymbol{\varepsilon}}_{\text{mel}}^{\text{ve}} = \frac{1}{\eta_{\text{mel}}^{\text{ve}}} \, \boldsymbol{\sigma} \, . \tag{4.52}$$

The viscous strains incorporate a fluid-like response, as a complete relaxation of the stresses is enabled.

Plastic strains

For the rate-independent evolution of the plastic strains $\boldsymbol{\varepsilon}_{\text{sol}}^{\text{pl}}$ as well as of the variable $k_{\text{sol}}^{\text{hard}}$ related to the isotropic hardening, the following dual dissipation function

$$\mathcal{C}^{\star\text{pl}} = \lambda \, \Phi = 0 \tag{4.53}$$

is used. In the aforementioned equation, λ denotes the Lagrange multiplier and Φ refers to the yield function. Following the same argumentation as in the previous section, the yield function

$$\Phi = \widehat{\Phi}(\mathcal{F}_{\text{loc}}^{\text{pl}}, \, \kappa_{\text{loc}}) \tag{4.54}$$

depends on the local driving forces

$$\mathcal{F}_{\text{loc}}^{\text{pl}} := -\frac{1}{\zeta_{\text{sol}}} \frac{\partial \overline{\psi}}{\partial \boldsymbol{\varepsilon}_{\text{sol}}^{\text{pl}}} \quad = \boldsymbol{\sigma} \, , \tag{4.55}$$

$$\kappa_{\text{loc}} := -\frac{1}{\zeta_{\text{sol}}} \frac{\partial \overline{\psi}}{\partial k_{\text{sol}}^{\text{hard}}} = -\frac{\xi_{\text{sol}}}{\zeta_{\text{sol}}} \, H_{\text{sol}} \, k_{\text{sol}}^{\text{hard}} \, , \tag{4.56}$$

which yields the associated evolution equation for the plastic strains

$$\dot{\boldsymbol{\varepsilon}}_{\text{sol}}^{\text{pl}} = \lambda \, \frac{\partial \Phi}{\partial \mathcal{F}_{\text{loc}}^{\text{pl}}} \, , \tag{4.57}$$

and for the hardening variable

$$\dot{k}_{\text{sol}}^{\text{hard}} = \lambda \, \frac{\partial \Phi}{\partial \kappa_{\text{loc}}} \, . \tag{4.58}$$

The yield function is specifically chosen as

$$\Phi := \left\| \mathcal{F}^{\mathrm{pl}}_{\mathrm{loc,dev}} \right\| - \sqrt{\frac{2}{3}} \left[\sigma^{\mathrm{y}}_{\mathrm{sol}} - \kappa_{\mathrm{loc}} \right] \tag{4.59}$$

$$= \left\| \boldsymbol{\sigma}^{\mathrm{dev}} \right\| - \sqrt{\frac{2}{3}} \left[\sigma^{\mathrm{y}}_{\mathrm{sol}} + \frac{\xi_{\mathrm{sol}}}{\zeta_{\mathrm{sol}}} H_{\mathrm{sol}} k^{\mathrm{hard}}_{\mathrm{sol}} \right] , \tag{4.60}$$

where $\sigma^{\mathrm{y}}_{\mathrm{sol}}$ refers to the yield stress of the solid phase and where $\bullet^{\mathrm{dev}} := \bullet - \frac{1}{3} \operatorname{tr}(\bullet) \, \boldsymbol{I}$ denotes the deviator of the quantity $\bullet$. With this, the flow direction can then be specified as

$$\boldsymbol{\nu} := \frac{\partial \Phi}{\partial \mathcal{F}^{\mathrm{pl}}_{\mathrm{loc}}} = \frac{\boldsymbol{\sigma}_{\mathrm{dev}}}{\left\| \boldsymbol{\sigma}_{\mathrm{dev}} \right\|} , \tag{4.61}$$

together with $\partial \Phi / \partial \kappa_{\mathrm{loc}} = \sqrt{2/3}$.

Remark 7. *In general, a driving force $\mathcal{F} = -\partial_{\mathcal{V}} \overline{\psi}$ is calculated for all internal variables $\mathcal{V}$. However, the evolution of the internal state variables $\dot{\mathcal{V}}$ of the corresponding material only depends on the local driving force $\mathcal{F}_{\mathrm{loc}}$, as discussed before. In contrast, the mechanical dissipation entry $\mathcal{D}_{\mathrm{mech}} = \mathcal{F} \bullet \dot{\mathcal{V}}$ regards the complete driving force, as the thermodynamic consistent driving force $\mathcal{F}$ is already weighted within $\mathcal{D}_{\mathrm{mech}}$ due to the homogenisation approach applied for $\overline{\Psi}$.*

4.1.5 Heat effects

Heat expansion and heat conduction are applied as introduced in Section 3.1.2. Thereby, the effective specific heat capacity is determined based on eq. (2.61) as

$$\begin{aligned} c_{\mathrm{eff}} &:= - \theta \, \partial^2_{\theta\theta} \overline{\Psi} \\ &= \frac{\mathrm{d}V_0}{\mathrm{d}m_0} \left[\xi_{\mathrm{pow}} \, \widetilde{c}_{\mathrm{pow}} + \xi_{\mathrm{mel}} \, \widetilde{c}_{\mathrm{mel}} + \xi_{\mathrm{sol}} \, \widetilde{c}_{\mathrm{sol}} \right] - \chi \end{aligned} \tag{4.62}$$

for the present model. It is worth noting that the specific heat capacity is dependent on the volume fraction $\xi_{\bullet}$ rather than on the mass fraction $\zeta_{\bullet}$. This is due to the direct dependence of the effective specific heat capacity with the averaged specific energy $\overline{\psi}$. Besides, quantity χ stems from the thermoelastic coupling via the thermal strains in the solid phase and is defined as

$$\chi = \frac{\mathrm{d}m_0}{\mathrm{d}V_0} \, \alpha^2_{\mathrm{sol}} \, \zeta^2_{\mathrm{sol}} \left[\widetilde{\mathbf{E}}^{-1} : \boldsymbol{I} \right] : \left[\boldsymbol{I} : \mathbf{E}^{\star} \right] . \tag{4.63}$$

However, in the present framework, this contribution turns out to be negligible due to the dependence on the square of the heat expansion coefficient. For the heat conduction model, the relation

$$\widetilde{k}_{\text{eff}} := \left[\frac{\zeta_{\text{pow}}}{k_{\text{pow}}} + \frac{\zeta_{\text{mel}}}{k_{\text{mel}}} + \frac{\zeta_{\text{sol}}}{k_{\text{sol}}} \right]^{-1} , \tag{4.64}$$

now represents the averaged heat conduction coefficient of the phase mixture according to a Reuss-type homogenisation with $k_{\bullet}$ as the respective heat conductivity of each phase.

Moreover, heat convection and radiation are regarded on the outer boundaries. In a standard manner, heat convection is considered by

$$q_{\text{conv}} = -h \left[\theta_{\text{surf}} - \theta_{\text{amb}} \right] , \tag{4.65}$$

where h refers to the convective heat transfer coefficient, i.e. the reference film coefficient. Furthermore, θ_{surf} and θ_{amb} denote the surface and ambient (sink) temperature of the surrounding media, respectively. In addition, radiation heat flow can be given by

$$q_{\text{rad}} = -\sigma_{\text{boltz}}\, \epsilon_{\text{emiss}} \left[[\theta - \theta_{\text{Z}}]^4 - [\theta_{\text{amb}} - \theta_{\text{Z}}]^4 \right] , \tag{4.66}$$

with $\sigma_{\text{boltz}} = 5.67 \times 10^{-8}\ \text{W}\,\text{m}^{-2}\,\text{K}^{-4}$ corresponding to the Stefan-Boltzmann constant, ϵ_{emiss} being the emissivity coefficient and with θ_{Z} defining the value of absolute zero on the specific temperature scale used. For further insight into the heat transfer mechanism the interested reader is referred to, e.g., [21].

4.2 Implementation and algorithmic treatment

In line with Section 3.2, the FE-based implementation of the present framework is carried out by using the software Abaqus. For the FE implementation, the time discretisation and the evolution of the volume fractions are necessary, which is part of Section 4.2.1. The constitutive model defined in Section 4.1 has to be incorporated into Abaqus via the subroutines UMAT and UMATHT, where important details regarding the implementation are discussed in Section 4.2.2.

4.2.1 Numerical solution strategies

The time discretisation introduced in eq. (2.77) is applied not only for the temperature and strain field rate, $\dot{\theta}$ and $\dot{\varepsilon}$, respectively, but also for all rates of internal variables $\dot{\mathcal{V}}$. The solution of the time-discretised versions of the evolution equations with respect to

$^{n+1}\mathcal{V}$ is discussed in the following. Eq. (4.52) can be explicitly solved for $\varepsilon_{\text{mel}}^{\text{ve}}$ by using the backward Euler scheme, such that

$$^{n+1}\varepsilon_{\text{mel}}^{\text{ve}} = \frac{\Delta t \, \boldsymbol{\sigma} \big({}^{n+1}\xi_{\text{mel}}, {}^{n+1}\xi_{\text{sol}}, {}^{n+1}\varepsilon_{\text{sol}}^{\text{pl}} \big)}{\eta_{\text{mel}}^{\text{ve}}} + {}^{n}\varepsilon_{\text{mel}}^{\text{ve}} \, . \tag{4.67}$$

Consecutively, the viscous strains are replaced with this analytical expression throughout the algorithm. The constraint (4.22) can be further reformulated by inserting relation (4.38) and by applying the forward difference quotient so that

$$\dot{\zeta}_{\text{pow}} \approx -\frac{{}^{n+1}\zeta_{\text{mel}} - {}^{n}\zeta_{\text{mel}}}{\Delta t} - \frac{{}^{n+1}\zeta_{\text{sol}} - {}^{n}\zeta_{\text{sol}}}{\Delta t} \, . \tag{4.68}$$

With this conversion at hand, the distinct set of inequality constraints introduced in eqs. (4.39) to (4.42) is now defined by

$$r_{\text{mel}} = - \, {}^{n+1}\zeta_{\text{mel}} \leq 0 \, , \tag{4.69}$$

$$r_{\text{sol}} = - \, {}^{n+1}\zeta_{\text{sol}} \leq 0 \, , \tag{4.70}$$

$$r_{\text{pow}} = -1 + {}^{n+1}\zeta_{\text{mel}} + {}^{n+1}\zeta_{\text{sol}} \leq 0 \, , \tag{4.71}$$

$$r_{\Delta} = - \, {}^{n+1}\zeta_{\text{mel}} + {}^{n}\zeta_{\text{mel}} - {}^{n+1}\zeta_{\text{sol}} + {}^{n}\zeta_{\text{sol}} \leq 0 \, , \tag{4.72}$$

which has to be fulfilled by the algorithm. The first two residuals emanating from the evolution equations with respect to the volume fractions of the molten and solid phase are specifically given by

$$r_1 = \frac{\mathrm{d}V_0}{\mathrm{d}m_0} \frac{\partial \overline{\psi}}{\partial \xi_{\text{mel}}} - \Gamma_{\text{mel}} + \frac{\rho_{\text{mel}} \, \mathrm{d}V_0}{\mathrm{d}m_0} \Gamma_{\text{pow}} - \frac{\rho_{\text{mel}} \, \mathrm{d}V_0}{\mathrm{d}m_0} \Gamma_{\Delta}$$
$$+ \quad \frac{\eta^{\xi}}{\Delta t} \left[{}^{n+1}\xi_{\text{mel}} - {}^{n}\xi_{\text{mel}} \right] - \frac{\eta^{\xi}}{\Delta t} \frac{\rho_{\text{mel}}}{\rho_{\text{pow}}} \left[{}^{n+1}\xi_{\text{pow}} - {}^{n}\xi_{\text{pow}} \right] \, , \tag{4.73}$$

$$r_2 = \frac{\mathrm{d}V_0}{\mathrm{d}m_0} \frac{\partial \overline{\psi}}{\partial \xi_{\text{sol}}} - \Gamma_{\text{sol}} + \frac{\rho_{\text{sol}} \, \mathrm{d}V_0}{\mathrm{d}m_0} \Gamma_{\text{pow}} - \frac{\rho_{\text{sol}} \, \mathrm{d}V_0}{\mathrm{d}m_0} \Gamma_{\Delta}$$
$$+ \quad \frac{\eta^{\xi}}{\Delta t} \left[{}^{n+1}\xi_{\text{sol}} - {}^{n}\xi_{\text{sol}} \right] - \frac{\eta^{\xi}}{\Delta t} \frac{\rho_{\text{sol}}}{\rho_{\text{pow}}} \left[{}^{n+1}\xi_{\text{pow}} - {}^{n}\xi_{\text{pow}} \right] \, , \tag{4.74}$$

where the dissipation function specified in eq. (4.43) is analogously discretised by using eq. (2.77), and where the explicit definition for ξ_{pow} is not inserted because the terms are already rather lengthy. Following Section 3.2.1, the compatibility conditions belonging to the constraints (4.69) - (4.72) shall be transformed into equality constraints by using the

regularised Fischer-Burmeister nonlinear complementarity function. Thus, the residual entries

$$r_3 = \sqrt{\Gamma_{\mathrm{mel}}^2 + r_{\mathrm{mel}}^2 + 2\,\delta^2} + r_{\mathrm{mel}} - \Gamma_{\mathrm{mel}} \,, \tag{4.75}$$

$$r_4 = \sqrt{\Gamma_{\mathrm{sol}}^2 + r_{\mathrm{sol}}^2 + 2\,\delta^2} + r_{\mathrm{sol}} - \Gamma_{\mathrm{sol}} \,, \tag{4.76}$$

$$r_5 = \sqrt{\Gamma_{\mathrm{pow}}^2 + r_{\mathrm{pow}}^2 + 2\,\delta^2} + r_{\mathrm{pow}} - \Gamma_{\mathrm{pow}} \,, \tag{4.77}$$

$$r_6 = \sqrt{\Gamma_{\Delta}^2 + r_{\Delta}^2 + 2\,\delta^2} + r_{\Delta} - \Gamma_{\Delta} \,, \tag{4.78}$$

can be implemented into the framework, where the perturbation parameter $\delta = 10^{-10}$ is used. With this parameter, a continuously differentiable function exists. Furthermore, eqs. (4.57) to (4.58) are discretised in time by using a backward Euler scheme, resulting in

$$\boldsymbol{r}_7 = {}^n\boldsymbol{\varepsilon}_{\mathrm{sol}}^{\mathrm{pl}} - {}^{n+1}\boldsymbol{\varepsilon}_{\mathrm{sol}}^{\mathrm{pl}} + \Delta t\,\lambda\,\boldsymbol{\nu}({}^{n+1}\xi_{\mathrm{mel}}, {}^{n+1}\xi_{\mathrm{sol}}, {}^{n+1}\boldsymbol{\varepsilon}_{\mathrm{sol}}^{\mathrm{pl}}) \,, \tag{4.79}$$

$$r_8 = {}^n k_{\mathrm{sol}}^{\mathrm{hard}} - {}^{n+1}k_{\mathrm{sol}}^{\mathrm{hard}} + \Delta t\,\lambda\,\sqrt{2/3} \,. \tag{4.80}$$

To calculate the consistency parameter λ in eqs. (4.79) and (4.80), the complementarity conditions related to the evolution of plastic strains are incorporated via

$$r_9 = \sqrt{\lambda^2 + \Phi^2 + 2\,\delta^2} + \Phi - \lambda \,. \tag{4.81}$$

The final residual

$$\mathbf{r} = [\,r_1, \, r_2, \, r_3, \, r_4, \, r_5, \, r_6, \, [\boldsymbol{r}_7]^{\mathrm{kel}}, \, r_8, \, r_9\,]^{\mathrm{t}} = \mathbf{0} \,, \tag{4.82}$$

has to be solved with respect to

$$\mathbf{f} = [\xi_{\mathrm{mel}}, \, \xi_{\mathrm{sol}}, \, \Gamma_{\mathrm{mel}}, \, \Gamma_{\mathrm{sol}}, \, \Gamma_{\mathrm{pow}}, \, \Gamma_{\Delta}, \, [\boldsymbol{\varepsilon}_{\mathrm{sol}}^{\mathrm{pl}}]^{\mathrm{kel}}, \, k_{\mathrm{sol}}^{\mathrm{hard}}, \, \lambda]^{\mathrm{t}} \,, \tag{4.83}$$

where the tensorial quantities $\boldsymbol{r}_7$ and $\boldsymbol{\varepsilon}_{\mathrm{sol}}^{\mathrm{pl}}$ are rewritten as vectors with the help of the Kelvin notation, compare Section 2.1, resulting in vectorial entries $[\boldsymbol{r}_7]^{\mathrm{kelv}}$ and $[\boldsymbol{\varepsilon}_{\mathrm{sol}}^{\mathrm{pl}}]^{\mathrm{kel}}$. In order to determine the unknowns $\mathbf{f}$ defined in eq. (4.83), a Newton-Raphson scheme is applicable, compare Remark 3. The local Jacobian $\mathbf{J}$ can be determined by using standard calculus methods and is not further specified at this point.

4.2.2 User-defined routines

As discussed in Section 3.2.2, the internal strategy of Abaqus – the command `MODEL CHANGE` – is used once more to model the layer construction during the LPBF process. Furthermore, the incorporation of the specific user-defined routines for LPBF processes

is discussed in Section 3.2.4. Within this section, only new aspects regarding the three subroutines, which are needed to specify the framework presented in Section 4.1, are pointed out.

As a thermomechancial coupling is present for the constitutive model, the coupling terms as introduced in Section 2.6.1 have to be determined within UMAT. Thus, not only RPL but also the respective (four) derivatives of the algorithmic tangent are necessary. The value of RPL corresponds to $\mathcal{D}_{\mathrm{mech}}$ as defined in Appendix B.1, whereas the time derivatives are implemented by using eq. (2.77). The derivation of all tangent contributions is summarised in Appendix B.2. However, these quantities are not absolutely necessary for the subroutine. Due to the rather small step size, the convergence is sufficiently good and not negatively influenced when the approximated tangent is used instead of the analytical one. In contrast, the complex calculations of the correct analytical tangent within the subroutine (for every element and time increment) resulted in noticeably longer simulation durations. Thus, for the current framework, only the mechanical tangent $\mathbf{E}^{\mathrm{algo}} \approx \partial_{\boldsymbol{\varepsilon}} \boldsymbol{\sigma} = \mathrm{d}m_0/\mathrm{d}V_0\, \widetilde{\mathbf{E}}^{-1} : [\mathbf{E}_{\mathrm{pow}} : \mathbf{E}_{\mathrm{mel}} : \mathbf{E}_{\mathrm{sol}}]$ is incorporated, while the remaining (three) derivatives are set to zero.

In addition, the subroutine UMATHT as defined in Section 2.6.2 has to be adapted again. For the model at hand, the effective density obviously changes during the process due to the evolution of the mass fractions. In analogy to eq. (4.16), the current density is defined as $\rho = \zeta_{\mathrm{pow}}\, \rho_{\mathrm{pow}} + \zeta_{\mathrm{mel}}\, \rho_{\mathrm{mel}} + \zeta_{\mathrm{sol}}\, \rho_{\mathrm{sol}}$. At the beginning of the simulation, the material completely consists of powder material in Abaqus, thus $\rho := \rho_{\mathrm{pow}}$. This can be implemented within the user subroutine UMATHT, where the effective heat capacity and density is artificially adapted, cf. the respective paragraph in Section 3.2.4 again. The contribution χ in eq. (4.63) it set to zero.

To complete the model, a volumetric moving heat flux as discussed in Section 3.2.3 is used to represent the laser beam. The external heat source is defined within the Abaqus subroutine DFLUX by eq. (3.58), where x_i' refers to the moving coordinate system whose origin lies in the centre of the laser beam at the top surface of the current powder layer, see Figure 4.8. Coordinates x_1' and x_2' are needed to define the laser movement in dependence of the laser velocity $\overline{v}^{\mathrm{lsr}}$ within the x_1-x_2-plane, coordinate x_3' is defined by eq. (3.60).

4.3 Numerical examples

In this section, different numerical examples are discussed. The material model is adapted to a $\mathrm{Ti}_6\mathrm{Al}_4\mathrm{V}$ titanium aluminium alloy with material parameters according to Table 4.1. The transformation strains are directly defined via the mass densities. The parameter η^{ξ} incorporated in the dissipation potential $\mathcal{D}^{\xi}$ is set to $\eta^{\xi} = 0.005$ for the examples at hand. This parameter can be used to adjust the temperature range, in which the phase changes occur in comparison to experimental findings, compare also Appendix C.2. Moreover, it can be used to potentially stabilise the global FE scheme

in terms of numerical robustness. In addition, the viscous strain parameter is chosen as $\eta_{\text{mel}}^{\text{ve}} = 70$, so that a high relaxation within the molten (fluid) phase is feasible. The mechanical parameters for an isotropic tensor, i.e. Poisson's ratio ν and Young's modulus E, as well as yield limit σ^{y}, are taken from the literature, see [121, 148, 173]. The hardening modulus H_{sol} is, at this stage, chosen without particular literature reference. The thermal material parameters, i.e. the expansion coefficient α, the specific heat capacity c, the conductivity k and the latent heat L, as well as the initial temperature θ^{ini} and the reference temperature θ^{ref} are parameters based on [121, 148]. The respective effective counterparts which are used to calculate the material response follow from the homogenisation approach introduced in the previous chapters in contrast to material models which directly incorporate temperature-dependent averaged material properties. Furthermore, the difference in the mass densities of the material's phases is rather large and, in consequence, the volume changes captured by the transformation strains. Therefore, one could argue that the small strain approach used may not be appropriate. However, the small strain formulation is considered acceptable, as little rotations are present, see Remark 8, and the rather large transformation strains are completely volumetric.

Table 4.1: Overview of the used material parameters of Ti_6Al_4V adapted from [121, 148, 173].

Material parameters		Powder	Melt	Solid
Mechanical parameters				
Density	ρ [kg/m^3]	2800	3800	4420
Poisson's ration	ν [$-$]	0.33	0.45	0.33
Young's modulus	E [GPa]	1.2	2.9	88.8
Yield limit	σ^{y} [GPa]	-	-	0.55
Hardening modulus	H [GPa]	-	-	1
Viscosity parameter	η^{ve}	-	70	-
Thermal parameters				
Expansion coefficient	α [1/K]	-	-	1.1e-05
Initial temperature	θ^{ini} [K]	-	-	273.15
Heat capacity	c [J/(kgK)]	750	750	750
Conductivity	k [W/(mK)]	9.5	33.4	17.8
Latent heat	L [kJ/kg]	286	-	286
Reference temperature	θ^{ref} [K]	1873.15	-	1873.15

Remark 8. *The deformation gradient $\boldsymbol{F}$ can be multiplicatively split into a rotation tensor $\boldsymbol{R}$ and a stretch tensor $\boldsymbol{U}$, so that $\boldsymbol{F} = \boldsymbol{R} \cdot \boldsymbol{U}$. With this, a different approach is possible by using the small strain theory. The general definition of the small strain tensor has been introduced in eq. (2.29). The small strain measure can also be introduced via the deformation gradient with eq. (2.23), so that, e.g., $\boldsymbol{\varepsilon} := \frac{1}{2}\left[\boldsymbol{F} + \boldsymbol{F}^{\text{t}}\right] - \boldsymbol{I}$. For negligible rotation $\boldsymbol{R} \approx \boldsymbol{I}$, it follows that $\boldsymbol{\varepsilon} \approx \boldsymbol{U} - \boldsymbol{I}$. For the model at hand, $\boldsymbol{\varepsilon} = \frac{1}{2}\left[\nabla_{\boldsymbol{X}}\boldsymbol{u} + [\nabla_{\boldsymbol{X}}\boldsymbol{u}]^{\text{t}}\right] \approx \boldsymbol{U} - \boldsymbol{I}$ is then valid.*
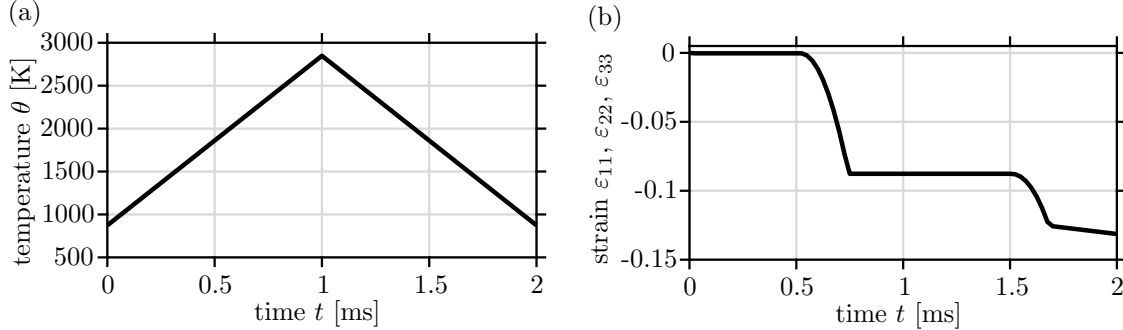
4.3.1 Proof of concept

Figure 4.6: Proof of concept via thermal cycle at material point level: (4.6a) prescribed temperature evolution and (4.6b) resulting strain evolution. The significant drops in the strain evolution occur during the transitions between powder, molten, and re-solidified material. Reprinted from [131] under the terms of the Creative Commons Attribution License (CC BY).

In order to investigate the pure material response of the proposed framework, the same temperature cycle as defined in Section 3.3.1, respectively Figure 4.6a, is prescribed at material point level with zero Neumann boundary conditions as a proof of concept. The resulting strain evolution is shown in Figure 4.6b, while Figure 4.7 illustrates the corresponding evolution of mass and volume fractions. The significant changes in the strains occur simultaneously to the evolution of phase fractions. For constant phase fractions, the strains are therefore also constant, except for the re-solidified phase where the strains decrease while the material cools down due to heat expansion. Due to the zero Neumann boundary conditions, no stresses arise so that no viscous or plastic strains are present in this conceptual proof.

In Figure 4.7, particularly the difference in the evolution of the mass and volume fractions for the three phases can be examined. The material initially purely consists of powder, thus $\xi_{\mathrm{pow}} = \zeta_{\mathrm{pow}} = 1$. With increasing temperature, the first phase change towards the molten phase starts at approximately $\theta \approx 1880\,\mathrm{K}$ and finishes at $\theta \approx 2330\,\mathrm{K}$. The solidification process begins at $\theta \approx 1870\,\mathrm{K}$ and ends at $\theta \approx 1520\,\mathrm{K}$. As already indicated above, the parameter η^ξ governs the time span and temperature interval in which the phase transition occurs. If no dissipation potential is incorporated, corresponding to $\eta^\xi = 0$, an immediate transition occurs, compare Figure 3.5. This jump is now replaced by a smooth transition due to the dissipation function $\mathcal{C}^\xi$ defined in eq. (4.43), cf. the evolution in Figure 4.7. In other words, it is possible to affect the mushy region between the solidus and liquidus temperature with the parameter η^ξ, as it controls the rate-dependent behaviour. From this numerical example it can be concluded that a volume change of approximately $36\,\%$ occurs during the process, which is captured by introducing the transformation strains in Section 4.1.2. Therefore, the framework based on mass fraction considerably improves the results in view of the changing mass densities compared to the previous Chapter 3.
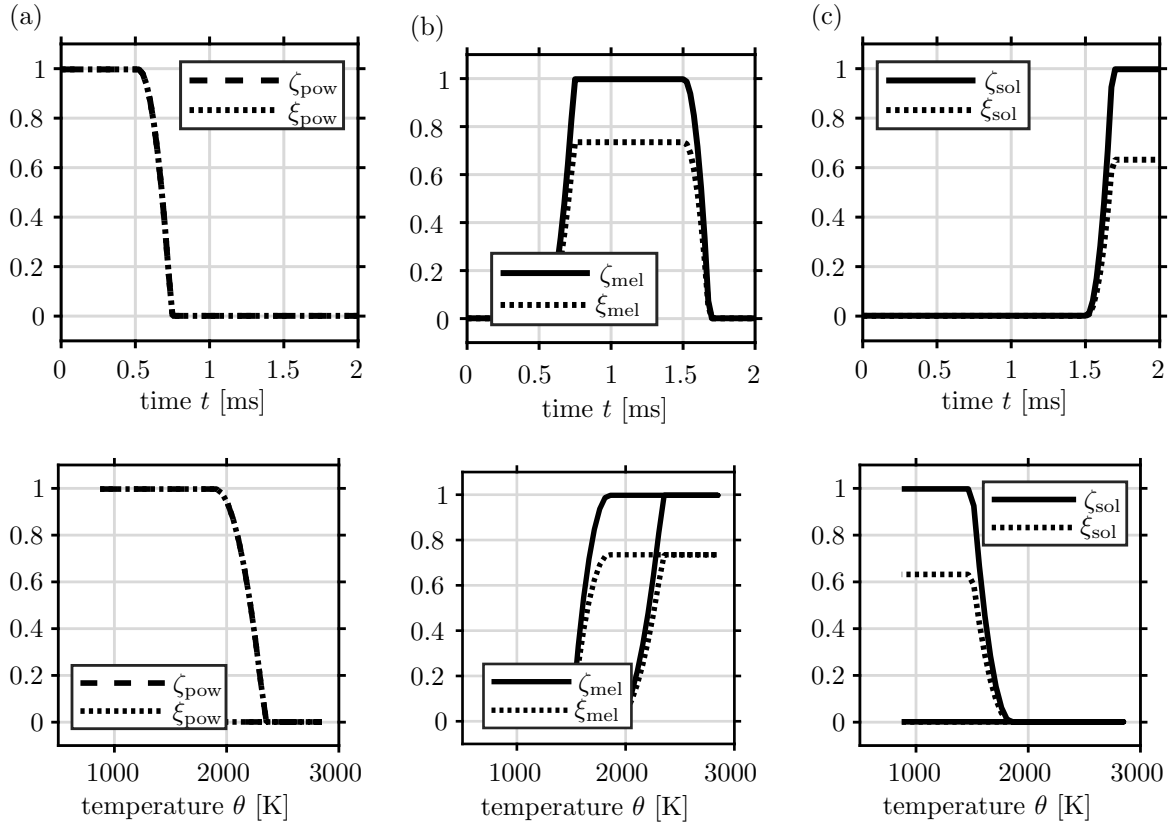
Figure 4.7: Evolution of the respective mass and volume fractions over time and temperature for the three phases: (4.7a) powder phase, (4.7b) molten phase and (4.7c) re-solidified material, with prescribed temperature evolution according to Figure (4.6a). Reprinted from [131] under the terms of the Creative Commons Attribution License (CC BY).

4.3.2 Simulation of basic processes

In the following, the modelling and simulation of basic LPBF processes are presented. The main geometrical model with all boundary conditions on $\partial \mathcal{B}$ is conceptually illustrated in Figure 4.8 for the representative build chamber. For the example at hand, homogeneous Dirichlet boundary conditions are prescribed for the displacement, so that

$$\partial \mathcal{B}_2 : \quad u_3 = 0 \quad \forall \quad x_3 = d \,, \tag{4.84}$$

$$\partial \mathcal{B}_3 : \quad u_2 = 0 \quad \forall \quad x_2 = w \,, \tag{4.85}$$

$$\partial \mathcal{B}_4 : \quad u_2 = 0 \quad \forall \quad x_2 = 0 \,, \tag{4.86}$$

$$\partial \mathcal{B}_5 : \quad u_1 = 0 \quad \forall \quad x_1 = l \,, \tag{4.87}$$

$$\partial \mathcal{B}_6 : \quad u_1 = 0 \quad \forall \quad x_1 = 0 \,. \tag{4.88}$$
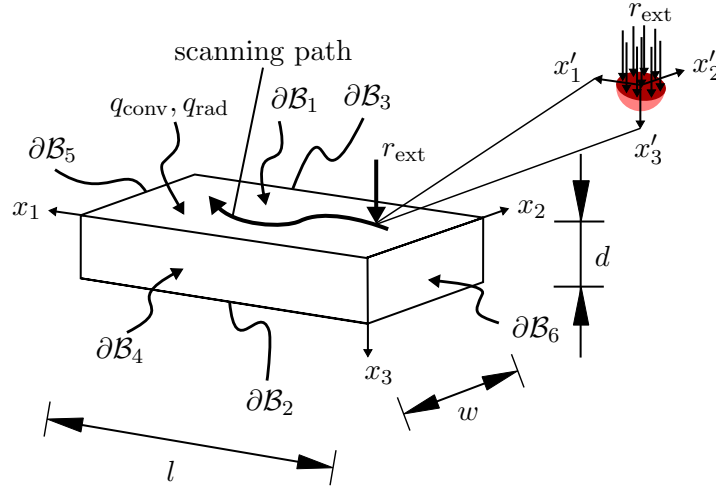
Figure 4.8: Definition of the boundaries for basic process simulations. Reprinted from [131] under the terms of the Creative Commons Attribution License (CC BY).

The temperature at the bottom surface is prescribed based on

$$\partial\mathcal{B}_2: \quad \theta = 373.15\,\text{K} \quad \forall \quad x_3 = d \,. \tag{4.89}$$

Additional heat flux terms due to convection q_{conv} and radiation q_{rad} are present at the top surface, i.e.

$$\partial\mathcal{B}_1: \quad q_{\text{conv}} \quad \forall \quad x_3 = 0 \,, \tag{4.90}$$

$$\partial\mathcal{B}_1: \quad q_{\text{rad}} \quad \forall \quad x_3 = 0 \,, \tag{4.91}$$

which have been neglected in the previous Chapter 3. In addition, the laser beam heat input which is represented by the volume-distributed heat source r_{ext} exists along the respective scanning path.

For the following simulations, the laser power is set to $P = 130\,\text{W}$ with velocity $\bar{v}^{\text{lsr}} = 1\,\text{m/s}$ and focus radius $r_0 = 0.15\,\text{mm}$. A convective heat transfer coefficient of air $h = 25\,\text{W}\,\text{K}^{-1}\,\text{m}^{-2}$ is used, whereas the emissivity of the titanium alloy is set to $\epsilon_{\text{emiss}} = 0.19$, cf. [9]. A layer height $h_{\text{lyr}} = 0.05\,\text{mm}$ is used, whereas the height of the base material is chosen to be larger (0.15 mm). Overall, once more a part made out of three layers $n_{\text{lyr}} = 3$ will be simulated.

The initial part only consists of powder material where the first layer of material is already activated. At first, the build chamber is homogeneously pre-heated to $\bar{\theta} = 373\,\text{K}$ subject to the respective boundary conditions. Afterwards, the laser beam is applied along the predefined scanning path and a cooling time is given before the next layer of powder is activated. This procedure is repeated until all three layers have been activated and until the laser beam has been applied. Finally, the work piece cools down to the build chamber temperature $\bar{\theta}$. For this simulation, the element type `C3D8HT` is chosen
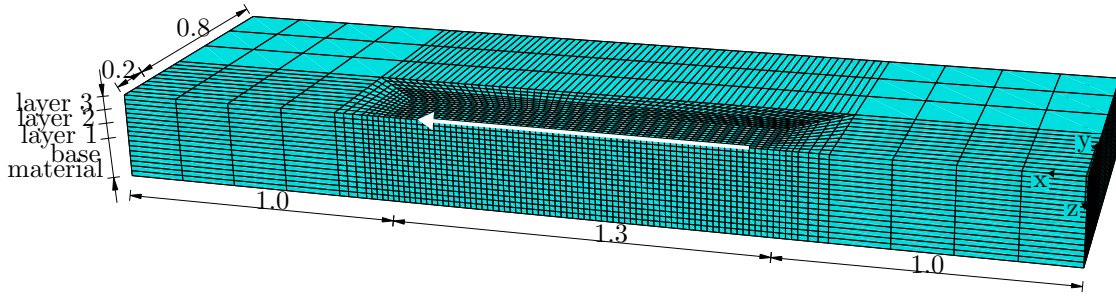
Figure 4.9: Geometry of the straight laser path model in mm with a layer height of 0.05 mm and a height of the base material of 0.15 mm. In addition, the corresponding mesh is visualised. Reprinted from [131] under the terms of the Creative Commons Attribution License (CC BY).
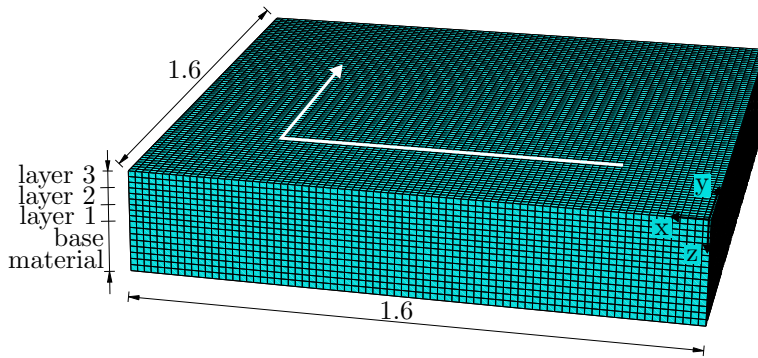

Figure 4.10: Geometry of the L-shaped laser path model in mm with a layer height of 0.05 mm and a height of the base material of 0.15 mm. In addition, the corresponding mesh is visualised. Reprinted from [131] under the terms of the Creative Commons Attribution License (CC BY).

because the Poisson's ratio of the molten phase represents almost incompressibility. The mesh for the straight laser path is in analogy to Figure 4.9, where a characteristic element length of $l_{\mathrm{char}} \approx 20\,\mu\mathrm{m}$ is applied. For the L-shaped laser path, a constant mesh of $l_{\mathrm{char}} \approx 20\,\mu\mathrm{m}$ is used, as shown in Figure 4.10. For both examples, three elements per layer are used in thickness direction. During the simulation, the automatic time incrementation included within Abaqus is used. The simulations are performed on the Linux HPC cluster (LiDO3) at TU Dortmund University, where one compute node using eight cores is taken for both simulations.

Straight laser path

For this example, the laser beam moves $1\,\mathrm{mm}$ along the x_1-direction. The geometry considered, respectively half of the part, is specified by $l = 3.3\,\mathrm{mm}$, $w = 1\,\mathrm{mm}$ and $d = 0.3\,\mathrm{mm}$ for the boundary conditions introduced in eqs. (4.85) to (4.89), respectively. In Figure 4.11, the temperature evolution $\theta(\boldsymbol{x}, t)$ and the evolution of the mass fraction of the molten phase ζ_{mel} is illustrated. The deformed mesh (with scale factor one) is plotted for all consecutive figures. The depth of the molten pool increases as can be seen
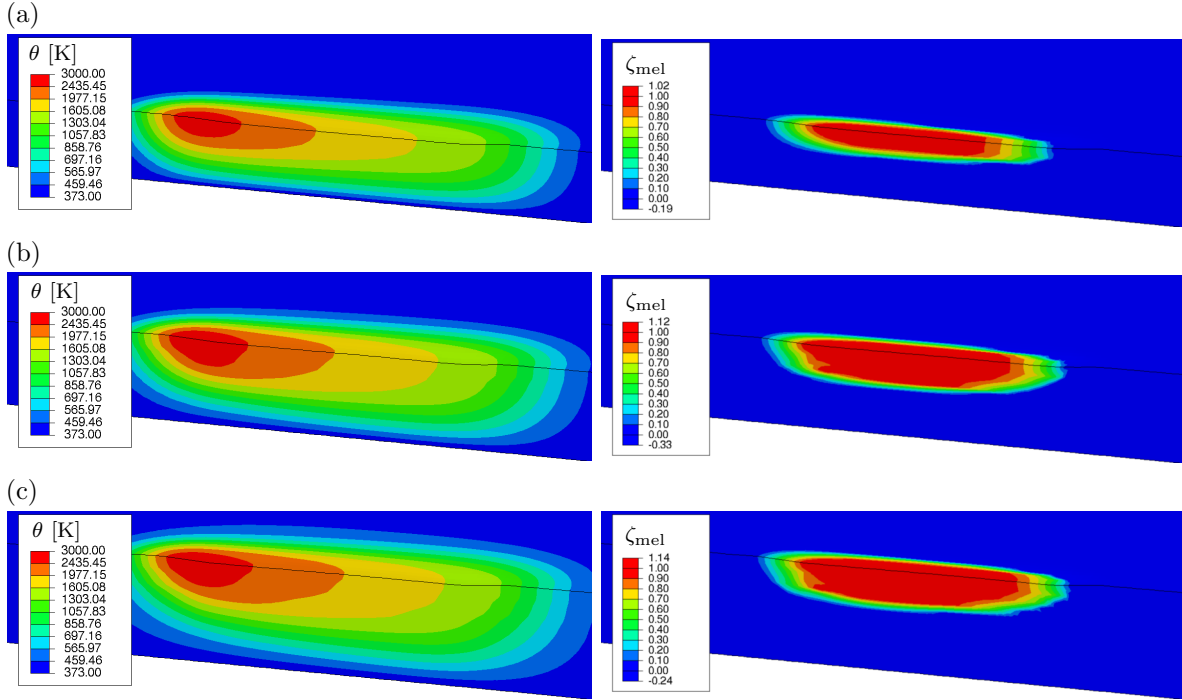
Figure 4.11: Distribution of temperature θ on the left side and the respective mass fraction ζ_{mel} of the molten phase on the right side for the same time step while scanning (4.11a) layer 1, (4.11b) layer 2 and (4.11c) layer 3, where the laser beam has reached the end of each straight line. Reprinted from [131] under the terms of the Creative Commons Attribution License (CC BY).

in Figures 4.11b and 4.11c compared to Figure 4.11a due to the higher conductivity of the already re-solidified layers. This allows the connection of newly added layers to previous ones so that there is one compound. The volume shrinkage of the material during the melting is indicated in Figure 4.11. After the application of all three layers and the consecutive cooling, the final re-solidified part can be identified in terms of the volume fraction ξ_{sol}, see Figure 4.12a and 4.12b, where in the latter Figure the solid part has been virtually extracted. These two Figures show the re-solidified material after applying the laser beam to three layers in contrast to Figure 4.11c, where only the current state of the molten material during the third scanning is visualised. The maximum value of the volume fraction of the solid phase equals 0.633 (i.e. $\max \xi_{\mathrm{sol}} = \rho_{\mathrm{pow}}/\rho_{\mathrm{sol}} = 0.633$) in contrast to the related mass fraction ($\max \zeta_{\mathrm{sol}} = 1$), compare Figure 4.7c.

The incorporation of r_{mech} in the subroutine `UMAT` as defined in eq. (2.62) is quite important. Without the coupling term `RPL`, the maximum temperature within the molten pool would be overestimated by approximately $200\,\mathrm{K}$, compare Appendix B.3. Within r_{mech}, not only the dissipative effects due to the internal state variables $\mathcal{V}$ are included, but also the latent heat effects are thermodynamically consistent incorporated into the framework. In the literature, mostly the apparent heat capacity method as introduced in [23] is used to capture the effects of the latent heat by an artificial increase of the heat
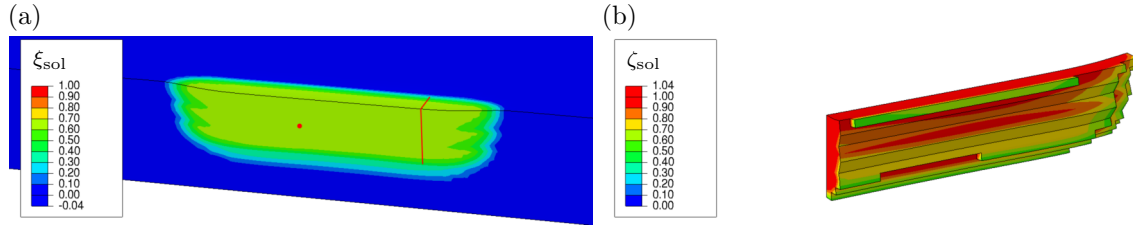
Figure 4.12: Final distribution of (4.12a) the re-solidified volume fraction ξ_{sol} and (4.12b) the final virtually extracted part with re-solidified mass fraction ζ_{sol} (cut at the red line displayed in (4.12a) and rotated; red dot used for graphs in Figure 4.14) after cooling down to the build chamber temperature. Reprinted from [131] under the terms of the Creative Commons Attribution License (CC BY).

capacity, see e.g. [36, 54, 56, 159, 165, 174]. An in-depth study on different methods to include latent heat effects during phase changes can be found in [145]. In [159], the influence of the latent heat for the solely thermal problem has been specifically examined, where results similar to those in our studies were obtained. Overall, eq. (2.62) mainly regulates the temperature evolution and thus the melt pool geometry, see Appendix B.3, rather than the absolute stress values. In general, the laser beam parameters influence the melt pool geometry which affects the hatching strategy and the layer height while simulating a complete part.

The residual stresses stemming from heat expansion and, more significantly, the volume changes due to the phase transitions, are illustrated in Figure 4.13. These stresses are particularly significant within the re-solidified part, as the powder material exhibits a small Young's modulus, compare Figure 4.13d. In the contour plots it can be observed in Figure 4.13a that particularly high tensile normal stresses are present in x_1-direction of the third layer, in other words along the direction of the moving heat source. In addition, high compressive normal stresses exist in x_2-direction which is perpendicular to the direction of the moving heat source, see Figure 4.13b. Negligible stresses are present in x_3-direction as visualised in Figure 4.13c. The shear stresses are not pictured, as they are negligible (for the coordinate system considered) compared to the highlighted normal stress contributions.

The temporal evolution of various significant quantities is exemplarily presented in Figure 4.14 to gain a better understanding of, e.g., the stress evolution. Therefore, one centred element indicated by a red dot in the first layer shall be considered in detail, see Figure 4.12. The values of the nodes are averaged for the element. In Figure 4.14a, the related temperature and the molten mass fraction are illustrated. A steep temperature increase is found when the laser beam is applied. During the second scanning, the top material re-melts, whereas during the scanning of the third layer, the first layer does not completely re-melt again. High total strains are present for ε_{22} and ε_{33} in Figure 4.14b. When examining the stress evolution in Figure 4.14c, the relaxation of the stress σ_{11} is noticeable during the scanning of the second layer. In contrast, stress σ_{22} increases because the expansion and contraction of the material in x_2-direction is hindered. After
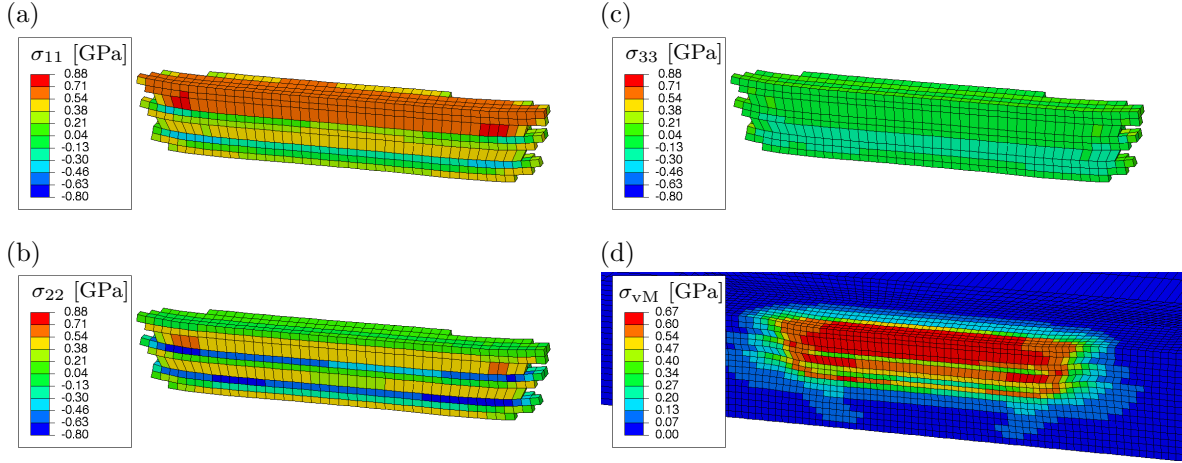
Figure 4.13: Distribution of normal stresses $\sigma_{\bullet\bullet}$ of the virtually extracted final re-solidified part in (4.13a) x_1-direction, (4.13b) x_2-direction and (4.13c) x_3-direction. The von Mises equivalence stress σ_{vM} for the overall part is shown in (4.13d). Reprinted from [131] under the terms of the Creative Commons Attribution License (CC BY).

cooling down for the third time, see Figure 4.14a, a steady-state is reached for the strains and stresses, as visualised in Figure 4.14c and 4.14b. The evolution of an accumulated inelastic strain,

$$\varepsilon^{\text{inel}} = \zeta_{\text{mel}} \left[\varepsilon^{\text{trans}}_{\text{mel}} + \varepsilon^{\text{ve}}_{\text{mel}} \right] + \zeta_{\text{sol}} \left[\varepsilon^{\text{trans}}_{\text{sol}} + \varepsilon^{\text{th}}_{\text{sol}} + \varepsilon^{\text{pl}}_{\text{sol}} \right] \tag{4.92}$$

is exemplarily plotted in Figure 4.14d. This averaged inelastic strain $\varepsilon^{\text{inel}}$ can be evaluated with the introduced model in a post-processing step. This quantity is comparable to the so-called inherent strain, as introduced in Section 1.1.2. However, most models, see e.g. [82, 102, 153, 158], use a phenomenological approach to define a macroscopic inelastic strain contribution that accumulates all inelastic processes, whereas in this framework the inelastic strain is micromechanically motivated. Due to the volumetric transformation strains, the evolution of the averaged inelastic strain is (quasi) volumetric for the particular boundary value problem considered up to the point where the part solidified. The accumulated inelastic strain evolution then differs: larger strains are found in x_2- and x_3-direction, while these strains almost coincide again during the second re-melting. After cooling, almost no further changes occur. Only one small peak is visible when the third layer is applied and molten. This is in accordance with Figure 4.14a, as the element does not completely re-melt during the third cycle. In the final state, high inelastic strains for the x_2- and x_3-direction are present.

L-shaped laser path

In addition to the aforementioned case, a more complex laser beam path is simulated. For this example, the laser beam moves $0.75\,\text{mm}$ along the x_1-direction and $0.75\,\text{mm}$ along
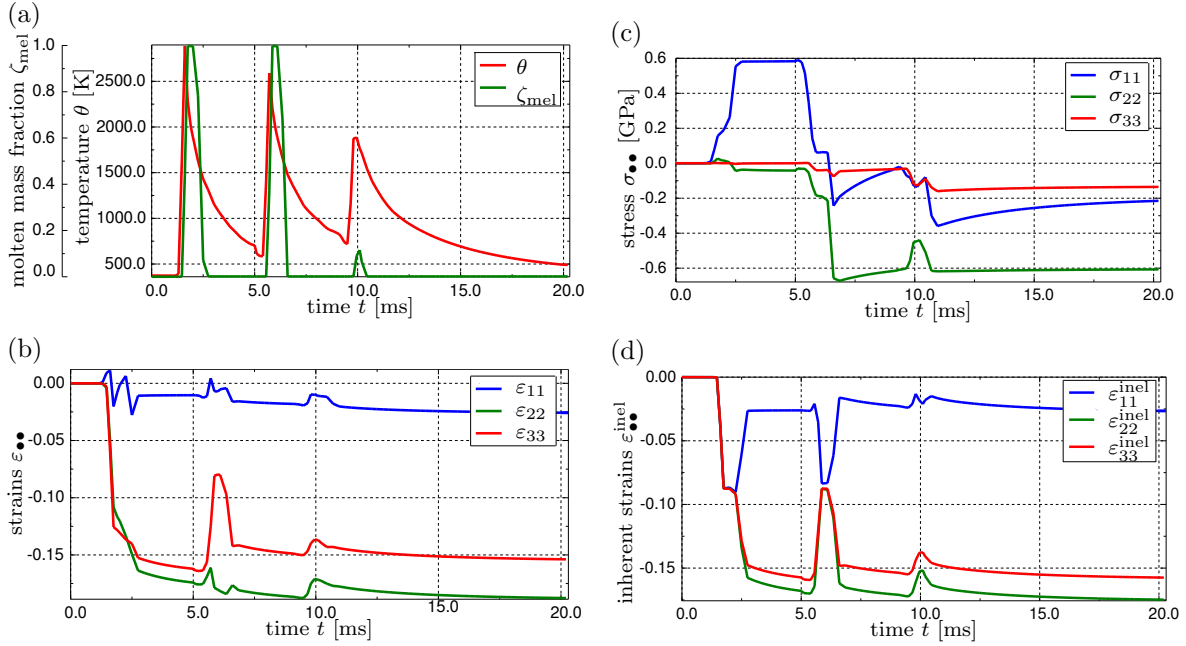
Figure 4.14: Temporal evolution of representative quantities for one centred element as indicated in Figure (4.12a): (4.14a) averaged temperature evolution θ and molten mass fraction ζ_{mel}, (4.14b) averaged total strains ε_{11}, ε_{22}, ε_{33}, (4.14c) averaged normal stress evolution σ_{11}, σ_{22}, σ_{33} and (4.14d) accumulated inelastic strains $\varepsilon_{11}^{\mathrm{inel}}$, $\varepsilon_{22}^{\mathrm{inel}}$, $\varepsilon_{33}^{\mathrm{inel}}$. Reprinted from [131] under the terms of the Creative Commons Attribution License (CC BY).

the x_2-direction. Similar to the example before, three layers are consecutively added. The boundary conditions defined in eqs. (4.85) to (4.89) are referred to a geometry with $l = 1.6\,\mathrm{mm}$, $w = 1.6\,\mathrm{mm}$ and $d = 0.3\,\mathrm{mm}$, cf. Figures 4.8 and 4.10. In theory, it is possible to model even more complex geometries. However, the computational time increases considerably with a larger number of elements and longer laser beam paths. When comparing both simulations, the straight laser path needs approximately 17 hours, where 27 693 elements are used. Overall, the model exhibits 151 821 degrees of freedom. The example of the L-shaped laser path, however, uses 108 800 elements and a total of 581 192 degrees of freedom. Altogether, the computational time increases to almost eight days. The final results of the L-shaped path are presented in what follows, where the solid part has been virtually extracted for all illustrations.

First of all, the normal and shear strain distribution is pictured in Figure 4.15, where the deformed mesh (with scale factor one) is presented. Here, a couple of effects are striking: the dependence of the strains and the laser path orientation is clearly visible, compare Figure 4.15a for normal strains ε_{11} and ε_{22}. While the beam moves along the x_1-direction, small tensile strains ε_{11} are present. The values of the strains change as soon as the laser beam turns and moves along the x_2-direction. The normal strains ε_{11} switch from tensile to compressive strains and small tensile strains ε_{22} are present. In addition, especially high normal compressive strains ε_{33} are found within the part, as
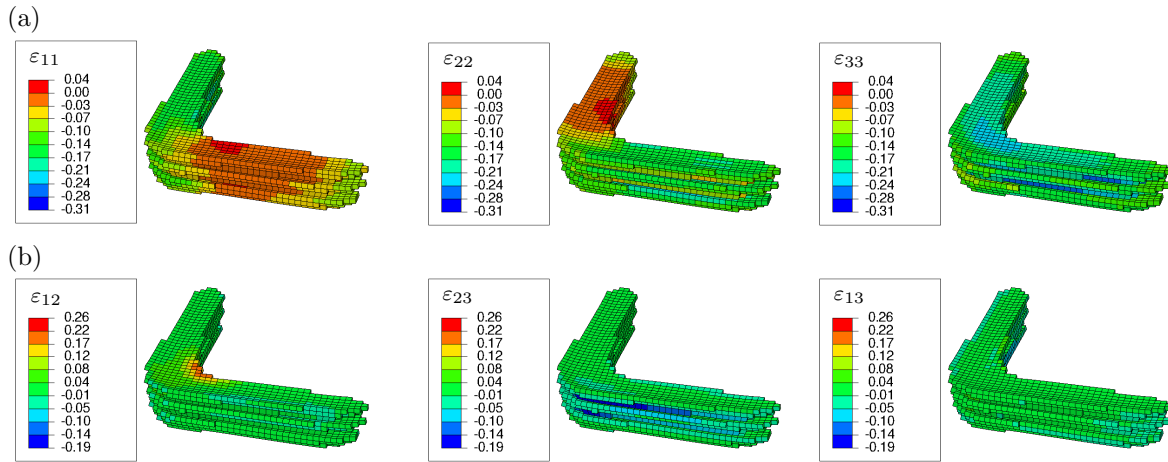
(a)

(b)

Figure 4.15: Distribution of total strains $\varepsilon_{\bullet\bullet}$ of the virtually extracted final re-solidified part: (4.15a) normal and (4.15b) shear strains. Reprinted from [131] under the terms of the Creative Commons Attribution License (CC BY).

it shrinks the most in depth. Due to the changing laser beam path, shear stresses are induced, as illustrated in Figure 4.15b. Large negative shear strains ε_{23} change to high positive shear strains ε_{13} after the kink, as a symmetry is present with respect to a plane parallel to $-x_1 = x_2$. Altogether, the strains are rather constant along the width of the re-solidified part and within one direction of each layer. In contrast – with an increasing number of layers – the magnitude of the strains increases.

Although the laser beam path, respectively the objective geometry, is symmetric with respect to the underlying symmetry plane and although the distribution of the strains is almost symmetric as well, the distribution of the resulting solid part is not completely symmetric. The widths of the two sides differ slightly. This can be explained by the rather coarse discretisation. In addition, the depth of the simulated workpiece increases at the turning point of the laser beam and the part is notably wider at the kink. Due to the turning of the laser, the heat influence takes place over a longer time period compared to the positions further afield and to the straight lines considered in Section 4.3.2. This effect has to be kept in mind when manufacturing more complex components.

Figure 4.16 shows the normal stresses which are significantly larger than the related shear stresses. In analogy to Figure 4.15a, the stresses vary according to the laser beam movement. This becomes especially visible when comparing Figures 4.16a and 4.16b. High tensile stresses σ_{11} and σ_{22}, respectively, can be found along the movement of the laser beam. High compressive strains exist perpendicularly to the laser movement, especially in the lower portion of each layer. In x_3-direction, less normal stresses σ_{33} are computed.

Finally, the equivalent inelastic strain $\bar{\varepsilon}^{\text{inel}}$ based on eq. (4.92) (in analogy to the equivalent von Mises stress) shall be analysed, as illustrated in Figure 4.17. Overall, the results show a symmetric distribution of $\bar{\varepsilon}^{\text{inel}}$ with respect to the loading path.
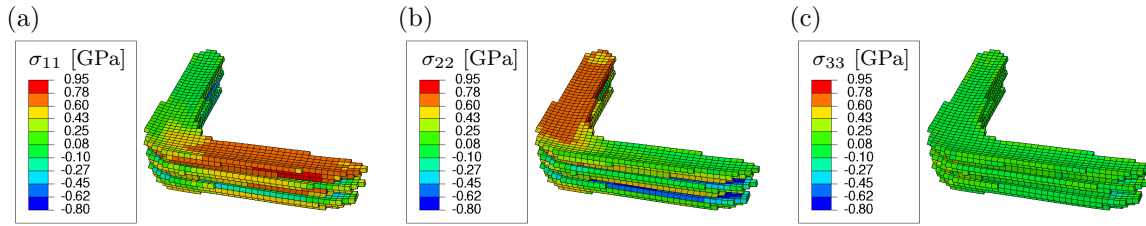
85

Figure 4.16: Distribution of normal stresses $\sigma_{\bullet\bullet}$ of the virtually extracted final re-solidified part in (4.16a) x_1-direction, (4.16b) x_2-direction and (4.16c) x_3-direction. Reprinted from [131] under the terms of the Creative Commons Attribution License (CC BY).
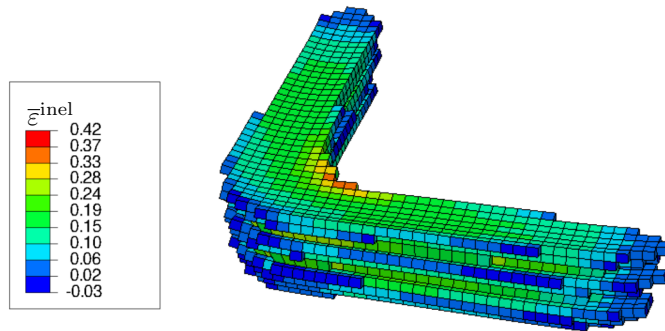

Figure 4.17: Equivalent inelastic strain $\overline{\varepsilon}^{\mathrm{inel}}$ (analogous to von Mises stress) of the virtually extracted final re-solidified part. Reprinted from [131] under the terms of the Creative Commons Attribution License (CC BY).

This coincides with the inherent strain method, where the orientation of the laser beam path is of utmost importance, cf. [82]. In summary, the values of strains and stresses themselves significantly change with respect to the loading path, but correlate to one another when taking into account the movement of the laser beam. This information may be incorporated in a phenomenological model by using an averaged inherent strain tensor.

B Appendix

B.1 Determination of mechanical working

For the specific case at hand the mechanical dissipation $\mathcal{D}_{\text{mech}}$ is defined via eq. (2.59) and the thermodynamic consistent driving force $\mathcal{F} = -\partial_{\mathcal{V}} \overline{\psi}$ for the phase transformation approach, compare Remark 7. With the internal variables $\mathcal{V}$ as introduced in eq. (4.37), the mechanical dissipation reads

$$\mathcal{D}_{\text{mech}} = -\frac{\partial \overline{\psi}}{\partial \xi_{\text{mel}}} \dot{\xi}_{\text{mel}} + \zeta_{\text{mel}} \, \boldsymbol{\sigma} : \dot{\boldsymbol{\varepsilon}}_{\text{mel}}^{\text{ve}} - \frac{\partial \overline{\psi}}{\partial \xi_{\text{sol}}} \dot{\xi}_{\text{sol}} + \zeta_{\text{sol}} \, \boldsymbol{\sigma} : \dot{\boldsymbol{\varepsilon}}_{\text{sol}}^{\text{mech}} - \frac{\partial \overline{\psi}}{\partial k_{\text{sol}}^{\text{hard}}} \, \dot{k}_{\text{sol}}^{\text{hard}} \,, \tag{4.93}$$

where the driving forces stemming from viscous strains, compare eq. (4.50), and from plastic strains based on eq. (4.55) are already incorporated. The specific derivatives of the averaged energy density can be further determined as

$$\frac{\partial \overline{\psi}}{\partial \xi_{\text{mel}}} = -\frac{\rho_{\text{mel}}}{\rho_{\text{pow}}} \psi_{\text{pow}} + \xi_{\text{pow}} \frac{\partial \psi_{\text{pow}}}{\partial \boldsymbol{\varepsilon}_{\text{pow}}} : \frac{\partial \boldsymbol{\varepsilon}_{\text{pow}}}{\partial \xi_{\text{mel}}}$$
$$+ \psi_{\text{mel}} + \xi_{\text{mel}} \frac{\partial \psi_{\text{mel}}}{\partial \boldsymbol{\varepsilon}_{\text{mel}}} : \frac{\partial \boldsymbol{\varepsilon}_{\text{mel}}}{\partial \xi_{\text{mel}}} + \xi_{\text{sol}} \frac{\partial \psi_{\text{sol}}}{\partial \boldsymbol{\varepsilon}_{\text{sol}}} : \frac{\partial \boldsymbol{\varepsilon}_{\text{sol}}}{\partial \xi_{\text{mel}}} \tag{4.94}$$

$$\frac{\partial \overline{\psi}}{\partial \xi_{\text{sol}}} = -\frac{\rho_{\text{sol}}}{\rho_{\text{pow}}} \psi_{\text{pow}} + \xi_{\text{pow}} \frac{\partial \psi_{\text{pow}}}{\partial \boldsymbol{\varepsilon}_{\text{pow}}} : \frac{\partial \boldsymbol{\varepsilon}_{\text{pow}}}{\partial \xi_{\text{sol}}}$$
$$+ \xi_{\text{mel}} \frac{\partial \psi_{\text{mel}}}{\partial \boldsymbol{\varepsilon}_{\text{mel}}} : \frac{\partial \boldsymbol{\varepsilon}_{\text{mel}}}{\partial \xi_{\text{sol}}} + \psi_{\text{sol}} + \xi_{\text{sol}} \frac{\partial \psi_{\text{sol}}}{\partial \boldsymbol{\varepsilon}_{\text{sol}}} : \frac{\partial \boldsymbol{\varepsilon}_{\text{sol}}}{\partial \xi_{\text{sol}}} \tag{4.95}$$

$$\frac{\partial \overline{\psi}}{\partial k_{\text{sol}}^{\text{hard}}} = \xi_{\text{sol}} \, H_{\text{sol}} \, k_{\text{sol}}^{\text{hard}} \,. \tag{4.96}$$

The remaining derivatives are not further specified, but follow from the partial derivatives of the energies, introduced in eqs. (4.3, 4.5, 4.7) and the partial derivatives of the optimal strains as defined in eqs. (4.26) to (4.28) in a straightforward manner.

In addition, the partial derivative of the mechanical dissipation with respect to the temperature follows from eq. (4.93) as

$$\frac{\partial \mathcal{D}_{\text{mech}}}{\partial \theta} = \zeta_{\text{sol}} \frac{\partial \boldsymbol{\sigma}}{\partial \theta} : \dot{\boldsymbol{\varepsilon}}_{\text{sol}}^{\text{mech}} + \zeta_{\text{mel}} \frac{\partial \boldsymbol{\sigma}}{\partial \theta} : \dot{\boldsymbol{\varepsilon}}_{\text{mel}}^{\text{ve}} - \frac{\partial \overline{\psi}}{\partial \xi_{\text{mel}} \partial \theta} \dot{\xi}_{\text{mel}} - \frac{\partial \overline{\psi}}{\partial \xi_{\text{sol}} \partial \theta} \dot{\xi}_{\text{sol}} \,, \tag{4.97}$$

where $-\dfrac{\partial \overline{\psi}}{\partial k_{\mathrm{sol}}^{\mathrm{hard}}\, \partial \theta} = 0$. Finally, the partial derivative of the stress with respect to the temperature reads

$$\frac{\partial \boldsymbol{\sigma}}{\partial \theta} = \frac{\mathrm{d}m_0}{\mathrm{d}V_0}\, \widetilde{\mathbf{E}}^{\,-1} : [\mathbf{E}_{\mathrm{pow}} : \mathbf{E}_{\mathrm{mel}} : \mathbf{E}_{\mathrm{sol}}] : [-\zeta_{\mathrm{sol}}\, \alpha_{\mathrm{sol}}\, \boldsymbol{I}]\ . \tag{4.98}$$

With this, all parts of the mechanical work r_{mech} as defined in eq. (2.62) are now specified.

B.2 Derivation of consistent tangent

To determine the consistently linearised Jacobian for the global Newton-Raphson of the FE framework, compare eq. (2.76), the total derivatives of the stress $\boldsymbol{\sigma}$, as defined in eq. (4.31), and the mechanical working r_{mech}, as specified in Appendix B.1, have to be determined. These read

$$\mathrm{d}\boldsymbol{\sigma} = \frac{\partial \boldsymbol{\sigma}}{\partial \theta}\, \mathrm{d}\theta + \frac{\partial \boldsymbol{\sigma}}{\partial \boldsymbol{\varepsilon}} : \mathrm{d}\boldsymbol{\varepsilon} + \frac{\partial \boldsymbol{\sigma}}{\partial \mathbf{f}} \bullet \mathrm{d}\mathbf{f} \tag{4.99}$$

$$\mathrm{d}r_{\mathrm{mech}} = \frac{\partial r_{\mathrm{mech}}}{\partial \theta}\, \mathrm{d}\theta + \frac{\partial r_{\mathrm{mech}}}{\partial \boldsymbol{\varepsilon}} : \mathrm{d}\boldsymbol{\varepsilon} + \frac{\partial r_{\mathrm{mech}}}{\partial \mathbf{f}} \bullet \mathrm{d}\mathbf{f}\ , \tag{4.100}$$

where $\mathbf{f}$ refers to all unknown variables of the minimisation as defined in eq. (4.83). For the consistent tangent moduli, the total derivatives with respect to strain $\boldsymbol{\varepsilon}$ at constant temperature θ as well as with respect to temperature θ at constant strain $\boldsymbol{\varepsilon}$ have to be determined for the stress

$$\mathrm{d}\boldsymbol{\sigma}\Big|_{\theta=\mathrm{const}} = \frac{\partial \boldsymbol{\sigma}}{\partial \boldsymbol{\varepsilon}} : \mathrm{d}\boldsymbol{\varepsilon} + \frac{\partial \boldsymbol{\sigma}}{\partial \mathbf{f}} \bullet \mathrm{d}\mathbf{f} = \mathbf{E}_{\mathrm{algo}} : \mathrm{d}\boldsymbol{\varepsilon}$$

$$\Leftrightarrow \quad \mathbf{E}_{\mathrm{algo}} = \frac{\mathrm{d}\boldsymbol{\sigma}}{\mathrm{d}\boldsymbol{\varepsilon}}\Big|_{\theta=\mathrm{const}}, \tag{4.101}$$

$$\mathrm{d}\boldsymbol{\sigma}\Big|_{\boldsymbol{\varepsilon}=\mathrm{const}} = \frac{\partial \boldsymbol{\sigma}}{\partial \theta}\, \mathrm{d}\theta + \frac{\partial \boldsymbol{\sigma}}{\partial \mathbf{f}} \bullet \mathrm{d}\mathbf{f} = \boldsymbol{\beta}_{\mathrm{algo}}\, \mathrm{d}\theta$$

$$\Leftrightarrow \quad \boldsymbol{\beta}_{\mathrm{algo}} = \frac{\mathrm{d}\boldsymbol{\sigma}}{\mathrm{d}\theta}\Big|_{\boldsymbol{\varepsilon}=\mathrm{const}}, \tag{4.102}$$

and analogously for the mechanical coupling term

$$\mathrm{d}r_{\mathrm{mech}}\Big|_{\theta=\mathrm{const}} = \frac{\partial r_{\mathrm{mech}}}{\partial \boldsymbol{\varepsilon}} : \mathrm{d}\boldsymbol{\varepsilon} + \frac{\partial r_{\mathrm{mech}}}{\partial \mathbf{f}} \bullet \mathrm{d}\mathbf{f} = \boldsymbol{\gamma}_{\mathrm{algo}} : \mathrm{d}\boldsymbol{\varepsilon}$$

$$\Leftrightarrow \quad \boldsymbol{\gamma}_{\mathrm{algo}} = \frac{\mathrm{d}r_{\mathrm{mech}}}{\mathrm{d}\boldsymbol{\varepsilon}}\Big|_{\theta=\mathrm{const}}, \tag{4.103}$$

$$\mathrm{d}r_{\mathrm{mech}}\Big|_{\boldsymbol{\varepsilon}=\mathrm{const}} = \frac{\partial r_{\mathrm{mech}}}{\partial \theta}\, \mathrm{d}\theta + \frac{\partial r_{\mathrm{mech}}}{\partial \mathbf{f}} \bullet \mathrm{d}\mathbf{f} = \delta_{\mathrm{algo}}\, \mathrm{d}\theta$$

$$\Leftrightarrow \quad \delta_{\mathrm{algo}} = \frac{\mathrm{d}r_{\mathrm{mech}}}{\mathrm{d}\theta}\Big|_{\boldsymbol{\varepsilon}=\mathrm{const}}. \tag{4.104}$$

Comparing the abbreviations with Table 2.1, eq. (4.101) is always necessary and refers to `DDSDDE`, while the remaining contributions are only necessary for a thermomechanical problem. Thereby, eq. (4.102) corresponds to `DDSDDT`, eq. (4.103) denotes `DRPLDE` and eq. (4.104) specifies `DRPLDT`.

The linearisation of the local problem, compare eqs. (4.73) to (4.82), is used to find a relation between $\mathrm{d}\mathbf{f}$ and $\mathrm{d}\boldsymbol{\varepsilon}$ and $\mathrm{d}\mathbf{f}$ and $\mathrm{d}\theta$, respectively, which results in

$$
\mathrm{d}\mathbf{r}\Big|_{\boldsymbol{\varepsilon}=\mathrm{const}} = \frac{\partial \mathbf{r}}{\partial \theta}\,\mathrm{d}\theta + \frac{\partial \mathbf{r}}{\partial \mathbf{f}} \bullet \mathrm{d}\mathbf{f} = \mathbf{0}
$$

$$
\Leftrightarrow \quad \mathrm{d}\mathbf{f}\Big|_{\boldsymbol{\varepsilon}=\mathrm{const}} = -\mathbf{J}^{-1} \cdot \frac{\partial \mathbf{r}}{\partial \theta}\,\mathrm{d}\theta \; , \tag{4.105}
$$

$$
\mathrm{d}\mathbf{r}\Big|_{\theta=\mathrm{const}} = \frac{\partial \mathbf{r}}{\partial \boldsymbol{\varepsilon}} : \mathrm{d}\boldsymbol{\varepsilon} + \frac{\partial \mathbf{r}}{\partial \mathbf{f}} \bullet \mathrm{d}\mathbf{f} = \mathbf{0}
$$

$$
\Leftrightarrow \quad \mathrm{d}\mathbf{f}\Big|_{\theta=\mathrm{const}} = -\mathbf{J}^{-1} \cdot \frac{\partial \mathbf{r}}{\partial \boldsymbol{\varepsilon}} : \mathrm{d}\boldsymbol{\varepsilon} \; , \tag{4.106}
$$

where $\mathbf{J} = \dfrac{\partial \mathbf{r}}{\partial \mathbf{f}}$ refers to the Jacobian of the local Netwon-Raphson scheme. Insert expression (4.105) into eqs. (4.101) and (4.103) and, respectively, eq. (4.106) into eqs. (4.102) and (4.104). Then, all unknowns of the four tangent moduli are determined, which read

$$
\mathbf{E}_{\mathrm{algo}} = \frac{\partial \boldsymbol{\sigma}}{\partial \boldsymbol{\varepsilon}} - \frac{\partial \boldsymbol{\sigma}}{\partial \mathbf{f}} \cdot \mathbf{J}^{-1} \cdot \frac{\partial \mathbf{r}}{\partial \boldsymbol{\varepsilon}} \; , \tag{4.107}
$$

$$
\boldsymbol{\beta}_{\mathrm{algo}} = \frac{\partial \boldsymbol{\sigma}}{\partial \theta} - \frac{\partial \boldsymbol{\sigma}}{\partial \mathbf{f}} \cdot \mathbf{J}^{-1} \cdot \frac{\partial \mathbf{r}}{\partial \theta} \; , \tag{4.108}
$$

$$
\boldsymbol{\gamma}_{\mathrm{algo}} = \frac{\partial r_{\mathrm{mech}}}{\partial \boldsymbol{\varepsilon}} - \frac{\partial r_{\mathrm{mech}}}{\partial \mathbf{f}} \cdot \mathbf{J}^{-1} \cdot \frac{\partial \mathbf{r}}{\partial \boldsymbol{\varepsilon}} \; , \tag{4.109}
$$

$$
\delta_{\mathrm{algo}} = \frac{\partial r_{\mathrm{mech}}}{\partial \theta} - \frac{\partial r_{\mathrm{mech}}}{\partial \mathbf{f}} \cdot \mathbf{J}^{-1} \cdot \frac{\partial \mathbf{r}}{\partial \theta} \; . \tag{4.110}
$$

Looking at eqs. (4.107) to (4.110), the derivatives with respect to the set of local internal variables $\mathbf{f}$ still have to be defined, as well as the derivatives regarding the local residuum $\mathbf{r}$. In contrast, the local Jacobian $\mathbf{J}$ is already specified when solving the local algorithm. Altogether, solely various partial derivatives are required using standard calculus methods to evaluate the given expressions of the tangent moduli.

B.3 Influence of using a thermomechanical setting

Based on the thermomechancial setting, the maximum temperature θ^{max} clearly changes, as summarised in Table 4.2. The difference in temperature based on the thermal boundary conditions, q_{conv} in eq. (4.65) and q_{rad} based on eq. (4.66), are minor. When comparing the temperature evolution for various thermal boundary conditions, no visible difference can be seen. Thus, the temperature evolution is mainly influenced by the heat flux model of the laser beam. In contrast, incorporating r^{mech} based on eq. (2.62)

is quite important for an LPBF model, i.e. using a thermodynamic consistent model highly influences the maximal temperature. Especially the effects with regard to the phase transformation make a considerable difference. For example, the incorporation of the latent heat in ψ_{pow} and ψ_{sol} mainly changes the maximal arising temperature. In addition, the latent heat terms also change the magnitude of heat conduction and the cooling speed.

Table 4.2: Influence on maximal temperature θ^{max} within the molten pool of first layer based on thermomechanical setting.

thermomechanical setting		max. temperature
r^{mech}	$q_{\mathrm{conv,rad}}$	θ^{max}
$= 0$	$= 0$	3176
$= 0$	$\neq 0$	3166
$\neq 0$	$= 0$	2927
$\neq 0$	$\neq 0$	2924

Overall, the melt pool geometry changes with the different temperature evolution as shown in Figure 4.18. This can be explained by a larger molten pool due to overall higher temperatures. In consequence, the part without mechanical working is slightly larger compared to the thermodynamic consistent model (approximately two elements in length and width, same depth). This influences different modelling assumptions such as hatching strategy and layer height. Furthermore, the size of the final part may slightly change. Therefore, using a thermodynamic consistent model and incorporating r^{mech} improves the accuracy of predicted simulation results.
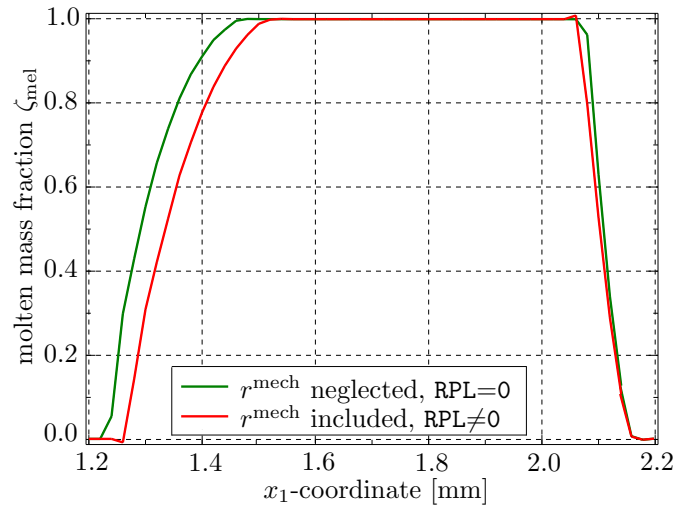
Figure 4.18: Influence on melt pool size in x_1-direction based on mechanical working r^{mech}, corresponding to RPL in Abaqus, for molten mass fraction ζ_{mel}.

5 A multiscale framework using the inherent strain method

For the broader industrial usage of metal additive manufactured parts, especially made by LPBF, a better prediction and understanding of the warpage and of eigenstresses within the final part are necessary. Due to the diverse and sophisticated metallurgical and thermal processes during production as explained in Section 1.1.1, the physically motivated simulations introduced in Chapter 3 and, based on this, Chapter 4 are rather complex and time consuming. Therefore, various simplifications concerning the process and material model are frequently made to develop reliable and useful models of large parts. This leads to practicable simulation times at the expense of physical accuracy. However, especially the material and heat source models influence the simulation results. If accurate predictions of residual stresses and deformation are desired, both complete temperature history and mechanical behaviour have to be included in a thermomechanical model. This motivates the procedure in this contribution: A multiscale approach combining various modelling levels, in particular regarding the heat source and the material model. Therefore, a simulation technique is developed to simulate complex parts in an efficient and precise manner by using the finite element (FE) method. By doing so, an acceptable computation time is ensured while having a physically sound model.

A detailed overview of the multiscale framework is given in Section 5.1. The model is based on three FE simulations on different levels and with distinct specific aims, i.e. the laser scan model in Section 5.1.1, the layer hatch model in Section 5.1.2 and the part model in Section 5.1.3. In Section 5.2, the implementation of the aforementioned models into Abaqus is presented. In addition, the extraction of the transfer parameters between the distinct scales is defined. Different simulation results are examined for the specific model scales in Section 5.3, demonstrating the influence of process parameters and scan patterns. Moreover, the capabilities of the present framework are investigated by simulations on the behaviour of a twin cantilever beam. The effects of the different process parameters on the overall material and on the structural response in terms of eigenstress evolution and deformation are examined.

5.1 Methodology of the multiscale framework

This section provides detailed information on the methodology of the employed multiscale framework which is based on, cf. [81, 82, 99]. In the current contribution, a thermodynamically fully coupled framework is presented which is based on the thermo-mechanical balance equations introduced in Chapter 2. The multiscale approach combines three separate FE simulations, namely with respect to the laser scan model, the layer hatch model and the part model. Thereby, the established approach is enhanced in terms of a micromechanically motivated material model of the laser scan model leading to improved inherent strains (IS) of the layer hatch model and elevated predictions of the complete part. In Figure 5.1, an illustration of the multiscale approach with the three models, i.e. the laser scan model (microscale), the layer hatch model (mesoscale) and the part model (macroscale), is visualised; see also Remark 9 in view of the determination of the respective levels of analysis. First, some general remarks are made, before the distinct models shall be introduced in detail in what follows, i.e. Sections 5.1.1 to 5.1.3, respectively.
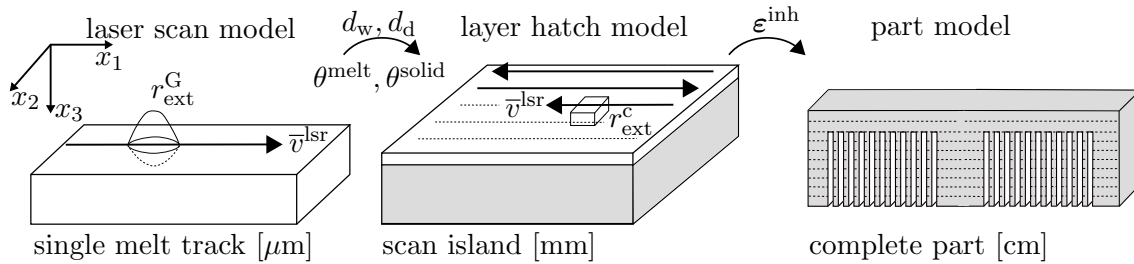
Figure 5.1: Visualisation of the three different levels (with respective dimension) considered in the multiscale approach, where the melt pool dimensions $d_{\mathrm{w}}, d_{\mathrm{d}}$, temperatures $\theta^{\mathrm{melt}}, \theta^{\mathrm{solid}}$ and the inherent strain $\varepsilon^{\mathrm{inh}}$ are passed from one level to the other. White structures are initially made of powder, grey body consists of solid material. Reprinted from [129] under the terms of the Creative Commons Attribution License (CC BY).

Remark 9. *In view of multiscale modelling frameworks for additive manufacturing processes, the terms microscale, mesoscale and macroscale are also used to indicate different model levels. Thereby, these denominations are used according to the level of analysis, see e.g. [6, 63, 81, 82, 99, 120, 179], which is in contrast to the understanding of the denomination micro, meso and macro in the context of, e.g. classic solid-state physics. The microscale then refers to the modelling and simulation of a single melt track, the mesoscale addresses the scan island, and the macroscale deals with the complete part. To be mentioned here is that a clear scale separation which is required in, e.g. standard homogenisation schemes, is not given in this context, cf. Table 5.1. In order to avoid any misunderstanding and confusion of denominations used in different communities, the terms micro, meso and macro are not used in a multiscale context in the present work, but direct reference to the respective level of analysis is made.*

For the smallest scale considered, a material model based on the sophisticated thermo-dynamically fully coupled model introduced in Chapter 4 is incorporated. A volumetric Goldak heat source $r_{\mathrm{ext}}^{\mathrm{G}}$ is used to model the laser beam, compare Figure 5.1, left side. The goal of this detailed simulation is to extract and calibrate an effective model of the heat source based on a physically sound material model. This can then be applied to the next level of simulation, i.e. the layer hatch model. Overall, the simulation of the laser scan model has to be conducted once for all considered combinations of material and process parameters.

The purpose of the layer hatch model, where a single scan island is simulated, is to extract the so-called inherent strains $\varepsilon^{\mathrm{inh}}$, which can then be transferred to the part model. A simplified constitutive model is used, where the critical phase transformation temperatures θ^{melt} and θ^{solid} are extracted from the simulation results of the single melt track. These temperatures directly impact the present phase of the layer hatch model, as no phase transformation framework is used. The heat input is approximated by a cuboid heat source $r_{\mathrm{ext}}^{\mathrm{c}}$ as visualised in Figure 5.1, middle. The simulations of the scan island can be defined for different process parameters, as well as layer heights and scan island sizes.

The inherent strains (IS) are then used to finally specify the part model, which uses a simpler purely mechanical simulation to efficiently and directly compute the residual stresses and deformations of arbitrary large parts. This approach is illustrated in Figure 5.1, right side. Here, no differentiation between any specific phases is conducted. The same IS can be used for identical material and laser parameters, regardless of the complexity of the complete part. Different scan patterns can be examined by using the same IS.

Altogether, the multiscale framework allows the establishment of a simulation where all significant details of the LPBF process are included. An accurate modelling approach of the laser scan model is necessary, as related simulation results directly influence the layer hatch model and thus also indirectly affect the part model. In view of the response at the larger scales considered, some simplifications are necessary in order to reduce computational costs, while still obtaining appropriate results. Overall, a model ansatz with an accurate simulation on the different levels is established. The characteristics at distinct levels, respectively of the underlying models, are summarised in Table 5.1. By using these models, a simulation of a complex macroscopic part manufactured by LPBF processes is enabled, while the computation time is kept within reasonable bounds.

5.1.1 Laser scan model – single melt track

As the results of the single melt track are relevant for both other modelling levels and therefore influence the overall results, it is required to model the formation of the single melt track as accurately as possible and take into account the various physical processes. Therefore, an elaborated and micromechanically motivated material model is used to examine the melting and solidification process during the LPBF process in detail. The

Table 5.1: Comparison of the main characteristics of the three different models considered in the present multiscale approach.

Characteristic	Laser scan model	Layer hatch model	Part model
Domain	single melt track	scan island	complete part
Scale	μm	mm	cm
FEM	thermomechanical	thermomechanical	mechanical
Load	volumetric Goldak heat source	cuboid heat source	inherent strains
Material model	phase transformation	temperature-dependent	elastic
Material state	powder, melt, solid	powder, melt, solid	solid
Aim	calibrate heat source	extract inherent strains	calculate eigenstresses and warpage

thermodynamic consistent and coupled material model for the laser scan model is based on the phase transformation algorithm presented in Chapter 4. Thus, the mechanical material model explicitly incorporates the three phases, namely the powder, the molten, and the re-solidified material, where the phase transformation is defined via a homogenisation approach and explicit evolution equations. In addition, a volumetric Goldak heat source similar to the one discussed in Section 3.2.3 is applied as external heat supply $r_{\text{ext}}^{\text{G}}$ to model the laser beam. The aim of the model is to calibrate the geometric parameters of the Goldak heat source corresponding to the laser beam heat input via experiments, so that the melt pool geometry of the simulation coincides with the one of experiments. Within the heat source resembling the laser beam, the process parameters laser velocity $\overline{v}^{\text{lsr}}$ and laser power P are included. This approach is visualised in Figure 5.1, left side.

With these simulation results, both melting and re-solidifying temperature, θ^{melt} and θ^{solid}, respectively, can be identified and extracted for the temperature-dependent material model of the next scale. In addition, the melt pool dimensions d_{w}^{G} and d_{d}^{G}, referring to the width and depth of the melt pool, are determined. These can then be passed to the layer hatch model as parameters of the cuboid heat source $r_{\text{ext}}^{\text{c}}$. The two modelling assumptions for the material model and the laser beam model will be described in detail in what follows. It is noted that the model performs properly for the conduction mode only, i.e. keyhole modes cannot be predicted correctly, see also Remark 10.

Remark 10. *For LPBF processes it is essential to choose correct process parameters, which have to lie within an appropriate processing window. This results in a continuous melt pool, an even surface and little porosity, see for example [43, 61, 77]. Outside the suitable range, either incomplete melting due to lack of fusion, also denoted as balling, or overheating based on the keyhole mode is present. The model at hand is capable of predicting non-continuous melt pools, cf. the results in Section 5.3, specifically Figure 5.14.*

However, the keyhole mode, where material vaporises and thus a high recoil pressure is present, cannot be modelled with the framework at hand. The keyhole mechanism leads to high penetration depths within the material as visualised in e.g. [43]. The focus of this work lies on the modelling of the complete part. There are various established models that focus on melt pool dynamics and the development of a keyhole in small scale simulations, e.g. [31, 118, 138, 186], but which do not include predictions of eigenstresses or of the final deformation of a complete part.

Constitutive framework

In what follows, only differences to the phase transformation approach introduced in Section 4.1 shall be discussed. For the laser scan model, the initial density ρ_0 always corresponds to the density of the powder phase ρ_{pow}. In contrast to Section 4.1.1, where a rate-independent plasticity approach is used, a visco-plastic material behaviour is chosen. On the one hand, a creep behaviour, i.e. a material behaviour strongly dependent on strain rates, can be observed for metals at high temperatures. This justifies the use of visco-plasticity for the solid phase, as the temperatures are elevated directly after the phase transformation. On the other hand, a viscous approach regularises and stabilises the framework, such that from a computational viewpoint larger time steps are possible compared to using rate-independent plasticity, see for example [161]. More complex material models for visco-plasticity may be implemented in the future, see for example [57, 133] and the references cited therein, where a combination of visco-plastic and rate-independent plastic material behaviour is used in dependence of the underlying temperature. For the current framework, a visco-plastic strain contribution $\boldsymbol{\varepsilon}_{\mathrm{sol}}^{\mathrm{vp}}$ is present resulting in the definition of the inelastic strains of the solid phase as

$$\boldsymbol{\varepsilon}_{\mathrm{sol}}^{\mathrm{inel}} = \boldsymbol{\varepsilon}_{\mathrm{sol}}^{\mathrm{trans}} + \boldsymbol{\varepsilon}_{\mathrm{sol}}^{\mathrm{vp}} + \boldsymbol{\varepsilon}_{\mathrm{sol}}^{\mathrm{th}} \; . \tag{5.1}$$

The rate-dependent evolution of the visco-plastic strains $\boldsymbol{\varepsilon}_{\mathrm{sol}}^{\mathrm{vp}}$, as well as of the quantity $k_{\mathrm{sol}}^{\mathrm{hard}}$ which is related to isotropic hardening can be defined with the help of the yield function Φ and the Lagrange multiplier

$$\Delta\lambda := \Delta t \, \frac{\langle \Phi \rangle}{\eta_{\mathrm{sol}}^{\mathrm{vp}}} \; , \tag{5.2}$$

where Δt refers to the time increment and where $\eta_{\mathrm{sol}}^{\mathrm{vp}}$ corresponds to the viscosity related material constant of the solid phase, such that

$$\dot{\boldsymbol{\varepsilon}}_{\mathrm{sol}}^{\mathrm{vp}} := \Delta\lambda \, \frac{\partial \Phi}{\partial \mathcal{F}_{\mathrm{loc}}^{\mathrm{vp}}} \; , \tag{5.3}$$

$$\dot{k}_{\mathrm{sol}}^{\mathrm{hard}} := \Delta\lambda \, \frac{\partial \Phi}{\partial \kappa_{\mathrm{loc}}} \; . \tag{5.4}$$

Here, $\langle \bullet \rangle$ denotes the Macaulay ramp function of the quantity $\bullet$ defined as $\langle \bullet \rangle = \max\{0, \bullet\} = [\bullet + |\bullet|]/2$. The quantities $\mathcal{F}_{\text{loc}}^{\text{vp}} = \boldsymbol{\sigma}$ and $\kappa_{\text{loc}} = -\frac{\xi_{\text{sol}}}{\zeta_{\text{sol}}} H_{\text{sol}} k_{\text{sol}}^{\text{hard}}$ correspond to the respective local driving forces. The ansatz used in eq. (5.3) is also referred to as Perzyna-type visco-plasticity. For the material model at hand, a standard isotropic yield function as defined in eq. (4.59) of the type

$$\Phi := \left\| \mathcal{F}_{\text{loc,dev}}^{\text{vp}} \right\| - \sqrt{\frac{2}{3}} \left[\sigma_{\text{sol}}^{\text{y}} - \kappa_{\text{loc}} \right] = \left\| \boldsymbol{\sigma}_{\text{dev}} \right\| - \sqrt{\frac{2}{3}} \left[\sigma_{\text{sol}}^{\text{y}} + \frac{\xi_{\text{sol}}}{\zeta_{\text{sol}}} H_{\text{sol}} k_{\text{sol}}^{\text{hard}} \right] \tag{5.5}$$

is chosen, where $\sigma_{\text{sol}}^{\text{y}}$ refers to the (so far temperature-independent and constant) yield stress, H_{sol} is the hardening modulus and $k_{\text{sol}}^{\text{hard}}$ denotes the equivalent plastic strain due to isotropic hardening of the solid phase. The abbreviation $\bullet_{\text{dev}} := \bullet - \text{tr}(\bullet)/3\,\boldsymbol{I}$ defines the deviator of the second order tensor $\bullet$. The additional factor scaling the isotropic hardening related contribution results from the local driving force κ_{loc}, as introduced in detail in Section 4.1.4. Due to the homogenisation framework, local driving forces have to be defined, which only consider the current region of the respective phase in contrast to the whole domain, such that $\mathcal{F}_{\text{loc}}^{\bullet} = \mathcal{F}^{\bullet}/\zeta^{\bullet}$.

In consequence, the advanced set of state variables of the present model is determined as $\mathcal{V} = \{\boldsymbol{\varepsilon}_{\text{mel}}^{\text{ve}}, \boldsymbol{\varepsilon}_{\text{sol}}^{\text{vp}}, k_{\text{sol}}^{\text{hard}}, \xi_{\text{pow}}, \xi_{\text{mel}}, \xi_{\text{sol}}\}$. Consequently, the mechanical dissipation introduced in eq. (2.62) can now be specified for the underlying material model to

$$\mathcal{D}_{\text{mech}} = -\frac{\partial \overline{\psi}}{\partial \xi_{\text{mel}}} \dot{\xi}_{\text{mel}} - \frac{\partial \overline{\psi}}{\partial \xi_{\text{sol}}} \dot{\xi}_{\text{sol}} + \mathcal{F}^{\text{ve}} : \dot{\boldsymbol{\varepsilon}}_{\text{mel}}^{\text{ve}} + \mathcal{F}^{\text{vp}} : \dot{\boldsymbol{\varepsilon}}_{\text{sol}}^{\text{vp}} + \kappa\, \dot{k}_{\text{sol}}^{\text{hard}}\,, \tag{5.6}$$

where the standard (total) driving forces $\mathcal{F}$ are required, cf. Remark 7.

One key advantage of the present modelling framework is exemplified by the fact that the process-induced inherent strains can be obtained in a straightforward manner via post-processing. Based on the inelastic strain contributions defined above, the inherent strain tensor $\boldsymbol{\varepsilon}^{\text{inh}}$ is, analogously to the accumulated inelastic strain in eq. (4.92), defined by

$$\boldsymbol{\varepsilon}^{\text{inh}} = \zeta_{\text{mel}} \left[\boldsymbol{\varepsilon}_{\text{mel}}^{\text{trans}} + \boldsymbol{\varepsilon}_{\text{mel}}^{\text{ve}} \right] + \zeta_{\text{sol}} \left[\boldsymbol{\varepsilon}_{\text{sol}}^{\text{trans}} + \boldsymbol{\varepsilon}_{\text{sol}}^{\text{th}} + \boldsymbol{\varepsilon}_{\text{sol}}^{\text{vp}} \right]\,. \tag{5.7}$$

Volumetric heat source

The present laser beam model is also based on a Gaussian distributed volumetric heat source introduced in [60] for welding simulations. However, compared to Section 3.2.3, a higher intensity is used, i.e. 95 % of the total energy lies within the maximum radius spot (concentration coefficient equals three). This modelling approach is more established in literature compared to the one presented in the previous chapter, namely Section 3.2.3. In addition, a double ellipsoidal volumetric heat source is used to better model the laser beam heat input $r_{\text{ext}}^{\text{G}}$. Therefore, some differences to the previous laser beam model are present.

In general, the temperature gradients related to the laser beam are not symmetric with respect to the current laser path. Thus, for the distribution in front of the laser beam r_f an ellipsoid different to the one for the rear dispersion r_r is chosen. Furthermore, an absorption coefficient η_ab is introduced to take into account the efficiency during the laser beam input. The heat input is thus defined as

$$r_\mathrm{f}(x_1', x_2', x_3') = \frac{6\sqrt{3}\,\eta_\mathrm{ab}\,P\,f_\mathrm{f}}{a_\mathrm{f}\,b\,c\,\pi\sqrt{\pi}} \exp\left(-3\left[\frac{x_1'^{\,2}}{a_\mathrm{f}^2} + \frac{x_2'^{\,2}}{b^2} + \frac{x_3'^{\,2}}{c^2}\right]\right)\,, \tag{5.8}$$

$$r_\mathrm{r}(x_1', x_2', x_3') = \frac{6\sqrt{3}\,\eta_\mathrm{ab}\,P\,f_\mathrm{r}}{a_\mathrm{r}\,b\,c\,\pi\sqrt{\pi}} \exp\left(-3\left[\frac{x_1'^{\,2}}{a_\mathrm{r}^2} + \frac{x_2'^{\,2}}{b^2} + \frac{x_3'^{\,2}}{c^2}\right]\right)\,, \tag{5.9}$$

where the total heat input is then determined via

$$r_\mathrm{ext}^\mathrm{G} = r_\mathrm{r} + r_\mathrm{f}\,. \tag{5.10}$$

To model this ellipsoid, the heat fractions f_f and f_r in front and rear of the centre, respectively, are determined as

$$f_\mathrm{f} = 2\,\frac{a_\mathrm{f}}{a_\mathrm{f} + a_\mathrm{r}}\,, \tag{5.11}$$

$$f_\mathrm{r} = 2 - f_\mathrm{f}\,. \tag{5.12}$$

Furthermore, the geometrical parameters $a_\mathrm{f}, a_\mathrm{r}, b, c$ affect the semi-axes of the ellipsoid as visualised in Figure 5.2, whereas P denotes the power of the laser beam and x_1', x_2', x_3' refer to the moving coordinate system, which depends on laser velocity $\overline{v}^\mathrm{lsr}$ and time t. The coordinates $x_i' = 0$ (with $i = 1, 2, 3$) define the centre of the laser beam. With the help of the coordinate x_1', the laser beam movement in x_1-direction can be defined based on the laser velocity $\overline{v}^\mathrm{lsr}$, time t and initial position x_{01} of the laser beam, such that $x_1' = x_1 - \overline{v}^\mathrm{lsr}\,t - x_{01}$ is valid for the single melt track considered here. Furthermore, the relations $x_2' = x_2$ and $x_3' = x_3$ apply for this case, as the laser beam moves only along the x_1-direction.

The dissipative quantity η^ξ in $\mathcal{C}^\eta$, which is formally introduced for the first time in eq. (4.43), can be fitted with experiments, so that the melt pool geometry in the simulation corresponds to the one observed in experiments.

5.1.2 Layer hatch model – scan island

In general, a standard size of a scan island simulation is between 1-5 mm, cf. [36, 82, 142] and [5, 112, 177], where the effect of different island sizes and scan strategies has experimentally been investigated in the latter contributions. A complete layer is made of continuous, see e.g. [158], or multiple island scans, where adjacent layers are rotated, cf. [57]. Further and more complex scan strategies are also examined in the literature,
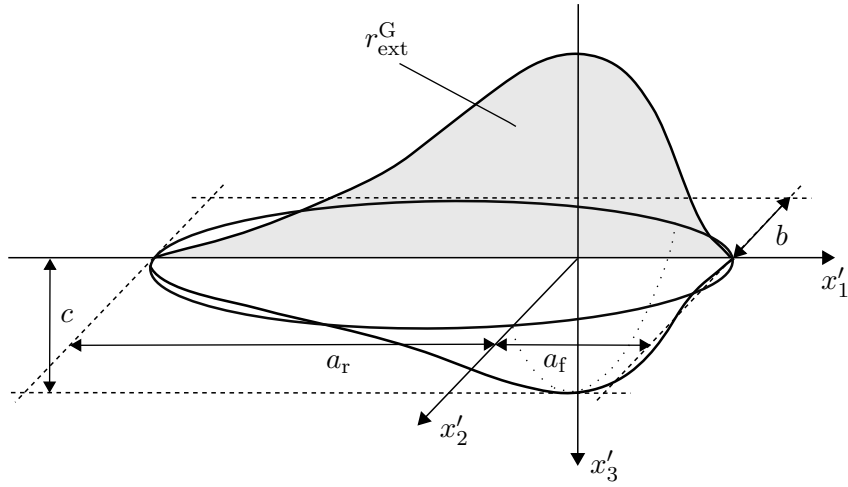
Figure 5.2: Schematic view of Goldak's ellipsoidal double well volumetric heat source $r_{\mathrm{ext}}^{\mathrm{G}}$. Reprinted from [132] under the terms of the Creative Commons Attribution License (CC BY).

see for example [33, 94, 113], but have so far not been established for manufacturing processes.

With the help of the layer hatch model, the scan pattern of an individual scan island can be analysed. According to the melt pool geometry of the single melt track, it is possible to study different hatching distances w_{h} and layer heights h_{lyr} by using the layer hatch model. The simulation has to be conducted once for each combination of material and process parameters, as well as hatching distance, layer height and scan island size. The purpose of the model is to extract the averaged inherent strain $\boldsymbol{\varepsilon}^{\mathrm{inh}}$ which can then be applied to the part model. The extraction of the IS tensor will be discussed in detail in Section 5.2.2. These eigenstrains are applicable for different parts with distinct scan patterns by using the part model.

To minimise the computational effort of the thermomechanically coupled FE analysis at hand, which set up on a geometrically larger scale than the laser scan model (mm in size), two simplifications are made:

At first, a constitutive material model based on temperature-dependent material parameters is adapted by using the corresponding critical phase transformation temperatures for melting, θ^{melt}, and solidification, θ^{solid}, similar to e.g. [99, 185]. This approach still captures the different states of the material, i.e. the powder, the molten, and the re-solidified phases. Therefore, in contrast to the laser scan model, no explicit evolution equations for the mass fractions have to be solved in order to determine the current phase of the process. Thus, the phase transformation only depends on the maximum temperature θ^{max}, the current temperature θ and the critical phase transformation temperatures θ^{melt} and θ^{solid}, which are extracted in advance by using the laser scan model, see Section 5.2.2.

Furthermore, the heat input for the layer hatch model of the scan island is approximated by a cuboid heat source $r_{\text{ext}}^{\text{c}}$ instead of Goldak's ellipsoidal double well. The cuboid heat source is calibrated by using the aforementioned determined melt pool dimensions width d_{w}^{G} and depth d_{d}^{G} and process parameters of the single melt track. A relation between the Goldak heat source and the cuboid heat source with parameters d_{w} and d_{d} is established in Section 5.2.2. This heat source moves along the top layer of the scan island in, for example, a meandering pattern, compare Figure 5.1 (middle). Due to the cuboid heat source, a larger element size can now be used in order to save computation time. The element size is chosen in accordance with the powder layer height and the hatching distance to reduce the overall element number in the FE analysis. This is the smallest possible element size at which it is still possible to simulate the scan pattern of the scan island, cf. [81].

Constitutive framework

To reduce the computational time for the scan island, no evolution equations for the mass fractions by using a phase transformation approach are included, but the phase change itself is purely temperature-dependent instead. This phenomenological approach seems to be appropriate for the layer hatch model, as the main focus of the scan island simulation is no longer set on the micromechanical behaviour of the material on a small scale, but on the overall material response and the respective inherent strains due to the scanning of a larger partition. Similar approaches are taken in, e.g., [99, 185]. Thus, the phase transformation now solely depends on the maximum temperature θ^{max}, the current temperature θ and the corresponding melting and solidification temperature, θ^{melt} and θ^{solid}, respectively. The melting and solidification temperature will be extracted from the single melt track simulation to resemble the material behaviour defined in the phase transformation model. In contrast to the phase transformation model in Section 5.1.1, the mass fractions are either zero or one – no phase mixture is assumed to exist here. Thus, the present phase strain $\boldsymbol{\varepsilon}_{\bullet}$ also corresponds to the total strain $\boldsymbol{\varepsilon}$. With this information, the phase change from the initial powder to melting and solidification can be described as a whole, as illustrated in Figure 5.3.
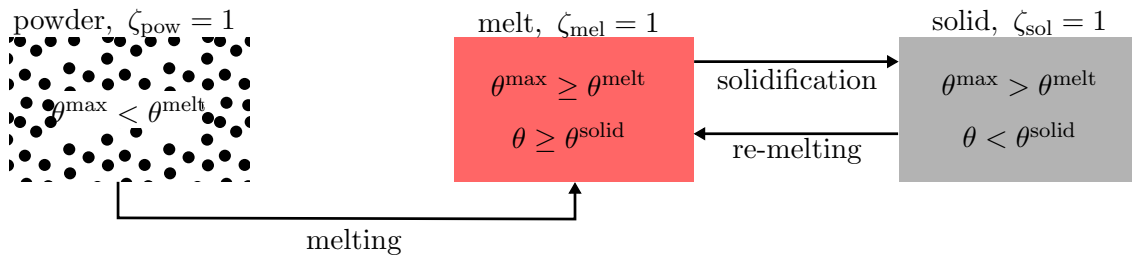
Figure 5.3: Illustration of the temperature-dependent phase transformation approach taken for the layer hatch model. Reprinted from [132] under the terms of the Creative Commons Attribution License (CC BY).

Due to the chosen ansatz of the layer hatch model, some features regarding the averaged energy densities and transformation strains shall be elaborated in the following. The lower part of the scan island already consists of solid material so that the solid phase is regarded as the parent phase here. It is assumed that the lower part consists of a perfect solid base layer without initial residual strains and stresses. The top layer, however, consists of powder, so that the powder phase is the parent phase, as also indicated in Figure 5.4. This necessitates a case differentiation for the two different parts, where

$$\overline{\Psi}_{\text{bot}} = \zeta_{\text{mel}} \, \Psi_{\text{mel}}(\boldsymbol{\varepsilon}, \theta, \boldsymbol{\varepsilon}_{\text{mel,bot}}^{\text{trans}}, \boldsymbol{\varepsilon}_{\text{mel}}^{\text{ve}}) + \zeta_{\text{sol}} \, \Psi_{\text{sol}}(\boldsymbol{\varepsilon}, \theta, \boldsymbol{\varepsilon}_{\text{sol,bot}}^{\text{trans}}, \boldsymbol{\varepsilon}_{\text{sol}}^{\text{th}}, \boldsymbol{\varepsilon}_{\text{sol}}^{\text{vp}}) \,, \tag{5.13}$$

$$\overline{\Psi}_{\text{top}} = \zeta_{\text{pow}} \, \Psi_{\text{pow}}(\boldsymbol{\varepsilon}, \theta) + \zeta_{\text{mel}} \, \Psi_{\text{mel}}(\boldsymbol{\varepsilon}, \theta, \boldsymbol{\varepsilon}_{\text{mel}}^{\text{trans}}, \boldsymbol{\varepsilon}_{\text{mel}}^{\text{ve}}) + \zeta_{\text{sol}} \, \Psi_{\text{sol}}(\boldsymbol{\varepsilon}, \theta, \boldsymbol{\varepsilon}_{\text{sol}}^{\text{trans}}, \boldsymbol{\varepsilon}_{\text{sol}}^{\text{th}}, \boldsymbol{\varepsilon}_{\text{sol}}^{\text{vp}}) \tag{5.14}$$

are the averaged energy densities for the bottom and top of the scan island, respectively. This also affects the phase transformation approach illustrated in Figure 5.3 due to the fact that for the lower part only the re-melting and solidification process is feasible. Moreover, eqs. (5.13) and (5.14) show the dependence of the particular energy density contributions on the respective inelastic strains considered. The newly introduced transformation strain $\boldsymbol{\varepsilon}_{\text{mel,bot}}^{\text{trans}}$ can now be defined as

$$\boldsymbol{\varepsilon}_{\text{mel,bot}}^{\text{trans}} = \frac{1}{3} \left[\frac{\rho_{\text{sol}}}{\rho_{\text{mel}}} - 1 \right] \boldsymbol{I} \,, \tag{5.15}$$

in analogy to eq. (4.10), where the solid phase is used as initial mass density. In consequence, no transformation strain is present for the solid phase of the bottom, i.e. $\boldsymbol{\varepsilon}_{\text{sol,bot}}^{\text{trans}} = \boldsymbol{0}$. In addition, the volume fraction of the molten phase has to be adjusted accordingly as the solid material is now considered to be the reference for the bottom material of the scan island. Corresponding to eq. (5.15), the volume fraction $\xi_{\text{mel,bot}} = \rho_{\text{sol}}/\rho_{\text{mel}}$ is defined, which can be derived by applying eqs. (4.14) and (4.15) to eq. (5.13). The remaining assumptions introduced in Sections 5.1.1 and 4.1 are still feasible. In other words, for the molten phase, a visco-elastic strain $\boldsymbol{\varepsilon}_{\text{mel}}^{\text{ve}}$ is present. Moreover, a thermal strain $\boldsymbol{\varepsilon}_{\text{sol}}^{\text{th}}$ and a visco-plastic strain $\boldsymbol{\varepsilon}_{\text{sol}}^{\text{vp}}$ exist in the solid phase. In addition, the resulting mechanical dissipation contribution no longer depends on the evolution of the volume fractions, cf. eq. (5.6), but solely on the present phase and the corresponding internal variables, such that

$$\mathcal{D}_{\text{mech}} = \begin{cases} 0 \,, & \text{if} \quad \zeta_{\text{pow}} = 1 \\ \mathcal{F}^{\text{ve}} : \dot{\boldsymbol{\varepsilon}}_{\text{mel}}^{\text{ve}} \,, & \text{if} \quad \zeta_{\text{mel}} = 1 \\ \mathcal{F}^{\text{vp}} : \dot{\boldsymbol{\varepsilon}}_{\text{sol}}^{\text{vp}} + \kappa \, \dot{k}_{\text{sol}}^{\text{hard}} \,, & \text{if} \quad \zeta_{\text{sol}} = 1 \end{cases} \,. \tag{5.16}$$

Finally, the process-induced inherent strains $\varepsilon^{\mathrm{inh}}$ of the layer hatch model can be calculated based on the total inelastic strain contributions analogously to eq. (5.7). Thus, the IS tensor can be determined directly in a post-processing step via

$$\varepsilon^{\mathrm{inh}} = \zeta_{\mathrm{mel}} \left[\varepsilon_{\mathrm{mel}}^{\mathrm{trans}} + \varepsilon_{\mathrm{mel}}^{\mathrm{ve}} \right] + \zeta_{\mathrm{sol}} \left[\varepsilon_{\mathrm{sol}}^{\mathrm{trans}} + \varepsilon_{\mathrm{sol}}^{\mathrm{th}} + \varepsilon_{\mathrm{sol}}^{\mathrm{vp}} \right] \overset{\zeta_{\mathrm{sol}}=1}{=} \varepsilon_{\mathrm{sol}}^{\mathrm{tans}} + \varepsilon_{\mathrm{sol}}^{\mathrm{th}} + \varepsilon_{\mathrm{sol}}^{\mathrm{vp}} , \quad (5.17)$$

where, in contrast to the modified IS method, e.g. [46, 103], the standard approach originated from welding to determine the IS is incorporated in the model at hand, cf. [26, 82] and Section 1.1.2. For the final state, where the part is cooled down to the ambient temperature, all the material is solidified. Thus, only the inelastic strains of the solid phase influence the inherent strains. During the process, the material model is still capable of predicting and taking the melting and re-solidification into account.

Cuboid heat source

To decrease the computational time of the layer hatch simulations, a cuboid heat source $r_{\mathrm{ext}}^{\mathrm{c}}$ is used to model the laser beam path of the scan island following a meandering pattern, introduced in [81, 82] as a so-called cubic heat source. A similar simplification to incorporate an equivalent body heat flux used for the layer hatch model is made in [99], whereas in [57] an approach for a likewise uniform heat source is used. For the case at hand, the size of this cuboid heat source is determined by the laser scan model in terms of the molten pool as defined in Section 5.2.2. Furthermore, the scan island is spatially discretised by finite elements, where each element of the regular mesh exhibits the size of the heat source. Thus, less elements are needed to resolve the layer hatch model. The newly introduced heat source can only be seen as an approximation of the laser beam heat source. It is assumed that the length of the heat source equals the width of the cuboid heat source. The edge length of the sides of the heat source is denoted by d_{w}, whereas d_{d} refers to the penetration depth. In general, the depth of the molten pool is larger than the height of the newly added layer h_{lyr}, which means $d_{\mathrm{d}} > h_{\mathrm{lyr}}$ has to be valid. With these approximations, the cuboid heat source can be defined as

$$r_{\mathrm{ext}}^{\mathrm{c}}(x_1', x_2', x_3') = \begin{cases} \dfrac{\eta_{\mathrm{ab}} \, P}{d_{\mathrm{w}}^2 \, d_{\mathrm{d}}} , & \text{if} \quad |x_{1,2}' - x_{1,2}| \leq \dfrac{d_{\mathrm{w}}}{2} \quad \wedge \quad h_{\mathrm{lyr}} - x_3 \leq d_{\mathrm{d}} \\ 0 , & \text{else} \end{cases} \quad (5.18)$$

depending on the current position (x_1', x_2', x_3') and including the aforementioned melt pool dimensions in width d_{w} and depth d_{d}. Moreover, P refers to the laser power and η_{ab} denotes the already introduced absorption coefficient. As a first approach, the heat source path will follow serpentine lines as used in [36, 81], which depend on the moving

coordinate system x'_1, x'_2, x'_3. For the example shown in Figure 5.4, the moving coordinate system is now defined via

$$x'_1 = \frac{1 - [-1]^n}{2} l_{\text{lyr}} + [-1]^n \left[\frac{d_{\text{w}}}{2} + \left[t - s \left\lfloor \frac{t}{s} \right\rfloor \right] \right] \overline{v}^{\text{lsr}} \ , \tag{5.19}$$

$$x'_2 = \frac{d_{\text{w}}}{2} + n \, w_{\text{h}} \ , \tag{5.20}$$

$$x'_3 = x_3 \ , \tag{5.21}$$

where the floor function $\lfloor \bullet \rfloor$ returns the largest integer value less than or equal to $\bullet$. Moreover, $n = \left\lfloor \frac{\overline{v}^{\text{lsr}} t}{l_{\text{lyr}} - d_{\text{w}}} \right\rfloor$ denotes the index of the scanned melt line, $s = \frac{l_{\text{lyr}} - d_{\text{w}}}{\overline{v}^{\text{lsr}}}$ is an abbreviation for the movement in x'_1-direction, l_{lyr} refers to the length and width of the scan island and w_{h} represents the hatching distance. For the present case, the hatching distance equals the size of the cuboid heat source, such that $w_{\text{h}} = d_{\text{w}}$, as the scan island is not resolved in detail. Altogether, this allows the use of larger elements corresponding to the hatching distance and layer thickness for the sake of significantly improved computational efficiency, so that the element size equals the heat source size.
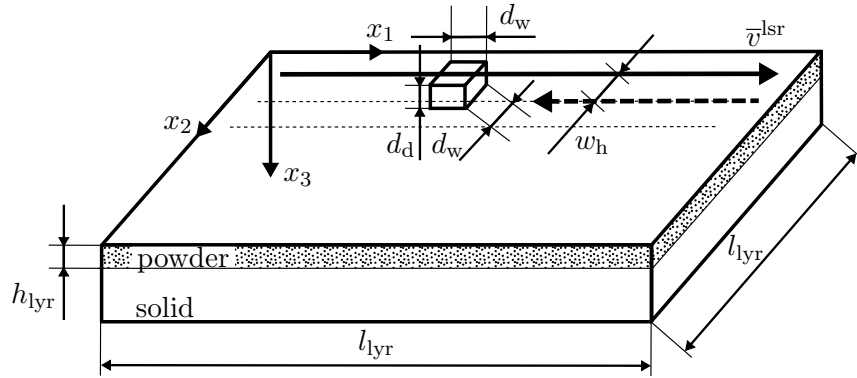
Figure 5.4: Schematic view of the cuboid heat source $r^{\text{c}}_{\text{ext}}$ and corresponding scan pattern. Reprinted from [132] under the terms of the Creative Commons Attribution License (CC BY).

5.1.3 Part model – complete part

In the part model, a purely mechanical simulation with an elastic material model is incorporated – in other words, thermomechanical coupling as well as further direct temperature influences are neglected in order to reduce the computing time. The determined inherent strains, cf. eq. (5.17), are applied as an external load-like contribution to, e.g., the frequently used benchmark structure of a cantilever beam, see illustration in Figure 5.1 (right), or any other arbitrary structure. The simplification of using the IS method is considered appropriate for the LPBF process, as each melt line undergoes a similar thermomechanical history. This also results in so-called global models where

complete layers are thermally loaded, see for example [91, 140, 183]. However, the overall used scan pattern of the final component can still be taken into account with the help of the multiscale framework, i.e. by rotating the corresponding inherent strain tensor for the respective sections. Therefore, the previously determined inherent strain tensor can be used to model various sets with different scan patterns, as long as the same process parameters are used. In general, this ansatz enables the efficient optimisation and reduction of the final residual stresses and the deformation of the part. The concept of the layer activation and application of the inherent strains is visualised in Figure 5.5, where the influence of the inherent strains on the current and final deformation is schematically illustrated. By doing so, not only the final deformation and distortion, also referred to as warpage, but also the eigenstresses of the part can be predicted.
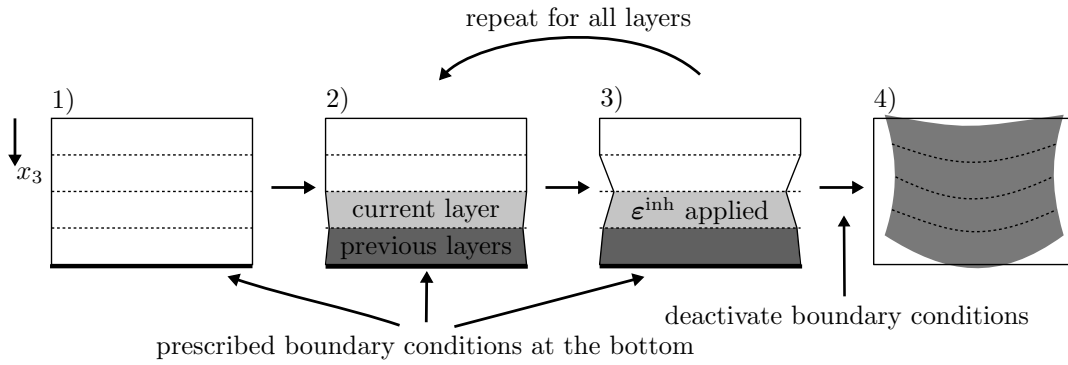
Figure 5.5: Schematic view of layer activation concept: 1) all (solid) layers initially deactivated, 2) one current layer activated, 3) inherent strain $\varepsilon^{\mathrm{inh}}$ applied as external load to current layer, 4) warpage of part after deactivation of boundary conditions. Reprinted from [129] under the terms of the Creative Commons Attribution License (CC BY).

To be specific, the stresses within the layers are determined by using the standard Hooke's law in the form

$$\boldsymbol{\sigma} = \mathbf{E}_{\mathrm{sol}} : \left[\boldsymbol{\varepsilon} - \widetilde{\boldsymbol{\varepsilon}}^{\,\mathrm{inh}} \right] \ , \tag{5.22}$$

where $\mathbf{E}_{\mathrm{sol}}$ refers to the elasticity tensor of the solid phase and $\widetilde{\boldsymbol{\varepsilon}}^{\,\mathrm{inh}}$ is the rotated inherent strain tensor. In accordance to the scan pattern of the corresponding layer, see for example Figure 5.6, the predefined inherent strain tensor is rotated by using a rotation tensor $\boldsymbol{R}$, so that $\widetilde{\boldsymbol{\varepsilon}}^{\,\mathrm{inh}} = \boldsymbol{R} \cdot \boldsymbol{\varepsilon}^{\mathrm{inh}} \cdot \boldsymbol{R}^{\mathrm{t}}$. The rotation tensor $\boldsymbol{R}(\boldsymbol{e}, \varphi)$ in the Euler-Rodrigues-representation is given by

$$\boldsymbol{R}(\boldsymbol{e}, \varphi) = [1 - \cos(\varphi)] \, \boldsymbol{e} \otimes \boldsymbol{e} + \cos(\varphi) \, \boldsymbol{I} - \sin(\varphi) \, \boldsymbol{\epsilon} \cdot \boldsymbol{e} \ , \tag{5.23}$$

where the unit vector $\boldsymbol{e}$ defines the rotation axis, here aligned with the x_3-axis, φ refers to the rotation angle, and where $\boldsymbol{\epsilon}$ denotes the third order permutation tensor. When incorporating appropriate case differentiations, which depend on layer number n_{lyr}, the

spatial location (x_1, x_2) and the rotation angle φ, it is now possible to explicitly model different scan patterns, as exemplarily indicated in Figure 5.6.
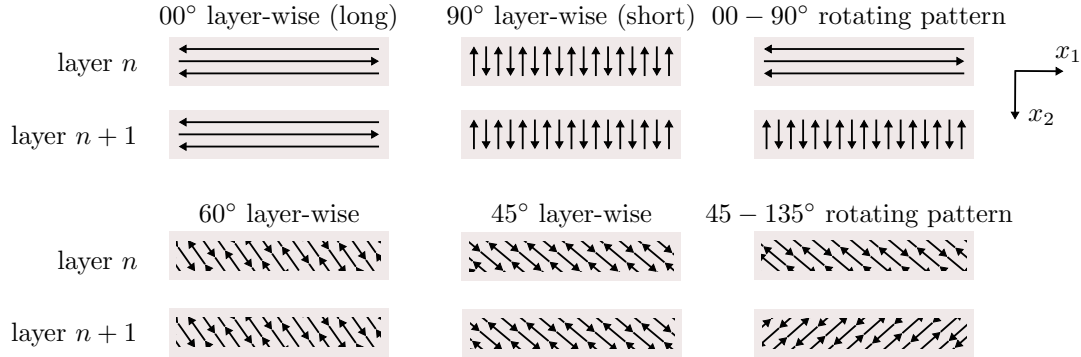
Figure 5.6: Overview of (an excerpt of) possible scan pattern combinations. Reprinted from [129] under the terms of the Creative Commons Attribution License (CC BY).

5.2 Implementation and algorithmic treatment

To give some insight into the implementation of the multiscale framework, the different user-defined subroutines are summarised in Section 5.2.1. Furthermore, the emphasis in Section 5.2.2 is set on the extraction of parameters, which are transferred between the different model scales. These are therefore of utmost interest for the implementation of the multiscale framework. With this information at hand, it is then possible to perform simulations and generate numerical results, which are presented in Section 5.3.

5.2.1 User-defined routines

In the following, some remarks on the user-defined subroutines for the different models are made.

Laser scan model

The laser scan model for a single melt track as introduced in Section 5.1.1 is implemented into the commercial FE software Abaqus. To incorporate the aforementioned material model, the user subroutines UMAT and UMATHT have to be used. Thereby, the strategies discussed in Section 4.2 are still valid. Furthermore, the subroutine DFLUX is called during the simulation which defines the volumetric moving heat source $r_{\text{ext}}^{\text{G}}$ in analogy to the model discussed in Section 3.2.

Layer hatch model

For the layer hatch model the user subroutine `UMAT` has to be adapted according to the material behaviour defined in Section 5.1.2. Due to the different initial material states for the scan island simulations, a case differentiation based on the underlying user-defined material name, referred to as `CMNAME`, is necessary. With this, the initial mass fractions, i.e. $\zeta_{sol} = 1$ or $\zeta_{pow} = 1$, and the material model are set for the base layer and the top layer. The implementation for the phenomenological approach without homogenisation is rather simple, resulting in a case differentiation based on Figure 5.3, where the maximum temperature has to be saved as internal variable. In addition, the inherent strain tensor is calculated and stored in the state dependent variable `SDV`. In contrast, little changes are necessary for the subroutine `UMATHT` developed for the laser scan model, now taking into account the different initial conditions of the material states. Within the subroutine `DFLUX`, the cuboid heat flux r_{ext}^{c} is implemented in a straightforward way as specified in Section 5.1.2.

Part model

For the following calculations of the part model, a self-written `UMAT` based on eq. (5.22) is used, in which the rotation of the inherent strain tensor for different layers is included. The current Abaqus versions, starting 2019, contain various special-purpose techniques for AM. This also makes it possible to directly define eigenstrain-based simulations within the so-called `AM-Modeler`. Thereby, table collections that begin with the name `ABQ_EIG` determine the analysis as described in [1]. The advantage of the `AM-Modeler` compared to the subroutine `UMAT` lies in the modelling of more complex scan patterns. However, in order to generate reliable results, new commands need to be understood and special attention has to be paid to the coordinate systems and the orientation of the part. A correct implementation can be better overseen and tested with the help of a self-written subroutine. Furthermore, it should be emphasised that the inherent strain tensor itself still needs to be previously determined elsewhere, if eigenstrain-based simulations are to be carried out using the `AM-Modeler`. Some insight into the implementation using the `AM-Modeler` is given in the Appendix C.1. Another way to implement the IS method in commercial FE codes is to use a modified thermal expansion with uniform temperature change, see e.g. [102] and Remark 11. However, the implementation of different scan patterns is rather straightforward when using the subroutine `UMAT` or the `AM-Modeler`.

Remark 11. *The equivalent thermal strain $\boldsymbol{\varepsilon}^{th}$ is determined by $\boldsymbol{\varepsilon}^{th} = \boldsymbol{\alpha}\,\Delta\theta$, where $\boldsymbol{\alpha}$ corresponds to the equivalent coefficients of thermal expansion (CTE) and where $\Delta\theta$ denotes the temperature change. Assuming the IS tensor corresponds to the thermal strains, i.e. $\widetilde{\boldsymbol{\varepsilon}}^{inh} := \boldsymbol{\varepsilon}^{th}$,*

$$\boldsymbol{\sigma} = \mathbf{E}_{sol} \colon \left[\boldsymbol{\varepsilon} - \widetilde{\boldsymbol{\varepsilon}}^{inh}\right] \overset{!}{=} \mathbf{E}_{sol} \colon \left[\boldsymbol{\varepsilon} - \boldsymbol{\varepsilon}^{th}\right] \tag{5.24}$$

is conceptually valid. The CTE then contains the coefficients of the previously determined inherent strain tensor, i.e. $\boldsymbol{\alpha} := \widetilde{\boldsymbol{\varepsilon}}^{\mathrm{inh}}$, if a uniform temperature change is applied to the model, i.e. $\Delta\theta = 1$ K. In consequence, the following static equilibrium analysis of eq. (5.24) yields the same results as eq. (5.22).

5.2.2 Extraction of transfer parameters

The transfer parameters of the laser scan model and layer hatch model, see Figure 5.1, are of central importance for the results of the part model. Thus, the procedure for defining and extracting these material parameters is now presented in detail. The detailed instructions on the BVP with the respective process parameters are given in the next Section 5.3. Due to the extraction of transfer parameters and the structure of the model framework, the determination of the inherent strains can straightforwardly be automatised. This way, the application is usable in the industry without requiring a profound knowledge of the underlying material model.

Laser scan model

As introduced in Section 5.1.1, four transfer parameters have to be extracted from the laser scan model. These are on the one hand the temperatures θ^{melt} and θ^{solid}, which are required for the material model of the layer hatch model, and on the other hand the melt pool dimensions d_{w} and d_{d}, which define the size of the cuboid heat source used in the layer hatch model.

The temperature vs. time curve and the molten mass fraction vs. time curve are visualised in Figure 5.7 for an element in the centre of the heat affected zone and for an element on the boundary of the heat affected zone, i.e. the transition zone from powder to re-solidified material, see also Figure 5.8. The temperature level in some elements significantly exceeds the evaporation temperature for the specific laser parameter set, see also Remark 12. For the simplified material model of the layer hatch model, θ^{melt} is the temperature where the material first considerably melts ($\zeta_{\mathrm{mel}} = 0.1$). The value is set to this magnitude as the temperature defines the molten pool for the layer hatch model. Figure 5.7a shows that the temperature evolves differently for different elements within the molten pool. This is in line with the viscous-type ansatz for the evolution of the mass fractions where the dissipation parameter η^{ξ} is employed. Here, the most outer element that completely melts is used to define that $\theta^{\mathrm{melt}} \approx 2000$ K is the appropriate temperature based for the proposed material model. This element is chosen because the focus of the layer hatch model lies on the lowest temperature for complete melting. The same approach ($\zeta_{\mathrm{mel}} = 0.9$, respectively) is used to define θ^{solid} in Figure 5.7b, where the material in the layer hatch model will be completely re-solidified. Here, the temperature for both elements takes similar values, as the cooling phase is longer and smaller temperature rates are present. For the element in the centre, a temperature plateau is nearly visible due to the latent heat of fusion. This behaviour is further
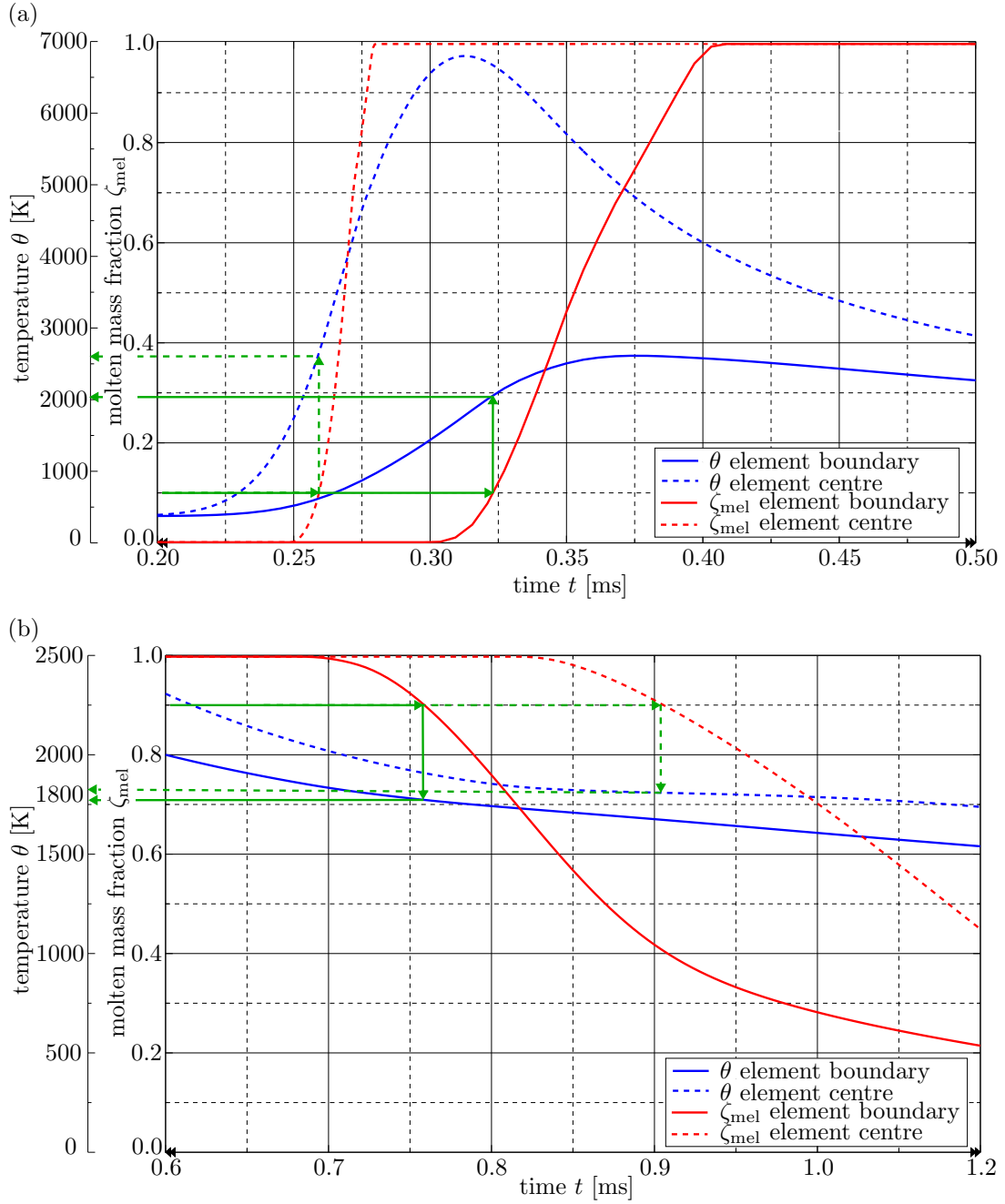
Figure 5.7: Evolution of temperatures θ and molten mass fraction ζ_{mel} during heating (5.7a) and cooling (5.7b) of the laser scan model to extract temperatures θ^{melt} and θ^{solid}, respectively, for the layer hatch model. Reprinted from [129] under the terms of the Creative Commons Attribution License (CC BY).

discussed in Appendix C.3. When focusing on the transition zone in detail, this transition zone corresponds to the inflection point of the curve. This finally leads to $\theta^{\mathrm{solid}} \approx 1800$ K. In literature, a liquidus temperature of 1933 K and a solidus temperature of 1878 K, can be found, cf. [25]. Hence, both extracted temperatures for the layer hatch model differ in the same magnitude from the literature values. Overall, the determined temperatures are located in an appropriate physical range.
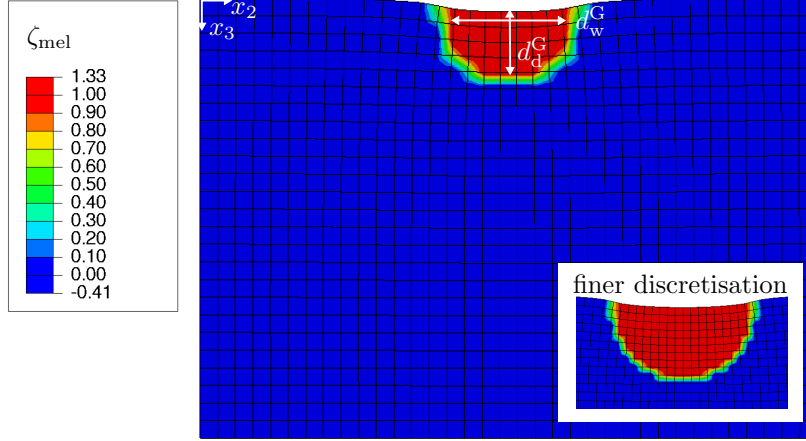
Figure 5.8: Contour plot of the molten mass fraction ζ_{mel} for a steady state size of the melt pool to extract the melt pool width $d_{\mathrm{w}}^{\mathrm{G}} = 0.14$ mm and depth $d_{\mathrm{d}}^{\mathrm{G}} = 0.08$ mm. Finer discretisation to distinctly mark melt pool shape. Reprinted from [129] under the terms of the Creative Commons Attribution License (CC BY).

Next, the melt pool size of the laser scan model is extracted to determine the heat source of the layer hatch model in such a way that the calculated areas of the heat sources coincide. With this assumption, the parameters d_{d} and d_{w} for the cuboid heat source of the layer hatch model can be meaningfully defined. As illustrated in Figure 5.8, the shape of the melt pool of the laser scan model is approximately elliptical which is made more easily visible by a finer discretisation. The depth $d_{\mathrm{d}}^{\mathrm{G}}$ and the width $d_{\mathrm{w}}^{\mathrm{G}}$ of the melt pool can be determined by a virtual measurement in a post-processing step. All elements where $\zeta_{\mathrm{mel}} \geq 0.9$ are taken into account in order to define these lengths. Based on the dimensions resulting from the simulation, the counterparts for the layer hatch model are determined as follows: The depth of the melt pool is assumed identical for both models, so that $d_{\mathrm{d}} = d_{\mathrm{d}}^{\mathrm{G}}$. As a consequence, the width of the melt pool for the layer hatch model is determined by $d_{\mathrm{w}} = \pi\, d_{\mathrm{w}}^{\mathrm{G}}/4$, where $d_{\mathrm{w}}^{\mathrm{G}}$ represents the vertical radius of the semi-ellipse and d_{w} the width of the rectangular heat source, respectively.

Remark 12. *For some elements, in particular in or close to the centre, the peak temperature significantly exceeds the evaporation temperature $\theta_{\mathrm{evap}} = 3200$ K for a short period of time. This is caused and amplified by the intensity profile of the heat source approach using a Gaussian distribution. This is physically not realistic. In the future, some*

modelling adjustments will be necessary. For example in [27, 108], the molten phase is represented by an artificially increased heat conductivity as proposed in [97]. By doing so, Marangoni flow within the molten pool is indirectly considered and the peak temperature decreases. From a physics viewpoint, it would be rather straightforward to consider an additional gas phase, so that the latent heat of evaporation is also incorporated. Its modelling, however, is rather complex, as the transition into gas is non-reversible. As a simpler version, an additional heat flux taking into account the thermal energy of evaporation (without mass flux) in line with e.g. [118] would be possible. For the model at hand, it turned out that the consideration of radiation or convection does not sufficiently influence the peak temperature, compare again the findings in Appendix B.3. Moreover, a different heat source approach, e.g. [64], could also be incorporated and compared to literature and experiments.

Layer hatch model

To determine the averaged inherent strain coefficients for the layer hatch model of the scan island, the corresponding values are extracted along different paths throughout the whole scan island and subsequently averaged. These paths are visualised in Figure 5.9a. The extracted results along these paths are exemplarily illustrated in Figure 5.9b for $\varepsilon_{11}^{\mathrm{inh}}$. The contour plot of the inherent strain coefficient $\varepsilon_{11}^{\mathrm{inh}}$ is also shown in Figure 5.9a. Within the middle region, the values along all paths are rather constant. However, on the boundaries large oscillations are visible, which occur due to the jump-type transition of $\boldsymbol{\varepsilon}^{\mathrm{inh}}$ from zero within the powder (see the red region in Figure 5.9a) to a (quasi) constant value in the re-solidified material (see the green region in Figure 5.9a) connected with the FE approximation using a C^0-continuous spatial discretisation. Thus, the contributions of the outer five elements are ignored when calculating the averaged inherent strain components (grey bounding box in Figure 5.9a and shaded in grey in Figure 5.9b). This is reasonable, as the values of the inner region are (quasi) constant and predominate the contributions of the transition zone. Overall, the values of the different paths are close to the average value (red path in Figure 5.9b). This strengthens the approach that extracting an inherent strain tensor $\boldsymbol{\varepsilon}^{\mathrm{inh}}$, which can be applied to the complete part, is an appropriate approximation for a computational efficient model, cf. for example [29, 81, 82, 102]. Since qualitatively similar responses are obtained for all coefficients of $\boldsymbol{\varepsilon}^{\mathrm{inh}}$, only the values for $\varepsilon_{11}^{\mathrm{inh}}$ are explicitly visualised.

5.3 Numerical examples

This section discusses numerical results based on the multiscale framework using the commercial FE programme Abaqus together with Fortran subroutines and external Python coding. First, the distinct thermomechanical material models of the laser scan model and the layer hatch model are compared in Section 5.3.1. The influence of the
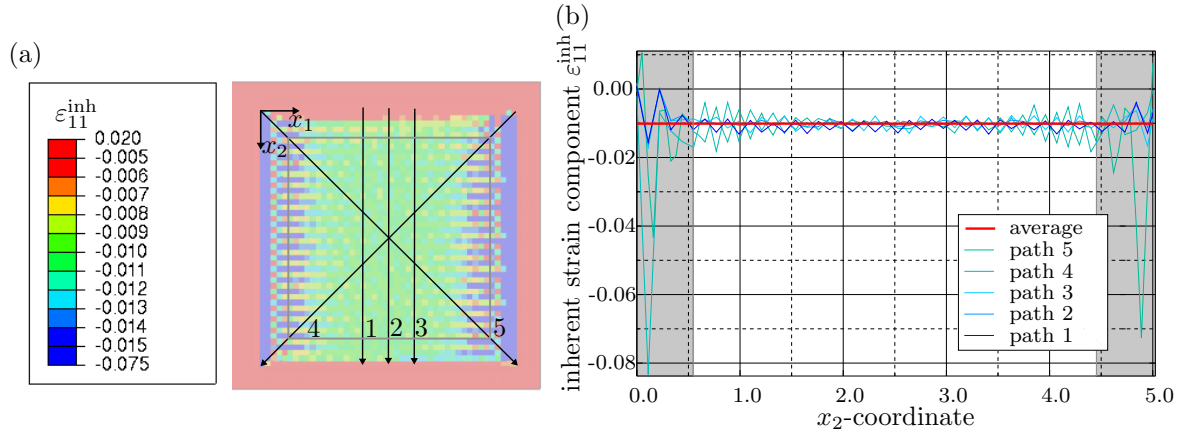
Figure 5.9: Sketch of paths used to illustrate inherent strain $\varepsilon_{11}^{\text{inh}}$-distribution with respective contour plot in the background (5.9a) and exemplarily extracted values for $\varepsilon_{11}^{\text{inh}}$ along the aforementioned paths and total determined averaged inherent strain $\varepsilon_{11}^{\text{inh}} = -0.0104$ (5.9b). Reprinted from [129] under the terms of the Creative Commons Attribution License (CC BY).

laser power and velocity are varied to examine the effects on the melt pool size and temperature, compare Section 5.3.2. Furthermore, the influence of the thermal behaviour on the residual stresses and inherent strains of the layer hatch model shall be analysed in Section 5.3.3. For a given set of material parameters and varied laser parameters, the presented multiscale approach is used to simulate a standard benchmark problem of a twin cantilever beam. The deformation and eigenstresses of this workpiece are illustrated and interpreted in Section 5.3.4. In addition, the influence of different laser parameters and scan patterns on the inherent strains and deformation is discussed.

As one of many appropriate materials for the LPBF process, a titanium aluminium alloy $\text{Ti}_6\text{Al}_4\text{V}$ is chosen for the examples at hand. The mechanical and thermal material parameters are summarised in Table 5.2. So far, the hardening modulus H_{sol} and the viscous parameters $\eta^{\text{v}\bullet}$ are meaningfully selected without particular literature reference. For the visco-elastic strains in the molten phase, a high viscosity parameter $\eta_{\text{mel}}^{\text{ve}} = 70$ is chosen to model the fluid-like behaviour. In contrast, a lower parameter is used for the visco-plastic behaviour of the solid phase, namely $\eta_{\text{sol}}^{\text{vp}} = 5$. Finally, the value of the dissipation parameter η^{ξ}, which is introduced for the phase change, has to be determined. As the experimental identification of dissipative quantities is typically difficult, the dissipation parameter has to be estimated as accurately as possible. The influence of this quantity is shown in Appendix C.2. The parameter choice influences the temperature range in which the phase transformation process takes place. In the future, this parameter could be adjusted to fit experimental results. As this work proceeds, different dissipation parameters are used. For the detailed results of Sections 5.3.2 and 5.3.3, a value of $\eta^{\xi} = 0.002$ is used, while for the results of the part simulations in Section 5.3.4 and the extraction of the transfer parameters in Section 5.2.2 a dissipation parameter of $\eta^{\xi} = 0.001$ is used. Altogether, the parameters $\eta^{\bullet}$ are also used to increase the numerical

Table 5.2: Summary of the material parameters used for Ti_6Al_4V, adjusted from [121, 148, 173].

Material parameters		Powder	Melt	Solid
Mechanical parameters				
Density	ρ [kg/m^3]	2800	3800	4420
Poisson's ratio	ν [$-$]	0.33	0.45	0.33
Young's modulus	E [GPa]	1.2	2.9	88.8
Yield limit	σ^{y} [GPa]	-	-	0.55
Hardening modulus	H [GPa]	-	-	1
Viscosity parameter	$\eta^{\mathrm{v}\bullet}$ [$-$]	-	70	5
Thermal parameters				
Expansion coefficient	α [1/K]	-	-	1.1e-05
Initial temperature	θ^{ini} [K]	-	-	1873.15
Heat capacity	c [J/(kgK)]	750	750	750
Conductivity	k [W/(mK)]	9.5	33.4	17.8
Latent heat	L [kJ/kg]	286	-	286
Reference temperature	θ^{ref} [K]	1873.15	-	1873.15

stability of the FE scheme regarding the step size. With the help of the densities $\rho_\bullet$, it is possible to directly calculate the transformation strains $\boldsymbol{\varepsilon}_\bullet^{\mathrm{trans}}$. Due to the large differences in mass densities, the volume changes incorporated by the transformation strains are rather large. As the transformation strains are purely volumetric and small rotations are present, the small strain formulation is still regarded appropriate at this point, as previously discussed in Section 4.3.

5.3.1 Proof of concept

Before presenting the results of the laser scan model and layer hatch model, the material models introduced in Section 5.1.1 and 5.1.2 shall be compared. Therefore, the time evolution of a completely molten element within the melt pool line is extracted for both simulations and visualised in Figures 5.10 and 5.11. For these results, the same model assumptions are used, only changing the material model incorporated in the subroutine `UMAT`. For the layer hatch model, both the melting temperature $\theta^{\mathrm{melt}} \approx 2000$ K and the solidification temperature $\theta^{\mathrm{solid}} \approx 1800$ K have been extracted from the results of the laser scan model, compare Section 5.2.2.

First, the mass fraction distributions are outlined in Figure 5.10, where the dashed line refers to the phase transformation approach and where the solid line indicates the material behaviour of the layer hatch model. Here, it can be seen how the phase transformation model allows an evolution of the mass fractions. Especially for the solid mass fraction ζ_{sol} an extended time span is necessary for solidification, as the cooling period takes longer than heating up the material above the melting point with the laser beam. After a time span of $t = 2.0$ ms, no further development of the mass fractions is visible,

as the temperature for the respective element has decreased below the melting point. In contrast, the mass fractions directly jump from zero to one when using the layer hatch approach.
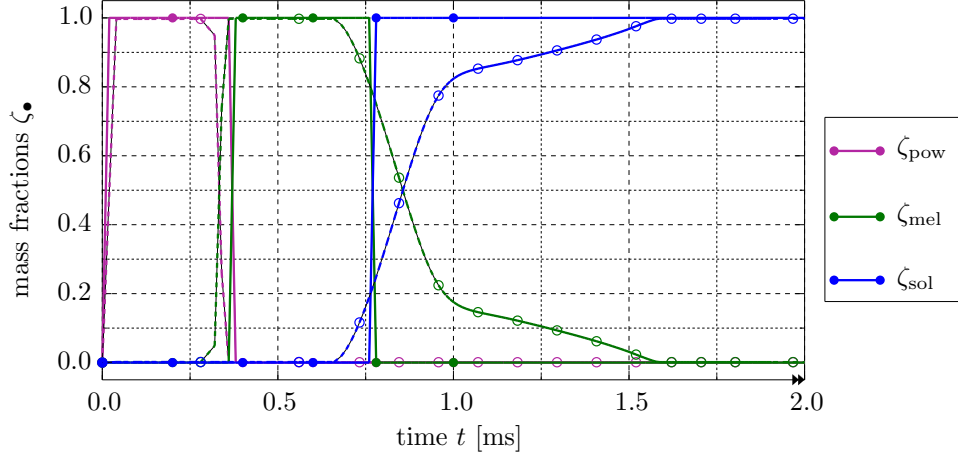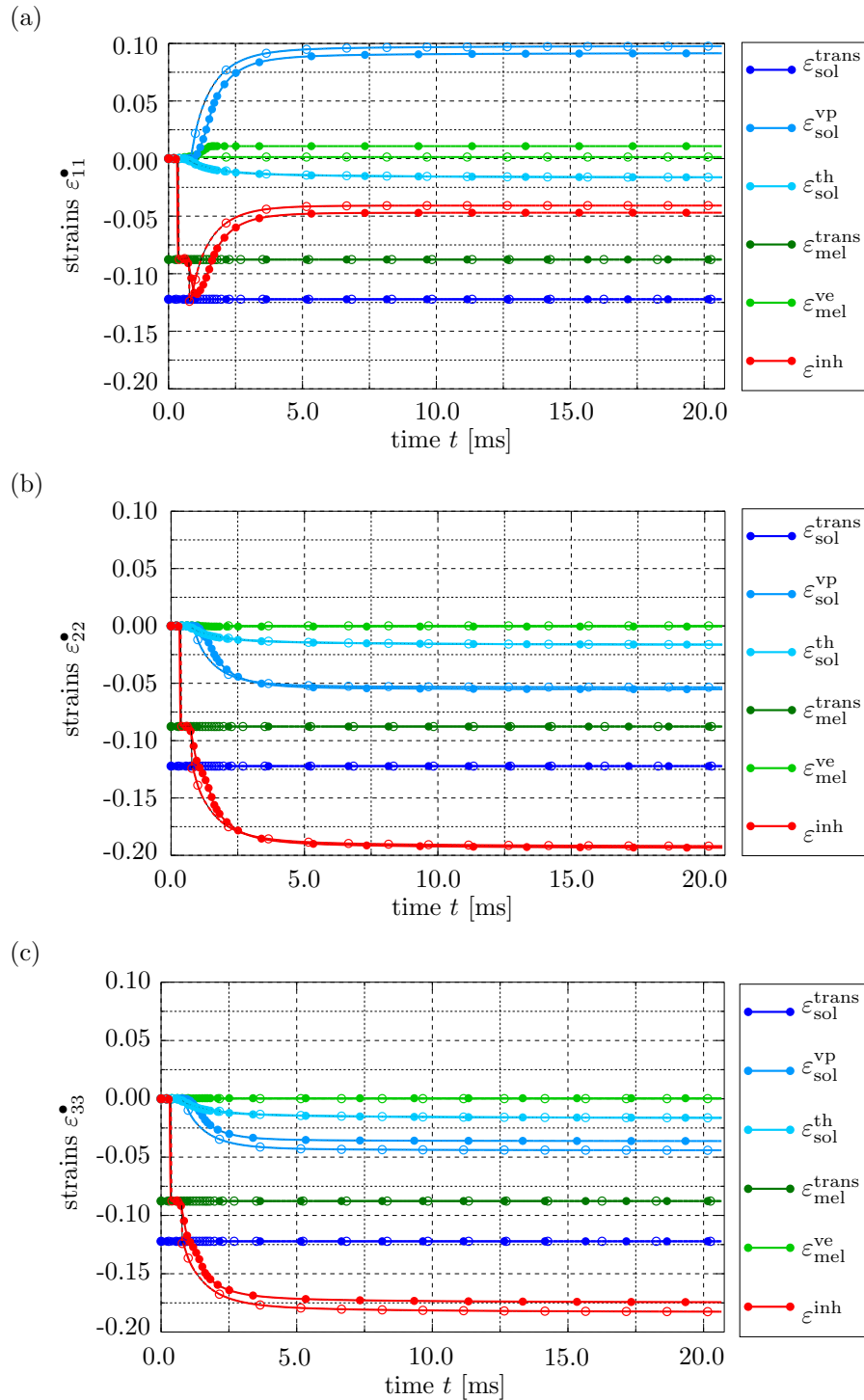

Figure 5.10: Comparison of phase transformation model (heat source approach – blank circles) and temperature-dependent material model (layer hatch approach – solid circles) exemplary for simulation case $P = 100\,\mathrm{W}$ and $\bar{v}^{\mathrm{lsr}} = 1.0\,\mathrm{mm/ms}$ for one representative element in the middle of the melt pool: excerpt of development of mass fractions over time. Reprinted from [132] under the terms of the Creative Commons Attribution License (CC BY).

The normal inelastic strain contributions and the corresponding inherent strains $\boldsymbol{\varepsilon}^{\mathrm{inh}}$ according to eq. (5.7) are visualised in Figure 5.11. In particular, the respective inherent strain $\varepsilon_{ij}^{\mathrm{inh}}$ can be calculated by weighting the appropriate inelastic strains with the mass fractions visualised in Figure 5.10. The coordinate system at hand corresponds to the principal axes up to numerical accuracies, i.e. $|\varepsilon_{ij}| \ll |\varepsilon_{ii}|$ (no summation with respect to i and $i \neq j$), such that the shear components are approximately zero for a single melt track. Therefore, only the normal components are visualised. The first drop in the inherent strains $\boldsymbol{\varepsilon}^{\mathrm{inh}}$ arises due to the transformation strain of the molten phase $\boldsymbol{\varepsilon}_{\mathrm{mel}}^{\mathrm{trans}}$, whereas the second drop and the following evolution is mainly governed by the transformation strain of the re-solidified material $\boldsymbol{\varepsilon}_{\mathrm{sol}}^{\mathrm{trans}}$ and the visco-plastic strain $\boldsymbol{\varepsilon}_{\mathrm{sol}}^{\mathrm{vp}}$. The influence of the visco-elastic strains of the molten phase $\boldsymbol{\varepsilon}_{\mathrm{mel}}^{\mathrm{ve}}$ is negligible as no previously present residual strains exist for the molten phase for a single melt track. Overall, high direction-dependent visco-plastic and inherent strain contributions are visible for the single melt track. A high visco-plastic tensile strain $\varepsilon_{11}^{\mathrm{vp}}$ is present in scanning direction, whereas all other strains are compressive. Especially high compressive inherent strains $\varepsilon_{22}^{\mathrm{inh}}$ and $\varepsilon_{33}^{\mathrm{inh}}$ exist transversally and vertically to the laser beam movement. The thermal strains and the transformation strains are uniformly distributed according to eqs. (3.45) and (4.10), respectively. During the evolution of the strains, larger differences can be seen in the range of $t_1 \approx 0.75$ ms to $t_2 \approx 4.0$ ms, as the different evolution of the mass fractions notably influences the respective values. However, during the following process of cooling, the discrepancy further reduces and a steady-state is reached. The final de-

(a)

(b)

(c)

Figure 5.11: Comparison of phase transformation model (heat source approach – blank circles) and temperature-dependent material model (layer hatch approach – solid circles) exemplary for simulation case $P = 100\,\text{W}$ and $\bar{v}^{\text{lsr}} = 1.0\,\text{mm/ms}$ for one representative element in the middle of the melt pool: (5.11a - 5.11c) evolution of all strain components over time. Reprinted from [132] under the terms of the Creative Commons Attribution License (CC BY).

113

viation at $t = 20.0$ ms, where the part has completely cooled down to $\theta^{\text{end}} \approx 393$ K, is minor compared to the absolute values of the quantities themselves. All in all, the conclusion is permitted that the layer hatch model is sufficiently accurate, if only the final residual strains for completely molten and re-solidified particles are relevant. However, the layer hatch model neither precisely covers the phase transformation behaviour nor can display partly molten particles in, e.g., the heat affected zone (HAZ).

5.3.2 Laser scan model

Definition of the laser scan model
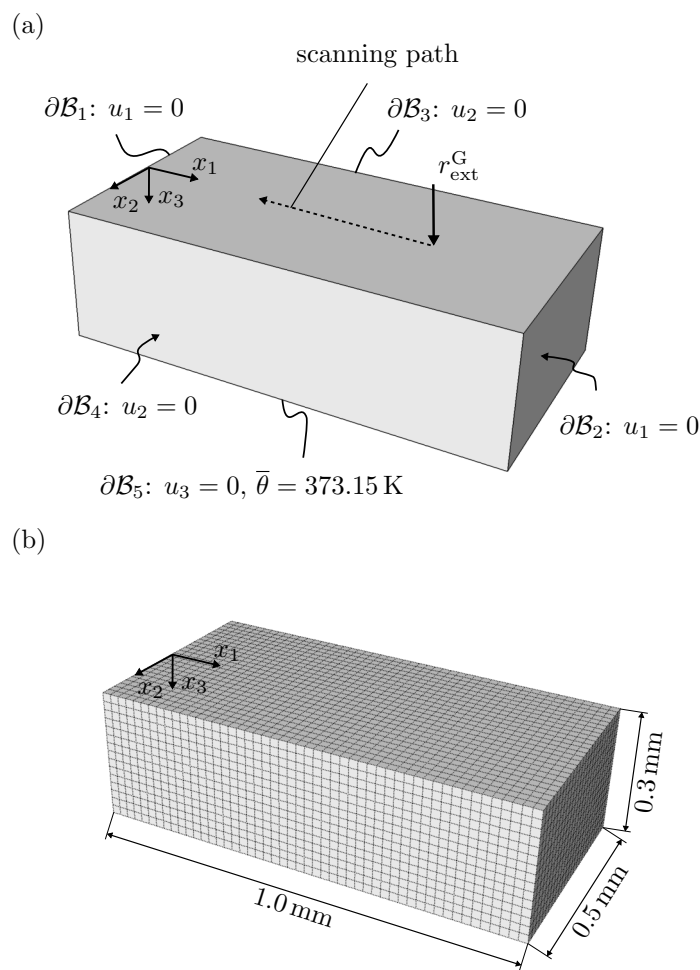
Figure 5.12: Specification of the simulation model for the laser scan model of a single melt track: (5.12a) boundary conditions and loads, (5.12b) overall dimensions with corresponding mesh (element size equals $20\,\mu$m). Reprinted from [132] under the terms of the Creative Commons Attribution License (CC BY).

Initially, the whole domain consists of powder so that $\zeta_{\mathrm{pow}} = 1$. Furthermore, the complete domain is preheated to $\overline{\theta} = 373.15\,\mathrm{K}$ to resemble the preheating of the build chamber. The domain with the corresponding Dirichlet boundary conditions on the boundaries $\partial\mathcal{B}$ is illustrated in Figure 5.12a. During the simulation, the temperature is set constant at the bottom of body considered, whereas all other sides are assumed to be insulated, so that heat convection and radiation are neglected. The volumetric moving heat source resembling the laser beam embeds thermal energy into the part. Afterwards, the unit cools down to the temperature of the build chamber. During the whole simulation, the displacements of the bottom and the sides of the component are fixed. The mesh and the geometric size of the domain is defined in Figure 5.12b. The element size is set to a characteristic length of $l_{\mathrm{char}} = 0.02$ mm which approximately corresponds to the range of the size of the powder particles, see e.g. [43]. This is also in accordance with [184] where a minimum of four elements per laser beam diameter is concluded to be sufficiently accurate. The element type is set to C3D8HT, an eight node thermally coupled hybrid brick element with trilinear approximation of displacements and temperature with constant pressure. The cause and influence on the results of a thermodynamically fully coupled model is discussed in Appendix C.3. During the simulations, an adaptive time step procedure provided by Abaqus is used, where a maximum temperature change of $\Delta\theta_{\mathrm{max}} = 1000$ K and and a maximum time step of $t_{\mathrm{max}} = 0.01$ ms is used as criteria to use smaller time steps.

The volume-distributed heat source $r_{\mathrm{ext}}^{\mathrm{G}}$ moves along the indicated scanning path in Figure 5.12a. For the single melt track simulation, constant parameters of the heat source are used for the semi-axis of the ellipsoid. For now, the variables are chosen to resemble a laser beam with a focus radius of $50\,\mu\mathrm{m}$. Therefore, the parameters $a_{\mathrm{f}} = a_{\mathrm{r}} = 50\,\mu\mathrm{m}$ and $b = 50\,\mu\mathrm{m}$ are used which corresponds to a hemispherical distribution in x_1- and x_2-direction, whereas the penetration depth is set to $c = 100\,\mu\mathrm{m}$. The absorption coefficient is selected as $\eta_{\mathrm{ab}} = 0.6$. For the values of the laser power P and the laser velocity $\overline{v}^{\mathrm{lsr}}$ different parameter combinations are used, where the influence of $P = \{50, 100, 150\}\,\mathrm{W}$ and $\overline{v}^{\mathrm{lsr}} = \{0.5, 1.0, 1.5\}\,\mathrm{m/s}$ is studied in the following.

Influence of parameter variation on melt pool size

First, the influence of laser power and laser velocity on the melt pool size is analysed. Therefore, both parameters are varied so as to examine the effects on the thermal behaviour. As it is difficult to determine the length of the melt pool in experiments, only the depth and the width of the melt pool are measured according to Figure 5.13b. One advantage of the phase transformation approach is the possibility to visualise the HAZ underneath the melting range which is often neglected in common approaches. Due to the evolution equations which are used for the mass fractions, it is not only distinguished between temperatures above and underneath the melting point, but the temperature history and residual strains also affect the final values of the mass fractions. The temperature profile during the simulation is exemplarily visualised in Figure 5.13a, where

(a)

(b)
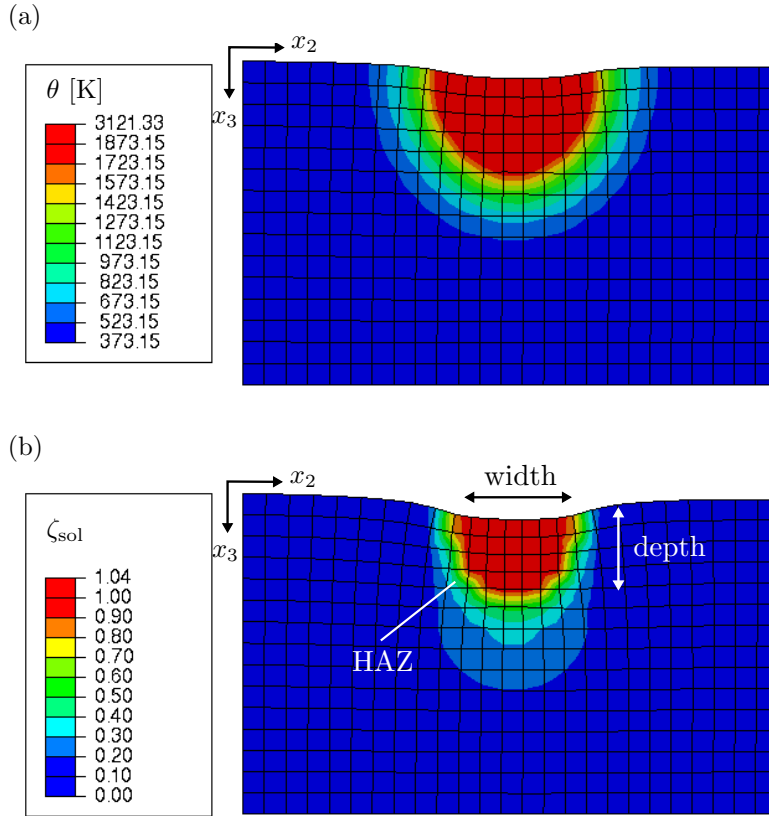
Figure 5.13: Cut at $x_1 = 0.5$ mm in the x_2-x_3-plane for simulation case $P = 150$ W and $\overline{v}^{\text{lsr}} = 1.0$ m/s: (5.13a) temperature profile θ during the simulation, (5.13b) solid mass fraction ζ_{sol} after cooling down, visualising the heat affected zone (HAZ) and dimensions of the solidified material. Reprinted from [132] under the terms of the Creative Commons Attribution License (CC BY).

the red colour refers to the temperature above the standard melting point of $\text{Ti}_6\text{Al}_4\text{V}$ in literature ($\theta^{\text{ref}} = 1873.15$ K). Overall, the maximum temperature increases drastically with growing laser power and fixed scan speed, whereas the cooling rate increases with reduced scan speed for fixed laser power. The HAZ in Figure 5.13b is similar to the one in the experiments, see for example [43], where a $\text{Ti}_6\text{Al}_4\text{V}$ baseplate has been used instead of working in a complete powder bed. With increasing distance from the actual melt pool, the influence on the material decreases and the solid mass fraction also reduces. Altogether, the temperature profile in Figure 5.13a and geometry of the melt pool region in Figure 5.13b resemble the shape of a bowl. The reduction in height, i.e. in x_3-direction, at the top layer of Figure 5.13a is due to the transformation strain $\boldsymbol{\varepsilon}_{\text{mel}}^{\text{trans}}$, whereas the larger height-wise decrease in Figure 5.13b stems from the additional transformation strain $\boldsymbol{\varepsilon}_{\text{sol}}^{\text{trans}}$ and the thermal shrinkage based on $\boldsymbol{\varepsilon}_{\text{sol}}^{\text{th}}$. The different sizes of the red bowl shapes in Figure 5.13 arise, as a temperature of $\theta^{\text{melt}} \approx 2000$ K (compare

Section 5.2.2) is necessary for a purely molten and then solidified material point when using the phase transformation approach, see also the explanations in Section 5.3.1.

(a)

(b)
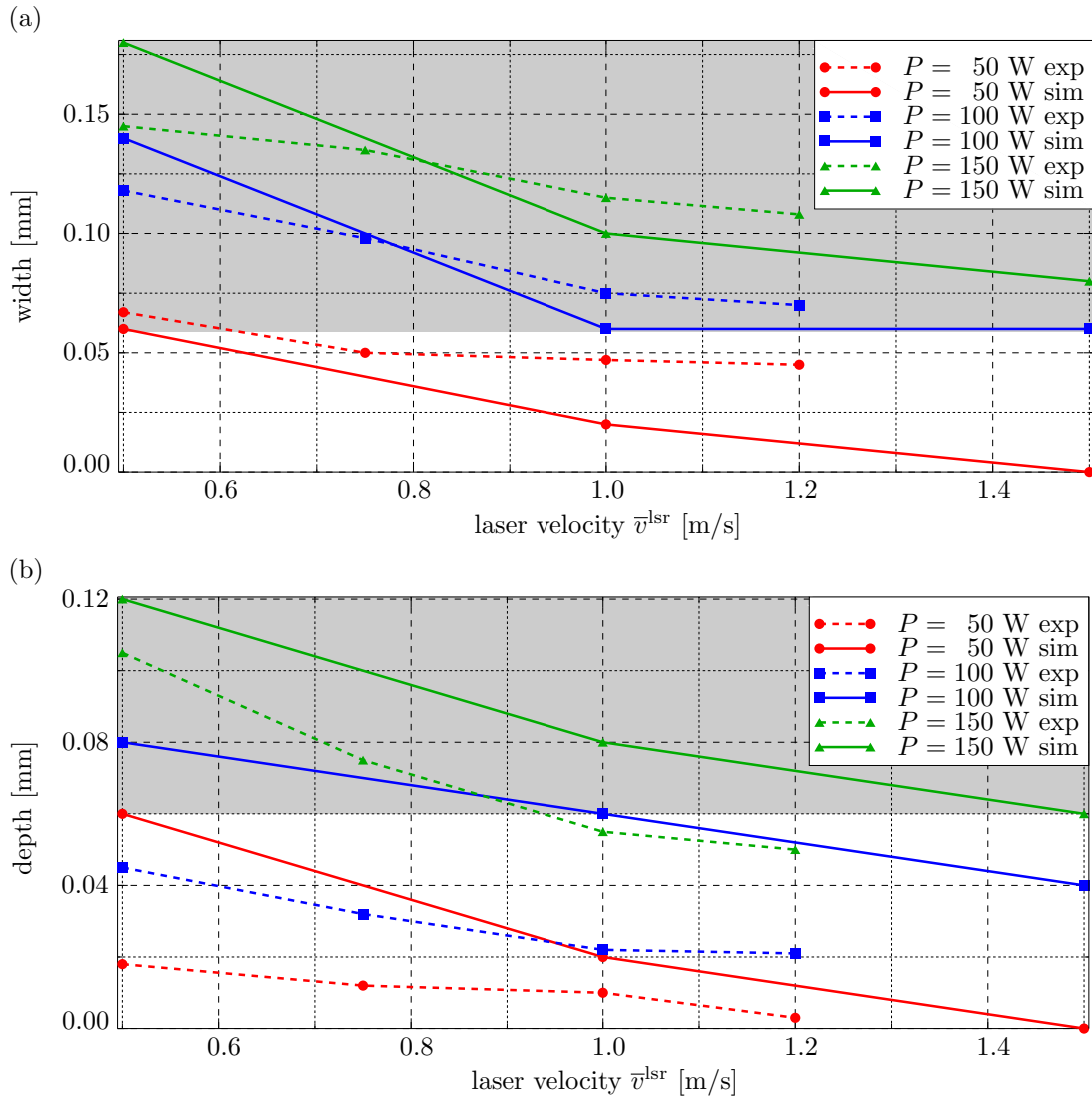
Figure 5.14: Size of melt pool in simulation based on phase transformation algorithm (solid line) compared to experimental results presented in [43] (dashed line): (5.14a) width and (5.14b) depth of the corresponding melt pool geometry. Grey colouring refers to minimum requirements for width and depth. Adapted from [132] under the terms of the Creative Commons Attribution License (CC BY).

With Figure 5.13b, it is possible to extract the melt pool geometry for all parameter combinations, as illustrated in Figure 5.14. It is visible that with an increase in laser power intensity, the width and depth of the melt pool increases, whereas both quantities decrease with increasing laser velocity. In this plot, the simulation results can be directly compared with experimental results shown in e.g. [43], where the same findings are made. Without any further parameter determination or validation, for example referring to

117

the semi-axes of the Goldak heat source or the heat absorption coefficient, a similar behaviour can be seen for the bead width of the melt pool size, see Figure 5.14a, whereas the depth of penetration seems to be constantly larger in our simulations than in the experimental investigations, compare Figure 5.14b. In a next step, parameter c of the Goldak heat source could therefore be adapted to fit the experimental results even better. Overall, the phase transformation algorithm is able to predict different melt pool geometries depending on the laser velocity and power. However, with such a model it is not possible to determine effects such as porosity or balling. For such simulation results, even more detailed models of the single powder particles are necessary. In contrast, it is possible to make predictions regarding the existence of a melt pool, e.g. a parameter combination of $P = 50$ W and $\overline{v}^{\mathrm{lsr}} = 1.5$ m/s is not sufficient for a regular continuous melt pool.

With the single track simulation results concerning the melt pool geometry, it is possible to extract the proper parameter combinations for the scan island simulation, where at least a melt pool width of 0.06 mm and depth of 0.06 mm are desired (coloured in grey in Figure 5.13). The influence of these six parameter combinations, namely 50 W - 0.5 m/s, 100 W - 0.5 m/s, 100 W - 1.0 m/s, 150 W - 0.5 m/s, 150 W - 1.0 m/s and 150 W - 1.5 m/s, on the eigenstrains and stresses shall be discussed when presenting the results of the suitable layer hatch model for the scan island simulations in the subsequent Section 5.3.3.

5.3.3 Layer hatch model

Definition of the layer hatch model
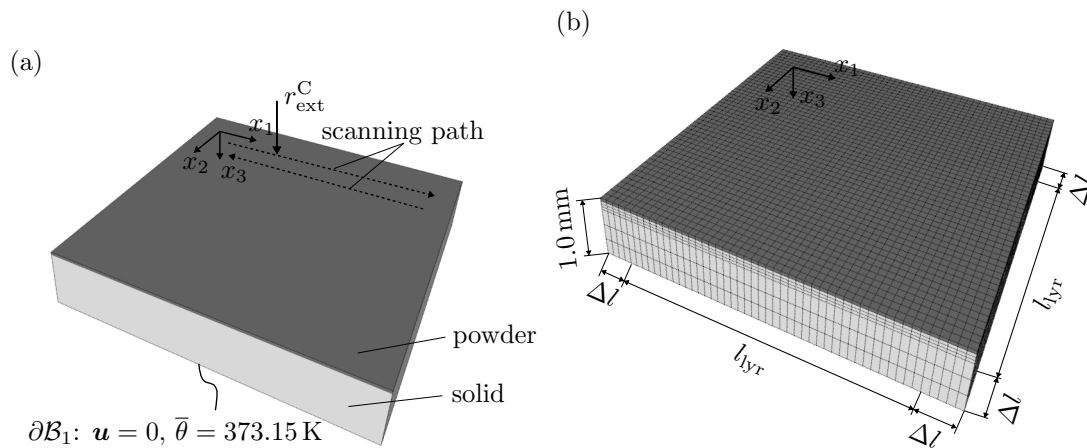
Figure 5.15: Specification of the simulation model for the layer hatch model: (5.15a) boundary conditions and loads, (5.15b) geometry of the scan island with corresponding mesh (element size equals cuboid heat source size). Reprinted from [132] under the terms of the Creative Commons Attribution License (CC BY).

A simple model resembling a single scan island is employed for the layer hatch model, where the lower portion is initially made out of solid material, thus $\zeta_{\text{sol}} = 1$. In contrast, the powder material with $\zeta_{\text{pow}} = 1$ is assigned to the top layer as indicated in Figure 5.15a. The complete domain is preheated to $\bar{\theta} = 373.15\,\text{K}$. During the simulation, this temperature is prescribed at the bottom of the body considered. In addition, no displacements are allowed at the bottom, while all other sides have no predefined conditions. All boundary conditions and loads are illustrated in Figure 5.15a. To ensure a continuous melt pool, a minimum of four time increments per cuboid heat source is used for the maximum time step size as proposed in [184]. The element type used is C3D8T, an eight node thermally coupled brick element with trilinear displacements and temperature approximations.

In the following, two different scan island sizes with the side length $l_{\text{lyr}} = \{3, 5\}$ mm are considered. The geometry is exemplarily shown in Figure 5.15b, where Δl refers to an additional domain of five elements of the respective simulation which are not molten by the laser beam heat source. These elements indicate the surrounding powder bed during the scanning of the scan island. This distance seems to be sufficient, as the surrounding powder has a low conductivity and Young's modulus. Thus, only a small buffer zone is necessary, see e.g. [36], where almost no temperature influence is visible on powder particles further away from the laser beam.

A distinct relation is present between the layer height and heat source depth. In general, the heat source depth needs to be larger than the layer height to ensure a re-melting of the underlying layers so that a bonding between layers can be assured. The height of the powder layer corresponds to the height of half an element, thus $h_{\text{lyr}} = d_{\text{d}}/2$, whereas the hatching distance equals the element length $w_{\text{h}} = d_{\text{w}}$. As already explained in Section 5.1.2, the element size equals the size of the cuboid heat source. However, sufficiently large melt pools are necessary to obtain a proper rapid process model, so that only the material combinations defined and summarised in Table 5.3 are considered. In consequence, the results presented in Figure 5.14 directly affect the layer hatch model, i.e. the hatch distance and the powder layer height. The two cursive values in Table 5.3 (penetration depth d_{d} for cases 4 and 5) are manually adapted to ensure a completely molten element because the initial energy input was not high enough to completely melt the element for these large melt pools. As the cuboid heat source size, i.e. element size, also influences the necessary melt line tracks of the meandering pattern, the time period to completely melt the scan island has to be adaptively chosen according to the laser beam velocity, the cuboid heat source size and the size of the scan island. After having scanned the complete scan island in a meandering pattern with the cuboid heat source $r_{\text{ext}}^{\text{c}}$ as marked in Figure 5.15a, an appropriate time span $t^{\text{end}} = 100$ ms is chosen so that the part can (almost) completely cool down to the initial temperature $\bar{\theta}$. The impact of these different process parameters, i.e. laser power, scan speed and island size, on the layer hatch model results are presented next.

Table 5.3: Overview of the laser beam parameters and size of cuboid heat source $r_{\text{ext}}^{\text{c}}$ for the layer hatch model.

Case	Laser power P	Laser velocity $\bar{v}^{\text{lsr}}$	Edge length d_{w}	Edge height d_{d}
1)	50 W	0.5 m/s	0.06 mm	0.06 mm
2)	100 W	0.5 m/s	0.14 mm	0.08 mm
3)	100 W	1.0 m/s	0.06 mm	0.06 mm
4)	150 W	0.5 m/s	0.18 mm	*0.10* mm
5)	150 W	1.0 m/s	0.10 mm	*0.06* mm
6)	150 W	1.5 m/s	0.06 mm	0.06 mm

Influence of parameter variation on scan island

An overview of the necessary scan tracks n and scan time t^{tot} is given in Table 5.4 for the smaller scan island $l_{\text{lyr}} = 3$ mm. In the following, especially the effect on the process time and the thermal material behaviour is analysed. The impact on the necessary time period t^{tot} and on the maximum average temperature θ^{avg}, i.e. the maximum temperature averaged over one element, is clearly visible. For a low laser power and velocity, the longest scan time is necessary (case 1). The process parameters of cases 4 - 6 create the scan islands the fastest time-wise. Especially keeping in mind that each complete part consists of multiple layers with many scan islands, the time period for manufacturing each scan island considerably affects the overall process time. This is also the reason why the remaining parameter combinations are not examined further.

Table 5.4: Summary of scan island results for $l_{\text{lyr}} = 3$ mm.

Case	Scan tracks n	Scan time t^{tot}	Avg. temp. θ^{avg}	End temp. θ^{end}
1)	50	294.00 ms	2616 K	430 K
2)	21	117.60 ms	2055 K	426 K
3)	50	147.00 ms	3225 K	455 K
4)	17	97.92 ms	2477 K	440 K
5)	30	87.00 ms	3373 K	444 K
6)	50	98.00 ms	4309 K	467 K

The average temperature of the element during scanning varies drastically due to the element size, laser velocity and power as summarised in Table 5.4. For a constant laser beam power, the temperature increases with increasing laser velocity when applying a cuboid heat source with a geometry as defined in Table 5.4. In contrast, the end temperature θ^{end} after cooling down for $t^{\text{end}} = 100$ ms barely differs. In Figure 5.16a, the temperature distribution for case 6 at the specific time frame $t^* = 29.4$ ms during the scanning period is illustrated, where a maximum temperature of $\theta^{\text{avg}} = 4308.99$ K is reached. Even though evaporation is possible above $\theta_{\text{evap}} = 3200$ K, it is appropriate to

neglect this process in the layer hatch model as the melt pool is considered as a whole. The corresponding size of the molten pool and the already solidified material is presented in Figure 5.16b. For all cases, the laser beam completely melts the powder within the inner region of $l_{\text{lyr}} = 3$ mm. In addition, the solid material underneath is also partly re-melted so that a compound with a proper bonding between the layers is formed. In addition, adjacent elements are heated up numerous times below the melting point due to the influence of neighbouring scan tracks. Changing the powder layer thickness and hatching distance can further influence the magnitude of re-melting of previous particles. However, these parameters are limited as a sufficient bonding between layers has to exist. Furthermore, it has to be kept in mind that they also regulate the production rate during manufacturing.
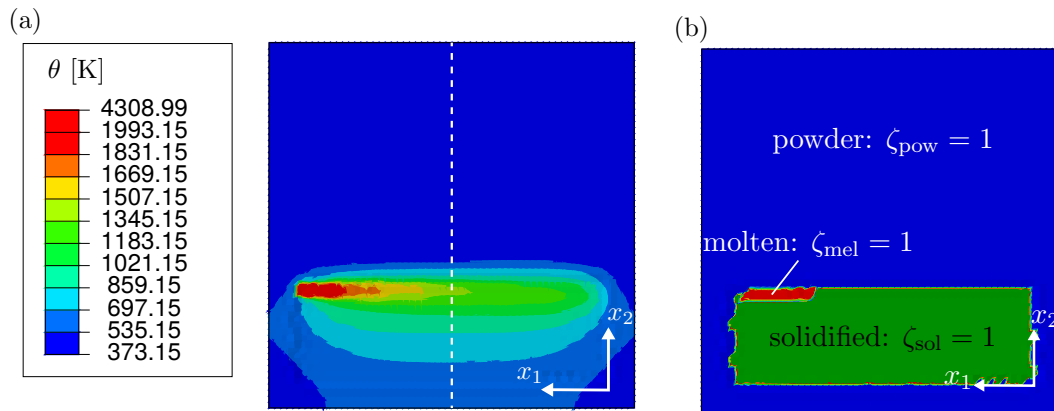
Figure 5.16: (5.16a) Temperature θ and (5.16b) corresponding material state for case 6 ($P = 150$ W, $\overline{v}^{\text{lsr}} = 1.5$ m/s) and $l_{\text{lyr}} = 3$ mm at $t^* = 29.4$ ms. Reprinted from [132] under the terms of the Creative Commons Attribution License (CC BY).

Analogous temperature ranges can be reported for the larger scan island $l_{\text{lyr}} = 5$ mm. However, slightly different cooling and re-heating rates are present due to the distinct length of the scan track. In [93], the influence on cooling and re-heating due to the length of scan vectors is discussed. Using larger scan vectors results in a slower re-scanning of adjacent tracks so that more cooling occurs in between. The number of scan tracks for $l_{\text{lyr}} = 5$ mm can be determined by scaling the respective results in Table 5.4 with 5/3, i.e. weighting the number of scan tracks with the size of the scan islands, whereas the overall time period has to be calculated with respect to the laser velocity. However, with regard to time efficiency, cases 4 - 6 are once again preferable.

Altogether, the thermal model of the scan island can be seen as a plausible approximation, where employing a cuboid heat source saves an enormous amount of computational time. However, using a cuboid heat source with an element size having the magnitude of the melt pool also results in some drawbacks. As the hatching distance equals the width of the melt pool, no studies on the influence of overlapping scan lines is possible, see for example [47]. These studies could albeit be incorporated into the laser scan model.

In addition, the cuboid heat source obviously no longer represents the real contour of the melt line compared to the Goldak heat source. Nevertheless, only these reasonable simplifications can provide computational efficient models for large parts.

Final inherent strain and eigenstress distribution

Next, the effect of the thermal behaviour and scan island size on the residual stresses and inherent strains shall be evaluated. The shear values and the x_3-component are considered throughout this thesis, as discussed in Remark 13. Therefore, the equivalent inherent strain

$$\bar{\varepsilon}^{\text{inh}} = \sqrt{\frac{1}{2}\left[\left[\varepsilon_{11}^{\text{inh}} - \varepsilon_{22}^{\text{inh}}\right]^2 + \left[\varepsilon_{22}^{\text{inh}} - \varepsilon_{33}^{\text{inh}}\right]^2 + \left[\varepsilon_{33}^{\text{inh}} - \varepsilon_{11}^{\text{inh}}\right]^2\right] + 3\left[\varepsilon_{12}^{\text{inh}\,2} + \varepsilon_{13}^{\text{inh}\,2} + \varepsilon_{23}^{\text{inh}\,2}\right]}$$

(5.25)

is defined analogously to the von Mises equivalent stress σ_{vM}. Both quantities are visualised for the computational efficient cases, i.e. referring to case 2 and cases 4 - 6, for either scan island size in Figure 5.17. The variables are plotted along the x_2-coordinate, where the corresponding position x_1 and the respective path for which the values are extracted, are marked in Figure 5.16a (this corresponds to path 2 in Figure 5.9a).

Remark 13. *No coefficients of the inherent strain tensor are set to zero for the part model, as is often seen in literature, in order to simplify the experimental determination of the inherent strains, cf. [158, 160]. Instead, all coefficients of ε^{inh} will be considered in the simulation of the twin cantilever beam, as these coefficients are directly determined when using the layer hatch model. From a modelling point of view, it may be argued that the $\varepsilon_{33}^{\text{inh}}$-component may be set to zero, as the shrinkage of the layer itself is negligible due to the re-coating/re-activation of the next layer. However, no model simplification is gained with this assumption. It is noted that the averaged inherent strain of the layer hatch model mostly depends on the laser parameters, but may also be influenced by the scan island size as discussed in Section 5.3.*

Considering Figure 5.17a first, the averaged inherent strains within the re-solidified material in the interval $x_2 \in [0.0, 3.0]$ mm, respectively $x_2 \in [0.0, 5.0]$ mm, are rather constant across the scan island itself. Only the inherent strains directly at the transition zone from powder to solid (especially close to $x_2 = 0.0$ mm) have to be excluded. This supports the approach defined in Section 5.2.2 for the extraction of the inherent strain tensor, where oscillating values at the transition zone are not taken into account. Overall, the range of the different equivalent inherent strains in Figure 5.17a is quite narrow for the middle region of the re-solidified material based on the underlying case and size. Altogether, stationary equivalent inherent strains can be extracted along the x_2-coordinate. The independence of the inherent strain from the scan island size supports the presented modelling approach of the IS method.
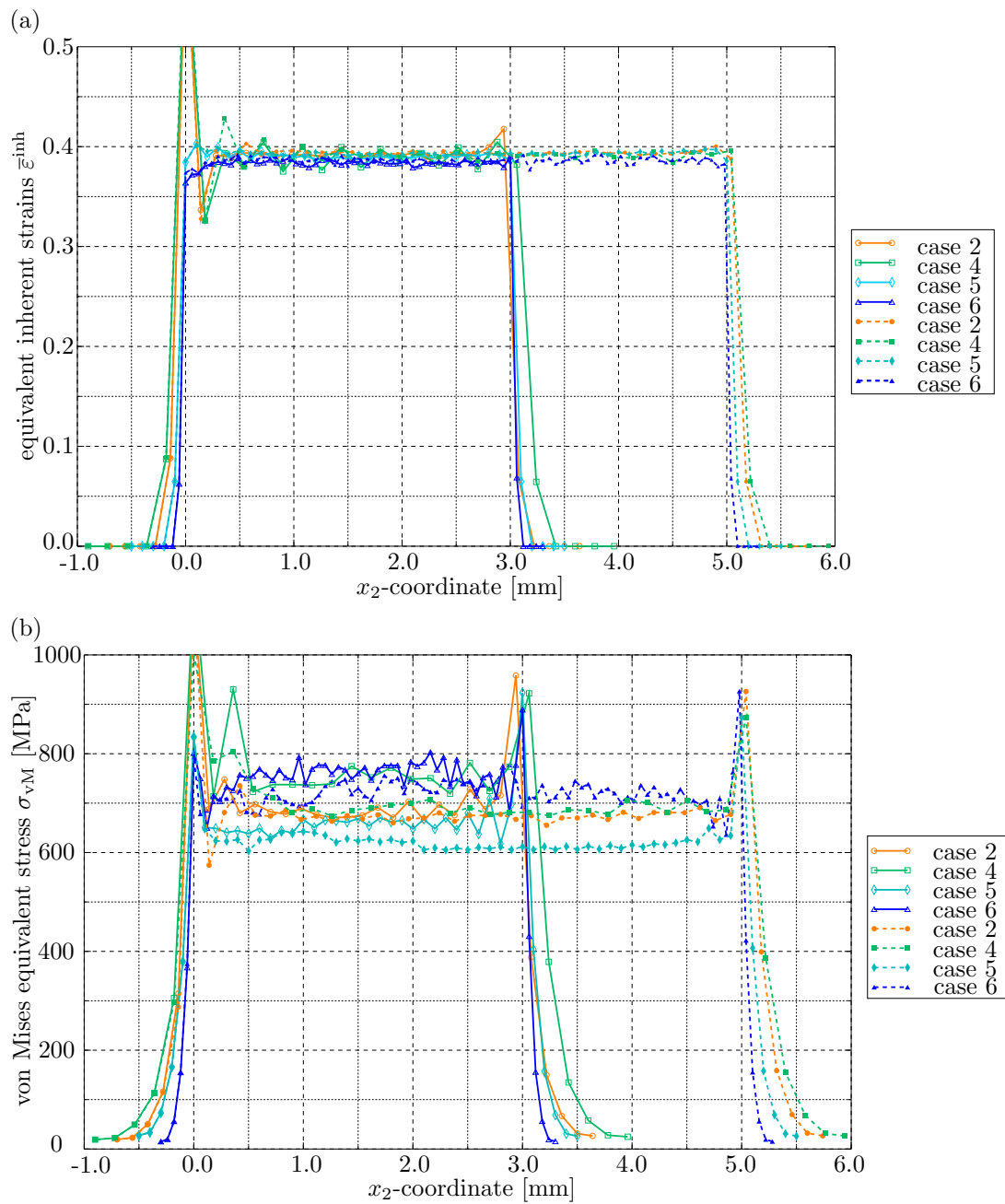
Figure 5.17: (5.17b) von Mises equivalent stress σ_{vM} and (5.17a) equivalent inherent strain $\bar{\varepsilon}^{\mathrm{inh}}$ along the x_2-direction for $l_{\mathrm{lyr}} = 3$ mm (solid line) and $l_{\mathrm{lyr}} = 5$ mm (dashed line) using the computational efficient cases according to Table 5.4. Reprinted from [132] under the terms of the Creative Commons Attribution License (CC BY).

However, the overall mean value of the von Mises equivalent stresses differs when regarding Figure 5.17b. Altogether, not only the case itself but also the length of the scanning vector considerably influences the residual stresses. It can be concluded that with increasing scan track length l_{lyr} the residual stresses decrease for all cases. This result coincides with the conclusions made in, for instance, [112] where 2×2, 3×3, 5×5 and 7×7 mm^2 island scanning strategies are experimentally compared for IN718. Here, the 5×5 mm^2 scan island pattern had the lowest residual stresses while having the best mechanical properties, with similar results for the 7×7 mm^2 specimen. In [94], it is reasoned that the influence of the orientation of scan vectors is major compared to the length of scan vectors themselves. In addition, the influence of the scan island size itself on the deflection of a complete part is negligible, while the overall result improves when using island scanning.
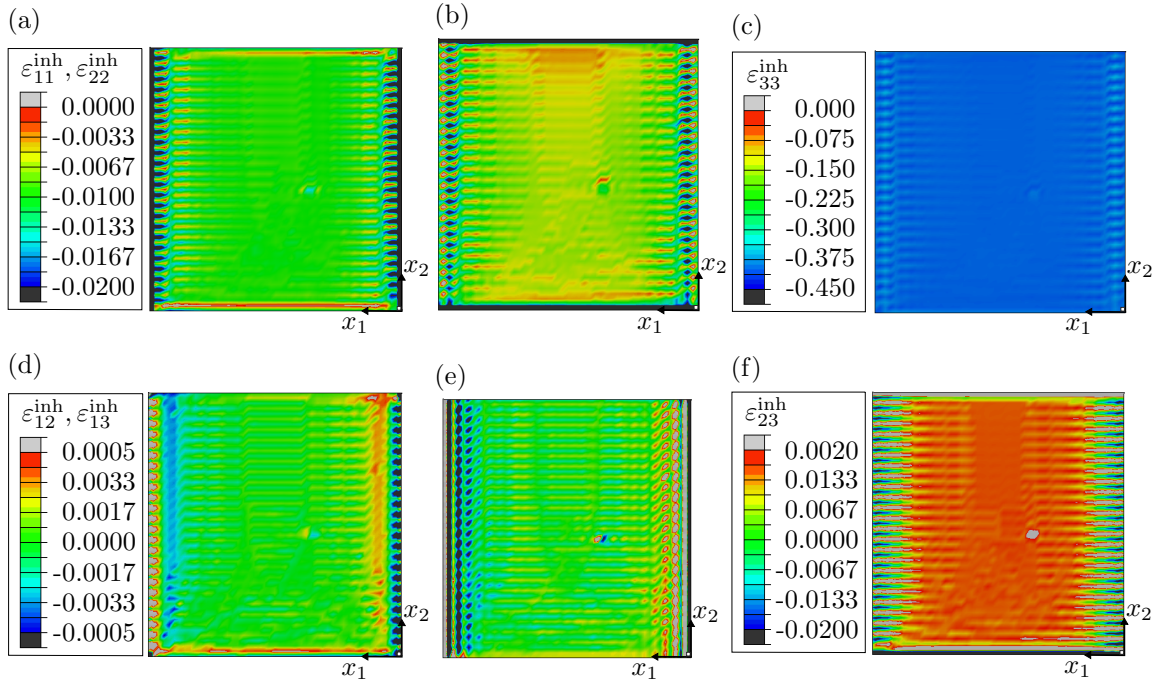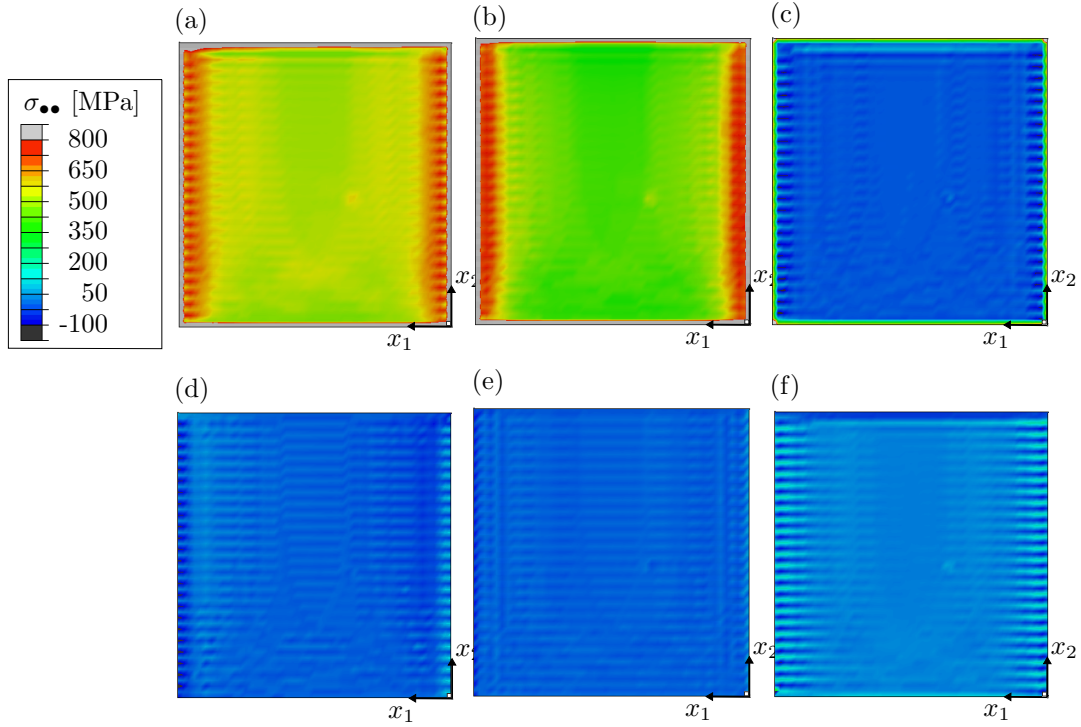

Figure 5.18: Inherent strain distribution of a single layer at the end of the simulation for case 5, i.e. $P = 150$ W, $\overline{v}^{\mathrm{lsr}} = 1.0$ m/s and $l_{\mathrm{lyr}} = 5$ mm: (5.18a) normal components $\varepsilon_{11}^{\mathrm{inh}}$, (5.18b) $\varepsilon_{22}^{\mathrm{inh}}$, (5.18c) $\varepsilon_{33}^{\mathrm{inh}}$, and shear components (5.18d) $\varepsilon_{12}^{\mathrm{inh}}$, (5.18e) $\varepsilon_{13}^{\mathrm{inh}}$, (5.18f) $\varepsilon_{23}^{\mathrm{inh}}$. (5.18a)–(5.18c) reprinted from [132] under the terms of the Creative Commons Attribution License (CC BY).

For the present simulations, the lowest residual equivalent stress is observed for case 5 and $l_{\mathrm{lyr}} = 5$ mm. For this case, the respective inherent strains along the x_1-, x_2- and x_3-direction are visualised in Figure 5.18, respectively. Here, only the re-solidified material of the newly added layer is shown. The oscillating values at the boundaries are neglected in the following discussion, as they arise due to the jump-type behaviour and projection operation applied as previously mentioned. It becomes visible that all direc-

tional inherent strains are negative due to the thermal shrinkage and the transformation strains. The normal components $\varepsilon_{11}^{\text{inh}}$ and $\varepsilon_{22}^{\text{inh}}$ are minor compared to $\varepsilon_{33}^{\text{inh}}$. Especially high $\varepsilon_{33}^{\text{inh}}$-contributions lead to shrinkage of the newly added layer and will not contribute to any stresses, as shrinkage is not constrained in x_3-direction. Due to the multiple re-coatings and slim layer height, the overall shrinkage of the part is small. Along the laser beam movement in x_1-direction and perpendicular in x_2-direction, almost the same inherent strain magnitude is visible. Upright, the strains are marginally higher and the distribution is not as uniform as it is for the other two directions. This is in contrast to the results in, e.g., [81] for SS316L, where higher inherent strains along the scanning direction are predicted. However, similar findings are made, e.g., in [29] for IN718, where a steady-state inherent strain tensor is extracted with uniform negative values for the transversal and longitudinal direction. These inherent strains are then applied to the model of the complete part.

Overall, the distribution of the inherent strains for the scan island is contrary to the results of the single melt track in Figure 5.11, where the normal components $\varepsilon_{22}^{\text{inh}} \approx \varepsilon_{33}^{\text{inh}}$, while $\varepsilon_{11}^{\text{inh}}$ is considerably lower. However, in comparison to a single melt track, the material cannot contract as freely for the scan island due to the preceding melt tracks and the solid build platform. Therefore, the distribution is more uniform in the x_1-x_2-plane with lower residual strains. Higher inherent strains are present in the x_3-direction i.e. the depth of the powder layer, where the shrinkage of the material caused by the transformation strains is mainly absorbed. For the current simulation, the shear components $\varepsilon_{12}^{\text{inh}}$ and $\varepsilon_{13}^{\text{inh}}$ are close to zero, compare Figures 5.18d and 5.18e, respectively. In addition, a rather high shear strain $\varepsilon_{23}^{\text{inh}}$ arises, which is not present for a single melt track, where all shear components are approximately zero. This shear component $\varepsilon_{23}^{\text{inh}}$ is illustrated in Figure 5.18f and lies within the (positive) range of $\varepsilon_{11}^{\text{inh}}$ and $\varepsilon_{22}^{\text{inh}}$, i.e. up to $\varepsilon_{23}^{\text{inh}} \approx 0.02$, compare also Table 5.6. This shear strain is expected to be present due to the successive solidification and shrinkage of the material (especially in depth, i.e. x_3-direction, and perpendicular to the melt track, i.e. x_2-direction). Therefore, the occurrence of a shear strain between the different seams of the laser tracks is necessary and reasonable. However, as a cuboid heat source and a coarse element size is chosen, it is possible that the value is overestimated. Overall, the inherent strains are (quasi-)constant within the not pictured layer height, i.e. in x_3-direction, as only one element is used per layer to establish a computational efficient simulation. In the literature, shear strains are often neglected a priori (for the coordinate system at hand) in the part model, cf. [81, 102], as the influence of these strain contributions is assumed to be insignificant, compare also Remark 13. This is not supported by the current model.

With these inherent strains, the residual stress distributions pictured in Figure 5.19 are gained. Within the inner region of the scan island, stationary residual stresses can be found. Thereby, the normal components σ_{11} and σ_{22} are positive tensile stresses, whereby the stresses in the x_1-direction visualised in Figure 5.19a are superior to the ones in x_2-direction in Figure 5.19b. Thus, the highest residual stresses are present along the melt line track. In x_3-direction, small negative compressive residual stresses exist, see

Figure 5.19: Residual stress distribution of a single layer at the end of the simulation for case 5, i.e. $P = 150$ W, $\overline{v}^{\mathrm{lsr}} = 1.0$ m/s and $l_{\mathrm{lyr}} = 5$ mm: normal components (5.19a) σ_{11}, (5.19b) σ_{22}, (5.19c) σ_{33}, and shear components (5.19d) σ_{12}, (5.19e) σ_{13}, (5.19f) σ_{23}. (5.19a)–(5.19c). Reprinted from [132] under the terms of the Creative Commons Attribution License (CC BY).

Figure 5.19c. The shear components σ_{12} and σ_{13}, which are illustrated in Figures 5.19d and 5.19f, respectively, are close to zero. This corresponds to the value of the respective inherent strain component. The σ_{23}-component visualised in Figure 5.19f is slightly higher, but not as dominant as the normal components σ_{11} and σ_{22}. The temperature gradient mechanism (TGM) is generally made responsible for the creation of stresses, where a bending of the body considered towards the laser beam, i.e. in direction of $-x_3$, is explained by different tension and compression stresses throughout the layers. Due to the surrounding solidified material, the thermal expansion induced by the laser beam is constrained and thus non-uniform compressive stresses and strains arise in x_1-and x_2-direction. During cooling, thermal shrinkage is also restricted resulting in tensile stresses and strains. Altogether, shear stresses are minor compared to normal stresses. Once the manufactured part is detached from the build platform, the bending and overall deformation will become visible as a stress relaxation takes place during this process. This feature can be observed in the next section, where a complete part is simulated.

5.3.4 Part model – twin cantilever beam

Definition of the part model
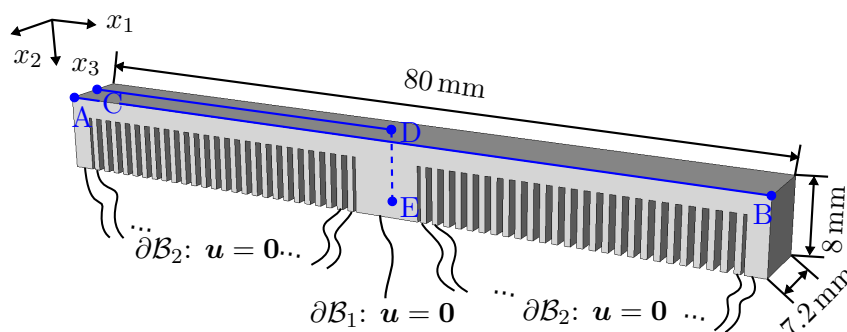
Figure 5.20: Boundary conditions and geometrical specification for the simulation of the part model: $\boldsymbol{u} = \boldsymbol{0}$ on $\partial\mathcal{B}_1$ is present during the whole simulation while $\boldsymbol{u} = \boldsymbol{0}$ on $\partial\mathcal{B}_2$ is enabled only during layer activation steps. Reprinted from [129] under the terms of the Creative Commons Attribution License (CC BY).

To examine the capabilities of the introduced model, a twin cantilever beam is simulated. This construction is frequently used as a benchmark structure, cf. [3, 29, 104, 155, 158, 160], and will also be employed in the following. The boundary conditions and the geometry are illustrated in Figure 5.20, where the detailed dimensions are taken from [26]. Two elements per rib width and a quadratic element formulation C3D20 are used for the beam-type geometries to properly capture the bending mode. First, the influence of the laser parameters is analysed, then the scan pattern is varied for the best parameter combination. During manufacturing, 267 physical layers are applied. To increase the computational efficiency, multiple physical layers are lumped in the following. The (relevant) quantities, such as u_3-displacement, σ_{11}- and σ_{22}-contributions, do not change significantly if at least 38 equivalent layers are used, i.e. seven physical layers are consolidated, see also the results of the convergence study in Appendix C.4.

Determined transfer parameters

Different laser parameters compared to Section 5.3.2 in terms of power and scan speed are used in the present section in order to study the influence of the laser parameters on the part model. The variation in laser power and scan speed not only results in different cuboid heat sources, but also in distinct scan times t^{tot} for the scan island. For the results of the part model, the parameters of the lower scales are defined as follows:

Laser scan model The Goldak heat source parameters are kept constant with $a = b = 0.8$ mm and $c = 0.9$ mm, whereas the absorption coefficient is set to $\eta_{\mathrm{ab}} = 0.5$, cf. Remark 14. The laser power and scan speed is varied as defined in Table 5.5. It is

assumed that a conduction mode is present for all parameter sets, see Remark 10. In addition, a dissipation parameter $\eta^\xi = 0.001$ is used. The diameters of the melt pool for the laser scan model are also summarised in Table 5.5. It is reasonable that, with decreasing velocity, the diameters of the melt pool increase while an intensification of power also elevates the size.

Table 5.5: Overview of extracted Goldak heat source parameters for varied laser parameters.

Laser power P	Scan speed $\overline{v}^{\text{lsr}}$	Width d_{w}^{G}	Depth d_{d}^{G}
180 W	1.2 mm/ms	0.14 mm	0.06 mm
180 W	1.0 mm/ms	0.14 mm	0.08 mm
180 W	0.7 mm/ms	0.18 mm	0.10 mm
250 W	1.2 mm/ms	0.14 mm	0.08 mm
250 W	1.0 mm/ms	0.18 mm	0.10 mm
250 W	0.7 mm/ms	0.22 mm	0.12 mm

Remark 14. *The parameters for the heat source are adapted from [30], whereas the absorption coefficient is used from [103] without further experimental validation. Overall, the range of the absorption coefficients for the titanium aluminium and the semi-axes of the Goldak heat source are rather large in literature, cf. [103] and [108]. In the following, it is noticed that the size of the heat source and the absorption coefficient not only influence the size of the melt pool, but also the maximum temperature of the model.*

Layer hatch model A standard island size of $l_{\text{lyr}} = 5$ mm is used for the model at hand. A layer height of $h_{\text{lyr}} = 0.03$ mm independent of the melted region is present. The obtained results for all inherent strain coefficients are summarised in Table 5.6. For lower scan speeds, especially the normal inherent strain component in x_2-direction decreases, as well as the shear component $\varepsilon_{23}^{\text{inh}}$. In contrast, the x_1-component marginally increases.

Before presenting the results of the part model, the values extracted for the inherent strain tensor with the present modelling approach shall be compared to values in literature. The explicit values as obtained by these approaches established in the literature are summarised in Table 5.7. It is obvious that some models yield volume conserving inherent strains, which is physically not sound regarding the overall phase transformation process from powder to re-solidified material. In addition, there is a discrepancy regarding the normal component $\varepsilon_{33}^{\text{inh}}$, which is sometimes set to zero, compare Remark 11. Hence, only the $\varepsilon_{11}^{\text{inh}}$- and $\varepsilon_{22}^{\text{inh}}$-contributions are considered when experimentally determining the inherent strain. In contrast, all components of the extracted inherent strain specified in Table 5.6 directly follow from the modelling framework presented here without further modifications. Altogether, the extracted $\varepsilon_{11}^{\text{inh}}$- and $\varepsilon_{22}^{\text{inh}}$-components lie in the same range as the results obtained by the models presented in the aforementioned references for $\text{Ti}_6\text{Al}_4\text{V}$. The calculated $\varepsilon_{33}^{\text{inh}}$-components are physically sound as a shrinkage

Table 5.6: Overview of extracted inherent strains $\varepsilon^{\mathrm{inh}}$ and scan times t^{tot} for scan island size $l_{\mathrm{lyr}} = 5$ mm and different laser parameters.

Laser power P	Scan speed $\overline{v}^{\mathrm{lsr}}$	Scan time t^{tot}	Averaged inherent strain $\varepsilon^{\mathrm{inh}}$					
			$\varepsilon_{11}^{\mathrm{inh}}$	$\varepsilon_{22}^{\mathrm{inh}}$	$\varepsilon_{33}^{\mathrm{inh}}$	$\varepsilon_{12}^{\mathrm{inh}}$	$\varepsilon_{13}^{\mathrm{inh}}$	$\varepsilon_{23}^{\mathrm{inh}}$
180 W	1.2 mm/ms	181 ms	-0.0086	-0.0068	-0.3996	0.0000	-0.0001	0.0135
180 W	1.0 mm/ms	217 ms	-0.0090	-0.0062	-0.3996	0.0000	-0.0001	0.0138
180 W	0.7 mm/ms	252 ms	-0.0094	-0.0049	-0.4005	0.0000	-0.0005	0.0104
250 W	1.2 mm/ms	181 ms	-0.0104	-0.0067	-0.3974	0.0000	0.0000	0.0131
250 W	1.0 mm/ms	176 ms	-0.0106	-0.0053	-0.3986	0.0001	-0.0002	0.0094
250 W	0.7 mm/ms	197 ms	-0.0107	-0.0041	-0.4001	-0.0002	0.0000	0.0083

Table 5.7: Literature overview of inherent strains for Ti_6Al_4V.

Reference	Averaged inherent strain $\varepsilon^{\mathrm{inh}}$			
	$\varepsilon_{11}^{\mathrm{inh}}$	$\varepsilon_{22}^{\mathrm{inh}}$	$\varepsilon_{33}^{\mathrm{inh}}$	
[103]	-0.0069	-0.002	0.008	
[30]	-0.02	-0.01	0.015	
[160]	-0.0047	-0.002	0	
[158]	-1*	-0.33*	0	* normalised value
[143]	0.001	0.001	-0.002	

rather than an expansion is expected due to the different densities of powder and solid. In e.g. [103], it is stated that the shear components are neglected, as these are minor compared to the normal components. This is not supported by the present results, where the $\varepsilon_{23}^{\mathrm{inh}}$-component significantly contributes to the total inherent strain. This shear component is also explicable as the process is non-symmetric.

A more complex material model for the single melt track or layer hatch model will result in a new and possibly longer calculation of these two scales. However, one main advantage is that the resulting (quantitatively improved) inherent strains are still applicable for an efficient simulation of the part model.

Influence of laser parameters

Table 5.8: Overview of maximal u_3-displacement for a constant 90° layer-wise (short) scan pattern and varied laser parameters.

Laser power P	Scan speed $\overline{v}^{\mathrm{lsr}}$	Max. u_3-displacement
180 W	1.2 mm/ms	-4.247 mm
180 W	1.0 mm/ms	-4.040 mm
180 W	0.7 mm/ms	-3.524 mm
250 W	1.2 mm/ms	-4.449 mm
250 W	1.0 mm/ms	-3.879 mm
250 W	0.7 mm/ms	-3.368 mm

First, a uniform scan pattern of 90° layer-wise (short), compare Figure 5.6, is used to study the influence of the final deformation of the twin cantilever beam based on different laser parameters. The results for the maximum deflection in x_3-direction after changing the boundary conditions, i.e. cutting the part from the build platform, except from the middle feet, are summarised in Table 5.8. In Figure 5.21, the displacements at the top longitudinal edge of this workpiece in the different directions are plotted. Generally, the u_1-displacements in Figure 5.21a occur due to the longitudinal necking and are symmetric as explained in e.g. [104]. The change in the u_2-displacements in Figure 5.21b arises due

(a)

(b)

(c)
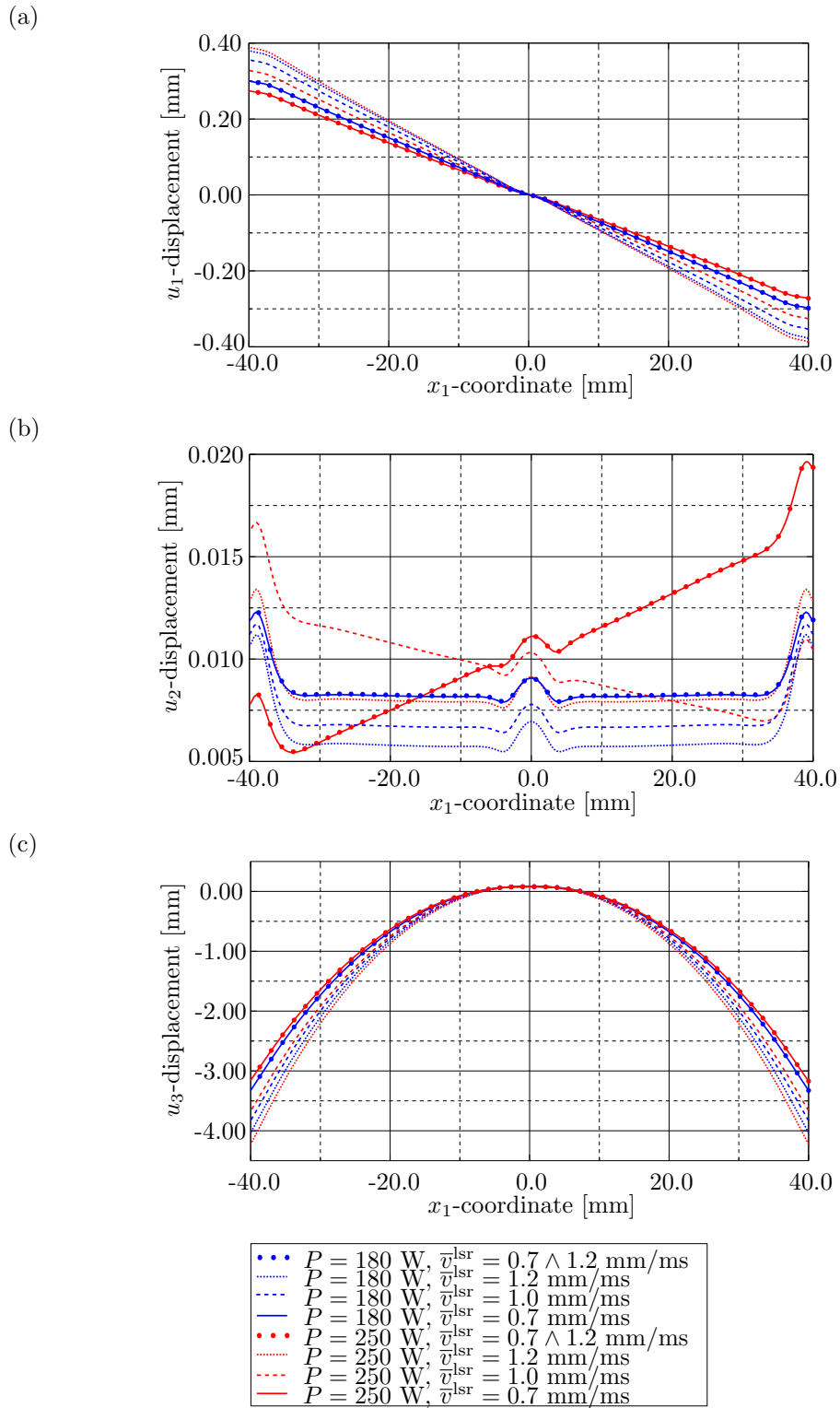
Figure 5.21: Displacements along x_1-coordinate at the top edge of the twin cantilever beam, along the path A-B as indicated in Figure 5.20, in the respective direction for the corresponding laser parameter sets. Reprinted from [129] under the terms of the Creative Commons Attribution License (CC BY).
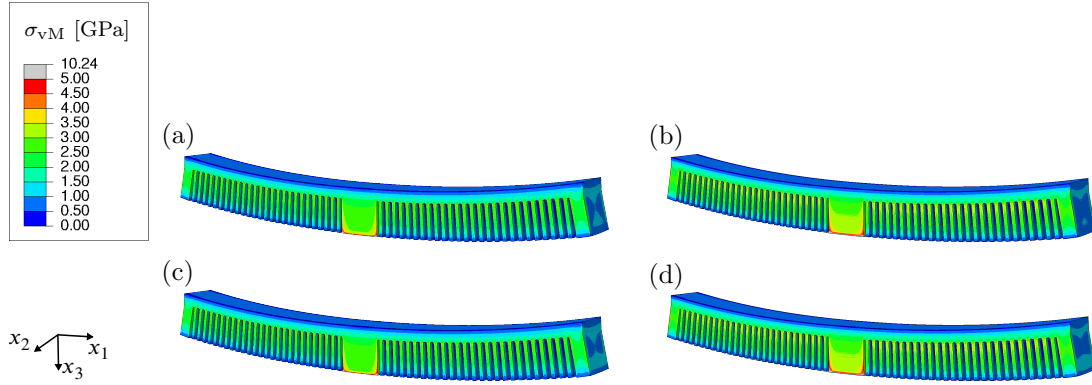
Figure 5.22: Distribution of σ_{vM}-stress and deformed configuration for different laser parameters: (5.22a) $\overline{v}^{\mathrm{lsr}} = 0.7$ mm/ms and $P = 180$ W, (5.22b) $\overline{v}^{\mathrm{lsr}} = 0.7$ mm/ms and $P = 250$ W, (5.22c) and (5.22d) combination of $\overline{v}^{\mathrm{lsr}} = 0.7$ mm/ms for upper continuous layers and $\overline{v}^{\mathrm{lsr}} = 1.2$ mm/ms for ribs with (5.22c) $P = 180$ W and with (5.22d) $P = 250$ W. Reprinted from [129] under the terms of the Creative Commons Attribution License (CC BY).

to the different $\varepsilon_{12}^{\mathrm{inh}}$ contributions, see Table 5.6. A non-zero value results in a non-symmetric course of the curve. Here, the slowest scan speed $\overline{v}^{\mathrm{lsr}} = 0.7$ mm/ms for both laser powers results in the lowest u_3-displacement at both ends of this construction, cf. Figure 5.21c. All u_3-displacements are symmetric for the examined scan patterns. Altogether, the smallest u_3-displacement is found for the parameter set $P = 250$ W and $\overline{v}^{\mathrm{lsr}} = 0.7$ mm/ms. The corresponding equivalent von Mises stress σ_{vM} and the deformed configuration (with scale-factor one) for the lowest scan speed is illustrated in Figures 5.22a and 5.22b. This coincides with the findings related to Table 5.6, where an increased laser speed seems to introduce larger eigenstrains. For the laser power $P = 250$ W the variation in displacement is more pronounced than for $P = 180$ W. This also correlates to the values of the extracted inherent strains in Table 5.6.

It has been examined that the residual stresses are mainly induced by the $\varepsilon_{11}^{\mathrm{inh}}$- and $\varepsilon_{22}^{\mathrm{inh}}$-contributions. In Figure 5.23, the stress distribution along the centred path in x_1- and x_3-direction is plotted for the σ_{11}-, σ_{22}- and σ_{vM}-contributions. Even though the values of $\varepsilon_{11}^{\mathrm{inh}}$ vary more than the $\varepsilon_{22}^{\mathrm{inh}}$-contributions, cf. Table 5.6, this is not the case for the stress distribution, compare Figures 5.23a and 5.23b. In view of the equivalent von Mises stress in Figure 5.23c, mainly the laser power P seems to influence the stress level, rather than the laser speed $\overline{v}^{\mathrm{lsr}}$. All other stress components are negligibly small compared to σ_{11} and σ_{22} and are therefore not explicitly displayed.

In general, a minimum deflection with uniformly distributed residual stresses and a fast production cycle is favourable. To gain less deflection, lower scan speeds should be chosen. However, the production time increases with decreasing scan speed, cf. Table 5.6. Obviously, these two goals require opposing scan strategies. A possible solution to obtain an appropriate compromise is to use different scan patterns for the ribs and the upper solid layers. If, for example, the cantilever is produced with a combination of scan speeds, the production time can be minimised. It is interesting to

(a)
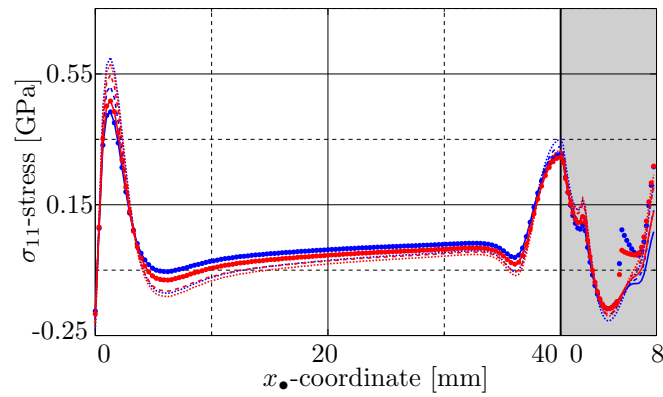
(b)
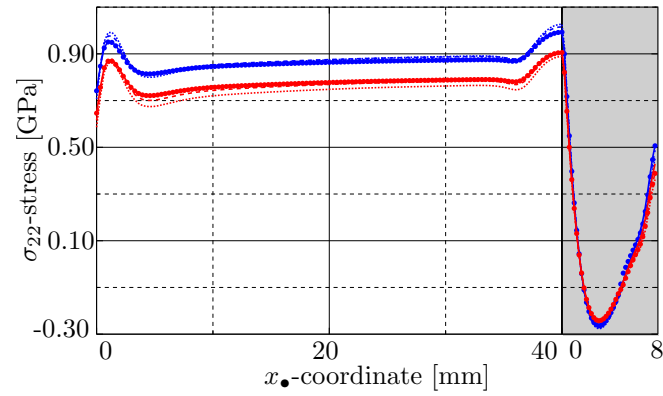
(c)
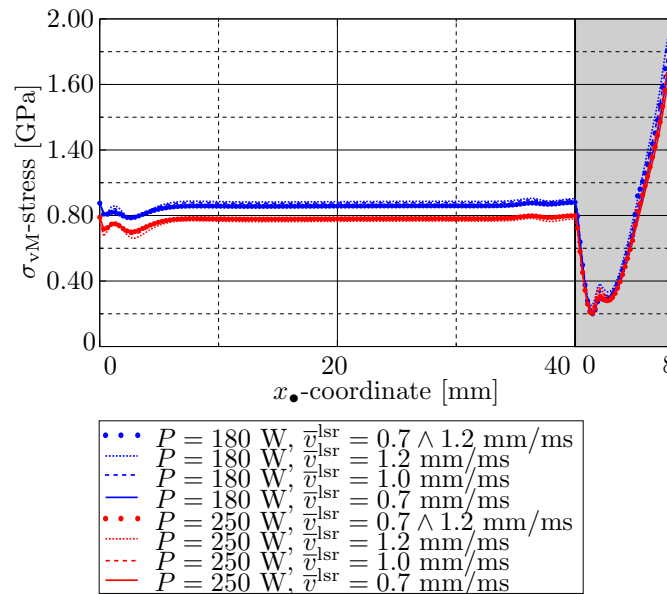
Figure 5.23: Stress distributions along x_1-coordinate (white) with $x_1(x_2 = 0, x_3 = 0)$ and x_3-coordinate (grey) with $x_3(x_1 = 40, x_2 = 0)$ at the centre of the twin cantilever beam, along the path C-D-E as indicated in Figure 5.20, in the respective direction for the corresponding laser parameter sets. Reprinted from [129] under the terms of the Creative Commons Attribution License (CC BY).

see in Figure 5.21c that the deflection does not increase if the ribs are manufactured with a scan speed $\overline{v}^{\mathrm{lsr}} = 1.2$ mm/ms, whereas the upper solid layers are manufactured with $\overline{v}^{\mathrm{lsr}} = 0.7$ mm/ms. With these parameter choices, the deflection still coincides with the one of a constant scan speed of $\overline{v}^{\mathrm{lsr}} = 0.7$ mm/ms, as visualised in Figure 5.21. In view of the von Mises stress σ_{vM}, only some minor differences are visible, as illustrated in Figures 5.22 and 5.23c. The same conclusion can be drawn when examining the σ_{11}- and σ_{22}-distributions in Figures 5.23a and 5.23b, respectively. Therefore, the use of faster scan speeds for the ribs can significantly reduce the production time while the distortion remains low.

Influence of scan pattern
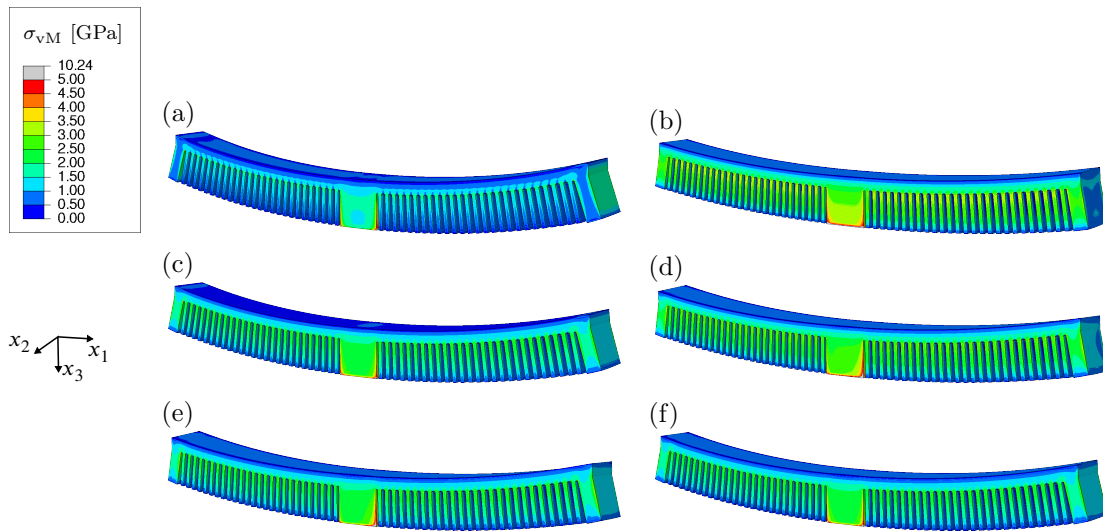
Figure 5.24: Distribution of σ_{vM}-stress and deformed configuration of twin cantilever beam for different scan patterns: (5.24a) $00°$ layer-wise (long), (5.24b) $90°$ layer-wise (short), (5.24c) $00 - 90°$ rotating pattern, (5.24d) $60°$ layer-wise, (5.24e) $45°$ layer-wise, (5.24f) $45 - 135°$ rotating pattern. Reprinted from [129] under the terms of the Creative Commons Attribution License (CC BY).

Next, the influence of different scan patterns is examined, whereby the optimal parameter set is taken with $P = 250$ W and $\overline{v}^{\mathrm{lsr}} = 0.7$ mm/ms. The manufacturing of the twin cantilever beam is simulated by using six different scan patterns, where the equivalent von Mises stress and the deformed configuration (with scale-factor one) is shown in Figure 5.24. The σ_{11}- and σ_{22}-coefficients as well as the σ_{vM}-distribution along a specific path in x_1- and x_3-direction are plotted in Figure 5.25. The results in terms of displacements are illustrated in Figure 5.26. Some specific aspects shall be discussed in the following.

When examining the displacements, it has to be distinguished between layer-wise scanning and rotating patterns. The results for the rotating patterns are rather symmetric. In contrast, especially for the non-symmetric $60°$ and $45°$ layer-wise scanning,
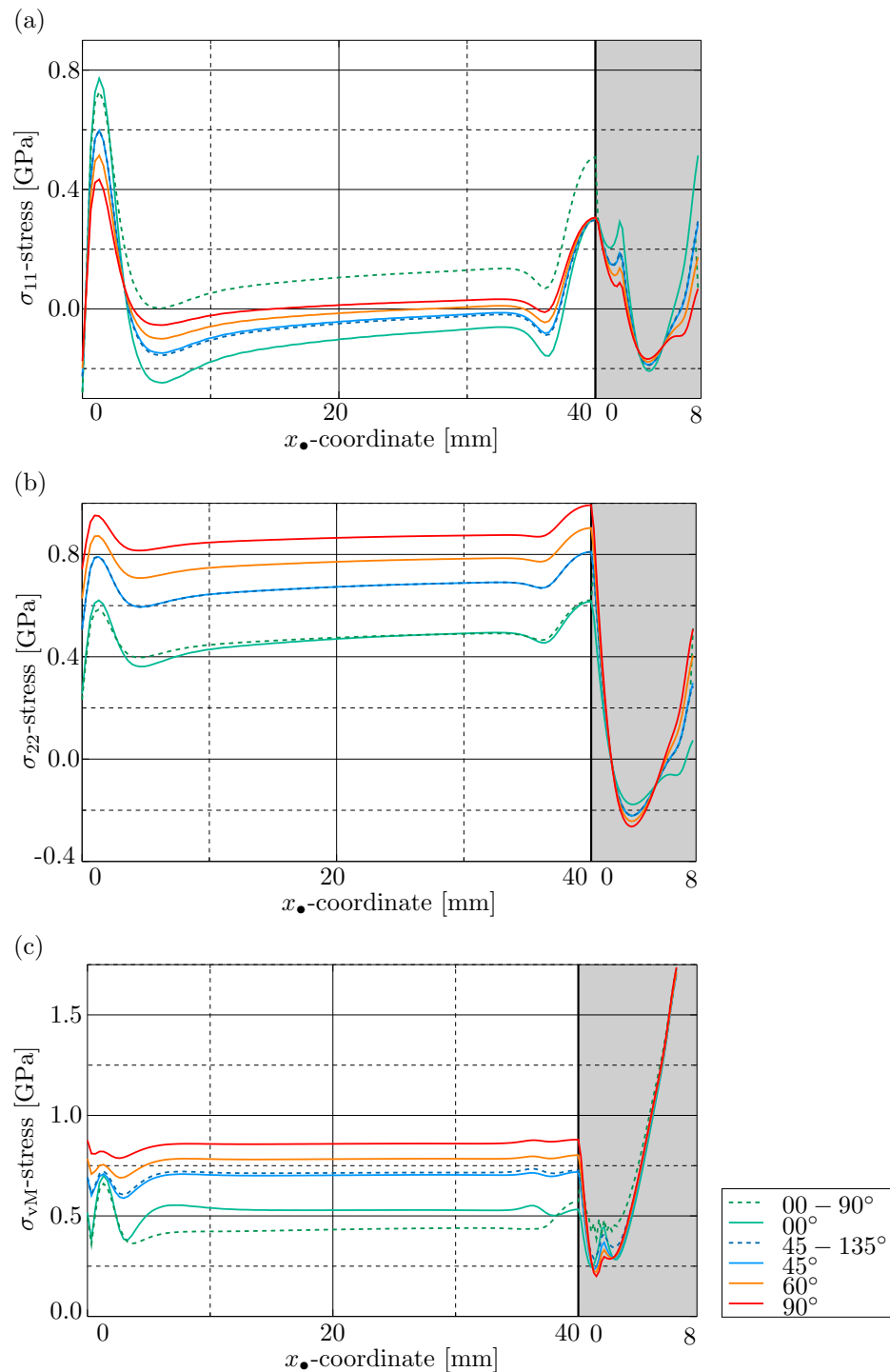
Figure 5.25: Stress distributions along x_1-coordinate (white) with $x_1(x_2 = 0, x_3 = 0)$ and x_3-coordinate (grey) with $x_3(x_1 = 40, x_2 = 0)$ at the centre of the twin cantilever beam, along the path C-D-E as indicated in Figure 5.20, in the respective direction due to different scan patterns. Reprinted from [129] under the terms of the Creative Commons Attribution License (CC BY).

(a)

(b)

(c)
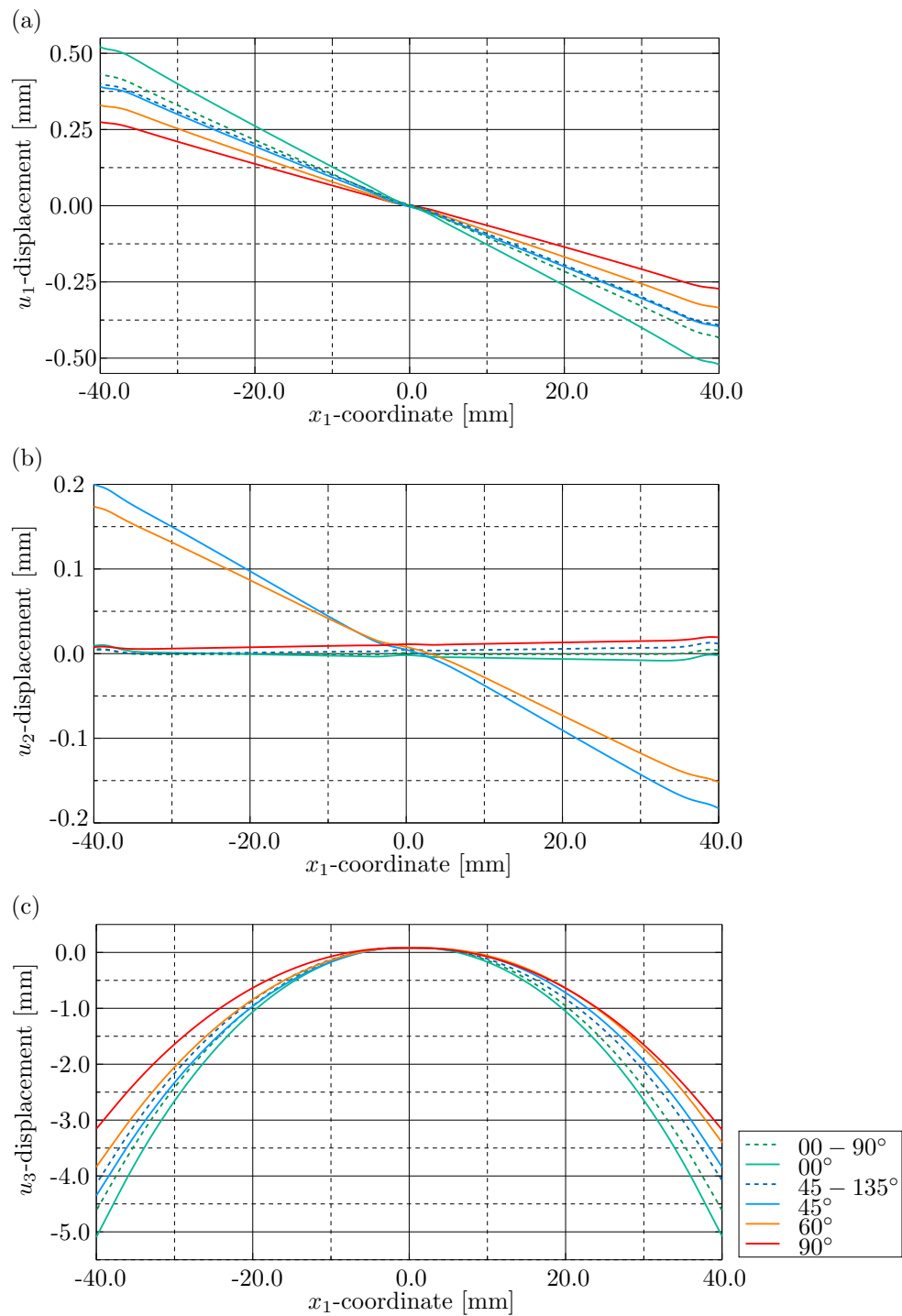
Figure 5.26: Displacements along x_1-coordinate at the top edge of the twin cantilever beam, along the path A-B as indicated in Figure 5.20, in the respective direction due to different scan patterns. Reprinted from [129] under the terms of the Creative Commons Attribution License (CC BY).
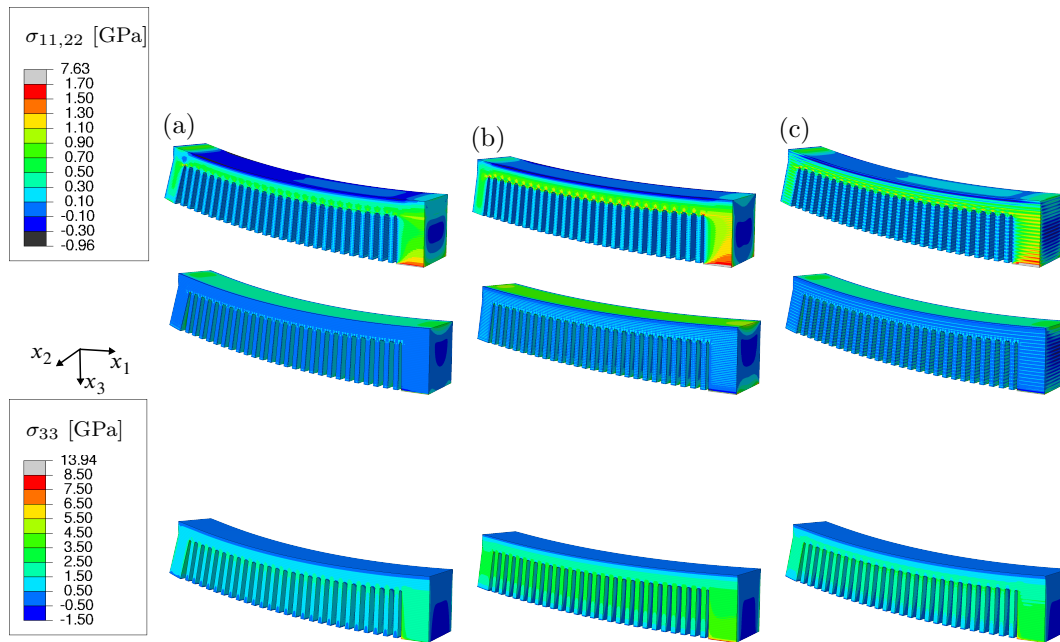
Figure 5.27: Stress contributions σ_{11} (first row), σ_{22} (second row) and σ_{33} (third row) and deformed configuration of half of twin cantilever beam for different scan patterns: (5.27a) $00°$ layer-wise (long), (5.27b) $90°$ layer-wise (short), (5.27c) $00 - 90°$ rotating pattern. Reprinted from [129] under the terms of the Creative Commons Attribution License (CC BY).

the twin cantilever beam is significantly twisted as visualised in Figure 5.26b and Figures 5.24d and 5.24e (scale-factor one). For these cases, the u_3-displacement at both edges is also different, compare Figure 5.26c. Here, also non-symmetric von Mises stress distributions are visible. Interestingly, the torsion of the twin cantilever beam is insignificant for the $45 - 135°$ rotating pattern. The highest necking and deformation while having the lowest σ_{11}- and σ_{22}-contributions, compare Figures 5.25a and 5.25b, respectively, are present for $00°$ layer-wise scanning as also pictured in Figure 5.24a, whereas the contrary behaviour is present for $90°$ layer-wise, cf. Figure 5.24c.

The general results are qualitatively comparable with the normalised vertical distortion shown in [158] and the longitudinal necking shrinkage behaviour reported in [104]. In general, the least bending of the specimen is present for the $90°$ scanning, see also [94]. Due to the different scan patterns, distinct maximal temperatures and temperature gradients are present in the physical process. For this modelling approach, temperature is only a degree of freedom in the laser scan model and layer hatch model. However, varying the scan pattern indirectly affects the results of the part model which can be explained due to the theoretical temperature history. The laser takes different time spans to reach the neighbouring laser track. While the highest temperature input is present for $90°$ layer-wise, the lowest is necessary for $00°$ layer-wise. It is concluded that, among other reasons, the residual stresses are reduced by lower thermal gradients, also referred to as temperature gradient mechanism, e.g. [33, 119]. When focusing on specific stress

contributions in detail, cf. Figures 5.27b, 5.27a, 5.25a and 5.25b, the stresses are higher for 90° layer-wise in comparison to 00° layer-wise. Especially in the centred support structure, a difference becomes visible for σ_{11} and σ_{22}-contributions between 00° and 90° layer-wise scan patterns. In general, the highest stresses can be found in x_3-direction. For the $00-90°$ rotating scan pattern, it is visible in Figure 5.27c how the σ_{11}- and σ_{22}-contributions are rotated for each layer due to the prescribed inherent strain pattern. Thus, the stress distribution and magnitude distinctly changes. As can be seen in Figure 5.25c, the von Mises stress distribution σ_{vM} is the lowest for $00-90°$. Therefore, rotating scan patterns may be favourable in terms of stress distributions. The highest magnitude is visible for 90°. However, the least bending is present for this scan pattern, cf. Figure 5.26c.

In summary, two different effects can be observed, compare Table 5.6. On the one hand, lower scan speeds, for example across the height of the structure, reduce the $\varepsilon_{22}^{\mathrm{inh}}$-component, while $\varepsilon_{11}^{\mathrm{inh}}$ is kept rather constant. On the other hand, a higher laser power increases the $\varepsilon_{11}^{\mathrm{inh}}$-component, but does not change the inherent strain magnitude of $\varepsilon_{22}^{\mathrm{inh}}$ for constant scan speeds. However, a higher laser power and lower scan speed increase the melt pool size. The simulations show that the use of different scan speeds for the ribs and the twin cantilever beam itself influences the overall deformation only marginally, whereas the manufacturing time of one production cycle is significantly reduced. Distortion of the workpiece is present for non-symmetric layer-wise scan patterns, whereas rotating scan patterns are preferential in terms of the σ_{11}- and σ_{22}-distribution.

Overall, however, the von Mises stress is far beyond the yield limit of $\mathrm{Ti_6Al_4V}$. The yield limit of the titanium aluminium alloy is only taken into account for the laser scan and layer hatch model, cf. eqs. (5.5) and (5.14), respectively. In contrast, a purely elastic material model is used for the complete part, see eq. (5.22). This is the current standard approach for the IS method, cf. [30, 103, 143, 158]. The question arises as to whether plasticity should be additionally considered for the part model in order to reduce the overall stress response to a realistic magnitude. This is the case for the inverse experimental approach in e.g. [160].

C Appendix

C.1 Implementation of inherent strain method using the `AM-Modeler`

The main advantage of the `AM-Modeler` lies in the simulation of more complicated scan patterns, e.g. island scan patterns. However, using this special purpose technique is not that straightforward. In the Abaqus manual, compare [1], the relevant information is summarised under *additive manufacturing process simulation*. If the inherent strain method shall be used, this is referred to as *eigenstrain-based simulation of additive manufacturing processes*. For the multiscale approach, a layer-by-layer activation approach is used, which leads to a *pattern-based* eigenstrain analysis. This is in contrast to a *trajectory-based* eigenstrain analysis, in which elements are activated according to the trajectory of e.g. the path of the laser beam in LPBF processes.

Table 5.9: Overview of necessary parameter tables `ABQ_AM_EigenStrain_`*keyword* for the table collection `ABQ_EIG.`*name* of an eigenstrain based analysis using the `AM-Modeler`.

Keyword	**Content**
Method	"PatternBased" activation
Define	components of eigenstrain tensor ε^{inh}
PatternBased_Activation	build parameters for layer activation, e.g. layer thickness, coordinate system, time,
PatternBased_Define	patch/island of scan pattern with local rotation angle, size and eigenstrain
PatternBased_ScanStrategy_Define	region of particular scan pattern strategy, i.e. patch/island, with global rotation angle between layers
PatternBased_ScanStrategies	list of labels of former keyword, e.g. to realise different scan strategies based on part height
PatternBased_Advanced	"layerbylayer" activation

In general, python scripts can be used to generate more complicated models in Abaqus. If the `AM-Modeler` shall be used, this database has to be imported by using the appropriate system path and subsequently installed. The regular model can then be imported, creating the corresponding AM-Model. Characteristic for this special purpose technique of an eigenstrain analysis is that a *table collection* has to be specified beginning with `ABQ_EIG.`*name*. Within this table collection, different *parameter tables* of the type `ABQ_AM_EigenStrain_`*keyword* have to be included as summarised in Table 5.9. In addition, the *progressive element activation* has to be defined. In the case of a pattern-based eigenstrain analysis, usually a complete layer is activated at once. Two steps are then necessary for the simulation: First, all layers are consecutively activated and the respective inherent strains are applied based on the predefined scan pattern. This is done via *activate elements* referring to the progressive element activation and

by using the table collection `ABQ_EIG.`*name*. Secondly, the boundary conditions are deactivated to release stresses and to visualise the warpage.

C.2 Influence of dissipation parameter η^ξ

The influence of the dissipation parameter η^ξ shall be briefly discussed. The liquidus and solidus temperatures for the titan aluminium alloy Ti_6Al_4V are given in [25] as 1923.15 K and 1878.15 K, respectively. The temperature range between liquidus and solidus depends on the used material and is rather small for the material at hand. To model a smooth transition of ζ_{mel} due to the evolving temperature, the parameter η^ξ is introduced in the time dependent dissipation function $\mathcal{C}^\xi$, compare eq. (4.43). As the dissipation quantity η^ξ is incorporated into the material model as a viscous-type quantity, the time and thus the laser beam velocity influences the result as well. In addition, the parameter also increases the numerical stability of the local FE-scheme in view of the time step size. To show the influence of the parameter η^ξ on the evolution of the molten pool, different dissipation parameters are used for a representative example with $P = 250$ W and $\overline{v}^{lsr} = 1.2$ m/s, as visualised in Figure 5.28. The temperature evolution in Figure 5.28a is almost independent of the values chosen for η^ξ, only the peak temperature increases visibly with larger η^ξ. It becomes obvious that evaporation would exist for this material parameter combination, which shall not further be discussed at this point, compare Remark 12. However, the corresponding distribution of the molten mass fraction ζ_{mel} as illustrated in Figure 5.28b varies considerably. For increasing η^ξ, the time span extends, mainly due to the longer conversion from molten to the re-solidified material. Without parameter η^ξ, two jumps of the molten mass fraction ζ_{mel} would exist.

C.3 Influence of thermomechanical coupling r_{mech}

For the dissipation parameter $\eta^\xi = 0.002$, an exemplary temperature evolution θ and the corresponding mass fraction of the molten phase ζ_{mel} are visualised for a centred element of the laser scan model, see Figure 5.29. Here, the temperature and mass fraction of an uncoupled model, where r_{mech} as introduced in eq. (2.62) is neglected, and of the coupled model at hand is illustrated. It becomes apparent that the thermomechanical coupling considerably influences not only the temperature but also the mass fraction evolution. Thus, it is important to incorporate the quantities for volumetric heat generation `RPL` within the Abaqus subroutine `UMAT`. The temperature plateau for the fully coupled model (solid line) is observable due to the influence of the latent heat of fusion. For the coupled model, a mixed region of powder and molten material is present between 1970 K and 5800 K and between molten pool and re-solidified material between 1830 K and 1711 K. The procedure based on which the temperatures θ^{melt} and θ^{solid} are extracted is explained in Section 5.2.2. The material in the layer hatch model will be completely solidified when θ^{solid} is reached, which lies within the temperature plateau.
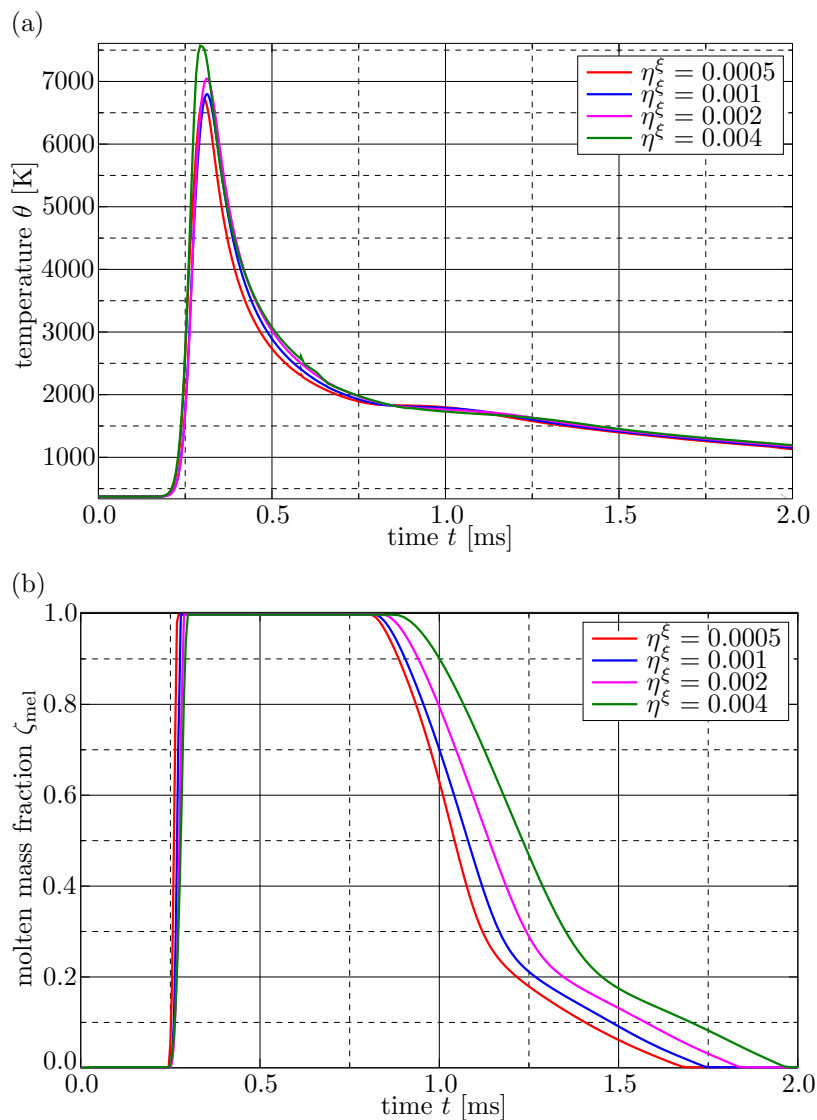
Figure 5.28: Evolution of temperature θ (5.28a) and molten mass fraction ζ_{mel} (5.28b) to show the influence of η^{ξ} for a centred element with laser parameters $P = 250$ W and $\overline{v}^{\mathrm{lsr}} = 1.2$ m/s. Reprinted from [129] under the terms of the Creative Commons Attribution License (CC BY).

C.4 Layer lumping

To gain reasonable results in terms of final deformation and residual stress, a case study based on the modelling of explicit layer numbers is performed, cf. [103]. The results for the twin cantilever beam are summarised in Figure 5.30, where a constant 90° layer-wise scan pattern is used. For a workpiece height of 8.0 mm with a layer height of 0.03 mm, 267 physical layers are necessary to manufacture the part. The simulations are performed for up to 188 physical layers, which means that two layers are lumped. Lumping describes
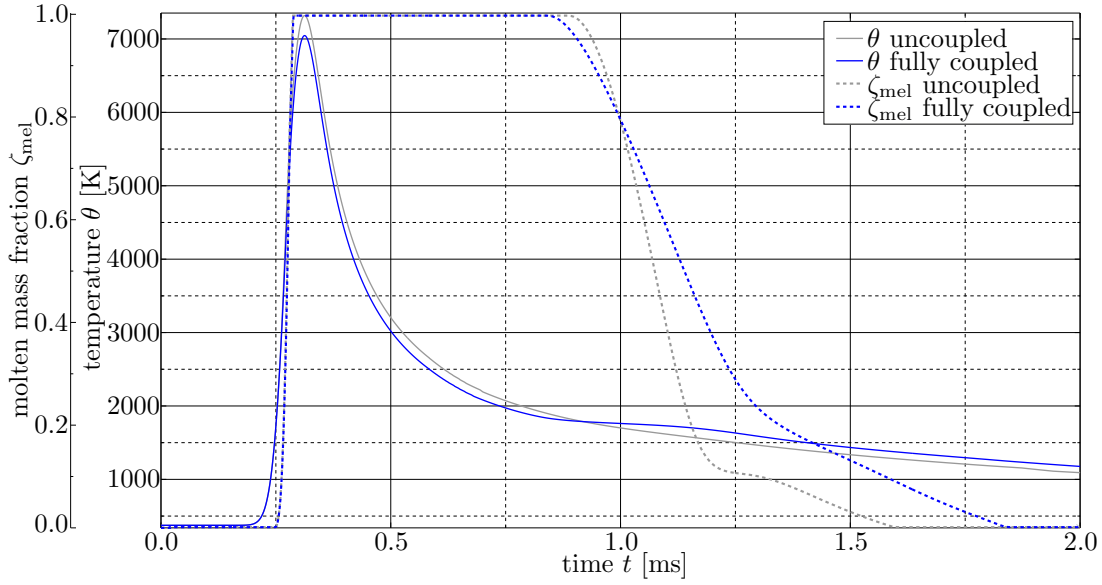
Figure 5.29: Evolution of temperature θ (solid) and molten mass fraction ζ_{mel} (dashed) in the middle of the melt pool for coupled model (blue) and uncoupled model (grey) with laser parameters $P = 250$ W and $\bar{v}^{\mathrm{lsr}} = 1.2$ m/s, while $\eta^{\xi} = 0.002$. Reprinted from [129] under the terms of the Creative Commons Attribution License (CC BY).

how many layers are consolidated in the simulation. In Figure 5.30a, the u_3-displacement vs. the equivalent layer number is visualised, whereas in Figure 5.30b the displacement vs. the number of lumped layers is illustrated. The displacement variance decreases for increasing equivalent layer numbers. As the simulation time increases with increasing equivalent layer numbers, the twin cantilever beam is simulated with 38 equivalent layers which corresponds to seven lumped layers. For this value, the change in u_3-displacement is minor.
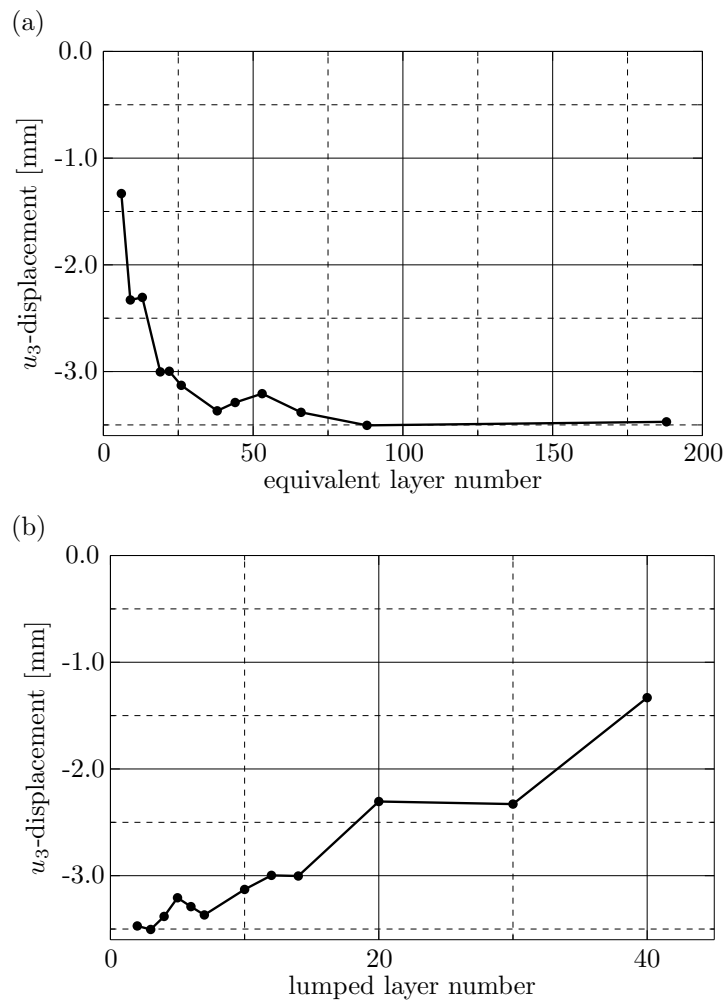
Figure 5.30: u_3-displacement vs. equivalent layer number (5.30a) and vs. lumped layer number (5.30b) for constant laser parameters with $P = 250$ W and $\overline{v}^{\mathrm{lsr}} = 0.7$ m/s and 90° layer-wise scan pattern. Reprinted from [129] under the terms of the Creative Commons Attribution License (CC BY).

6 A phase transformation model for titan aluminium alloys

Titan aluminium alloys as, e.g., Ti_6Al_4V, belong to the group of α-β-alloys, which are used for many applications in industry due to their advantageous mechanical properties. For LPBF processes, Ti_6Al_4V is one of the most frequently used titanium alloys, compare, e.g., [45]. Therefore, this alloy is used for all process simulations in Chapters 3 to 5. However, the composition of the crystal structure and the respective magnitude of the solid fraction highly influences the material properties of titan aluminium alloys. Specifically, the thermal history, i.e. the cooling rate, determines the phase composition and microstructure for example during heat treatment and LPBF processes. For that reason, this chapter introduces a phase transformation framework based, amongst others, on energy densities and thermodynamically consistent evolution equations similar to Chapter 4, which is able to capture the different material compositions in the solid-state resulting from various cooling and heating rates. The evolution of the underlying phases is governed by a specifically designed dissipation function, the coefficients of which are determined by a parameter identification process based on available continuous cooling temperature (CCT) diagrams. In order to calibrate the model and its preparation for further applications such as the simulation of additive manufacturing (AM) processes, these CCT diagrams are computationally reconstructed. In contrast to empirical formulations, the developed thermodynamically consistent and physically sound model can straightforwardly be extended to further phase fractions and different materials. With this formulation, it is possible to predict not only the microstructure evolution during processes with high temperature gradients, as occurring in, e.g., LPBF processes, but also the evolving strains during and at the end of the process on a local scale.

This chapter is structured as follows: At first, more insight into the material properties of the titan aluminium alloy is given in Section 6.1. In Section 6.2, the general concept of the melt-solid-solid phase transformation framework with an extended dissipation function is presented. Thereafter, the algorithmic implementation is summarised in Section 6.3, where a focus is set on the parameter identification process for the dissipation function. In Section 6.4, the reproduced CCT diagram and examples of different boundary value problems on a local scale demonstrate the capability of the model at hand.

6.1 Material properties of titan aluminium alloy Ti$_6$Al$_4$V

Ti$_6$Al$_4$V belongs to the group of α-β-alloys, which possess different phases with distinct crystal structures, compare Figure 6.1. Therefore, consideration of the transitions between the β- and the different α-phases is of great importance for the modelling and simulation of, e.g., LPBF processes. Table 6.1 gives an overview of the chemical composition. It influences the volume fractions of the α- and β-phases along specific temperature paths. The α-phase is stabilised by aluminium and the β-phase is stabilised by vanadium. In addition, the β-transus temperature $\theta_{\beta,\text{trans}}$ depends on the material composition. Especially the content of oxygen, as well as the heat treatment define the final crystal structure of the material. The α-phase can consist of lamellar or equiaxed microstructures as well as a combination of both, see [25, 98] for further information. The lamellar structure of the α-phase can be influenced by the cooling rate or heat treatment with e.g. furnace, air, water or gas. This may result in plate-like α-, acicular α-, Widmanstaetten α-, hcp martensite α'- or in orthorhombic martensite α''-phases. Based on the resulting microstructure, the thermal and mechanical properties of the titanium alloy differ significantly, respectively are considerably influenced.
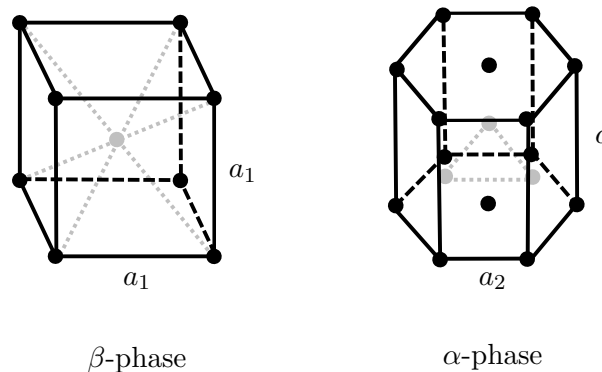
Figure 6.1: Crystal structures of unit cell for β- and α-phases of Ti$_6$Al$_4$V with lattice parameters $a_1 = 0.319$ nm for bcc and $a_2 = 0.2925$ nm, $c = 0.4670$ nm for hcp, cf. [25]. Reprinted from [130] under the terms of the Creative Commons Attribution License (CC BY).

Table 6.1: Chemical composition of Ti$_6$Al$_4$V (mass fraction in %) according to, e.g., DIN EN ISO 5832-3 [44].

Element	Al	V	Fe	O	N	C	H	Ti
min.	5.50	3.5	–	–	–	–	–	balance
max.	6.75	4.5	0.30	0.20	0.05	0.08	0.015	balance

Especially high heating and cooling rates (up to 10^3-10^8 K/s) are characteristic during and shortly after the material is heated by the laser beam, cf. [17, 105, 117, 166]. In addition, process parameters influence the overall temperature history and thus the microstructure, resulting in fine acicular α'-martensite structures, as illustrated in Figure 6.2a, or in β-grain boundaries with α'-martensites in-between, cf. [137, 163]. Subjacent layers and previous melt tracks exhibit significantly different temperature gradients, while low rates are present during the final cooling period. If subsequent annealing is used, a new and distinct temperature cycle is applied to the material changing the overall microstructure, compare Figure 6.2b, and mechanical behaviour, cf. the experimental investigations in [105, 111, 178].
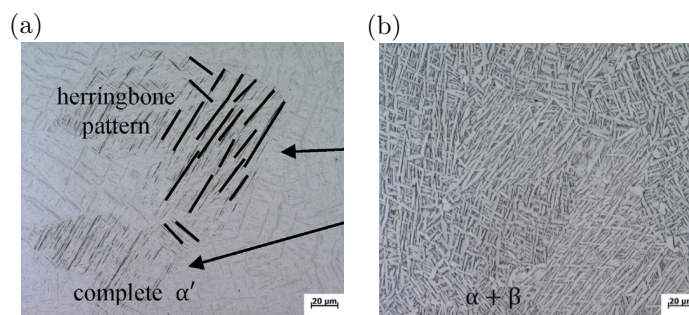
Figure 6.2: In-plane microstructure of Ti_6Al_4V parts manufactured by LPBF: (6.2a) as fabricated ($P = 280$ W, $\overline{v}^{\text{lsr}} = 1.2$ m/s) resulting in complete α' martensite with herringbone pattern and columnar grains due to alternating scanning direction, (6.2b) heat treated at $900°$ C resulting in $\approx 30\%$ β-phase. Reprinted from Journal of Alloys and Compounds, 782, Liang, Z., Sun, Z., Zhang, W., Wu, S., Chang, H., The effect of heat treatment on microstructure evolution and tensile properties of selective laser melted Ti6Al4V alloy, 1041–1048, Copyright (2019), with permission from Elsevier, [105].

Therefore, not only time temperature transformation (TTT) diagrams, but mostly CCT diagrams are necessary to understand the material's behaviour and to calibrate material models. Experimental studies of $\beta \rightarrow \alpha$ phase transformation during continuous cooling can be found in, e.g., [4, 39, 74, 115, 144]. In the previously mentioned literature, one has to distinguish between cooling curves that were actually measured on the specimen, also denoted as part, and are therefore not constant in the cooling rate $\dot{\theta}$ (e.g. [4, 39, 167]) and constant cooling curves (e.g. [74, 115]), where the prescribed constant temperature rate $\dot{\theta}$ is used to construct the CCT diagram. A schematic CCT diagram was first published in [4], compare Figure 6.3, where the continuous cooling by using water or helium gas was monitored by thermocouples. An overview of different critical cooling rates and characteristic temperatures is provided in Tables 6.2 and 6.3.

In [115], experimental investigations on the time-dependent evolution of phase fractions are presented. This evolution is generally characterised by an asymptotic behaviour towards values of zero and one. Furthermore, a clear tendency towards faster transformations for higher cooling rates is shown. In addition, at slow cooling rates it is observed that the considered specimen exhibits a residual β-phase fraction of 9% in the final
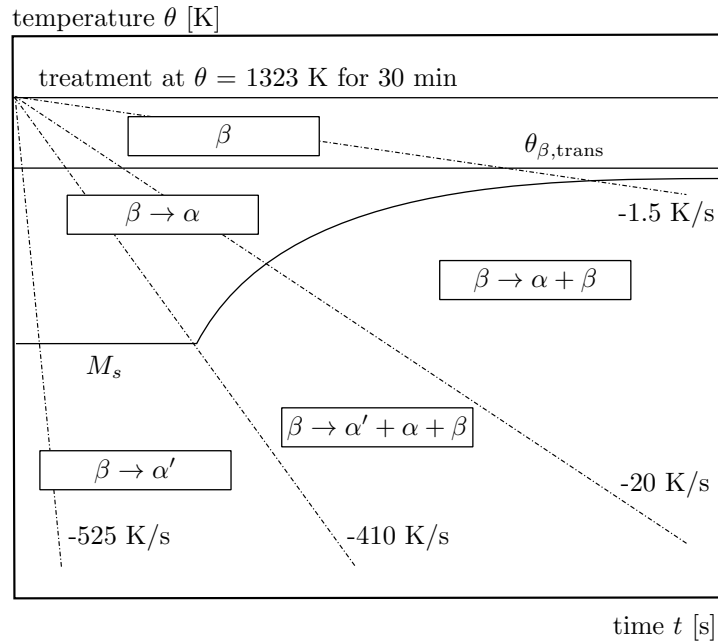
temperature θ [K]

Figure 6.3: Schematic CCT diagram for Ti$_6$Al$_4$V. At the temperature $\theta_{\beta,\text{trans}}$, the β-phase first transforms (partially) into the α-phase. Subsequently, different α-phases form depending on the temperature and cooling rate, where M_s refers to the martensitic start temperature. Reprinted from Materials Science and Engineering, 243, Ahmed, T., Rack, H., Phase transformations during cooling in $\alpha+\beta$ titanium alloys, 206-2011, Copyright (1998), with permission from Elsevier, [4].

cooled state. In [74], it is reported that the amount of residual β-phase depends on the cooling rates ranging from 12.7 % for higher cooling rates to 6.5 % for lower cooling rates. The experimentally obtained results shown in [167] also confirm the occurrence of residual β-phase. The state of research uniformly confirms that the morphology of the α-phase depends on the cooling rate: decreasing the cooling rate results in increased lamella, respectively grain size, whereas the morphology changes from Widmannstaetten lamellas to equiaxed grain.

Table 6.2: Literature overview of critical cooling rates $\dot{\theta}$ for the different transformation possibilities of Ti$_6$Al$_4$V.

Reference	Diffusive $\beta \to \alpha + \beta$	Mixed $\beta \to \alpha' + \alpha + \beta$	Diffusionless (martensitic) $\beta \to \alpha'$
[4]	< 20 K/s	20 – 410 K/s	> 410 K/s
[115]	0.167 – 0.83 K/s	-	-
[74]	0.01 – 10 K/s	-	18 – 200 K/s
[39]	0.012 – 2.5 K/s	7.3 K/s	23.1 K/s

Table 6.3: Literature overview of characteristic temperatures of $\text{Ti}_6\text{Al}_4\text{V}$ during cooling.

Reference	β-transus $\theta_{\beta,\text{trans}}$	Martensitic start M_s	Martensitic finish M_f
[4]	1267 K	848 K	-
[115]	1243 K	-	-
[144]	1268 K	-	-
[74]	1243 K	1143 K	998 K
[39]	1243 K	1188 K	963 K

6.2 Constitutive framework

The phase transformation framework is based on the consideration of two solid phases, which is important for the underlying titan aluminium alloy as explained in Section 6.1. In analogy to Chapter 4, the constitutive framework is briefly summarised in the following. For the current material model, three distinct phase energy densities are used, namely the molten phase, the solid β-phase and the solid α-phase, which are introduced in Section 6.2.1. In addition, the homogenisation approach is recapitulated. Furthermore, the evolution equations with the corresponding parameters are introduced, which are used to adapt the material behaviour of the phase transformation model for different cooling rates. In contrast to Chapter 4, the focus is set on a non-standard dissipation function, which is introduced in Section 6.2.2.

6.2.1 Material model

The constitutive framework used in this work is based on the model established in Section 4.1. While focusing on the transformation from the molten to the solid phases in the present work, the framework of Chapter 4 is extended in terms of the consideration of two solid-phases, namely the β- and α-phases. As this work proceeds, no distinction between α- and α'-phases shall be made and the material behaviour in the solid phases is assumed purely elastic. However, related model extensions would be possible in a straightforward manner.

First, the phase energy density of the molten phase is introduced in a small strain setting as

$$\psi_{\text{mel}} := \frac{1}{2} \left[\boldsymbol{\varepsilon}_{\text{mel}} - \boldsymbol{\varepsilon}_{\text{mel}}^{\text{trans}} \right] : \mathbf{E}_{\text{mel}} : \left[\boldsymbol{\varepsilon}_{\text{mel}} - \boldsymbol{\varepsilon}_{\text{mel}}^{\text{trans}} \right] - \widetilde{c}_{\text{mel}} \, \theta \ln(\theta) - L_{\text{mel}} \frac{\theta - \theta_{\text{mel}}^{\text{ref}}}{\theta_{\text{mel}}^{\text{ref}}} \, , \quad (6.1)$$

where $\boldsymbol{\varepsilon}_{\bullet}$ refers to the total strain, $\mathbf{E}_{\bullet}$ represents the fourth-order isotropic elasticity tensor, $\widetilde{c}_{\bullet} = \rho_{\bullet} \, c$ denotes the weighted heat capacity, θ is the absolute temperature, and $L_{\bullet} = \rho_{\bullet} \, L$ indicates the weighted latent heat with reference temperature $\theta_{\bullet}^{\text{ref}}$ of the corresponding phase. Moreover, $\boldsymbol{\varepsilon}_{\text{mel}}^{\text{trans}}$ determines the transformation strains between

the solid and molten phase, compare eq. (4.10) and Remark 15. The visco-elastic strain contributions considered in Section 4.1 are neglected here since these mainly evolve during the powder-melt transformation which is not taken into account in the present work.

In addition, the respective energy densities of the solid phases are defined as

$$\psi_{\mathrm{sol},\beta} := \frac{1}{2} \left[\boldsymbol{\varepsilon}_{\mathrm{sol},\beta} - \boldsymbol{\varepsilon}_{\mathrm{sol},\beta}^{\mathrm{inel}} \right] : \mathbf{E}_{\mathrm{sol},\beta} : \left[\boldsymbol{\varepsilon}_{\mathrm{sol},\beta} - \boldsymbol{\varepsilon}_{\mathrm{sol},\beta}^{\mathrm{inel}} \right] - \widetilde{c}_{\mathrm{sol},\beta}\, \theta \ln(\theta) - L_{\mathrm{sol},\beta}\, \frac{\theta - \theta_{\mathrm{sol},\beta}^{\mathrm{ref}}}{\theta_{\mathrm{sol},\beta}^{\mathrm{ref}}} \;,$$
$$(6.2)$$

$$\psi_{\mathrm{sol},\alpha} := \frac{1}{2} \left[\boldsymbol{\varepsilon}_{\mathrm{sol},\alpha} - \boldsymbol{\varepsilon}_{\mathrm{sol},\alpha}^{\mathrm{inel}} \right] : \mathbf{E}_{\mathrm{sol},\alpha} : \left[\boldsymbol{\varepsilon}_{\mathrm{sol},\alpha} - \boldsymbol{\varepsilon}_{\mathrm{sol},\alpha}^{\mathrm{inel}} \right] - \widetilde{c}_{\mathrm{sol},\alpha}\, \theta \ln(\theta) \;, \tag{6.3}$$

where

$$\boldsymbol{\varepsilon}_{\mathrm{sol},\bullet}^{\mathrm{inel}} = \boldsymbol{\varepsilon}_{\mathrm{sol},\bullet}^{\mathrm{th}} + \boldsymbol{\varepsilon}_{\mathrm{sol},\bullet}^{\mathrm{trans}} \tag{6.4}$$

determines the inelastic strain contributions of the respective solid phase. A transformation strain $\boldsymbol{\varepsilon}_{\mathrm{sol},\bullet}^{\mathrm{trans}}$ and a thermal strain $\boldsymbol{\varepsilon}_{\mathrm{sol},\bullet}^{\mathrm{th}}$ is considered for the solid phases to take into account the shrinkage after melting and the expansion, respectively shrinkage due to the heat input. The thermal strains are included based on a standard linear heat expansion approach with the isotropic heat expansion coefficient $\alpha_{\mathrm{sol},\bullet}$ and the respective reference temperature $\theta_{\mathrm{sol},\bullet}^{\mathrm{ref}}$, compare eq. (3.45), while the solid-transformation strain which is assumed to be spherical is based on eq. (4.10). Further enhancements of the material model are possible, compare Section 4.1, where visco-elasticity and plasticity are incorporated, and Section 5.1.1, where visco-plasticity is considered.

Remark 15. *The (infinitesimal) initial volume* $\mathrm{d}V_0$ *is defined based on eq. (4.8). Here, the initial mass density* ρ_0 *is defined by the mass density of the initially present phase, i.e. either melt or solid-β in the present work, which depends on the boundary value problem. With this at hand, it is possible to derive the transformation strain according to eq. (4.10).*

Based on the approach of homogenisation via energy relaxation, compare e.g. Sections 3.1.1 and 4.1.3, material models can be developed that are unconditionally thermodynamically consistent and mathematically well-posed. The basic approach stems from martensitic phase transformations, where volume fractions and the averaged volume specific energy are used, see, e.g., [135]. For the application at hand, the algorithm is formulated with respect to the mass fractions $\zeta_\bullet = \mathrm{d}m_\bullet/\mathrm{d}m_0$, compare eq. (4.13), where $\mathrm{d}m_\bullet$ corresponds to the mass contribution of phase $\bullet$ and $\mathrm{d}m_0$ to the initial mass, both referred to a material point. In consequence, the averaged mass specific energy $\overline{\Psi}$ can be introduced based on the different mass densities in the solid and molten phase, see Chapter 4 for a more detailed overview. Moreover, it is possible to relate the mass fractions $\zeta_\bullet$ to the volume fractions $\xi_\bullet$ via eq. (4.14). The overall energy $\overline{\Psi}$ is calculated

via a linear mixture rule of the mass specific phases Ψ as defined in eq. (4.15). This averaged energy density is minimised subject to the constraints of feasible mass fraction domains, i.e. $\zeta_\bullet \in \mathcal{A}$ with

$$\mathcal{A} := \{ 0 \leq \zeta_\bullet \leq R_\bullet^{\mathrm{up}} \, , \; \zeta_{\mathrm{mel}} + \zeta_{\mathrm{sol},\beta} + \zeta_{\mathrm{sol},\alpha} = 1 \} \, , \tag{6.5}$$

and the domain of the admissible strain distributions, also denoted compatibility condition, i.e. $\varepsilon_\bullet \in \mathcal{E}$ with

$$\mathcal{E} = \{ \zeta_{\mathrm{mel}} \, \varepsilon_{\mathrm{mel}} + \zeta_{\mathrm{sol},\beta} \, \varepsilon_{\mathrm{sol},\beta} + \zeta_{\mathrm{sol},\alpha} \, \varepsilon_{\mathrm{sol},\alpha} = \varepsilon \} \, . \tag{6.6}$$

Therein, $R_\bullet^{\mathrm{up}}$ defines the upper bound of the respective mass fraction $\bullet$, which will be discussed in Section 6.3.1. The constrained minimisation as introduced in eq. (4.21) would result in the so-called convex hull $\mathrm{C}\overline{\Psi}$ of $\overline{\Psi}$, which is identical to the Reuss bound. In the present approach however, only the different total strains in each phase are determined via

$$\{ \varepsilon_\bullet \} = \arg \inf_{\varepsilon_\bullet \in \mathcal{E}} \overline{\Psi} \, . \tag{6.7}$$

The evolution of mass fractions is, in contrast to strains, associated with dissipation and thus treated differently as discussed in the subsequent section. The evolution of mass fractions is, in contrast to strains, associated with dissipation and thus treated differently as discussed in the subsequent section. In line with the hyperelastic format, stresses are determined via eq. (4.31).

6.2.2 Evolution equations

As indicated above, the evolution of volume, respectively mass fractions is associated with dissipation. According to, e.g., [22], and already applied in Section 4.1.4, variational principles can be used to define

$$\frac{\partial \overline{\psi}}{\partial \xi_\bullet} + \frac{\partial \mathcal{C}}{\partial \dot{\xi}_\bullet} = 0 \tag{6.8}$$

as representation of evolution equations for the variables $\xi_\bullet$ depending on the dissipation function $\mathcal{C}$. Therein, notation $\dot{\bullet}$ indicates the derivative with respect to time. The first term in eq. (6.8) includes the so-called driving forces $\mathcal{F}_\bullet := -\partial_{\xi_\bullet} \overline{\psi}$. In the present work, the dissipation function is chosen as

$$\mathcal{C} = \sum_\bullet Y_\bullet |\dot{\xi}_\bullet| + \frac{\eta_\bullet}{2} \dot{\xi}_\bullet^{\,2} - \mathcal{C}_\bullet'(\xi_\bullet) |\dot{\xi}_\bullet| \, . \tag{6.9}$$

The coefficients $Y_\bullet \geq 0$ and $\eta_\bullet \geq 0$ can be interpreted as a threshold $Y_\bullet$ where the phase transformation is initiated, and as a viscosity-like parameter $\eta_\bullet$ that influences the range of the (rate-dependent) phase transformation. For further insight into these parameters, the interested reader is referred to [16] and Remark 16. The additional term $\mathcal{C}'_\bullet(\xi_\bullet)$ is here defined as

$$\mathcal{C}'_\bullet(\xi_\bullet) = a_{\bullet 1}\, \xi_\bullet + a_{\bullet 2}\, \xi_\bullet^2 + a_{\bullet 3}\, \xi_\bullet^3 \tag{6.10}$$

and adopted from [16], where bainitic phase transformations are considered. As shown in [115], $\text{Ti}_6\text{Al}_4\text{V}$ behaves quite similarly to bainite in terms of the evolution of phase fractions, in particular for slow cooling rates, as visualised in Figure 6.4, see also Remark 16. The coefficients $Y_\bullet$, $\eta_\bullet$, $a_{\bullet 1}$, $a_{\bullet 2}$ and $a_{\bullet 3}$ significantly affect the material behaviour. Therefore, special attention will be paid to the determination of these coefficients in Section 6.3.3.
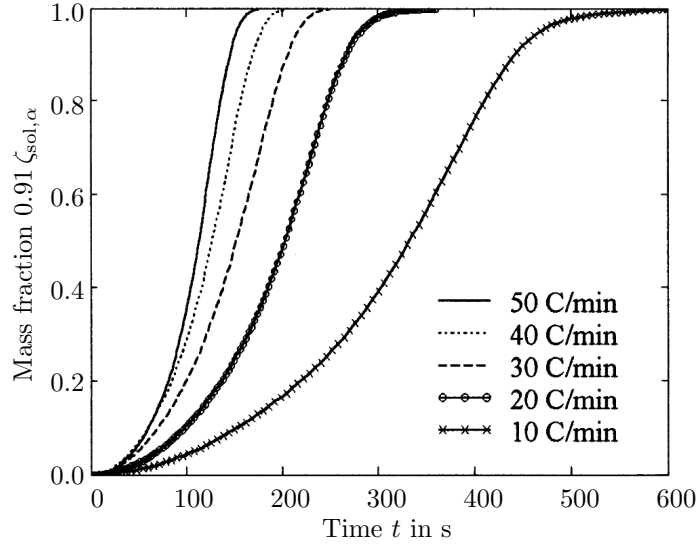
Figure 6.4: Transformed mass fraction $\zeta_{\text{sol},\alpha}$ as a function of time, where a "fully" completed transformation corresponds to 91% of $\zeta_{\text{sol},\alpha}$ and 9% remaining $\zeta_{\text{sol},\beta}$ in the transformed state. Reprinted from Metallurgical and Materials Transactions A, 32(4), Malinov, S., Guo, Z., Sha, W., Wilson, A., Differential scanning calorimetry study and computer modeling of $\beta \rightarrow \alpha$ phase transformation in a Ti-6Al-4V alloy, 879–887. Copyright (2001), with permission from Springer Nature, [115].

With the specific choice for the dissipation function at hand, the evolution equation introduced in eq. (6.8) for each phase fraction is in general given by

$$-\mathcal{F}_\bullet + [Y_\bullet - \mathcal{C}'_\bullet(\xi_\bullet)]\,\text{sign}\left(\dot{\xi}_\bullet\right) + \eta_\bullet\, \dot{\xi}_\bullet = 0 \tag{6.11}$$

leading to

$$\dot{\xi}_\bullet = \frac{1}{\eta_\bullet} \left\langle |\mathcal{F}_\bullet| - Y_\bullet + \mathcal{C}'_\bullet(\xi_\bullet) \right\rangle \operatorname{sign}(\mathcal{F}_\bullet) \ , \tag{6.12}$$

where

$$\langle \bullet \rangle = \max\{\bullet, 0\} \tag{6.13}$$

refers to the Macaulay brackets. As discussed in [16], the non-standard format of the dissipation function requires the investigation of thermodynamic consistency. In this context, it must be shown that

$$\mathcal{C} \geq 0 \ , \tag{6.14}$$

which is satisfied for

$$Y_\bullet - \mathcal{C}'_\bullet(\xi_\bullet) \geq 0 \quad \Leftrightarrow \quad \mathcal{C}'_\bullet(\xi_\bullet) \leq Y_\bullet \tag{6.15}$$

since $\eta_\bullet \geq 0$. This condition is always fulfilled if

$$\mathcal{C}'_{\bullet\max} := \mathcal{C}'_\bullet(\xi_{\bullet\max}) \leq Y_\bullet \tag{6.16}$$

with

$$\xi_{\bullet\max} = \frac{-a_{\bullet 2} - \sqrt{-c_{\bullet 1}}}{3\,a_{\bullet 3}} \tag{6.17}$$

and

$$c_1 := -a_{\bullet 2}{}^2 + 3\,a_{\bullet 3}\,a_{\bullet 1} \ . \tag{6.18}$$

In conclusion, two inequality constraints are derived, namely

$$c_{\bullet 1} := -a_{\bullet 2}{}^2 + 3\,a_{\bullet 3}\,a_{\bullet 1} \leq 0 \tag{6.19}$$

and

$$c_{\bullet 2} := a_{\bullet 3}\,\xi^3_{\bullet\max} + a_{\bullet 2}\,\xi^2_{\bullet\max} + a_{\bullet 1}\,\xi_{\bullet\max} - Y_\bullet \leq 0 \ . \tag{6.20}$$

These conditions, eqs. (6.19) and (6.20), have to be implemented into the parameter identification process, which will be discussed in Section 6.3.3.

Remark 16. *In [16], an approach for phase transformations is developed to reproduce the temporal behaviour of bainite. Based on this, an extension of the evolution equation to model the characteristic material behaviour of bainite is sought, which is suitable for the*

modelling of the rate dependent behaviour of titan aluminum alloy, compare Figure 6.4. This means that changing velocities, respectively rates, of solid mass fractions during the phase transformation (from small to large to small), as well as changing accelerations, respectively the time derivative of the rates, (from positive to negative) have to be captured by the dissipation function. As a result, the cubic polynomial in $\xi_\bullet$ has been proposed as a dissipation function contribution in [16], see eq. 6.10.

For the present phase transformation framework, it is assumed that the additional term (6.10) acts as a fully dissipative contribution. Therefore, $\mathcal{C}'_\bullet$ is added to eq. (6.9) and acts as an additional threshold contribution to the yield limit Y. However, as discussed in [16], it is also possible to assign this contribution to the energy by using an additional surface-type energy density $\psi^{\mathrm{surf}}_\bullet = -\int \mathcal{C}'_\bullet \, \mathrm{d}\xi_\bullet$, which is added to the corresponding phase energy density. This can be interpreted as a contribution related to the interaction between the different phases, which is not accounted for within the standard energy density of the bulk material. By using a weighting factor, it is possible to allocate $\mathcal{C}'_\bullet$ as a contribution to either energy density or dissipation function or a combination of both.

6.3 Implementation and algorithmic treatment

In general, the solution of eq. (6.12) determines the phase fractions of the material and with it the predicted material behaviour. Due to the variational nature of the problem, the associated constraints can be incorporated by using, e.g., smoothed Fischer-Burmeister nonlinear complementarity functions, and standard solvers such as the Newton-Raphson scheme can be applied. Further insight into the implementation and the calculation of the phase fractions and resiudal strains, respectively stresses, is given in Section 4.2. In the following, some specific aspects of the algorithmic implementation shall be addressed for the melt-solid-solid phase transformation at hand.

6.3.1 Case differentiation

In general, the consideration of several and potentially co-existing phases is possible, compare [12], but may become challenging in view of numerical stability and especially efficiency. The goal of this section is to show as to how the implementation can significantly be simplified by case differentiation. In general, the specimen is molten above the melting point $\theta^{\mathrm{melt}} = \theta^{\mathrm{ref}}_{\mathrm{mel}} = 1873.15$ K. As discussed in Section 6.1, $\mathrm{Ti}_6\mathrm{Al}_4\mathrm{V}$ completely consists of the β-phase above the β-transus temperature, cf. Figure 6.3. Depending on the initial temperature, the reference state is either $\zeta_{\mathrm{mel}} = 1$ or $\zeta_{\mathrm{sol},\beta} = 1$. Only below the temperature $\theta_{\beta,\mathrm{trans}}$, the β-phase (partially) transforms into further phases, where the focus is here laid on the α-phase as indicated above, while α' is so far neglected. Due to the physical behaviour of the titanium alloy, it is possible to consider only two phases at the same time, which simplifies the related model, respectively mathematical

problem. Therefore, several sets of variables along with corresponding constraints need to be defined and considered within the model. In view of the melt $\rightarrow \beta$ transformation, constraints

$$\{\zeta_{\mathrm{mel}}, \zeta_{\mathrm{sol},\beta}\} \in \mathcal{A}_1 \quad , \quad \{\boldsymbol{\varepsilon}_{\mathrm{mel}}, \boldsymbol{\varepsilon}_{\mathrm{sol},\beta}\} \in \mathcal{E}_1 \tag{6.21}$$

with

$$\mathcal{A}_1 := \{0 \leq \zeta_{\mathrm{sol},\beta} \leq 1 \,,\; \zeta_{\mathrm{mel}} + \zeta_{\mathrm{sol},\beta} = 1\} \tag{6.22}$$

and

$$\mathcal{E}_1 = \{\zeta_{\mathrm{mel}}\, \boldsymbol{\varepsilon}_{\mathrm{mel}} + \zeta_{\mathrm{sol},\beta}\, \boldsymbol{\varepsilon}_{\mathrm{sol},\beta} = \boldsymbol{\varepsilon}\} \tag{6.23}$$

are introduced. Subsequently, the sets

$$\{\zeta_{\mathrm{sol},\beta}, \zeta_{\mathrm{sol},\alpha}\} \in \mathcal{A}_2 \quad , \quad \{\boldsymbol{\varepsilon}_{\mathrm{sol},\beta}, \boldsymbol{\varepsilon}_{\mathrm{sol},\alpha}\} \in \mathcal{E}_2 \tag{6.24}$$

with

$$\mathcal{A}_2 := \left\{1 - R_{\mathrm{sol},\alpha}^{\mathrm{up}} \leq \zeta_{\mathrm{sol},\beta} \leq 1 \,,\; \zeta_{\mathrm{sol},\beta} + \zeta_{\mathrm{sol},\alpha} = 1\right\} \tag{6.25}$$

and

$$\mathcal{E}_2 = \left\{\zeta_{\mathrm{sol},\beta}\, \boldsymbol{\varepsilon}_{\mathrm{sol},\beta} + \zeta_{\mathrm{sol},\alpha}\, \boldsymbol{\varepsilon}_{\mathrm{sol},\alpha} = \boldsymbol{\varepsilon}\right\} \tag{6.26}$$

are used for the solid-$\beta \rightarrow$ solid-α transformation, where $R_{\mathrm{sol},\alpha}^{\mathrm{up}}$ is the upper bound for the α-phase. Experiments show that the maximum value of the α-phase does not necessarily have to be one and depends mainly on the given cooling rate. More precisely speaking, the results presented in, e.g., [74, 115, 167] show that this holds for relatively slow cooling rates. Based on these observations, the assumption

$$R_{\mathrm{sol},\alpha}^{\mathrm{up}} = \begin{cases} 1.00 \rightarrow \zeta_{\mathrm{sol},\alpha}, & \text{for high } |\dot{\theta}| \\ 0.95 \rightarrow \zeta_{\mathrm{sol},\alpha}, & \text{for medium } |\dot{\theta}| \\ 0.90 \rightarrow \zeta_{\mathrm{sol},\alpha}, & \text{for low } |\dot{\theta}| \end{cases} \tag{6.27}$$

is made in the present model. The values for medium and low cooling rates are approximated based on available literature data. The model relies in particular on the results presented in [4], see also Remark 17. This leads to the definitions

$$\begin{array}{lll} \text{high:} & 410\,\mathrm{K/s} < |\dot{\theta}| \\ \text{medium:} & 20\,\mathrm{K/s} \leq |\dot{\theta}| \leq 410\,\mathrm{K/s} \\ \text{low:} & |\dot{\theta}| < 20\,\mathrm{K/s} \end{array} \tag{6.28}$$

for the temperature rates. Moreover, the equality constraints in eqs. (6.22) and (6.25) allow for the substitutions

$$\zeta_{\text{mel}} = 1 - \zeta_{\text{sol},\beta} \quad \text{or} \quad \zeta_{\text{sol},\alpha} = 1 - \zeta_{\text{sol},\beta} \; , \tag{6.29}$$

so that in both cases only one mass fraction is used as variable. With this, the general approach introduced in eq. (6.9) simplifies to one summand, i.e. only one independent mass fraction remains for the particular case considered, cf. eqs. (6.21, 6.24, 6.29). Thus, no distinction between coefficients related to different phases in the dissipation function $\mathcal{C}$ is necessary as this work proceeds.

In addition, it is possible to consider cooling from melting or cooling from the β-phase. In view of the parameter identification approach discussed in Section 6.3.3, only solid-$\beta \rightarrow$ solid-α transformation is considered. For the LPBF process, all three phases are present. This results in an adjustment of the initial composition of the material, i.e. mass fraction $\zeta_\bullet$ and mass density ρ_0, cf. Remark 15. Moreover, the respective transformation strains according to eq. (4.10) have to be adapted in terms of the reference mass density ρ_0. In conclusion, based on the particular process, e.g. heat treatment or AM, one may either start with cooling from the molten phase, so that $\theta^{\text{start}} > \theta^{\text{ref}}_{\text{mel}}$, or with $\theta^{\text{ref}}_{\text{mel}} > \theta^{\text{start}} > \theta^{\text{ref}}_{\text{sol},\beta}$, where the initial material composition lies purely within the β-phase. A consecutive heating and additional cooling of the material is also captured by the implementation.

Remark 17. *As summarised in Table 6.2 and also stated in the literature, see e.g. [166, 167], the explicit values chosen for the critical rates, martensitic start temperature and maximum values vary significantly. The model at hand can straightforwardly be adapted to new experimental results, so that one could use improved maximum values for the phase fractions and critical cooling rates. It would therefore be possible to determine more reliable parameters for the dissipation function, see Section 6.3.3.*

6.3.2 Stress-free states

In order to evaluate the material response of the present framework, the behaviour under stress-free boundary conditions shall be analysed. Within the proposed material model, the constitutive relation for the stresses is highly non-linear in terms of strains and temperature. This, in general, requires an iterative computational approach to solve for the unknown quantities. As this work proceeds, such algorithm shall be denoted as constitutive driver, cf. Algorithm 6.1. Within this constitutive driver, different types of temperature evolution, i.e. cooling and heating profiles $\bar{\theta}(t)$ depending on time t, are prescribed at material point level. Accordingly, one seeks the strain state ε_n for the prescribed temperature path $\bar{\theta}(t)$ at a particular instant in time t_n with prescribed

Initialisation of strains $\varepsilon_{n=0} = \mathbf{0}$ and internal variables $\mathcal{V}_{n=0}$

for $n = 1$: steps

    Set iteration index $i = 1$, strains $\varepsilon_n^1 = \varepsilon_{n-1}$, and internal variables $\mathcal{V}_n^1 = \mathcal{V}_{n-1}$

    while $\left\| \boldsymbol{\sigma}_n^i \left(\varepsilon_n^i, \overline{\theta}_n, \dot{\overline{\theta}}_n, \mathcal{V}_n^i \right) \right\| > \text{tol}$

        Compute constitutive relations and tangent
$$\left\{ \boldsymbol{\sigma}_n^i, \mathbf{E}_n^i, \mathcal{V}_n^i \right\} \quad \text{based on} \quad \left\{ \varepsilon_n^i, \overline{\theta}_n, \dot{\overline{\theta}}_n \, \mathcal{V}_{n-1} \right\}$$

        Update of strains
$$\varepsilon_n^{i+1} = \varepsilon_n^i - \left[\mathbf{E}_n^i \right]^{-1} : \boldsymbol{\sigma}_n^i$$

        Update of iteration index
$$i \leftarrow i + 1$$

    end while

    Save strains $\varepsilon_n = \varepsilon_n^i$ and internal variables $\mathcal{V}_n = \mathcal{V}_n^{i-1}$

end for

Algorithm 6.1: Constitutive driver – temperature-induced stress-free transformations

temperature $\overline{\theta}_n$ and temperature rate $\dot{\overline{\theta}}_n$ which results in $\boldsymbol{\sigma}_n = \mathbf{0}$. The determination of strains includes the calculation of internal variables

$$\mathcal{V}_n = \mathcal{V}\left(\boldsymbol{\varepsilon}_n, \overline{\theta}_n, \dot{\overline{\theta}}_n \right) = \left[\zeta_{\text{mel}}, \zeta_{\text{sol},\alpha}, \zeta_{\text{sol},\beta} \right]_n \ , \tag{6.30}$$

where index n refers to the current time step. In summary, the relation

$$\boldsymbol{\sigma}_n \left(\boldsymbol{\varepsilon}_n, \overline{\theta}_n, \dot{\overline{\theta}}_n, \mathcal{V}_n \right) = \mathbf{0} \ . \tag{6.31}$$

needs to be solved using e.g. a Newton-Raphson scheme. Herein, the stresses $\boldsymbol{\sigma}_n$ are evaluated based on eq. (4.31). A sketch of the related constitutive driver with its most important equations is summarised in Algorithm 6.1. Therein, $\mathbf{E}^{\text{algo}} \approx \mathbf{E} = \partial_{\boldsymbol{\varepsilon}} \boldsymbol{\sigma}$ denotes the algorithmic tangent operator, here approximated by underlying isotropic elasticity tensors.

6.3.3 Parameter identification

A classic Parameter Identification (PI) framework, as introduced in e.g. [20, 114], is used to determine suitable values for the material parameters at hand. The PI is based on the transformation behaviour as discussed in Section 6.3.1, so that all previously introduced model simplifications can be applied. As this work proceeds, a subset $\boldsymbol{\kappa} = \{Y, \eta, a_1, a_2, a_3\}$ of the underlying model parameters shall be considered within the PI, whereas the remaining model parameters are prescribed, respectively taken from literature. This means that the PI design variables, respectively material parameters $\boldsymbol{\kappa}$, are used to sufficiently match the material response of the simulation $\mathcal{R}^{\text{sim}}(\boldsymbol{\kappa})$ to the

available experimental data $\mathcal{R}^{\mathrm{exp}}$. Thus, a phenomenological relation can be established between the material parameters $\boldsymbol{\kappa}$ and the cooling rate $\dot{\theta}$. For the particular cooling rates, $\zeta_{\mathrm{sol},\alpha}$ as predicted by the proposed model is compared to the related pairs of points of the CCT diagram published in [128]. The two datasets are explicitly compared at all the points in time t_n considered. Therefore, the values in between the extracted points and the maximum value $R^{\mathrm{up}}_{\mathrm{sol},\alpha}$ of $\zeta_{\mathrm{sol},\alpha} = \left\{ 0.01, 0.05, 0.15, 0.45, 0.55, 0.85, R^{\mathrm{up}}_{\mathrm{sol},\alpha} \right\}$ are computed via linear interpolation, as only these discrete values can be directly extracted from [128, Figure 6].

The overall framework corresponds to an inverse problem, whereby the least squares functional

$$f(\boldsymbol{\kappa}) = \sum_{i=1}^{n_t} \tfrac{1}{2} \left[\mathcal{R}^{\mathrm{sim}}_i(\boldsymbol{\kappa}) - \mathcal{R}^{\mathrm{exp}}_i \right]^2 \tag{6.32}$$

is used as objective function, where n_t denotes the number of time points considered. The dataset $\mathcal{R}^{\mathrm{sim}}_i(\boldsymbol{\kappa})$ is calculated with the help of the constitutive driver presented in Section 6.3.2 for the respectively given cooling rate $\dot{\theta}$. The optimal values for $\boldsymbol{\kappa}$ are determined by minimising $f(\boldsymbol{\kappa})$. This procedure is repeated for all cooling curves as discussed in the next Section 6.3.4.

Prior to the use of $\boldsymbol{\kappa}$ within the constitutive driver the related inequality constraints (6.18) and (6.20) are checked. In the case where these constraints are violated, the respective design variables are set to the related limit values. The gradient free fminsearch-algorithm (a Nelder-Mead simplex algorithm) available within the commercial software MATLAB is used for the PI by minimising the objective function defined in eq. (6.32). The thermodynamic consistency constraints (6.19) and (6.20) are checked after the PI is performed and, for the applications considered in this work, always turned out to be satisfied. As no general proof can be established for the determination or existence of the global minimum of the underlying least squares functional, multiple local minima are to be expected. Thus, a set of different initial values of the design variables $\boldsymbol{\kappa}$ is used. Conceptually speaking, a (coarse) grid search approach is applied to identify different minima for $\boldsymbol{\kappa}$. Section 6.4.1 discusses how the values between the identified points are approximated.

6.3.4 Summary of complete workflow

For the present modelling framework, 18 cooling curves with the respective material composition are extracted from the CCT diagram published in [128]. In line with experiments, the temperature profiles are not assumed to be linear functions in time. Rather, the calculated temperature-time curves depicted in Figure 6.5 are used, see also Remark 18. The procedure for generating the temperature profiles is described in detail in Appendix D.1. It is obvious that the cooling rate is generally not constant in time.

In order to introduce a representative value for the particular cooling rate, the slope of these curves at temperature 1173 K is used. This results in the following cooling rates

$$\dot{\theta} = \{0.01, 0.05, 0.1, 0.5, 1, 1.5, 5, 10, 20, 25, 30, 75, 100, 200, 300, 410, 525, 600\} \, \text{K/s} \, . \tag{6.33}$$

The temperature-time curves are then used as input for the constitutive driver. For all of these cooling rates the optimal design variables $\boldsymbol{\kappa}$ are determined with the help of the PI approach introduced in Section 6.3.3. With this framework at hand, it is possible to generate a complete CCT diagram by varying a cooling rate related scaling parameter s_g, cf. Appendix D.1. Based on this, e.g., 100 cooling rates between 0.01 K/s $< \dot{\theta} < 600$ K/s are generated. Within the framework, the respective set of design variables $\boldsymbol{\kappa}$ is chosen and interpolated according to the prescribed cooling rate. The distribution of the design variables as well as the complete CCT diagram is the subject of the next section, where different boundary value problems are also discussed.
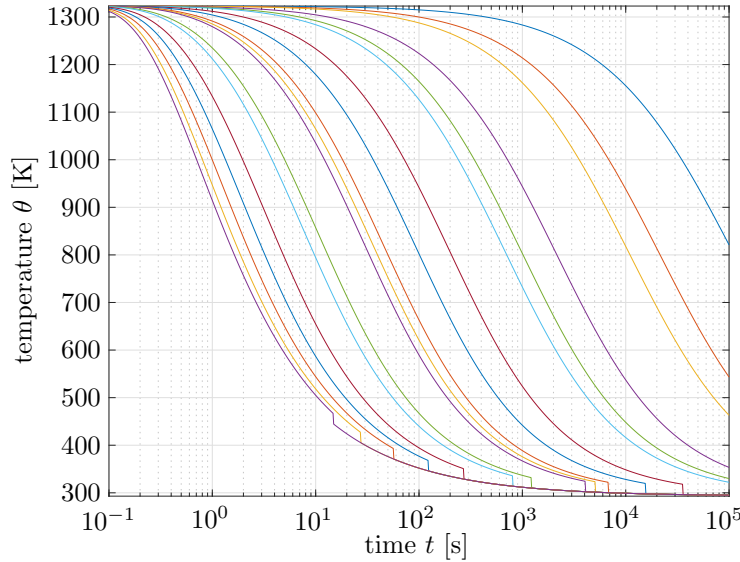
Figure 6.5: Temperature profiles generated with the numerical approach presented in Appendix D.1 and in [128]. Reprinted from [130] under the terms of the Creative Commons Attribution License (CC BY).

Remark 18. *The temperature drops in Figure 6.5 arise from the structure of the analytical solution since eq. (6.37), see Appendix D.1, approaches infinity for some combinations of t and s_g, while eq. (6.39) takes value zero. For these cases, only eq. (6.38) contributes to the calculation of the temperature profile, resulting in a non-smooth curve.*

6.4 Numerical examples

The results of the phase transformation framework are presented in the following. The mechanical and thermal material parameters used for the titanium alloy Ti_6Al_4V are summarised in Table 6.4.

Table 6.4: Summary of the Ti_6Al_4V material parameters used for the phase transformation framework, adapted from [17, 121].

Material parameters		Melt	Solid-β	Solid-α
Mechanical parameters				
Density	ρ [kg/m^3]	3800	4420	4420
Poisson's ratio	ν [$-$]	0.45	0.33	0.33
Young's modulus	E [GPa]	10^{-9}	10	109
Thermal parameters				
Expansion coefficient	α [1/K]	-	13e-06	11e-06
Initial temperature	θ^{ini} [K]	-	1873.15	1873.15
Heat capacity	c [J/(kgK)]	750	750	750
Latent heat	L [kJ/kg]	286	48	-
Reference temperature	θ^{ref} [K]	1873.15	1268.15	-

6.4.1 Fitting of dissipation function parameters

Depending on the respective starting points for the minimisation of the objective function, different results are determined for the material parameters $\boldsymbol{\kappa}$, which also yield different values for the minima of the objective function. Obviously, the objective function exhibits several local minima. However, the selection of the parameters that resulted in the lowest values of the objective function in each case led to non-smooth progressions of the phenomenological correlations $\boldsymbol{\kappa}(\dot{\theta})$. In terms of numerical stability when using these correlations in finite element simulations, this should be avoided. Therefore, parameter sets $\boldsymbol{\kappa}$ were partly selected which did not yield the smallest value of the objective function (and yet corresponded to a local minimum), but ensured a rather smooth function $\boldsymbol{\kappa}(\dot{\theta})$.

Time discrete values for the experimental curve $\mathcal{R}^{\mathrm{exp}}$ are taken from [128], whereas the simulation results of $\zeta_{\mathrm{sol},\alpha}$ exemplary depicted in Figure 6.6 are generated via interpolation, as discussed in Section 6.3.3. Therein, six different curves are exemplarily chosen in order to highlight the accuracy of the results. The results for the prescribed fast, intermediate and slow cooling rates are visualised in Figure 6.6, where the concentration of the α-phase, i.e. the mass fraction $\zeta_{\mathrm{sol},\alpha}$, is plotted over time. The comparison of Figure 6.6a and Figure 6.6b clearly shows the influence of the prescribed cooling rate on the effective material composition. With the exception of some significant deviations

for the two highest cooling rates, the results obtained with the present framework show satisfactory agreement with the experimental results. Here, the cubic polynomial $\mathcal{C}'$ cannot fully capture the course of the experimental curves. However, the approximation is considered sufficient for the current fundamental study. In addition, the need to choose different maximum values for the mass fraction $\zeta_{\mathrm{sol},\alpha}$ depending on the cooling rate becomes evident.

(a)

(b)
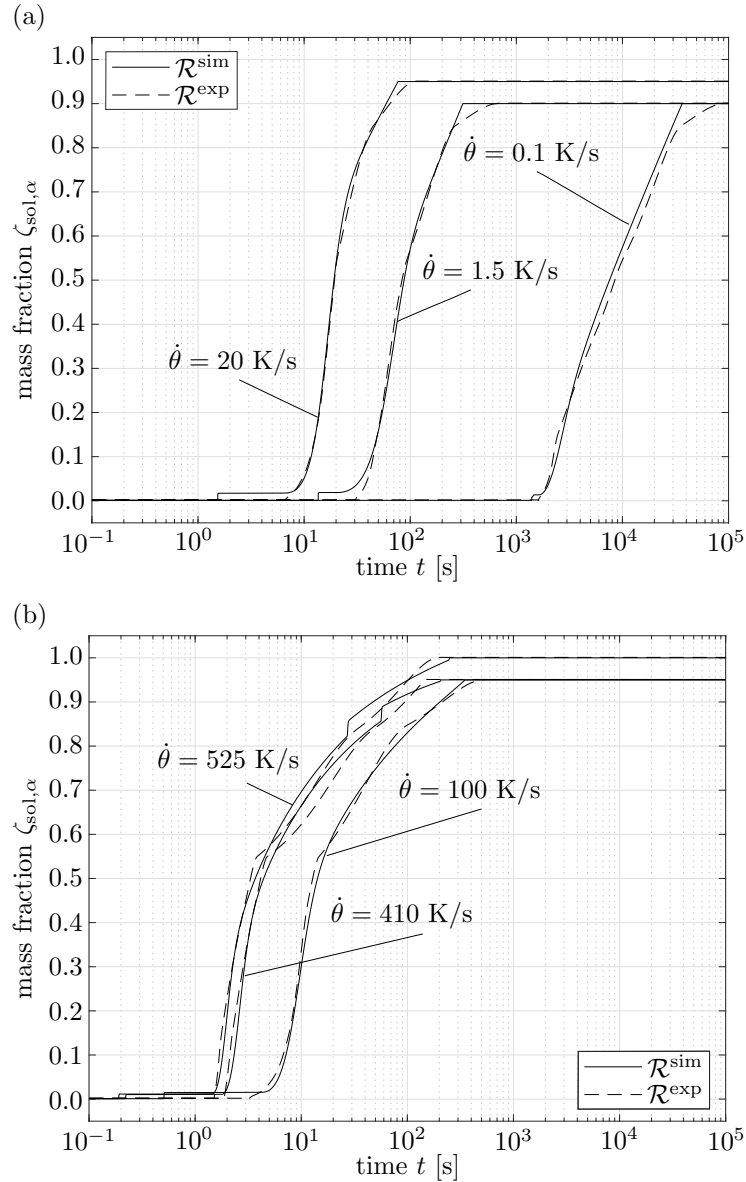
Figure 6.6: Exemplary verification of calculated material response $\mathcal{R}^{\mathrm{sim}}(\boldsymbol{\kappa})$ based on experimental data $\mathcal{R}^{\mathrm{exp}}$ used for the PI considering rather steady cooling rates, Figure 6.6a, and rapid cooling rates Figure 6.6b. Reprinted from [130] under the terms of the Creative Commons Attribution License (CC BY).

161

The values of the parameters in the subset $\boldsymbol{\kappa}$ obtained by the PI depend on the cooling rate $\dot{\theta}$ via interpolation of the specific data points. Other approaches are also feasible, cf. Remark 19. These phenomenological relations are illustrated in Figure 6.7. For the viscosity parameter η shown in Figure 6.7a, a steep descent is visible for slow cooling rates, whereas the slope changes and decreases for higher cooling rates. For both, the threshold Y highlighted in Figure 6.7b and the parameters a_1, a_2, a_3 visualised in Figure 6.7c, (quasi-) constant values are generated below $\dot{\theta} < 1$ K/s, specifically $a_1 = -0.002$, $a_2 = -0.007$, $a_3 = -0.004$ GPa and above $\dot{\theta} > 525$ K/s, in particular $a_1 = 0.033$, $a_2 = -0.0621$, $a_3 = 0.009$ GPa. In between, the cooling rates significantly affect the phase changes and the temporal evolution of mass fractions. Thus, the parameters $\boldsymbol{\kappa}$ of the dissipation function change accordingly in order to capture the correct material response.

As there is a rather weak basis for CHT diagrams in the literature, the parameters of the dissipation function for re-heating are not fitted to experiments. Therefore, only the standard dissipation function is used, so that a_1, a_2 and a_3 are set to zero a priori. The remaining parameters Y and η are identified by a trial and error process to reproduce the material behaviour and to appropriately reflect the material's transformation properties such that solid-α exists below $\theta_{\beta,\mathrm{trans}}$ and solid-β emerges above $\theta_{\beta,\mathrm{trans}}$. This results in the following case differentiation

$$\{\eta, Y\} = \begin{cases} \{100\,\mathrm{GPa\,s},\ 500\,\mathrm{GPa}\} & \text{for } \theta < \theta_{\beta,\mathrm{trans}} \\ \{\ \ 0\,\mathrm{GPa\,s},\ \ \ \ 0\,\mathrm{GPa}\} & \text{else} \end{cases}. \tag{6.34}$$

These parameters cause a phase transformation to the β-phase only above the β-transus temperature $\theta_{\beta,\mathrm{trans}}$.

For the phase transformation from molten to the β-phase, only the standard dissipation potential is used, as no complex phase transformation behaviour is assumed. The following parameters are identified in a trial and error process to ensure melting in the range of θ^{melt},

$$\{\eta, Y\} = \left\{ \frac{2\,\mathrm{K/s}}{\dot{\theta}}\,\mathrm{GPa\,s},\ 0\,\mathrm{GPa} \right\}, \tag{6.35}$$

whereas $\eta = 0\,\mathrm{GPa\,s}$ for $\dot{\theta} = 0\,\mathrm{K/s}$ within the examples considered in the present work. According to our results, the rate dependence of η implies that the transformation from molten to the β-phase always starts and ends at the approximate same temperature.

Remark 19. *For the current framework, the identified values of the subset $\boldsymbol{\kappa} = \{Y, \eta, a_1, a_2, a_3\}$ are interpolated based on the cooling rate. Thus, a piece-wise linear relation in $\dot{\theta}$ of the specified values is assumed. A more sophisticated approximation is possible by using a regression model based on, e.g., a least squares approach.*

In general, a more elaborated approach would be the direct identification of the coefficients of smooth functions. In a next step, the current results could be used as a basis to

(a)

(b)

(c)
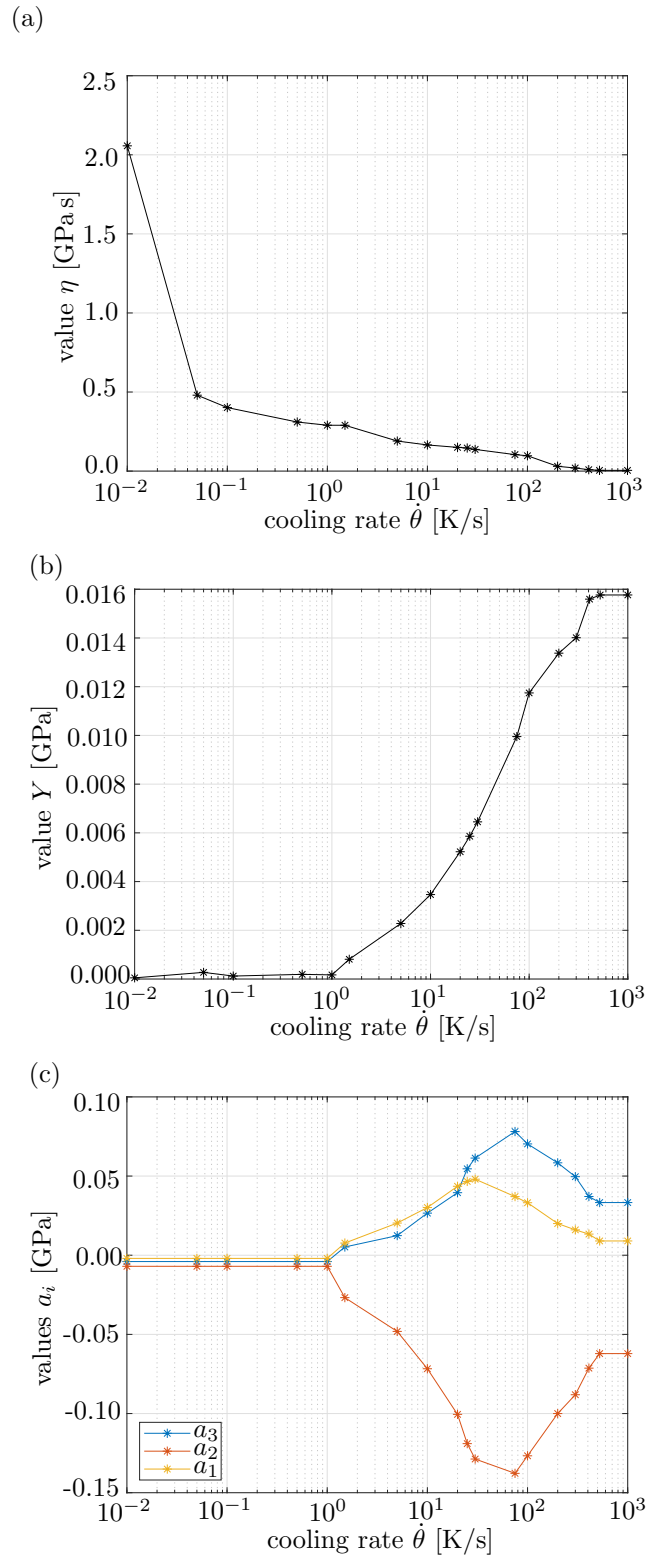
Figure 6.7: Identified curves for parameters in dissipation function $\mathcal{C}$: (6.7a) parameter η and (6.7b) parameter Y, both introduced in eq. (6.9), and (6.7c) parameters a_1, a_2 and a_3 as stated in eq. (6.10). Reprinted from [130] under the terms of the Creative Commons Attribution License (CC BY).

163

develop a PI algorithm that determines the coefficients of, e.g., exponential, hyperbolic tangens and piecewise linear functions for all temperature rates simultaneously.

6.4.2 CCT diagram
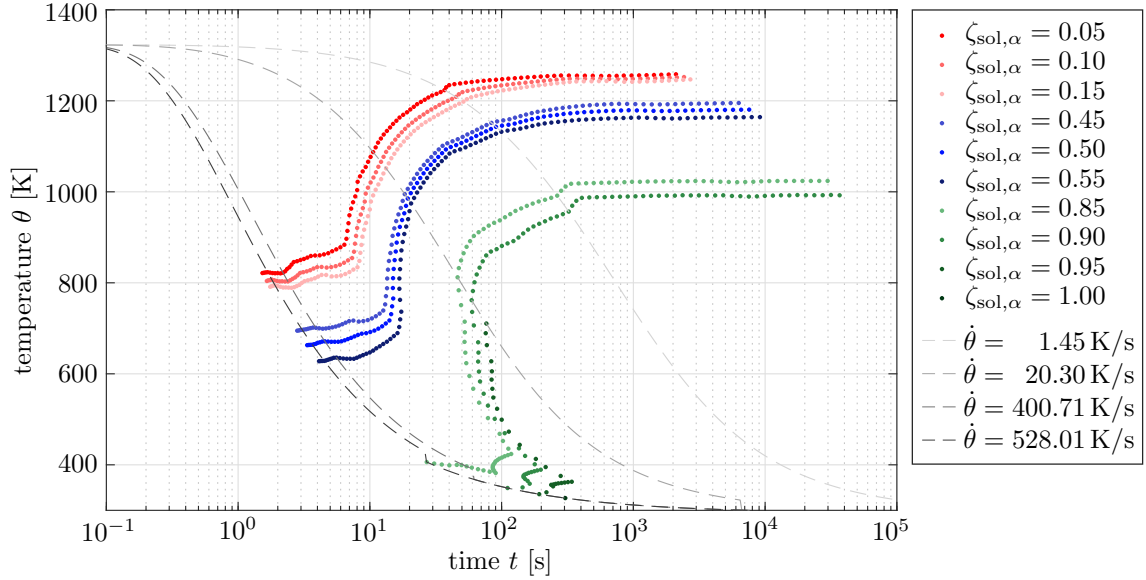
Figure 6.8: Computed CCT diagram for 100 cooling rates from $\dot{\theta} = 0.01$ K/s to $\dot{\theta} = 600$ K/s, where different mass fractions $\zeta_{\text{sol},\alpha}$ for the respective cooling rates are visualised. Exemplarily, four characteristic cooling rates $\dot{\theta}$ according to Figure 6.3 are plotted in the CCT diagram. Reprinted from [130] under the terms of the Creative Commons Attribution License (CC BY).

With the presented rate dependent parameters it is now possible to generate a complete CCT diagram for Ti$_6$Al$_4$V. Therefore, the parameter s_g in eq. (**??**) is varied so that 100 logarithmic spaced curves are generated. The related cooling rates vary between 0.01 K/s $\leq \dot{\theta} \leq$ 600 K/s and the resulting CCT diagram is illustrated in Figure 6.8. Within this Figure, the isolines for different α-concentrations $\zeta_{\text{sol},\alpha}$ are shown. The computed CCT diagram is capable of predicting different α-fractions. The evolution of mass fractions significantly depends on the cooling rate and is highly nonlinear in time, in particular for medium cooling rates. Thus, the phase transformation begins and ends at distinct temperatures. For slow cooling rates, with $\dot{\theta} < 20$ K/s, and high cooling rates, with $\dot{\theta} > 400$ K/s, almost constant martensitic start temperatures M_s are present.

These general characteristics of the CCT diagram have been documented in the experimental findings of [4, 39, 74], whereas values characteristic for the transformation process, such as those summarised in Tables 6.2 and 6.3, differ in literature, compare also Remark 20. Since the curves given in [128] (which correspond to the experimental results of the schematic CCT diagram in [4]) are used to identify the material parameters in the present work, the agreement between these and the present results is sufficiently

accurate. More precisely speaking, a β-transus temperature between 1250-1255 K is obtained, which is close to $\theta_{\beta,\text{trans}} = 1268.15$ K found in literature, cf. Table 6.3. A martensitic start temperature $M_s \approx 820$ K is present for fast cooling rates, which agrees with the findings in [4, 128]. However, the present model, and with it the predicted results, also takes into account the upper bound of $\zeta_{\text{sol},\alpha}$ depending on the applied cooling rate, cf. eq. (6.27). The lower bound for slow cooling rates has a value of $\zeta_{\text{sol},\alpha} = 0.85$ and lies around 400 K, which corresponds to the results in [128].

Remark 20. *A comprehensive overview of the current state of the art is given in [166], in particular with respect to CHT diagrams, CCT diagrams and microstructures for Ti_6Al_4V. Among other things, the authors point out the lack of accurate models to predict and control the microstructural evolution during AM processes and the diverse and contradicting values for significant model parameters provided in literature. This is supported by Tables 6.2 and 6.3. As the absolute values of the characteristic temperatures during cooling differ in the experimental results of [4, 39, 74], it is not entirely clear which characteristic temperatures for M_s and $\theta_{\beta,\text{trans}}$ should be chosen, compare Tables 6.2 and 6.3. However, the proposed framework can straightforwardly be adapted to different CCT data not only of this alloy, but can also be applied to other materials. If other literature data is used as a basis, different material parameters $\boldsymbol{\kappa}$ would be identified by the PI, resulting in, e.g., higher martensitic start temperature M_s as found in [39, 74].*

6.4.3 Boundary value problems

First, academic examples with simple prescribed temperature profiles are discussed as a proof of concept for the proposed framework. Thereafter, temperature profiles extracted from realised LPBF simulations, cf. Section 5.3.3, are subsequently used to illustrate the explicit phase transformation of the solid for real process-based examples.

Proof of concept

In Figure 6.9, different temperature profiles characterised by different cooling rates (high and low) as well as final temperatures (373 K vs. 573 K) are prescribed, whereby the corresponding simulated strain and mass fraction evolution over time t is visualised. For all examples, the temperature starts above the melting point and the initial material state corresponds to completely molten material. Due to the simpler dissipation ansatz of the transformation melt $\rightarrow$ solid-β, the transformation starts at the same temperature. Based on the cooling rate, the phase transformation takes places during different time periods. The phase change solid-β $\rightarrow$ solid-α is initiated at a later point for a slower cooling rate. Furthermore, a longer time period is required until a phase change from both melt $\rightarrow$ solid-β and solid-β $\rightarrow$ solid-α is completed. Overall, this qualitatively corresponds to the expected physical behaviour of the titanium aluminium alloy. Due to the maximum constraint in eq. (6.27), a portion of solid-β remains for the temperature profiles prescribed in Figure 6.9a even for the complete transformation. For the higher
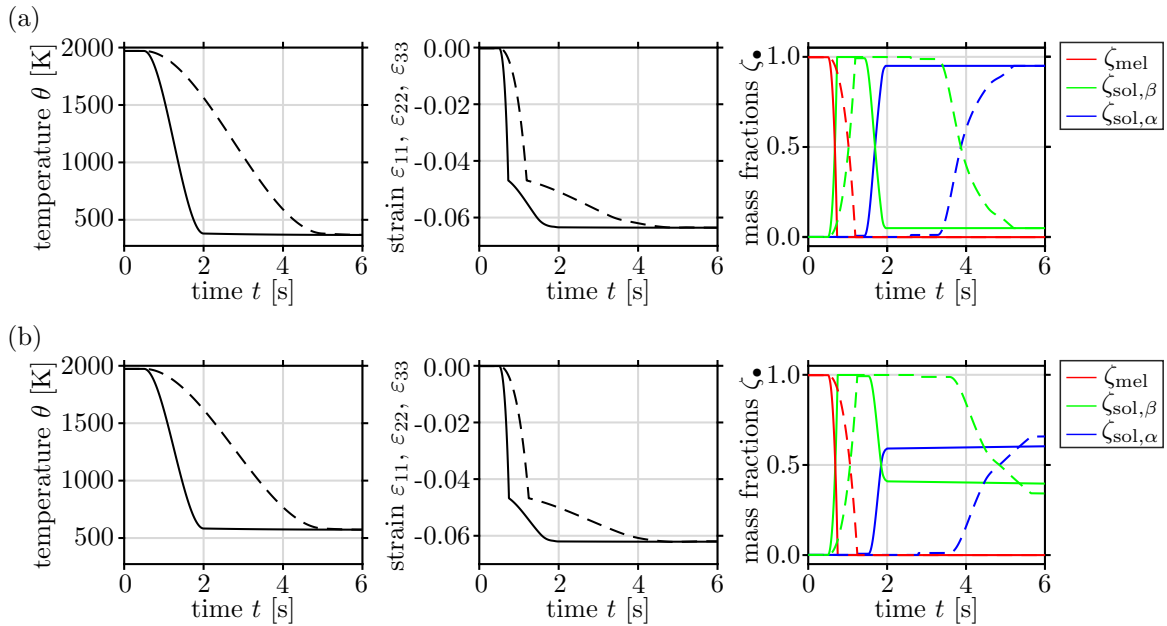
Figure 6.9: Temporal evolution of homogeneous strains $\varepsilon_{\bullet\bullet}$ and mass fractions $\zeta_\bullet$ for the high (solid lines) and low (dashed lines) cooling rate. The upper and lower figures differ from each other in terms of the final temperatures, which are precisely given by 373 K for (6.9a) and 573 K for (6.9b). Reprinted from [130] under the terms of the Creative Commons Attribution License (CC BY).

end-temperature in Figure 6.9b no complete phase change from solid-β to solid-α is obtained, but a phase mixture exists. This corresponds to the findings in e.g. [128], where different final temperatures, which - in view of LPBF processes - may refer to different base plate temperatures, have been evaluated. The base plate temperature highly influences the final percentage of solid-α and solid-β. The middle graph depicts the evolution of the corresponding strain state. Here, especially the jump during the phase transformation from molten material to solid due to the transformation strains is visible. Furthermore, an increase of strains takes place as long as the temperature decreases due to the thermal strain contribution. Once the temperature is constant, the strains do not further evolve. In summary, the model is capable of predicting physically meaningful results not only based on different temperature rates, but also based on the final temperature.

Real process-based examples

For the real process-based example, a simulation of a scan island with 5×5 mm is used as a basis to extract the respective temperature profiles, as defined is Section 5.3.3. An illustration of the underlying simulation is given in Figure 6.10. The results which are based on the stress-free driver introduced in Section 6.3.2 are shown in Figures 6.11 and 6.12 for the centred element C of the scan island, as indicated in Figure 6.10.
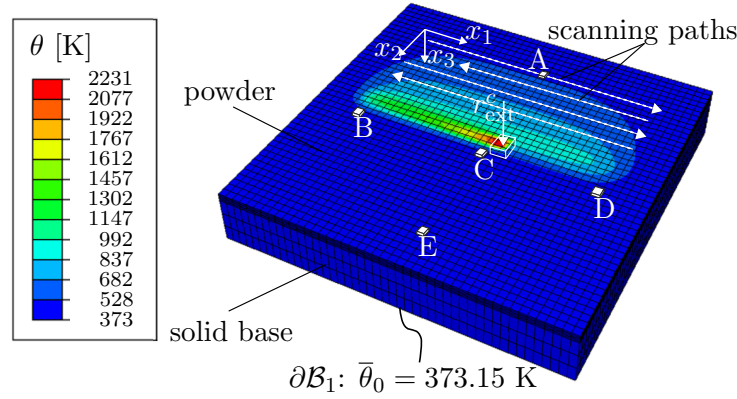
Figure 6.10: Scan island simulation with scan island size 5×5 mm (side length $l_{\mathrm{lyr}} = 5$ mm) with the current temperature profile at $t = 0.08$ s due to cuboid heat source r_{ext}^c with laser power $P = 250$ W and laser velocity $\overline{v}^{\mathrm{lsr}} = 1.0$ m/s as defined in Table 5.5 from which the temperature history $\overline{\theta}$ is extracted for elements A–E. Reprinted from [130] under the terms of the Creative Commons Attribution License (CC BY).

For the example, the transformation considered begins in the molten phase (not powder phase), where the current temperature is above the melting point, i.e. $\theta^{\mathrm{melt}} = 1873.15$ K, and the initial mass fraction is set to $\zeta_{\mathrm{mel}} = 1$. The prescribed temperature profile, the resulting temperature rate, the calculated homogeneous strain evolution and the determined distribution of the mass fractions are illustrated in Figure 6.11, where the detailed temperature history and resulting evolution at the beginning is pictured in Figure 6.12. The temperature rapidly decreases to $\theta < 1000$ K, where the characteristic high cooling rates present in LPBF processes are also recognisable. Due to the high cooling rates and the identified material parameters, an instantaneous transition from molten to solid-β occurs. This corresponds to a jump in the strain state. Solid-β then almost linearly decreases while solid-α simultaneously increases until $t \approx 0.3$ s, compare Figure 6.11. In addition, the temperature rate decreases almost linearly until $t = 1$ s. The oscillations in the temperature rate are mathematical artefacts due to the temperature import from Abaqus associated with the small time steps in Matlab and can therefore be neglected. After the first rapid cooling, the temperature is below the martensitic start temperature $M_s \approx 820$ K, compare Figure 6.8. This particular martensitic start temperature is the consequence of the simulations and occurs for all high cooling rates $\dot{\theta} > 400$ K/s. This choice seems reasonable, as M_s is reported to remain rather constant for high cooling rates in experimental work. The kinks in the evolution of mass fractions at $t \approx 0.3$ s occur due to the constantly decreasing cooling rate and increasing M_s temperature, as $\dot{\theta} < 400$ K/s is now valid. In consequence, the transformation of the remaining mass fraction takes place slower. The conversation reaches a plateau at $t = 1$ s with $\zeta_{\mathrm{sol}}^{\alpha} = 0.83$ and, in consequence, $\zeta_{\mathrm{sol}}^{\beta} = 0.17$, where $\dot{\theta} < 0.01$ K/s. This is supported in [74, 115], where a small solid-β fraction is present for low cooling rates. A similar curve is shown in [32], where the authors discuss the

influence of neighbouring scan tracks and of inter-track idle time on the microstructure of a low-temperature transformation alloy during and at the end of the process using the KM equation. With idle-time, a complete transformation is enforced, while a small amount of solid-β is present for the standard process. The temperature cycles, i.e. heat treatment and cooling rate, not only influence the phase composition and structure, but also the hardness of the part, cf. the experimental studies in e.g. [38, 80, 122]. An analogous material behaviour can be observed in the experimental investigations in [83] where the material has been melted and reheated with decreasing laser power. This results in different temperature levels and, accordingly, the phase composition changes, which has been measured by a diffractometer. Similarly, different temperature profiles are prescribed in the simulations elaborated in [185], which result in different solid phase fractions and evolution.
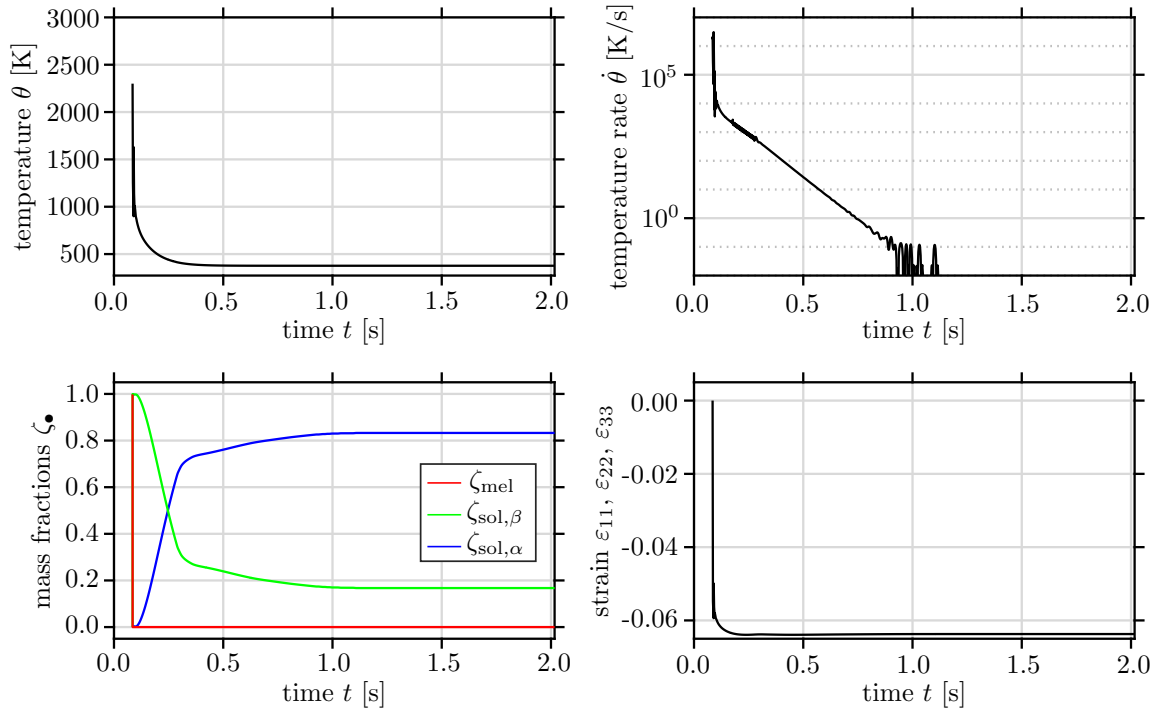
Figure 6.11: Temporal evolution of homogeneous strains $\varepsilon_{\bullet\bullet}$ and mass fractions $\zeta_\bullet$ based on a prescribed temperature profile $\bar{\theta}$ and resulting temperature rate $\dot{\bar{\theta}}$ extracted from Abaqus simulation for the centred element C, compare Figure 6.10. Reprinted from [130] under the terms of the Creative Commons Attribution License (CC BY).

In Table 6.5, final solid-α concentrations $\zeta_{\text{sol}}^\alpha$ for different elements, as indicated in Figure 6.10, are summarised. Due to the different cooling rates as visualised in Figure 6.14, especially at the lower edge of the scan island, the value of $\zeta_{\text{sol}}^\alpha$ varies considerably. As the scan island is surrounded by powder material, heat conduction is different for all elements at the boundary of the scan island. Furthermore, no additional laser pass is present for the bottom element E, resulting in a slightly shorter cooling period and
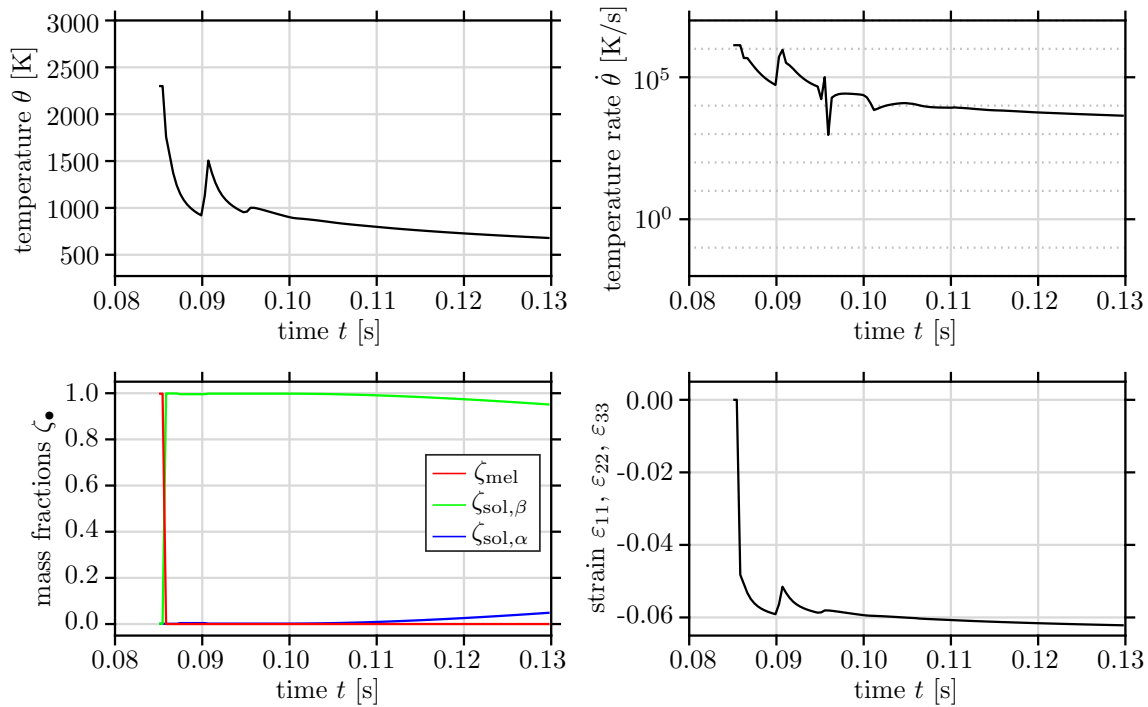
Figure 6.12: Detail of temporal evolution of homogeneous strains $\varepsilon_{\bullet\bullet}$ and mass fractions $\zeta_{\bullet}$ at the beginning of the prescribed temperature profile $\bar{\theta}$ and temperature rate $\dot{\bar{\theta}}$ illustrated in Figure 6.11. Reprinted from [130] under the terms of the Creative Commons Attribution License (CC BY).
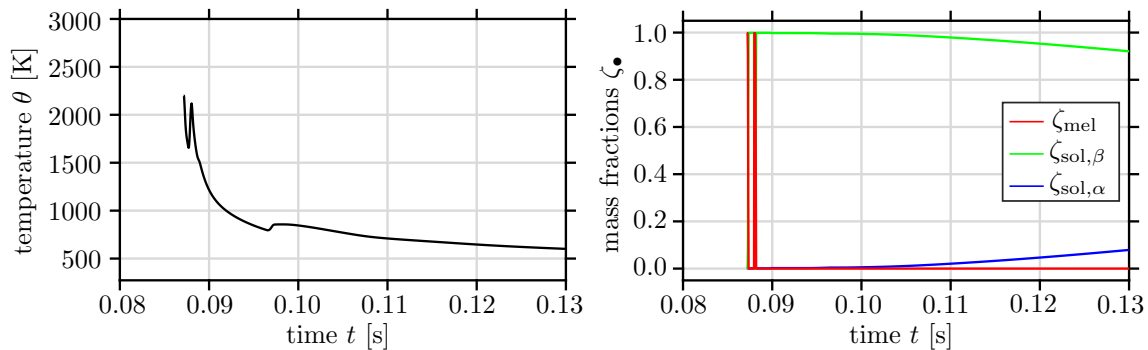
Figure 6.13: Detail of temporal evolution of mass fractions $\zeta_{\bullet}$ based on a prescribed temperature profile $\bar{\theta}$ extracted from Abaqus simulation for element B, compare Figure 6.10. Reprinted from [130] under the terms of the Creative Commons Attribution License (CC BY).

thus a considerably lower $\zeta_{\text{sol}}^{\alpha}$ value. Re-melting arises for the left and right elements B and D, as the laser beam changes the direction at the end of the scan island. Therefore, the subsequent laser pass of the neighbouring scan track results in a re-melting of these elements as visualised in Figure 6.13 for element B. These elements B and D have also very similar cooling rates, compare Figure 6.14. Overall, the visualised differences in the cooling rates explain the changing final mass concentration, where a low cooling rate

Table 6.5: Final solid-α (martensite) fraction of different elements as indicated in Figure 6.10.

Position	Label	α-concentration $\zeta_{\text{sol}}^{\alpha}$
top, centre	A	0.84072
middle, left	B	0.81728
middle, centre	C	0.83268
middle, right	D	0.81435
bottom, centre	E	0.71600

results in small α_{sol} (element E) and high cooling rates in high α_{sol} (elements A and C) concentrations. Altogether, the typical characteristics of an LPBF process are captured, including re-melting and different heating and cooling rates due to neighbouring laser scan tracks. In conclusion, from a physics viewpoint the model proposed at least qualitatively correctly captures the material properties.
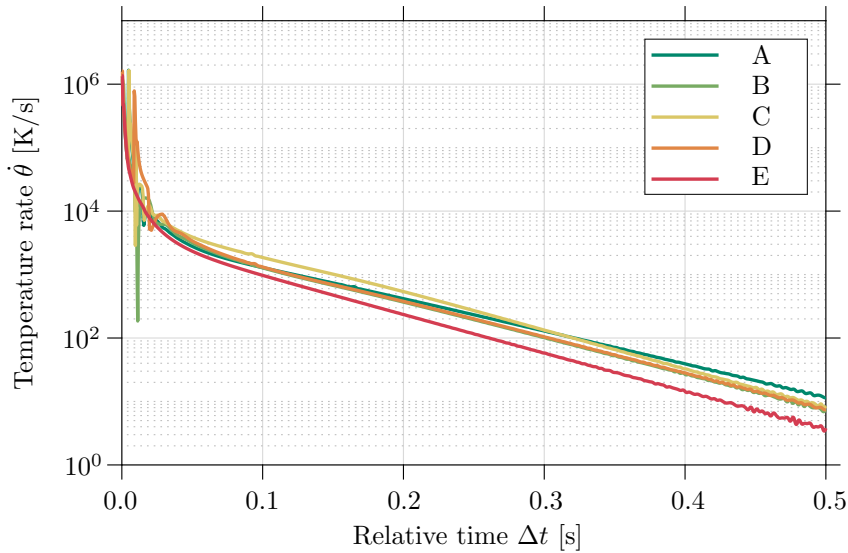
Figure 6.14: Temperature rate $\dot{\theta}$ in dependence of relative cooling time Δt of all elements indicated in Figure 6.10, where $\Delta t = 0$ corresponds to the specific time at which the laser beam has induced the highest temperature. Reprinted from [130] under the terms of the Creative Commons Attribution License (CC BY).

D Appendix

D.1 Calculation of temperature profiles

As the current framework as well as the model introduced in [128] is based on the experimental data generated in [4], the same ansatz as in [128] is used in the present work to generate the temperature curves. This means that the current temperature at position x and time t is defined via

$$\theta(x,t) = \big[\theta_\infty - \theta_0\big]\big[f_{\text{erfc1}}(x,t) - a\, f_{\text{erfc2}}(x,g,t)\big] + \theta_0 \tag{6.36}$$

with

$$a = \exp\!\big(g\,x + g^2\alpha\,t\big)\;, \tag{6.37}$$

$$f_{\text{erfc1}}(x,t) = \operatorname{erfc}\left(\frac{x}{2\sqrt{\alpha\,t}}\right)\;, \tag{6.38}$$

$$f_{\text{erfc2}}(x,g,t) = \operatorname{erfc}\left(\frac{x}{2\sqrt{\alpha\,t}} + g\sqrt{\alpha\,t}\right)\;. \tag{6.39}$$

Here, erfc refers to the complementary error function, which includes several (so far) unknown parameters. Motivated by the experimental investigations in [3], the following parameters are used in the present work: $\theta_0 = 1323$ K, which denotes the temperature of the solid at the beginning of the experiment, and $\theta_\infty = 293.15$ K, representing the temperature of the cooling fluid. The position parameter is set to $x = 3.2$ mm. The material parameter α defines the thermal diffusivity and is set to $\alpha = 10$ mm^2/s. Finally, the material related scalar g defines the ratio of convective heat transfer and thermal conductivity and is determined based on the current temperature θ and a quadratic ansatz so that

$$g(\theta) = s_g\left[a_g + b_g\frac{\theta - \theta_\infty}{\theta_\infty} + c_g\left[\frac{\theta - \theta_\infty}{\theta_\infty}\right]^2\right]\;. \tag{6.40}$$

The parameters $[a_g, b_g, c_g] = [73.8, -39.3, 6.3]$ m^{-1} have inversely been identified in [128] and s_g is introduced as a scaling parameter to generate arbitrary cooling curves. In order to generate the temperature profiles in Figure 6.5, the following values are used for the scaling parameter s_g, i.e.

$$\begin{aligned}
s_g = \{&0.01, 0.029, 0.045, 0.134, 0.225, 0.29, 0.7, 1.19, 2.05, 2.47, 2.87, 6.38,\\
&8.44, 17.69, 30.2, 50.8, 83.9, 125\}\;.
\end{aligned} \tag{6.41}$$

7 Concluding remarks

In this work, micromechanically motivated thermomechanical modelling approaches for the simulation of laser powder bed fusion (LPBF) processes are presented. A phase transformation model for the respective additive manufacturing (AM) process is developed in Chapter 3 based on a framework stemming from solid-solid phase transformation approaches in shape memory alloys. This model is further advanced in Chapter 4, where the algorithm is formulated with respect to mass fractions, so that the mass is the conserved quantity which is important for the changing mass densities of the process at hand. In addition, a more suitable and advanced material model is incorporated. The focus in Chapter 5 is set on the modelling of complete parts rather than on single melt tracks as in the previous chapters. Therefore, a multiscale framework by using the inherent strain (IS) method is developed, where the deformation and residual stress of complete parts is predicted. Finally, in Chapter 6, a non-standard dissipation function is introduced to capture the rate-dependent phase transformation of the titan aluminium alloy Ti_6Al_4V, which can predict the fraction of α- and β-phases with the corresponding residual strains. A more detailed summary of the respective chapters is given in Section 7.1, whereas further research questions are discussed in Section 7.2.

7.1 Summary and conclusion

Altogether, **Chapter 3** deals with a three-dimensional and thermomechanical finite element framework for the simulation of LPBF processes, where mechanical dissipation is neglected. The small strain constitutive model is established in the form of a phase transformation approach where, in contrast to common approaches for LPBF models, the different states of the material – powder, molten, and re-solidified – are explicitly captured as single phases with respective volume fractions. These volume fractions are determined via energy minimisation of the phase energy densities, where each phase is modelled as linear elastic. Thermal strains are additionally considered for the re-solidified phase. The finite element model of the manufacturing process itself incorporates approaches for the laser beam heat source and the layer build-up which necessitates non-straight-forward interventions with respect to the utilised finite element code, in this case the commercial programme Abaqus. The overall model is, at this stage, capable

of predicting at least qualitative results concerning the workpiece's final geometry and process-induced residual stresses for a single melt track with three deposition cycles.

In **Chapter 4**, a thermodynamically consistent and fully thermomechanically coupled framework is presented based on the phase transformation model of the previous chapter. Thereby, the model relies on the different states of the material with the respective mass densities, where the mass fractions are determined via homogenisation and energy minimisation. With this approach it is possible to include the changes in mass density and to assure conservation of mass. The phase distribution is not coupled one-to-one to the temperature distribution, e.g. the melting point, but is a result of the calculated distribution of the mass fractions and of a dissipation parameter which is defined within the minimisation problem. Furthermore, the volume change during the changes of the material state is considered through physically sound transformation strains. In addition, the model incorporates further material-based inelastic strain contributions, i.e. a viscous strain in the molten phase to capture the fluid behaviour and a plastic strain in the re-solidified phase to model the material behaviour of the solid phase. These strains are derived via dissipation functionals. Moreover, a thermal strain is included in the re-solidified material. This constitutive model is then implemented into Abaqus to simulate the LPBF process by using the same simulation model as in the previous chapter. With this, a three-line-layer deposition with a straight laser path and with an L-shape are simulated. Due to the micromechanically properly motivated material model, it is possible to predict the process induced residual stresses and the temperature evolution in a reasonable manner. In a post-processing step, the accumulated inelastic strains present are calculated which are usable for phenomenological models of e.g. complete parts as discussed in the subsequent chapter.

The scope of **Chapter 5** is to present a multiscale framework which is based on three modelling levels incorporating specific loading conditions and different material models. With this approach a micromechanically motivated phase transformation model for the single melt track is combined with the inherent strain method so that residual stresses of realistically sized parts are predictable within a reasonable amount of time. A coupled thermomechanical simulation is introduced by using Abaqus, differentiating between the laser scan model and the layer hatch model, whereas a purely mechanical simulation is used for the part model. For the laser scan model, a phase transformation model with a non-uniform volumetric Goldak heat source is used to simulate a single melt track. In contrast, the phase changes are purely temperature-dependent for the material model of the layer hatch model, where a cuboid heat source is used, so that a complete scan island can be efficiently simulated. It is demonstrated that the layer hatch model is capable of reproducing the residual strains and stresses of the laser scan model. Different sets of technological parameters (laser beam, scan velocity, island size) are considered in order to examine the influence on the inherent strains and residual stresses. Altogether, physically motivated inherent strains are determined, which depend on the underlying process parameters. Based on these findings, a larger scan island is preferable. Altogether, the framework adequately predicts different melt pool geometries and reasonable residual

stresses. It is concluded that constant inherent strains can be extracted for the layer hatch model to be applied to the simulation of a complete part. The part model rests upon the established inherent strain method, whereas the determination of the inherent strain tensor is micromechanically motivated and thermodynamically sound. With the determined inherent strains, the laser scan model and layer hatch model simulations do not have to be performed again. It is now possible to use not only the simulation of this part model but also the incorporation of arbitrary, more complex real structures and laser beam paths since the inherent strains are already set. This enables the simulation of large parts in a computationally efficient manner. To ensure a satisfactory process efficiency, an appropriate choice regarding laser velocity and melt pool size is necessary. The part model, where a twin cantilever beam is simulated, is capable of predicting the deformation, i.e. warpage and distortion, and residual stresses which have a reasonable magnitude for different laser parameters and scan patterns. The determined inherent strain tensors are qualitatively compared to results found in literature and are critically scrutinised. The simulations show that the use of different scan speeds and laser powers influences not only the magnitude of the inherent strains and overall deformation, but also the manufacturing time of the scan island, respectively the part.

In **Chapter 6**, a melt-solid-solid phase transformation model is proposed and applied to Ti_6Al_4V to explicitly capture the material behaviour of the molten, β- and α-phases of this material as well as combinations thereof. This is of importance as the composition of the crystal structure and material properties vary for the different phases. In consequence, the prediction of eigenstrains and eigenstresses can significantly be improved. The thermodynamically consistent and thermomechanically coupled framework is based on phase energy densities, cf. Chapter 4, where a non-standard dissipation function is used to calibrate the model to experimental data in terms of a continous cooling transformation (CCT) diagram. With this, a model-based CCT diagram can be implemented that consistently reflects available literature data. Therefore, only a limited number of experiments is necessary to determine the coefficients of the introduced dissipation function. Once these parameters are fitted in dependence of the present cooling rate, the remaining data, which is necessary for the dissipation function, is interpolated. The modelling and prediction of the evolution of the underlying strain contributions in addition to the microstructure composition can be considered physically plausible since a thermodynamically consistent and fully thermomechanically coupled phase transformation approach is used. The proposed framework is applied on a local scale using a stress-free driver to the elaboration of academically chosen examples as well as real process-based LPBF temperature profiles extracted from Abaqus simulations of the previous chapter. The simulations yield physically meaningful results in view of, e.g., strains and phase fraction evolution of the underlying microstructure on a local scale. The modelling and simulation framework proposed can straightforwardly be applied to different process parameters during LPBF processes which is of significant advantage since related experimental investigations are typically expensive and time consuming.

7.2 Outlook

In general, various enhancements are possible which can be differentiated based on necessity, effort and area. It shall be emphasised that the framework can straightforwardly be transferred and adapted to other materials which possess multiple solid phases, as the approach is generally applicable and derived from energy densities. Moreover, it can also be used for the simulation of other additive manufacturing processes based on metallic powder, for example laser cladding or direct energy deposition, as well as the examination of subsequent heat treatments. Machine learning concepts may be incorporated for the laser scan model and layer hatch model to generate and store inherent strains based on process parameters, e.g. laser power, laser velocity, layer height, scanning strategy and others.

One of the future (short-term) objectives lies in the advancement of the material model of the melt-solid-solid phase transformation framework in Chapter 6. For example, a more complex material model for each phase can be incorporated in the framework, cf. Chapters 4 and 5, where viscous and (visco)plastic strain contributions model the different inelastic effects of the molten and solid phases. Finally, a coupling and implementation with these extensions into the previously developed multiscale framework in Chapter 5 by using the commercial finite element programme Abaqus is of utmost interest. This may further improve the predicted residual stresses and deformation, while giving insight into the microstructure evolution. Once implemented, diverse parameter studies can be performed to find optimal initial conditions for industrial applications, e.g. applying different scan speeds should be further studied because the first results described in Section 5.3.4 are promising. In addition, it is important to examine the influence on the microstructure by using different preheating temperatures, scan patterns and to study subsequent annealing. With such an finite element approach, the effects on the composition and structure of the part – as well as the process-induced distortion and residual stresses – can be examined, cf. the experimental findings regarding the scan pattern in e.g. [95].

In the long term, research may focus on different areas:

- Looking into an increase in **computational efficiency** of the simulation frameworks, e.g. a mesh optimisation or code optimisation, could save further computational time. From a micromechanical viewpoint an enhancement of the material model for the layer hatch model, i.e. the scan island simulation, would be preferential, where for example the cooling rate is explicitly taken into account. However, to be able to use the phase transformation algorithm for the layer hatch model, this framework has to be computationally optimised beforehand.

- The quality and accurateness of the final results are highly influenced by the underlying **material model**. A more advanced material model may be used regarding

the developed phase transformation approach, so that e.g. the occurrence of tension in the powder and molten phases can be omitted in the spirit of [49] and the references cited therein. This means that only compressive strain contributions in the powder and the melt phases are taken into account for stress, while the material no longer stores any energy under tension. A further differentiation into α' (martensite), solid-α and solid-β and combinations thereof during cooling can be conducted in a straightforward manner with the proposed homogenisation approach. The constitutive framework can also be enhanced in terms of the modelling and simulation of subsequent heat treatments, compare Figure 6.2b, or post-LPBF damage mechanisms which may significantly be influenced by, e.g., the residual stresses and microstructure caused by the additive manufacturing process itself. In addition, it has to be investigated if the assumption of constant material parameters for each phase is valid or if, in contrast, for example temperature-dependent material parameters for each phase should be used. This also includes examining the need for a temperature-dependent yield limit for the plastic strains. An overview of material behaviour and physical characteristics in the literature is given in [17], which could be used to inlcude temperature-dependet material porperties for the underlying thermal and mechanical material parameters of the α- and β-phases in order to quantitatively improve the results. Due to the highly changing mass densities and relatively large inelastic strains, an extension of the constitutive framework to a large strain formulation needs to be investigated with regard to the influence on predicted stresses and deformations.

- In view of the **model calibration and verification**, different aspects are important. It is of utmost interest to verify the proposed multiscale modelling approach. Experiments need to be performed especially for the laser scan model. The parameters of the Goldak heat source have to be calibrated with experiments in order to achieve reliable results. In addition, some parameters, e.g. the dissipation parameter, need to be identified which requires comparisons to available experimental data. In this way, the material model parameters can be calibrated in comparison to experiments to further improve the simulation results. With these outcomes, it would be possible to quantitatively verify the deformation of the part simulation with experiments for the test structure of a twin cantilever beam. To ensure the transferability of the simulation results from this test structure to more complex parts, other geometries shall also be considered in the verification process.

Bibliography

[1] Abaqus. *Documentation, Version 2021*. Dassault Systèmes, Simulia Corp, United States, 2021.

[2] R. Ahluwalia, R. Laskowski, N. Ng, M. Wong, S. S. Quek, and D. T. Wu. Phase field simulation of α/β microstructure in titanium alloy welds. *Materials Research Express*, 7(4):046517, 2020. doi:10.1088/2053-1591/ab875a.

[3] B. Ahmad, S. O. van der Veen, M. E. Fitzpatrick, and H. Guo. Residual stress evaluation in selective-laser-melting additively manufactured titanium (Ti-6Al-4V) and inconel 718 using the contour method and numerical simulation. *Additive Manufacturing*, 22:571–582, 2018. doi:10.1016/j.addma.2018.06.002.

[4] T. Ahmed and H. J. Rack. Phase transformations during cooling in $\alpha + \beta$ titanium alloys. *Materials Science and Engineering: A*, 243(1-2):206–211, 1998. doi:10.1016/S0921-5093(97)00802-2.

[5] H. Ali, H. Ghadbeigi, and K. Mumtaz. Effect of scanning strategies on residual stress and mechanical properties of Selective Laser Melted Ti6Al4V. *Materials Science and Engineering: A*, 712:175–187, 2018. doi:10.1016/j.msea.2017.11.103.

[6] J. B. Allen. Mesoscale modeling of metal-based selective laser melting: Evolution of the vapor capillary. *Engineering Research Express*, 3(1):015026, 2021. doi:10.1088/2631-8695/abe9fc.

[7] ASTM International. ISO/ASTM 52900:2015, standard terminology for additive manufacturing – general principles – terminology. Technical report, ASTM International, West Conshohocken, 2015.

[8] M. Avrami. Kinetics of Phase Change. I General Theory. *The Journal of Chemical Physics*, 7(12):1103–1112, 1939. doi:10.1063/1.1750380.

[9] M. Azizpour, M. Ghoreishi, and A. Khorram. Numerical simulation of laser beam welding of Ti6Al4V sheet. *Journal of Computational and Applied Research in Mechanical Engineering*, 4(2):145–154, 2015. doi:10.22061/JCARME.2015.272.

[10] N. S. Bailey, C. Katinas, and Y. C. Shin. Laser direct deposition of AISI H13 tool steel powder with numerical modeling of solid phase transformation, hardness, and residual stresses. *Journal of Materials Processing Technology*, 247:223–233, 2017. doi:10.1016/j.jmatprotec.2017.04.020.

[11] T. Bartel and K. Hackl. A novel approach to the modelling of single-crystalline materials undergoing martensitic phase-transformations. *Materials Science and*

Engineering: A, 481-482:371–375, 2008. doi:10.1016/j.msea.2006.12.231.

[12] T. Bartel and K. Hackl. A micromechanical model for martensitic phase-transformations in shape-memory alloys based on energy-relaxation. *Zeitschrift für Angewandte Mathematik und Mechanik*, 89(10):792–809, 2009. doi:10.1002/zamm.200900244.

[13] T. Bartel, A. Menzel, and B. Svendsen. Thermodynamic and relaxation-based modeling of the interaction between martensitic phase transformations and plasticity. *Journal of the Mechanics and Physics of Solids*, 59(5):1004–1019, 2011. doi:10.1016/j.jmps.2011.02.006.

[14] T. Bartel, I. Guschke, and A. Menzel. Towards the simulation of Selective Laser Melting processes via phase transformation models. *Computers & Mathematics with Applications*, 78(7):2267–2281, 2019. doi:10.1016/j.camwa.2018.08.032.

[15] T. Bartel, R. Schulte, A. Menzel, B. Kiefer, and B. Svendsen. Investigations on enhanced Fischer–Burmeister NCP functions: Application to a rate-dependent model for ferroelectrics. *Archive of Applied Mechanics*, 89(6):995–1010, 2019. doi:10.1007/s00419-018-1466-7.

[16] T. Bartel, G.-L. Geuken, and A. Menzel. A thermodynamically consistent modelling framework for strongly time-dependent bainitic phase transitions. *International Journal of Solids and Structures*, 232:111172, 2021. doi:10.1016/j.ijsolstr.2021.111172.

[17] K. Bartsch, D. Herzog, B. Bossen, and C. Emmelmann. Material modeling of Ti–6Al–4V alloy processed by laser powder bed fusion for application in macro-scale process simulation. *Materials Science and Engineering: A*, 814:141237, 2021. doi:10.1016/j.msea.2021.141237.

[18] M. Bayat, C. G. Klingaa, S. Mohanty, D. De Baere, J. Thorborg, N. S. Tiedje, and J. H. Hattel. Part-scale thermo-mechanical modelling of distortions in Laser Powder Bed Fusion – Analysis of the sequential flash heating method with experimental validation. *Additive Manufacturing*, 36:101508, 2020. doi:10.1016/j.addma.2020.101508.

[19] C. Baykasoğlu, O. Akyildiz, M. Tunay, and A. C. To. A process-microstructure finite element simulation framework for predicting phase transformations and microhardness for directed energy deposition of Ti6Al4V. *Additive Manufacturing*, 35:101252, 2020. doi:10.1016/j.addma.2020.101252.

[20] E. M. Berkovich, A. A. Golubeva, E. G. Shadek, and L. K. Tukh. Use of methods of solving inverse problems of heat conduction to establish the coefficient of heat transfer in jet cooling. *Journal of Engineering Physics*, 34(5):619–624, 1978. doi:10.1007/BF00860863.

[21] R. Berthelsen, D. Tomath, R. Denzer, and A. Menzel. Finite element simulation of coating-induced heat transfer: Application to thermal spraying processes.

Meccanica, 51(2):291–307, 2016. doi:10.1007/s11012-015-0236-7.

[22] M. A. Biot. *Mechanics of Incremental Deformations*. John Wiley & Sons, 1965.

[23] C. Bonacina, G. Comini, A. Fasano, and M. Primicerio. Numerical solution of phase-change problems. *International Journal of Heat and Mass Transfer*, 16(10): 1825–1832, 1973. doi:10.1016/0017-9310(73)90202-0.

[24] J. Bonet and R. D. Wood. *Nonlinear continuum mechanics for finite element analysis*. Cambridge University Press, Cambridge, UK;, 2nd edition, 2008. doi:10.1017/CBO9780511755446.

[25] R. Boyer, G. Welsch, and E. W. Collings. *Materials properties handbook: Titanium alloys*. Materials properties handbook. ASM International, Materials Park, Ohio, 4. printing edition, 1994.

[26] M. Bugatti and Q. Semeraro. Limitations of the inherent strain method in simulating powder bed fusion processes. *Additive Manufacturing*, 23:329–346, 2018. doi:10.1016/j.addma.2018.05.041.

[27] J. Cao, M. A. Gharghouri, and P. Nash. Finite-element analysis and experimental validation of thermal residual stress and distortion in electron beam additive manufactured Ti-6Al-4V build plates. *Journal of Materials Processing Technology*, 237:409–419, 2016. doi:10.1016/j.jmatprotec.2016.06.032.

[28] F. Chen and W. Yan. High-fidelity modelling of thermal stress for additive manufacturing by linking thermal-fluid and mechanical models. *Materials & Design*, 196:109185, 2020. doi:10.1016/j.matdes.2020.109185.

[29] Q. Chen, X. Liang, D. Hayduke, J. Liu, L. Cheng, J. Oskin, R. Whitmore, and A. C. To. An inherent strain based multiscale modeling framework for simulating part-scale residual deformation for direct metal laser sintering. *Additive Manufacturing*, 28:406–418, 2019. doi:10.1016/j.addma.2019.05.021.

[30] Q. Chen, H. Taylor, A. Takezawa, X. Liang, X. Jimenez, R. Wicker, and A. C. To. Island scanning pattern optimization for residual deformation mitigation in laser powder bed fusion via sequential inherent strain method and sensitivity analysis. *Additive Manufacturing*, 46:102116, 2021. doi:10.1016/j.addma.2021.102116.

[31] Q. Chen, G. Guillemot, C.-A. Gandin, and M. Bellet. Three-dimensional finite element thermomechanical modeling of additive manufacturing by selective laser melting for ceramic materials. *Additive Manufacturing*, 16:124–137, 2017. doi:10.1016/j.addma.2017.02.005.

[32] W. Chen, L. Xu, Y. Han, L. Zhao, and H. Jing. Control of residual stress in metal additive manufacturing by low-temperature solid-state phase transformation: An experimental and numerical study. *Additive Manufacturing*, 42:102016, 2021. doi:10.1016/j.addma.2021.102016.

[33] B. Cheng, S. Shrestha, and K. Chou. Stress and deformation evaluations of scanning strategy effect in selective laser melting. *Additive Manufacturing*, 12:240–251, 2016. doi:10.1016/j.addma.2016.05.007.

[34] J. Cheon and S.-J. Na. Prediction of welding residual stress with real-time phase transformation by CFD thermal analysis. *International Journal of Mechanical Sciences*, 131–132:37–51, 2017. doi:10.1016/j.ijmecsci.2017.06.046.

[35] B. D. Coleman and W. Noll. The thermodynamics of elastic materials with heat conduction and viscosity. *Archive for Rational Mechanics and Analysis*, 13:167–178, 1963. doi:10.1007/BF01262690.

[36] P. Conti, F. Cianetti, and P. Pilerci. Parametric Finite Elements Model of SLM Additive Manufacturing process. *Procedia Structural Integrity*, 8:410–421, 2018. doi:10.1016/j.prostr.2017.12.041.

[37] K. Dai and L. Shaw. Finite element analysis of the effect of volume shrinkage during laser densification. *Acta Materialia*, 53(18):4743–4754, 2005. doi:10.1016/j.actamat.2005.06.014.

[38] W. J. Davids, H. Chen, K. Nomoto, H. Wang, S. Babu, S. Primig, X. Liao, A. Breen, and S. P. Ringer. Phase transformation pathways in Ti-6Al-4V manufactured via electron beam powder bed fusion. *Acta Materialia*, 215:117131, 2021. doi:10.1016/j.actamat.2021.117131.

[39] R. Dąbrowski. The kinetics of phase transformations during continuous cooling of the Ti6Al4V alloy from the single–phase β range. *Archives of Metallurgy and Materials*, 56(3):703–707, 2011. doi:10.2478/v10172-011-0077-x.

[40] D. De Baere, M. Bayat, S. Mohanty, and J. H. Hattel. Part-scale mechanical modelling of LPBF including microstructural evolution effects. *IOP Conference Series: Materials Science and Engineering*, 861:012013, 2020. doi:10.1088/1757-899X/861/1/012013.

[41] H. Dehghani, I. Noll, R. Penta, A. Menzel, and J. Merodio. The role of microscale solid matrix compressibility on the mechanical behaviour of poroelastic materials. *European Journal of Mechanics - A/Solids*, 83:103996, 2020. doi:10.1016/j.euromechsol.2020.103996.

[42] E. R. Denlinger, J. Irwin, and P. Michaleris. Thermomechanical modeling of additive manufacturing large parts. *Journal of Manufacturing Science and Engineering*, 136(6):061007, 2014. doi:10.1115/1.4028669.

[43] J. J. S. Dilip, S. Zhang, C. Teng, K. Zeng, C. Robinson, D. Pal, and B. Stucker. Influence of processing parameters on the evolution of melt pool, porosity, and microstructures in Ti-6Al-4V alloy parts fabricated by selective laser melting. *Progress in Additive Manufacturing*, 2(3):157–167, 2017. doi:10.1007/s40964-017-0030-2.

[44] DIN EN ISO 5832-3. Chirurgische Implantate - Metallische Werkstoffe- Teil 3: Titan 6-Aluminium 4-Vanadium Knetlegierung (ISO 5832-3:2021); Deutsche Fassung EN ISO 5832-3:2021. Standard, Beuth Verlag GmbH, 2022.

[45] DIN EN ISO/ASTM 52911-1. Additive Fertigung - Konstruktion - Teil 1: Laser-basierte Pulverbettfusion von Metallen (ISO/ASTM 52911-1:2019); Deutsche Fassung EN ISO/ASTM 52911-1:2019. Standard, Beuth Verlag GmbH, 2020.

[46] W. Dong, X. Liang, Q. Chen, S. Hinnebusch, Z. Zhou, and A. C. To. A new procedure for implementing the modified inherent strain method with improved accuracy in predicting both residual stress and deformation for laser powder bed fusion. *Additive Manufacturing*, 47:102345, 2021. doi:10.1016/j.addma.2021.102345.

[47] Z. Dong, Y. Liu, W. Wen, J. Ge, and J. Liang. Effect of hatch spacing on melt pool and as-built quality during selective laser melting of stainless steel: Modeling and experimental approaches. *Materials*, 12(1):50, 2019. doi:10.3390/ma12010050.

[48] D. K. Dusthakar, A. Menzel, and B. Svendsen. Comparison of phenomenological and laminate-based models for rate-dependent switching in ferroelectric continua. *GAMM-Mitteilungen*, 38(1):147–170, 2015. doi:10.1002/gamm.201510008.

[49] M. Ekh, A. Menzel, K. Runesson, and P. Steinmann. Anisotropic damage with the MCR effect coupled to plasticity. *International Journal of Engineering Science*, 41(13-14):1535–1551, 2003. doi:10.1016/S0020-7225(03)00032-6.

[50] J. X. Fang, S. Y. Dong, Y. J. Wang, B. S. Xu, Z. H. Zhang, D. Xia, and P. He. The effects of solid-state phase transformation upon stress evolution in laser metal powder deposition. *Materials & Design*, 87:807–814, 2015. doi:10.1016/j.matdes.2015.08.061.

[51] A. Fischer. A special Newton-type optimization method. *Optimization*, 24(3–4): 269–284, 1992. doi:10.1080/02331939208843795.

[52] M. Frémond. Matériaux à mémoire de forme. *Comptes rendus de l'Académie des sciences*, 304(7):239–244, 1987.

[53] C. H. Fu and Y. B. Guo. Three-dimensional temperature gradient mechanism in selective laser metling of Ti-6Al-4V. *Journal of Manufacturing Science and Engineering*, 136(6):061004, 2014. doi:10.1115/1.4028539.

[54] M. Galati, L. Iuliano, A. Salmi, and E. Atzeni. Modelling energy source and powder properties for the development of a thermal FE model of the EBM additive manufacturing process. *Additive Manufacturing*, 14:49–59, 2017. doi:10.1016/j.addma.2017.01.001.

[55] M. Galati, A. Snis, and L. Iuliano. Powder bed properties modelling and 3d thermo-mechanical simulation of the additive manufacturing Electron Beam Melting process. *Additive Manufacturing*, 30:100897, 2019. doi:10.1016/j.addma.2019.100897.

[56] R. K. Ganeriwala and T. I. Zohdi. A coupled discrete element-finite difference model of selective laser melting. *Granular Matter*, 18:21, 2016. doi:10.1007/s10035-016-0626-0.

[57] R. K. Ganeriwala, M. Strantza, W. E. King, B. Clausen, T. Q. Phan, L. E. Levine, D. W. Brown, and N. E. Hodge. Evaluation of a thermomechanical model for prediction of residual stress during laser powder bed fusion of Ti-6Al-4V. *Additive Manufacturing*, 27:489–502, 2019. doi:10.1016/j.addma.2019.03.034.

[58] R. K. Ganeriwala, N. E. Hodge, and J. M. Solberg. Towards improved speed and accuracy of laser powder bed fusion simulations via multiscale spatial representations. *Computational Materials Science*, 187:110112, 2021. doi:10.1016/j.commatsci.2020.110112.

[59] I. Gibson, D. Rosen, B. Stucker, and M. Khorasani. *Additive Manufacturing Technologies*. Springer, Cham, 3rd edition, 2021. doi:10.1007/978-3-030-56127-7.

[60] J. Goldak, A. Chakravarti, and M. Bibby. A new finite element model for welding heat sources. *Metallurgical Transactions B*, 15:299–305, 1984. doi:10.1007/BF02667333.

[61] H. Gong, K. Rafi, H. Gu, T. Starr, and B. Stucker. Analysis of defect generation in Ti–6Al–4V parts made using powder bed fusion additive manufacturing processes. *Additive Manufacturing*, 1-4:87–98, 2014. doi:10.1016/j.addma.2014.08.002.

[62] M. Gouge, E. Denlinger, J. Irwin, C. Li, and P. Michaleris. Experimental validation of thermo-mechanical part-scale modeling for laser powder bed fusion processes. *Additive Manufacturing*, 29:100771, 2019. doi:10.1016/j.addma.2019.06.022.

[63] D. Gu, C. Ma, M. Xia, D. Dai, and Q. Shi. A multiscale understanding of the thermodynamic and kinetic mechanisms of laser additive manufacturing. *Engineering*, 3(5):675–684, 2017. doi:10.1016/J.ENG.2017.05.011.

[64] A. V. Gusarov, I. Yadroitsev, P. Bertrand, and I. Smurov. Model of radiation and heat transfer in laser-powder interaction zone at Selective Laser Melting. *Journal of Heat Transfer*, 131(7):072101, 2009. doi:10.1115/1.3109245.

[65] I. Guschke, T. Bartel, and A. Menzel. A thermomechanical finite element based framework for phase transitions in laser based additive manufacturing processes. In T. Gleim and S. Lange, editors, *Proceedings of 8th GACM Colloquium on Computational Mechanics*, pages 327–330, Kassel, Germany, 2019. Kassel University Press. doi:10.19211/KUP9783737650939.

[66] I. Guschke, T. Bartel, and A. Menzel. A thermomechanical modelling framework for selective laser melting based on phase transformations. *Proceedings in Applied Mathematics and Mechanics*, 19(1):e201900059, 2019. doi:10.1002/pamm.201900059.

[67] M. R. Hill and D. V. Nelson. The inherent strain method for residual stress determination and its application to a long welded joint. *ASME Pressure Vessels*

and Piping Division, 318:343–352, 1995.

[68] N. E. Hodge, R. M. Ferencz, and J. M. Solberg. Implementation of a thermo-mechanical model for the simulation of selective laser melting. *Computational Mechanics*, 54(1):33–51, 2014. doi:10.1007/s00466-014-1024-2.

[69] N. E. Hodge, R. M. Ferencz, and R. M. Vignes. Experimental comparison of residual stresses for a thermomechanical model for the simulation of selective laser melting. *Additive Manufacturing*, 12:159–168, 2016. doi:10.1016/j.addma.2016.05.011.

[70] G. A. Holzapfel. *Nonlinear Solid Mechanics: A Continuum Approach for Engineering*. John Wiley & Sons, Chichester; New York, 1st edition, 2000.

[71] Y. Huang, L. J. Yang, X. Z. Du, and Y. P. Yang. Finite element analysis of thermal behavior of metal powder during selective laser melting. *International Journal of Thermal Sciences*, 104:146–157, 2016. doi:10.1016/j.ijthermalsci.2016.01.007.

[72] A. Hussein, L. Hao, C. Yan, and R. Everson. Finite element simulation of the temperature and stress fields in single layers built without-support in selective laser melting. *Materials & Design*, 52:638–647, 2013. doi:10.1016/j.matdes.2013.05.070.

[73] M. Itskov. *Tensor Algebra and Tensor Analysis for Engineers*. Mathematical Engineering. Springer International Publishing, Springer Cham, 4th edition, 2015. doi:10.1007/978-3-319-16342-0.

[74] A. Janda, S. Ebenbauer, A. Prestl, I. Siller, and H. Clemens. Microstructural adjustment of hot-rolled Ti–6Al–4V based on a CCT diagram. *Materials Science and Technology*, 38(13):957–964, 2022. doi:10.1080/02670836.2022.2068243.

[75] S. H. Jeong, E. G. Park, J. W. Kang, J. Y. Cho, J. H. Kim, and K. Kim. Thermal analysis for simulation of metal additive manufacturing process considering temperature- and history-dependent material properties. *International Journal of Aeronautical and Space Sciences*, 22(1):52–63, 2021. doi:10.1007/s42405-020-00283-6.

[76] W. A. Johnson and R. F. Mehl. Reaction kinetics in processes of nucleation and growth. *Transactions of the Metallurgical Society of AIME*, 135:416–442, 1939.

[77] V. Juechter, T. Scharowsky, R. F. Singer, and C. Körner. Processing window and evaporation phenomena for Ti–6Al–4V produced by selective electron beam melting. *Acta Materialia*, 76:252–258, 2014. doi:10.1016/j.actamat.2014.05.037.

[78] P. Junker and K. Hackl. A thermo-mechanically coupled field model for shape memory alloys. *Continuum Mechanics and Thermodynamics*, 26(6):859–877, 2014. doi:10.1007/s00161-014-0345-x.

[79] C. Kanzow. Some noninterior continuation methods for linear complementarity problems. *SIAM Journal on Matrix Analysis and Applications*, 17(4):851–868, 1996. doi:10.1137/S0895479894273134.

[80] F. R. Kaschel, R. K. Vijayaraghavan, A. Shmeliov, E. K. McCarthy, M. Canavan, P. J. McNally, D. P. Dowling, V. Nicolosi, and M. Celikin. Mechanism of stress relaxation and phase transformation in additively manufactured Ti-6Al-4V via in situ high temperature XRD and TEM analyses. *Acta Materialia*, 188:720–732, 2020. doi:10.1016/j.actamat.2020.02.056.

[81] N. Keller. *Verzugsminimierung bei selektiven Laserschmelzverfahren durch Multi-Skalen-Simulation*. PhD thesis, Universität Bremen, 2017.

[82] N. Keller and V. Ploshikhin. New method for fast predicitons of residual stresses and distortion of AM part. In D. L. Bourell, editor, *Solid Freeform Fabrication Symposium*, volume 25, pages 1229–1237, Austin, USA, 2014. University of Texas at Austin.

[83] C. Kenel, D. Grolimund, X. Li, E. Panepucci, V. A. Samson, D. F. Sanchez, F. Marone, and C. Leinenbach. In situ investigation of phase transformations in Ti-6Al-4V under additive manufacturing conditions combining laser melting and high-speed micro-X-ray diffraction. *Scientific Reports*, 7:16358, 2017. doi:10.1038/s41598-017-16760-0.

[84] S. A. Khairallah and A. Anderson. Mesoscopic simulation model of selective laser melting of stainless steel powder. *Journal of Materials Processing Technology*, 214 (11):2627–2636, 2014. doi:10.1016/j.jmatprotec.2014.06.001.

[85] B. Kiefer, T. Bartel, and A. Menzel. Implementation of numerical integration schemes for the simulation of magnetic sma constitutive response. *Smart Materials and Structures*, 21:094007, 2012. doi:10.1088/0964-1726/21/9/094007.

[86] B. Kiefer, T. Waffenschmidt, L. Sprave, and A. Menzel. A gradient-enhanced damage model coupled to plasticity—multi-surface formulation and algorithmic concepts. *International Journal of Damage Mechanics*, 27(2):253–295, 2018. doi:10.1177/1056789516676306.

[87] D. P. Koistinen and R. E. Marburger. A general equation prescribing the extent of the austenite-martensite transformation in pure iron-carbon alloys and plain carbon steels. *Acta Metallurgica*, 7(1):59–60, 1959. doi:10.1016/0001-6160(59)90170-1.

[88] S. Kollmannsberger, A. Özcan, M. Carraturo, N. Zander, and E. Rank. A hierarchical computational model for moving thermal loads and phase changes with applications to Selective Laser Melting. *Computers & Mathematics with Applications*, 75(5):1483–1497, 2018. doi:10.1016/j.camwa.2017.11.014.

[89] S. Kollmannsberger, M. Carraturo, A. Reali, and F. Auricchio. Accurate prediction of melt pool shapes in Laser Powder Bed Fusion by the non-linear temperature equation including phase changes. *Integrating Materials and Manufacturing Innovation*, 8(2):167–177, 2019. doi:10.1007/s40192-019-00132-9.

[90] A. N. Kolmogorov. On the Statistical Theory of Metal Crystallization. *Bulletin of the Academy of Sciences of the USSR, Mathematics Series*, pages 335–359, 1937.

[91] T. A. Krol, C. Seidel, J. Schilp, M. Hofmann, W. Gan, and M. F. Zaeh. Verification of structural simulation results of metal-based additive manufacturing by means of neutron diffraction. *Physics Procedia*, 41:849–857, 2013. doi:10.1016/j.phpro.2013.03.158.

[92] T. A. Krol, S. Westhäuser, M. F. Zäh, J. Schilp, and G. Groth. Development of a simulation-based process chain – strategy for different levels of detail for the preprocessing definitions. *SNE Simulation Notes Europe*, 21(3-4):135–140, 2011. doi:10.11128/sne.21.tn.10081.

[93] J.-P. Kruth, L. Froyen, J. Van Vaerenbergh, P. Mercelis, M. Rombouts, and B. Lauwers. Selective laser melting of iron-based powder. *Journal of Materials Processing Technology*, 149(1-3):616–622, 2004. doi:10.1016/j.jmatprotec.2003.11.051.

[94] J.-P. Kruth, J. Deckers, E. Yasa, and R. Wauthlé. Assessing and comparing influencing factors of residual stresses in selective laser melting using a novel analysis method. *Proceedings of the Institution of Mechanical Engineers, Part B: Journal of Engineering Manufacture*, 226(6):980–991, 2012. doi:10.1177/0954405412437085.

[95] P. Kumar, O. Prakash, and U. Ramamurty. Micro-and meso-structures and their influence on mechanical properties of selectively laser melted Ti-6Al-4V. *Acta Materialia*, 154:246–260, 2018. doi:10.1016/j.actamat.2018.05.044.

[96] C. Körner, A. Bauerreiß, and E. Attar. Fundamental consolidation mechanisms during selective beam melting of powders. *Modelling and Simulation in Materials Science and Engineering*, 21:085011, 2013. doi:10.1088/0965-0393/21/8/085011.

[97] C. Lampa, A. F. H. Kaplan, J. Powell, and C. Magnusson. An analytical thermodynamic model of laser welding. *Journal of Physics D: Applied Physics*, 30(9): 1293, 1997. doi:10.1088/0022-3727/30/9/004.

[98] C. Leyens and M. Peters, editors. *Titanium and Titanium Alloys: Fundamentals and Applications*. John Wiley & Sons, Ltd, Weinheim, 2003. doi:10.1002/3527602119.

[99] C. Li, J. F. Liu, X. Y. Fang, and Y. B. Guo. Efficient predictive model of part distortion and residual stress in selective laser melting. *Additive Manufacturing*, 17:157–168, 2017. doi:10.1016/j.addma.2017.08.014.

[100] R. Li, Y. Shi, J. Liu, H. Yao, and W. Zhang. Effects of processing parameters on the temperature field of selective laser melting metal powder. *Powder Metallurgy and Metal Ceramics*, 48(3–4):186–195, 2009. doi:10.1007/s11106-009-9113-z.

[101] Y. Li and D. Gu. Parametric analysis of thermal behavior during selective laser melting additive manufacturing of aluminum alloy powder. *Materials and Design*, 63:856–867, 2014. doi:10.1016/j.matdes.2014.07.006.

[102] X. Liang, L. Cheng, Q. Chen, Q. Yang, and A. C. To. A modified method for estimating inherent strains from detailed process simulation for fast residual distortion prediction of single-walled structures fabricated by directed energy deposition. *Additive Manufacturing*, 23:471–486, 2018. doi:10.1016/j.addma.2018.08.029.

[103] X. Liang, Q. Chen, L. Cheng, D. Hayduke, and A. C. To. Modified inherent strain method for efficient prediction of residual deformation in direct metal laser sintered components. *Computational Mechanics*, 64(6):1719–1733, 2019. doi:10.1007/s00466-019-01748-6.

[104] X. Liang, W. Dong, Q. Chen, and A. C. To. On incorporating scanning strategy effects into the modified inherent strain modeling framework for laser powder bed fusion. *Additive Manufacturing*, 37:101648, 2021. doi:10.1016/j.addma.2020.101648.

[105] Z. Liang, Z. Sun, W. Zhang, S. Wu, and H. Chang. The effect of heat treatment on microstructure evolution and tensile properties of selective laser melted Ti6Al4V alloy. *Journal of Alloys and Compounds*, 782:1041–1048, 2019. doi:10.1016/j.jallcom.2018.12.051.

[106] M. Lindroos, T. Pinomaa, A. Antikainen, J. Lagerbom, J. Reijonen, T. Lindroos, T. Andersson, and A. Laukkanen. Micromechanical modeling approach to single track deformation, phase transformation and residual stress evolution during selective laser melting using crystal plasticity. *Additive Manufacturing*, 38:101819, 2021. doi:10.1016/j.addma.2020.101819.

[107] I.-S. Liu. *Continuum Mechanics*. Advanced Texts in Physics. Springer Berlin Heidelberg, Berlin, Heidelberg, 1st edition, 2002. doi:10.1007/978-3-662-05056-9.

[108] M. Liu, L. N. S. Chiu, C. Vundru, Y. Liu, A. Huang, C. Davies, X. Wu, and W. Yan. A characteristic time-based heat input model for simulating selective laser melting. *Additive Manufacturing*, 44:102026, 2021. doi:10.1016/j.addma.2021.102026.

[109] S. Liu and Y. C. Shin. Prediction of 3D microstructure and phase distributions of Ti6Al4V built by the directed energy deposition process via combined multi-physics models. *Additive Manufacturing*, 34:101234, 2020. doi:10.1016/j.addma.2020.101234.

[110] R. Long, W. Liu, F. Xing, and H. Wang. Numerical simulation of thermal behavior during laser metal deposition shaping. *Transactions of Nonferrous Metals Society of China*, 18(3):691–699, 2008. doi:10.1016/S1003-6326(08)60120-X.

[111] H. Lu, W. Deng, K. Luo, Y. Chen, J. Wang, and J. Lu. Tailoring microstructure of additively manufactured Ti6Al4V titanium alloy using hybrid additive manufacturing technology. *Additive Manufacturing*, 63:103416, 2023. doi:10.1016/j.addma.2023.103416.

[112] Y. Lu, S. Wu, Y. Gan, T. Huang, C. Yang, L. Junjie, and J. Lin. Study on the microstructure, mechanical property and residual stress of SLM Inconel-718 alloy

manufactured by differing island scanning strategy. *Optics & Laser Technology*, 75:197–206, 2015. doi:10.1016/j.optlastec.2015.07.009.

[113] L. Ma and H. Bin. Temperature and stress analysis and simulation in fractal scanning-based laser sintering. *The International Journal of Advanced Manufacturing Technology*, 34(9–10):898–903, 2007. doi:10.1007/s00170-006-0665-5.

[114] R. Mahnken and E. Stein. Parameter identification for finite deformation elasto-plasticity in principal directions. *Computer Methods in Applied Mechanics and Engineering*, 147(1-2):17–39, 1997. doi:10.1016/S0045-7825(97)00008-X.

[115] S. Malinov, Z. Guo, W. Sha, and A. Wilson. Differential scanning calorimetry study and computer modeling of $\beta \rightarrow \alpha$ phase transformation in a Ti-6Al-4V alloy. *Metallurgical and Materials Transactions A*, 32(4):879–887, 2001. doi:10.1007/s11661-001-0345-x.

[116] V. Manvatkar, A. De, and T. DebRoy. Heat transfer and material flow during laser assisted multi-layer additive manufacturing. *Journal of Applied Physics*, 116 (12):124905, 2014. doi:10.1063/1.4896751.

[117] C. Meier, R. W. Penny, Y. Zou, J. S. Gibbs, and A. J. Hart. Thermophysical phenomena in metal additive manufacturing by Selective Laser Melting: Fundamentals, modeling, simulation and experimentation. *Annual Review of Heat Transfer*, 20:241–316, 2017. doi:10.1615/AnnualRevHeatTransfer.2018019042.

[118] C. Meier, S. L. Fuchs, A. J. Hart, and W. A. Wall. A novel smoothed particle hydrodynamics formulation for thermo-capillary phase change problems with focus on metal additive manufacturing melt pool modeling. *Computer Methods in Applied Mechanics and Engineering*, 381:113812, 2021. doi:10.1016/j.cma.2021.113812.

[119] P. Mercelis and J.-P. Kruth. Residual stresses in selective laser sintering and selective laser melting. *Rapid Prototyping Journal*, 12(5):254–265, 2006. doi:10.1108/13552540610707013.

[120] J. G. Michopoulos, A. P. Iliopoulos, J. C. Steuben, A. J. Birnbaum, and S. G. Lambrakos. On the multiphysics modeling challenges for metal additive manufacturing processes. *Additive Manufacturing*, 22:784–799, 2018. doi:10.1016/j.addma.2018.06.019.

[121] K. C. Mills. *Recommended Values of Thermophysical Properties for Selected Commercial Alloys*. Woodhead Publishing, Cambridge; UK, 1st edition, 2002.

[122] M. Muhammad, J. W. Pegues, N. Shamsaei, and M. Haghshenas. Effect of heat treatments on microstructure/small-scale properties of additive manufactured Ti-6Al-4V. *The International Journal of Advanced Manufacturing Technology*, 103 (9-12):4161–4172, 2019. doi:10.1007/s00170-019-03789-w.

[123] H. Murakawa, D. Deng, N. Ma, and J. Wang. Applications of inherent strain and interface element to simulation of welding deformation in thin plate structures. *Computational Materials Science*, 51(1):43–52, 2012.

doi:10.1016/j.commatsci.2011.06.040.

[124] E. Neiva, S. Badia, A. F. Martín, and M. Chiumenti. A scalable parallel finite element framework for growing geometries. Application to metal additive manufacturing. *International Journal for Numerical Methods in Engineering*, 119(11): 1098–1125, 2019. doi:10.1002/nme.6085.

[125] E. Neiva, M. Chiumenti, M. Cervera, E. Salsi, G. Piscopo, S. Badia, A. F. Martín, Z. Chen, C. Lee, and C. Davies. Numerical modelling of heat transfer and experimental validation in powder-bed fusion with the virtual domain approximation. *Finite Elements in Analysis and Design*, 168:103343, 2020. doi:10.1016/j.finel.2019.103343.

[126] F. Neugebauer, N. Keller, V. Ploshikhin, F. Feuerhahn, and H. Koehler. Multi Scale FEM Simulation for Distortion Calculation in Additive Manufacturing of Hardening Stainless Steel. In *International Workshop on Thermal Forming and Welding Distortion*, volume 54, pages 1–11, Bremen, Germany, 2014. BIAS Verlag.

[127] P. Nie, O. A. Ojo, and Z. Li. Numerical modeling of microstructure evolution during laser additive manufacturing of a nickel-based superalloy. *Acta Materialia*, 77:85–95, 2014. doi:10.1016/j.actamat.2014.05.039.

[128] J. Nitzler, C. Meier, K. W. Müller, W. A. Wall, and N. E. Hodge. A novel physics-based and data-supported microstructure model for part-scale simulation of laser powder bed fusion of Ti-6Al-4V. *Advanced Modeling and Simulation in Engineering Sciences*, 8:16, 2021. doi:10.1186/s40323-021-00201-9.

[129] I. Noll, L. Koppka, T. Bartel, and A. Menzel. A micromechanically motivated multiscale approach for residual distortion in laser powder bed fusion processes. *Additive Manufacturing*, 60:103277, 2022. doi:10.1016/j.addma.2022.103277.

[130] I. Noll, T. Bartel, and A. Menzel. A thermodynamicall consistent phase transformation model for multiphase alloys – Application to Ti_6Al_4V in LPBF processes. *Computational Mechanics*, 2024. doi:10.1007/s00466-024-02479-z.

[131] I. Noll, T. Bartel, and A. Menzel. A computational phase transformation model for selective laser melting processes. *Computational Mechanics*, 66(6):1321–1342, 2020. doi:10.1007/s00466-020-01903-4.

[132] I. Noll, T. Bartel, and A. Menzel. On the incorporation of a micromechanical material model into the inherent strain method – Application to the modeling of selective laser melting. *GAMM-Mitteilungen*, 44(3):e202100015, 2021. doi:10.1002/gamm.202100015.

[133] P. Oppermann, R. Denzer, and A. Menzel. A thermo-viscoplasticity model for metals over wide temperature ranges – Application to case hardening steel. *Computational Mechanics*, 69(2):541–563, 2022. doi:10.1007/s00466-021-02103-4.

[134] R. Ostwald, E. Kuhl, and A. Menzel. On the implementation of finite deformation gradient-enhanced damage models. *Computational Mechanics*, 64(3):847–877,

2019. doi:10.1007/s00466-019-01684-5.

[135] S. Pagano, P. Alart, and O. Maisonneuve. Solid-solid phase transition modelling. Local and global minimizations of non-convex and relaxed potentials. Isothermal case for shape memory alloys. *International Journal of Engineering Science*, 36 (10):1143–1172, 1998. doi:10.1016/S0020-7225(98)00010-X.

[136] D. Pal, N. Patil, K. H. Kutty, K. Zeng, A. Moreland, A. Hicks, D. Beeler, and B. Stucker. A generalized feed-forward dynamic adaptive mesh refinement and derefinement finite-element framework for metal laser sintering – Part II: Nonlinear thermal simulations and validations. *Journal of Manufacturing Science and Engineering*, 138(6):061003, 2016. doi:10.1115/1.4032078.

[137] S. Pal, N. Gubeljak, R. Hudák, G. Lojen, V. Rajťúková, T. Brajlih, and I. Drstvenšek. Evolution of the metallurgical properties of Ti-6Al-4V, produced with different laser processing parameters, at constant energy density in selective laser melting. *Results in Physics*, 17:103186, 2020. doi:10.1016/j.rinp.2020.103186.

[138] C. Panwisawas, B. Perumal, R. M. Ward, N. Turner, R. P. Turner, J. W. Brooks, and H. C. Basoalto. Keyhole formation and thermal fluid flow-induced porosity during laser fusion welding in titanium alloys: Experimental and modelling. *Acta Materialia*, 126:251–263, 2017. doi:10.1016/j.actamat.2016.12.062.

[139] C. Panwisawas, Y. T. Tang, and R. C. Reed. Metal 3D printing as a disruptive technology for superalloys. *Nature Communications*, 11:2327, 2020. doi:10.1038/s41467-020-16188-7.

[140] L. Papadakis, A. Loizou, J. Risse, and J. Schrage. Numerical computation of component shape distortion manufactured by Selective Laser Melting. *Procedia CIRP*, 18:90–95, 2014. doi:10.1016/j.procir.2014.06.113.

[141] H. Parisch. *Festkörper-Kontinuumsmechanik*. Vieweg+Teubner Verlag, Wiesbaden, 2003. doi:10.1007/978-3-322-80052-7.

[142] L. Parry, I. A. Ashcroft, and R. D. Wildman. Understanding the effect of laser scan strategy on residual stress in selective laser melting through thermo-mechanical simulation. *Additive Manufacturing*, 12:1–15, 2016. doi:10.1016/j.addma.2016.05.014.

[143] N. Patil, R. K. Ganeriwala, J. M. Solberg, N. E. Hodge, and R. M. Ferencz. Benchmark multi-layer simulations for residual stresses and deformation in small additively manufactured metal parts. *Additive Manufacturing*, 45:102015, 2021. doi:10.1016/j.addma.2021.102015.

[144] R. Pederson, O. Babushkin, F. Skystedt, and R. Warren. Use of high temperature X-ray diffractometry to study phase transitions and thermal expansion properties in Ti-6Al-4V. *Materials Science and Technology*, 19(11):1533–1538, 2003. doi:10.1179/026708303225008013.

[145] S. D. Proell, W. A. Wall, and C. Meier. On phase change and latent heat models in metal additive manufacturing process simulation. *Advanced Modeling and Simulation in Engineering Sciences*, 7(1):24, 2020. doi:10.1186/s40323-020-00158-1.

[146] D. Radaj. *Eigenspannungen und Verzug beim Schweißen: Rechen- und Meßverfahren*. DVS-Verlag, Düsseldorf, 2002.

[147] A. Reuss. Berechnung der Fließgrenze von Mischkristallen auf Grund der Plastizitätsbedingung für Einkristalle. *Zeitschrift für Angewandte Mathematik und Mechanik*, 9(1):49–58, 1929. doi:10.1002/zamm.19290090104.

[148] D. Riedlbauer, P. Steinmann, and J. Mergheim. Thermomechanical finite element simulations of selective electron beam melting process: Performance considerations. *Computational Mechanics*, 54(1):109–122, 2014. doi:10.1007/s00466-014-1026-0.

[149] D. Riedlbauer, P. Steinmann, and J. Mergheim. Thermomechanical simulation of the selective laser melting process for PA12 including volumetric shrinkage. *AIP Conference Proceedings*, 1664(1):160005, 2015. doi:10.1063/1.4918512.

[150] I. A. Roberts, C. J. Wang, R. Esterlein, M. Stanford, and D. J. Mynors. A three-dimensional finite element analysis of the temperature field during laser melting of metal powders in additive layer manufacturing. *International Journal of Machine Tools and Manufacture*, 49(12-13):916–923, 2009. doi:10.1016/j.ijmachtools.2009.07.004.

[151] S. Roy, M. Juha, M. S. Shephard, and A. M. Maniatty. Heat transfer model and finite element formulation for simulation of selective laser melting. *Computational Mechanics*, 62(3):273–284, 2018. doi:10.1007/s00466-017-1496-y.

[152] S. Saeb, P. Steinmann, and A. Javili. Aspects of computational homogenization at finite deformations: A unifying review from Reuss' to Voigt's bound. *Applied Mechanics Reviews*, 68(5):050801, 2016. doi:10.1115/1.4034024.

[153] E. Salvati, A. J. G. Lunt, S. Ying, T. Sui, H. J. Zhang, C. Heason, G. Baxter, and A. M. Korsunsky. Eigenstrain reconstruction of residual strains in an additively manufactured and shot peened nickel superalloy compressor blade. *Computer Methods in Applied Mechanics and Engineering*, 320:335–351, 2017. doi:10.1016/j.cma.2017.03.005.

[154] M. Schmidt-Baldassari. Numerical concepts for rate-independent single crystal plasticity. *Computer Methods in Applied Mechanics and Engineering*, 192(11-12): 1261–1280, 2003. doi:10.1016/S0045-7825(02)00563-7.

[155] M. Schänzel, A. Ilin, and V. Ploshikhin. New approach for fast numerical prediction of residual stress and distortion of AM parts from steels with phase transformations. In C. Sommitsch, N. Enzinger, and P. Mayr, editors, *Mathematical Modelling of Weld Phenomena*, volume 12, pages 1–21, Graz, Austria, 2019. Verlag der Technischen Universität Graz. doi:10.3217/978-3-85125-615-4-54.

[156] M. Schänzel, D. Shakirov, A. Ilin, and V. Ploshikhin. Coupled thermo-mechanical process simulation method for selective laser melting considering phase transformation steels. *Computers & Mathematics with Applications*, 78(7):2230–2246, 2019. doi:10.1016/j.camwa.2019.01.019.

[157] C. Seidel and M. F. Zaeh. Multi-scale modelling approach for contributing to reduced distortion in parts made by Laser-based Powder Bed Fusion. *Procedia CIRP*, 67:197–202, 2018. doi:10.1016/j.procir.2017.12.199.

[158] I. Setien, M. Chiumenti, S. O. von der Veen, M. S. Sebastian, F. Garciandía, and A. Echeverría. Empirical methodology to determine inherent strains in additive manufacturing. *Computers & Mathematics with Applications*, 78(7):2282–2295, 2019. doi:10.1016/j.camwa.2018.05.015.

[159] N. Shen and K. Chou. Thermal modeling of electron beam additive manufacturing process: Powder sintering effects. In *ASME 2012 International Manufacturing Science and Engineering Conference*, pages 287–295. ASME, 2012. doi:10.1115/MSEC2012-7253.

[160] M. Siewert, F. Neugebauer, J. Epp, and V. Ploshikhin. Validation of Mechanical Layer Equivalent Method for simulation of residual stresses in additive manufactured components. *Computers & Mathematics with Applications*, 78(7):2407–2416, 2019. doi:10.1016/j.camwa.2018.08.016.

[161] J. C. Simo and T. J. R. Hughes. *Computational Inelasticity*. Number 7 in Interdisciplinary Applied Mathematics. Springer New York, New York, 1st edition, 1998. doi:10.1007/b98904.

[162] M. Strantza, R. K. Ganeriwala, B. Clausen, T. Q. Phan, L. E. Levine, D. C. Pagan, J. P. C. Ruff, W. E. King, N. S. Johnson, R. M. Martinez, V. Anghel, G. Rafailov, and D. W. Brown. Effect of the scanning strategy on the formation of residual stresses in additively manufactured Ti-6Al-4V. *Additive Manufacturing*, 45:102003, 2021. doi:10.1016/j.addma.2021.102003.

[163] D. Sun, D. Gu, K. Lin, J. Ma, W. Chen, J. Huang, X. Sun, and M. Chu. Selective laser melting of titanium parts: Influence of laser process parameters on macro- and microstructures and tensile property. *Powder Technology*, 342:371–379, 2019. doi:10.1016/j.powtec.2018.09.090.

[164] M. Sun and J. Beaman. A three dimensional model for selecive laser sintering. In H. L. Marcus, J. J. Beaman, J. W. Barlow, D. L. Bourell, and R. H. Crawford, editors, *Solid Freeform Fabrication Symposium Proceedings*, volume 2, pages 102–109. University of Texas at Austin, 1991.

[165] S. Sun, L. Zheng, Y. Liu, J. Liu, and H. Zhang. Selective laser melting of Al-Fe-V-Si heat-resistant aluminum alloy powder: modeling and experiments. *International Journal of Advanced Manufacturing Technology*, 80(9-12):1787–1797, 2015. doi:10.1007/s00170-015-7137-8.

[166] J. T. Tchuindjang, H. Paydas, H.-S. Tran, R. Carrus, L. Duchêne, A. Mertens, and A.-M. Habraken. A new concept for modeling phase transformations in Ti6Al4V alloy manufactured by Directed Energy Deposition. *Materials*, 14(11):2985, 2021. doi:10.3390/ma14112985.

[167] J. Teixeira, D. Maréchal, R. C. Wimpory, S. Denis, F. Lefebvre, and R. Frappier. Formation of residual stresses during quenching of Ti17 and Ti–6Al–4V alloys: Influence of phase transformations. *Materials Science and Engineering: A*, 832: 142456, 2022. doi:10.1016/j.msea.2021.142456.

[168] C. Truesdell and W. Noll. *The Non-Linear Field Theories of Mechanics*. Springer Berlin Heidelberg, Berlin, Heidelberg, 3rd edition, 2004. doi:10.1007/978-3-662-10388-3.

[169] Y. Ueda, K. Fukuda, K. Nakacho, and S. Endo. A new measuring method of residual stresses with the aid of finite element method and reliability of estimated values. *Journal of the Society of Naval Architects of Japan*, 1975(138):499–507, 1975. doi:10.2534/jjasnaoe1968.1975.138_499.

[170] G. Vastola, G. Zhang, Q. X. Pei, and Y.-W. Zhang. Modeling the microstructure evolution during additive manufacturing of Ti6Al4V: A comparison between Electron Beam Melting and Selective Laser Melting. *The Journal of The Minerals, Metals & Materials Society*, 68(5):1370–1375, 2016. doi:10.1007/s11837-016-1890-5.

[171] W. Voigt. Über die Beziehung zwischen den beiden Elastizitätskonstanten isotroper Körper. *Annalen der Physik*, 274(12):573–587, 1889. doi:10.1002/andp.18892741206.

[172] H. Wang, Q. Chao, H. S. Chen, Z. B. Chen, S. Primig, W. Xu, S. P. Ringer, and X. Z. Liao. Formation of a transition V-rich structure during the α' to $\alpha + \beta$ phase transformation process in additively manufactured Ti-6Al-4V. *Acta Materialia*, 235:118104, 2022. doi:10.1016/j.actamat.2022.118104.

[173] S. H. Wang, M. D. Wei, and L. W. Tsay. Tensile properties of LBW welds in Ti–6Al–4V alloy at evaluated temperatures below 450°C. *Materials Letters*, 57 (12):1815–1823, 2003. doi:10.1016/S0167-577X(02)01074-1.

[174] H. Wessels, C. Weißenfels, and P. Wriggers. Metal particle fusion analysis for additive manufacturing using the stabilized optimal transportation meshfree method. *Computer Methods in Applied Mechanics and Engineering*, 339:91–114, 2018. doi:10.1016/j.cma.2018.04.042.

[175] H. Wessels, T. Bode, C. Weißenfels, P. Wriggers, and T. I. Zohdi. Investigation of heat source modeling for selective laser melting. *Computational Mechanics*, 63(5): 949–970, 2019. doi:10.1007/s00466-018-1631-4.

[176] P. Wriggers. *Nonlinear Finite Element Methods*. Springer, Berlin, Heidelberg, 1st edition, 2010. doi:10.1007/978-3-540-71001-1.

[177] A. S. Wu, D. W. Brown, M. Kumar, G. F. Gallegos, and W. E. King. An experimental investigation into additive manufacturing-induced residual stresses in 316L stainless steel. *Metallurgical and Materials Transactions A*, 45(13):6260–6270, 2014. doi:10.1007/s11661-014-2549-x.

[178] I. Yadroitsev, P. Krakhmalev, and I. Yadroitsava. Selective laser melting of Ti6Al4V alloy for biomedical applications: Temperature monitoring and microstructural evolution. *Journal of Alloys and Compounds*, 583:404–409, 2014. doi:10.1016/j.jallcom.2013.08.183.

[179] W. Yan, S. Lin, O. L. Kafka, Y. Lian, C. Yu, Z. Liu, J. Yan, S. Wolff, H. Wu, E. Ndip-Agbor, M. Mozaffar, K. Ehmann, J. Cao, G. J. Wagner, and W. K. Liu. Data-driven multi-scale multi-physics models to derive process–structure–property relationships for additive manufacturing. *Computational Mechanics*, 61(5):521–541, 2018. doi:10.1007/s00466-018-1539-z.

[180] X. Yang, R. A. Barrett, M. Tong, N. M. Harrison, and S. B. Leen. Towards a process-structure model for Ti-6Al-4V during additive manufacturing. *Journal of Manufacturing Processes*, 61:428–439, 2021. doi:10.1016/j.jmapro.2020.11.033.

[181] Y. P. Yang, M. Jamshidinia, P. Boulware, and S. M. Kelly. Prediction of microstructure, residual stress, and deformation in laser powder bed fusion process. *Computational Mechanics*, 61(5):599–615, 2018. doi:10.1007/s00466-017-1528-7.

[182] M. Yuan and Y. Ueda. Prediction of residual stresses in welded T- and I-joints using inherent strains. *Journal of Engineering Materials and Technology*, 118(2):229–234, 1996. doi:10.1115/1.2804892.

[183] M. F. Zaeh and G. Branner. Investigations on residual stresses and deformations in selective laser melting. *Production Engineering*, 4(1):35–45, 2010. doi:10.1007/s11740-009-0192-y.

[184] L. Zhang, E. W. Reutzel, and P. Michaleris. Finite element modeling discretization requirements for the laser forming process. *International Journal of Mechanical Sciences*, 46(4):623–637, 2004. doi:10.1016/j.ijmecsci.2004.04.001.

[185] Q. Zhang, J. Xie, Z. Gao, T. London, D. Griffiths, and V. Oancea. A metallurgical phase transformation framework applied to SLM additive manufacturing processes. *Materials & Design*, 166:107618, 2019. doi:10.1016/j.matdes.2019.107618.

[186] T. Zhang, H. Li, S. Liu, S. Shen, H. Xie, W. Shi, G. Zhang, B. Shen, L. Chen, B. Xiao, and M. Wei. Evolution of molten pool during selective laser melting of Ti-6Al-4V. *Journal of Physics D: Applied Physics*, 52(5):055302, 2018. doi:10.1088/1361-6463/aaee04.

[187] W. Zhang, M. Tong, and N. M. Harrison. Resolution, energy and time dependency on layer scaling in finite element modelling of laser beam powder bed fusion additive manufacturing. *Additive Manufacturing*, 28:610–620, 2019. doi:10.1016/j.addma.2019.05.002.

[188] Z.-D. Zhang, O. Ibhadode, U. Ali, C. F. Dibia, P. Rahnama, A. Bonakdar, and E. Toyserkani. Topology optimization parallel-computing framework based on the inherent strain method for support structure design in laser powder-bed fusion additive manufacturing. *International Journal of Mechanics and Materials in Design*, 16:897–923, 2020. doi:10.1007/s10999-020-09494-x.

[189] M. Zhu and R. Michalowski. Simulation of heat transfer in freezing soils using Abaqus. ABAQUS Users' Conference, 2005.

[190] T. I. Zohdi. *Modeling and Simulation of Functionalized Materials for Additive Manufacturing and 3D Printing: Continuous and Discrete Media*, volume 60 of *Lecture Notes in Applied and Computational Mechanics*. Springer International Publishing, Springer Cham, 1st edition, 2018. doi:10.1007/978-3-319-70079-3.

Publication series of the Institute of Mechanics

published to date:

2010/01   Palnau, V.: Implementierung eines netzfreien Diskretisierungsverfahrens und seine Anwendung auf die Scherbandanalyse.
ISBN 978-3-921823-51-4

2010/02   Klusemann, B.: Application of homogenization methods and crystal plasticity to the modeling of heterogeneous materials of technological interest.
ISBN 978-3-921823-53-8

2011/01   Hortig, C.: Local and non-local thermomechanical modeling and finite-element simulation of high-speed cutting.
ISBN 978-3-921823-54-5

2011/02   Parvizian, F.: Modeling of microstructure evolution in aluminum alloys during hot extrusion.
ISBN 978-3-921823-56-9

2011/03   Noman, M.: Characterization and model identification for the simulation of the forming behavior of ferritic steels.
ISBN: 978-3-921823-55-2

2011/04   Kayser, T.: Characterization of microstructure in aluminum alloys based on electron backscatter diffraction.
ISBN: 978-3-921823-57-6

2011/05   Bargmann, S.: Computational modeling of material behavior on different scales based on continuum mechanics.
ISBN: 978-3-921823-58-3

2013/01   Waffenschmidt, T.: Modelling and simulation of adaptation and degradation in anisotropic biological tissues.
ISBN: 978-3-921823-61-3

2015/01   Ostwald, R.: Modelling and simulation of phase-transformations in elastoplastic polycrystals.
ISBN: 978-3-921823-66-8

2016/01   Subramanian, M.: Phenomenological modelling and simulation of ferroelectric ceramics.
ISBN: 978-3-921823-74-3

2016/02   Clausmeyer, T.: Evolution of plastic anisotropy in metals.
ISBN: 978-3-921823-76-7

2017/01   Holtermann, R.: Computational multiscale modelling of grinding processes.
ISBN: 978-3-921823-86-6

2017/02   Bartels, A.: Modelling of evolving microstructures at different scales.
ISBN: 978-3-921823-93-4

2017/03   Dusthakar Kumar Rao, D. K.: Computational modelling of single and polycrystalline ferroelectric materials.
ISBN 978-3-921823-94-1

2019/01   Buckmann, K.: Microstructure evolution in functional magnetic materials.
ISBN 978-3-947323-09-8

2019/02   Kaiser, T.: Computational modelling of non-simple and anisotropic materials.
ISBN 978-3-947323-14-2

2019/03   Heitbreder, T.: Modelling of material interfaces at different length scales.
ISBN 978-3-947323-18-0

2020/01   Berthelsen, R.: Computational homogenisation of thermomechanical problems.
ISBN 978-3-947323-19-7

2020/02   Sievers, C.: Describing the macroscopic behavior of surfaces based on atomistic models.
ISBN 978-3-947323-24-1

2022/01   Rose, L.: Optimisation based parameter identification using optical field measurements.
ISBN 978-3-947323-31-9

2023/01   Langenfeld, K.: Continuum modeling of brittle and ductile damage: theory and computational frameworks.
ISBN 978-3-947323-41-8

2023/02   Schulte, R.: Parameter identification approaches with application to different classes of materials.
ISBN 978-3-947323-45-6

2023/03   Kaiser, T.: Multiscale multiphysics material modelling.
ISBN 978-3-947323-46-3

2024/01   Noll, I.: Thermomechanical modelling and simulation of laser powder bed fusion processes.
ISBN 978-3-947323-49-4